From the holdings of the Department of Special Collections , Princeton University Library, Princeton, NJ

These documents are either in the public domain, or can only be used for educational and research purposes (Fair use) as per U.S. Copyright law (text below). By accessing this file, all users agree that their use falls in the public domain or within fair use as defined by the copyrightlaw. We do not charge any permission or usage fees for the publication of images of material inour collections, including those provided by Princeton University Library, via our website, catalog, or directly from staff.For more information regarding copyright, credit, and citation please review the information onthe Copyright, Credit and Citation Guidelines page of our website.
https://library.princeton.edu/special-collections/policies/copyright-credit-and-citation-guidelines. If you have any questions, including how to order higher-quality images from the collection, contact Special Collections Public Services via our Ask Us! Form. https://library.princeton.edu/special-collections/ask-us

---

Doctoral Dissertations, 2011-2026 Astrophysical Sciences

2012

Non-ideal Magnetohydrodynamic Effects in Protoplanetary Disks

Bai, Xuening

Princeton, NJ : Princeton University

---

http://arks.princeton.edu/ark:/88435/dsp01vx021f147

U.S. Copyright law: The copyright law of the United States (Title 17, §108, United States Code) governs the making of photocopies or other reproductions of copyrighted material. Under certain conditions specified in the law, libraries and archives are authorized to furnish a photocopy or other reproduction. One of these specified conditions is that the photocopy or reproduction is not to be used for any purpose other than private study, scholarship, or research. If a user makes a request for, or later uses, a photocopy or reproduction for purposes in excess of fair use that user may be liable for copyright infringement. This institution reserves the right to refuse to accept a copying order if, in its judgment, fulfillment of the order would involve a violation of copyright law. https://www.copyright.gov/title17/title17.pdf

NON-IDEAL MAGNETOHYDRODYNAMIC EFFECTS IN PROTOPLANETARY DISKS

Xue-Ning Bai

A DISSERTATION

PRESENTED TO THE FACULTY

OF PRINCETON UNIVERSITY

IN CANDIDACY FOR THE DEGREE

OF DOCTOR OF PHILOSOPHY

RECOMMENDED FOR ACCEPTANCE

BY THE DEPARTMENT OF

ASTROPHYSICAL SCIENCES

ADVISOR: JAMES M. STONE

SEPTEMBER, 2012

© Copyright 2012 by Xue-Ning Bai
All rights reserved.

I certify that I have read this thesis and that in my opinion it is fully adequate, in scope and in quality, as a dissertation for the degree of Doctor of Philosophy.

James M. Stone
(Principal Advisor)

I certify that I have read this thesis and that in my opinion it is fully adequate, in scope and in quality, as a dissertation for the degree of Doctor of Philosophy.

Jeremy J. Goodman

I certify that I have read this thesis and that in my opinion it is fully adequate, in scope and in quality, as a dissertation for the degree of Doctor of Philosophy.

Stephen H. Lubow

Approved for the Princeton University Graduate School:

Dean of the Graduate School

Dedicated to my parents, Xiaoling Wang and Bin Bai

Abstract

The gas dynamics in protoplanetary disks (PPDs), particularly the level of turbulence as well as their global structure and evolution, are of crucial importance to many aspects of planet formation. Magnetic field is widely believed to play a crucial role in the gas dynamics, mainly via the magneto-rotational instability (MRI) or the magneto-centrifugal wind (MCW). In PPDs, however, these mechanisms are strongly affected by non-ideal magnetohydrodynamics (MHD) effects, including Ohmic resistivity, Hall effect and ambipolar diffusion (AD), due to the weak ionization level in PPDs. While Ohmic resistivity has been routinely included in the study of PPD gas dynamics, the Hall effects and AD have been largely ignored, even though they play an equally, if not more, important role.

In this thesis, the effect of AD is thoroughly explored via numerical simulations and the results are applied to estimate the effectiveness of the MRI in PPDs. The simulations show that MRI can always operate in the presence of AD for appropriate magnetic field strength and geometry. Stronger AD requires weaker magnetic field, and the most favorable field geometry involves the presence of both net vertical and net toroidal magnetic fluxes. Applying these results to PPDs, together with the results in the literature on the effect of Ohmic resistivity and the Hall term, a new theoretical framework is proposed to make optimistic estimates of the MRI-driven accretion rate. It is found that the MRI inevitably becomes inefficient in driving rapid accretion in the inner regions (~ 1 AU) of PPDs. It becomes more efficient in the outer disk ($\gtrsim 15$ AU), especially assisted by the presence of tiny grains.

The fact that MRI becomes inefficient at the inner PPDs makes the MCW scenario a promising alternative. By performing vertically stratified shearing-box simulations of PPDs that simultaneously include the effects of both Ohmic resistivity and AD in a self-consistent manner, it is found that in the presence of a weak net vertical magnetic field (plasma $\beta \sim 10^5$ at midplane), the MRI is completely suppressed in the inner region of PPDs, where the gas flow is purely laminar.

A strong MCW is launched robustly that efficiently carries away the disk angular momentum, with the resulting wind-driven accretion rate consistent with observations. This thesis concludes by proposing a new scenario on the accretion process in PPDs where the MCW and MRI operate at the inner and outer disks respectively.

Preface and Acknowledgements

This thesis collects part of my own work conducted at the Department of Astrophysical Sciences, Princeton University. The raw materials are based on five papers, four of which are already published:

1. *Heat and Dust in Active Layers of Protostellar Disks*, **Xue-Ning Bai & Jeremy Goodman**, ApJ 701, 737 (2009)

2. *Effect of Ambipolar Diffusion on the Nonlinear Evolution of the Magnetorotational Instability in Weakly Ionized Disks*, **Xue-Ning Bai & James M. Stone**, ApJ 736, 144 (2011)

3. *Magnetorotational-instability-driven Accretion in Protoplanetary Disks*, **Xue-Ning Bai**, ApJ 739, 50 (2011)

4. *The Role of Tiny Grains on the Accretion Process in Protoplanetary Disks*, **Xue-Ning Bai**, ApJ 739, 51 (2011)

5. *Non-turbulent Accretion of Protoplanetary Disks: Suppression of the MRI and Launching of Disk Winds*, **Xue-Ning Bai & James M. Stone**, in preparation

These materials are combined, re-organized and updated to provide the content of this thesis. More specifically, Bai & Stone (2011) forms the basis of Chapter 2; Bai (2011a) and Bai (2011b) are combined to form Chapter 3; Chapter 4 is based on Bai & Stone (2012b), which is close to be finished upon the submission of this thesis. Common materials that are broadly used throughout this thesis are either introduced in Chapter 1, or detailed in the Appendices. In particular, Appendix A contains the basic formulation of non-ideal MHD effects described in Bai (2011a,b); Appendix B contains the code tests in Bai & Stone (2011), as well as unpublished results on the implementation of the Hall effect; the chemistry model developed in Bai & Goodman (2009) is described Appendix C.

More materials could have been included in this thesis, especially my own work on the numerical simulations of planetesimal formation. It can be considered as an important physical implication of the non-ideal MHD gas dynamics of PPDs, and has lead to three publications (Bai & Stone 2010a,b,c). However, planetesimal formation is already a large topic by itself, while the current content of the thesis is much more logically-connected and self-contained.

I am indebted to my advisor Prof. James M. Stone, for providing me with the powerful tool: the Athena MHD code that he developed for years as the basis of my thesis research, for sharing with me his great expertise on both numerical techniques as well as scientific insight, for his generosity that supports me to travel world-wide and interact with international colleagues, especially at the initial stage of my thesis work, for his guidance on many aspects of my career development, and for always being open-minded and supportive to give me freedom to pursue my own research and personal interest.

I thank Prof. Jeremy Goodman, who first guided me into the field of planetary astrophysics where I found great research interest. With his continuous support and encouragement thereafter, my semester project with him eventually evolves into part of my thesis. Profs. Eugene Chiang, and Arieh Konigl, as well as Mr. Daniel Perez-Beker have provided valuable feedback to the content that appears in Chapters 3 and 4 of this thesis work. Altogether, I thank Profs. Bruce Draine, Jeremy Goodman, Roman Rafikov, and Ed Turner for serving in my thesis committee, and thank Profs. Jeremy Goodman and Steve Lubow for being willing to serve as my thesis readers.

I am very grateful my first semester project advisor Prof. Anatoly Spitkovsky, not only for offering me a great project to work on, but also for his patience that made me acquainted with many useful tools and greatly improved my scientific writing skills.

A substantial fraction of my knowledge is acquired from attending conferences and visiting other universities or institutions. Among them I would like to specially acknowledge the Issac Newton institute and other organizers for organizing and hosting the *Dynamics of Disks and Planets* programme in the Fall of 2009, when I just started my thesis. The experience was extremely helpful for me to establish the big picture of planet formation and to set my thesis work into context. I also thank Pascale Garaud and co-organizers for initiating and organizing the ISIMA program which I participated for two consecutive years with great experiences. I thank Doug Lin and co-organizers for hosting several conferences/workshops on disks and planets at the KIAA in Beijing that brought international experts together with fruitful achievements. More thanks are

deserved to Roy van Boekel and Greg Herczeg for organizing the Ringberg workshop for Transport Processes and Accretion in YSOs in 2011, and to Ralph Pudritz for organizing the conference on Origins of Stars and their Planetary Systems in 2012, when parts of this thesis were presented for the first time.

I thank Shane Davis, Tom Gardiner, Jake Simon and Zhaohuan Zhu for discussions with technical issues with the Athena MHD code, and together, I thank Alfred Glassgold, Geoffroey Lesur, Doug Lin, Gordon Ogilvie, Neal Turner, and Mark Wardle for helpful discussions. I also thank many of my colleagues (there are so many of them that I am simply unable to provide a full list of names) whom I have interacted with either in face, or via emails. The interactions were fruitful and I have benefited a lot.

The Department of Astrophysical Sciences at Princeton University has provided me with great academic resources and an extremely friendly atmosphere. I have benefited a great deal from the PhD program, especially from the semester project system and the graduate student seminar which substantially broadened my research horizon, from our director of graduate studies Prof. Jill Knapp, who is always so kind and supportive, from all the professors, colleagues and fellow students for creating and maintaining the highly intellectual environment, and from all the supportive staff members for their warm helps on technical and administrative affairs.

Most of the computer simulations in this thesis are performed on the computer resources provided by the Princeton Institute for Computational Science and Engineering (PICSciE), without whose resources and support this thesis research would not be possible. I also acknowledge NASA for continuous support during the last three years of my PhD program by awarding me the NASA Earth and Space Science Fellowship.

Finally and most importantly, I owe a great deal to my parents, for their constant and sustained care and support on my life and study. Although most of the time we live in different hemispheres, they are always with me in my heart.

Contents

Abstract **v**

Preface and Acknowledgements **vii**

1 Introduction **1**

1 Observations of Protoplanetary Disks 3

2 The Minimum-mass Solar Nebular Disk Model 8

3 Non-ideal MHD Effects 10

4 Mechanisms of Angular Momentum Transport 14

5 The Picture of Active Layer and Dead Zone 19

2 Effect of Ambipolar Diffusion on the Magnetorotational Instability **23**

1 Introduction 23

2 Simulation Setup 26

3 Net Vertical Flux Simulations 29

4 Net Toroidal Flux Simulations 40

5 Simulations with Both Vertical and Toroidal Fluxes 48

6 MRI with Ambipolar Diffusion: A Quantitative Criterion 53

3 Magnetorotational-Instability-Driven Accretion in Protoplanetary Disks **58**

1 Calculations of Non-ideal MHD Effects in PPDs 59
2 Criteria for MRI Turbulence and Efficient MRI-driven Accretion 64
3 Active Layer in the Fiducial Model 68
4 Parameter Study 80
5 Effect of Tiny Grains 87
6 Summary and Discussions 94

4 Launching Magneto-centrifugal Wind from Protoplanetary Disks 98

1 Introduction 99
2 Simulation Setup 102
3 Fiducial Simulations and Results 106
4 Nature of the Laminar Wind Solution 114
5 Parameter Study 123
6 Summary and Discussions 127

5 Conclusions and Outlook 133

1 Major Achievements 133
2 A New Scenario for the Accretion Process in PPDs 138
3 Future Directions 141

A A General Derivation of Non-ideal MHD Terms in Weakly Ionized Gas 145

1 General Derivation of Magnetic Diffusivities 145
2 The Effect of Charged Tiny Grains 147

B The Athena MHD Code and Implementation of Non-ideal MHD Terms 152

1 Basic Equations and Numerical Algorithms 152

2 Shearing-Box Approximation 153

3 Non-ideal MHD Terms: Implementation 155

4 Non-ideal MHD Terms: Tests 157

C Chemical Reaction Network: Description and Implementation 165

1 Gas-phase Reactions 165

2 Reactions with Dust Grains 166

3 Numerical Method 171

Bibliography 172

Chapter 1

Introduction

Protoplanetary disks (PPDs) are rotationally supported structures of gas surrounding pre-main-sequence stars, which form from the collapse of protostellar cores and angular momentum conservation (Adams et al. 1987). With a typical lifetime of $1 - 10$ Myrs (e.g., Hillenbrand et al. 1998; Sicilia-Aguilar et al. 2006), PPDs feed gas onto the central protostar, power outflows and/or jets, and provide raw materials for the formation of planetary systems. Although disks surrounding Classical T Tauri stars (low-mass pre-main-sequence stars that are actively accreting) are the most observationally studied prototypes, similar physical processes operate in disks around brown dwarfs and more massive stars. The structure, evolution and dispersal of PPDs are of crucial importance in understanding a wide range of physical problems, especially in the area of planet formation. Below I provide three examples.

- The initial stage of planet formation involves the growth of small interstellar medium (ISM) grains to millimeter or larger sizes. The ultimate grain size distribution, which provides the initial condition for planetesimal formation, is mainly determined by their collision velocities (see Blum & Wurm 2008 for a detailed review). The relative velocities between grains strongly depend on global disk structure and the level of turbulence: weak turbulence and small radial pressure gradient in PPDs are favorable for grain growth (Ormel & Cuzzi 2007; Brauer et al. 2008; Zsom et al. 2010).

- The second stage of planet formation is the assembly of millimeter or larger sized grains (or pebbles, rocks!) into planetesimals, which are kilometer sized bodies whose internal strength is dominated by self-gravity (see Chiang & Youdin 2010 for a detailed review). Being probably the least understood process in planet formation, the regime of planetesimal

formation involves mutual aerodynamic interactions between dust and gas, which is intimately connected to the gas dynamics and global structure of the PPDs (Johansen et al. 2007, 2009b; Bai & Stone 2010b,c; Lee et al. 2010; Youdin 2011).

- When planets form, their gravitational interactions with the gaseous PPDs leads to exchange of angular momentum and planet migration (see Kley & Nelson 2012 for a detailed review). Several regimes of planet-disk interaction exist, mainly depending on planet mass (Goldreich & Tremaine 1980; Lin & Papaloizou 1986), while in all cases, the torque exerted on the planet depends intricately on the disk physics. For example, the rate of type-I migration sensitively depends on the radial entropy gradient (Paardekooper et al. 2010), and density waves from disk turbulence leads to stochastic migration (Johnson et al. 2006; Nelson & Gressel 2010).

The global structure and evolution PPDs are intimately connected to the gas dynamics on small scales. There are two aspects that enter this connection: the mechanism of angular momentum transport, which largely determines the global structure and evolution of PPDs, and the level of turbulence, which provides turbulent diffusion and is generally believed to give rise to angular momentum transport. It is certain that magnetic fields play a critical role in these processes (see the review by Stone et al. 2000, and more recently by Armitage 2011), while in PPDs, the extremely weak level of ionization substantially reduces the coupling between gas and magnetic fields, as opposed to the case for fully ionized gas where magnetic flux is frozen in to the conducting plasma. The imperfect coupling between gas and magnetic fields (or finite gas conductivity) gives rise to non-ideal magnetohydrodynamics (MHD) effects, which turn out to be crucial in most regions of PPDs. This thesis explores in detail the non-ideal MHD effects on the angular momentum transport and turbulence in PPDs, and is organized as follows.

In Chapter 1, I provide the broad context of this thesis work, including a summary of observational properties of the PPDs, introduction to various mechanisms of angular momentum transport, particularly the magnetorotational instability (MRI, Balbus & Hawley 1991), explanations of the non-ideal MHD effects, current understanding of the PPD structure and evolution, as well as the fiducial PPD model that I will be using throughout this thesis work.

In Chapter 2, I describe our numerical simulations of the MRI that for the first time, take into account for the effect of ambipolar diffusion (AD, one of the non-ideal MHD effects) in an appropriate manner that is applicable to PPDs. The outcome of the simulations, combined with past work in the literature, is a set quantitative criteria on whether the MRI could operate given

the strength of the non-ideal MHD effects and the corresponding strength of the MRI turbulence. This chapter is based on the work of Bai & Stone (2011).

In Chapter 3, I apply the results obtained in Chapter 2 to PPDs and study the MRI driven accretion in PPDs. This requires evolving a large chemical reaction network to calculate the ionization level of the disk, which then gives the strength of non-ideal MHD effects. With a thorough exploration of parameter space, it is found that MRI driven accretion is insufficient to account for the observed accretion rate in most PPDs, contrary to general expectations. This chapter is based on the work of Bai & Goodman (2009) and Bai (2011a,b).

In Chapter 4, numerical simulations are performed for a local patch of a PPD that takes into account both Ohmic resistivity and AD. The diffusion coefficients of the non-ideal MHD terms are evaluated self-consistently based on chemistry calculations. It is found that MRI is completely suppressed in the inner region PPDs due to the non-ideal MHD effects and the amplification of magnetic field. In the mean time, a strong disk wind is launched that carries away angular momentum at a rate that is expected to be consistent with observations. This chapter is based on the work in progress Bai & Stone (2012b).

I summarize the main points of this thesis in Chapter 5, with an overlook of future developments in this field. Particularly, it will be crucial to perform global simulations of PPDs with different magnetic field geometries in order to fully understand the structure and evolution of PPDs.

Three appendices are attached to the end of this thesis providing most technical details. In Appendix A I give the most general formulation of all non-ideal MHD effects in the single-fluid framework applicable to weakly ionized gas. Various limits are derived, highlighting the limit in the presence of abundant tiny grains (Bai 2011b). In Appendix B I describe the Athena MHD code used in the numerical simulations in Chapters 2 and 4, with particular focus on the implementation of the non-ideal MHD terms. In Appendix C I provide the details of the complex chemical reaction network used in my calculations for Chapters 3 and 4, which is developed in the work of Bai & Goodman (2009).

1. Observations of Protoplanetary Disks

In this section the basic observational facts of PPDs that are most relevant to this thesis is summarized. More details can be found in the recent review by Williams & Cieza (2011).

1.1 Classification

Observationally, young stellar objects (YSOs) are classified based on the slope $\alpha_{\rm IR}$ of the spectral energy distribution (SED) between about 2μm and 25μm (Lada 1987; Greene et al. 1994). Class 0 and Class I objects have large $\alpha_{\rm IR} > 0.3$ and are generally heavily obscured by the envelope that still undergoes gravitational infall onto the protostar. They have relatively short lifetime of the order 10^5 years. The entire disk become visible for Class II objects, with $-1.6 \lesssim \alpha_{\rm IR} \lesssim -0.3$. They generally exhibit signatures of active accretion and have typical lifetime of 10^6 to 10^7 years. Class III objects have $\alpha_{\rm IR} < -1.6$, with little evidence of accretion, and are generally considered to be passive as the disk gradually disperses away. In parallel, YSOs with optically visible disks are commonly classified into classical T Tauri stars (CTTS) and weak-lined T Tauri stars (WTTS). This classification scheme is accretion based: CTTS show strong Hα and UV emission, a signature of active accretion, while WTTS have little or no indication of accretion. They are closely related (though not exactly) to Class II and III objects respectively.

This thesis focuses on the Class II or the CTTS phase of a YSO which marks the end of envelope infall and the PPD has become visible and is actively accreting. PPDs spend most of the time in this phase during which planet formation takes place.

1.2 Dust in PPDs

PPDs contain about 1% in mass of dust grains with a wide size range from sub-micron up to millimeter or larger (see Natta et al. 2007 for a review). They absorb protostellar light, and reemit at longer wavelengths, giving rise to excess emission on top of the protostellar spectrum from infrared (IR), which is highly opaque, to millimeter wavelengths, which is mostly optically thin. The disk SEDs contain rich information about dust size and composition. Although parameters for modeling PPD SEDs are very degenerate (Chiang et al. 2001), there is strong evidence that a substantial fraction of grains have grown to micron size or larger (D'Alessio et al. 2001; van Boekel et al. 2004, 2005). Moreover, by detailed modeling of the SEDs from recent mid- and near-IR observations (Hartmann et al. 2005), D'Alessio et al. (2006) found that grains in the disk upper layer should be depleted by at least a factor of 10 relative to interstellar dust-to-gas ratios, and perhaps by 10^2 to 10^3. Observations at (sub)millimeter wavelength further reveal the common

existence of millimeter and even centimeter sized grains (Wilner et al. 2005), and such large grains are likely to be in place within 1 Myr for the majority of PPDs (Rodmann et al. 2006).

1.3 Disk Mass and Structure

The dust emission is the primary diagnostics of PPD structure and composition. PPDs are well known to have flared (concaved) surface due to the super-heated dust by the intensive protostellar radiation that gives rise to a relatively slow decline of the SED with increasing wavelength (Chiang & Goldreich 1997, 1999). The surface density distribution and total mass of PPDs are best determined from (sub)millimeter (interferometric) observations of the dust. Given the dust opacity and assuming optically thin (almost always the case), the disk mass can be estimated by assuming some dust to gas mass ratio, commonly taken to be 1%. The measured disk mass in nearby low-mass star formation regions is generally $10^{-2\pm1}M_{\odot}$ (Andrews & Williams 2005), and the surface density distribution in the outer disk ($\gtrsim$ 40AU) roughly follows a power law dependence on radius with an averaged slope of around -0.9, and has an exponential cutoff at around 100 AU (Andrews et al. 2009, 2010). It is yet to probe the density profiles at the inner disk, which is expected to occur soon as *ALMA* is now in operation.

1.4 Molecular Gas

The gas component in PPDs is much more difficult to detect than dust since it only produces line emission at specific wavelengths which requires high-resolution spectroscopy to study the kinematics. At optical to IR wavelength when the dust emission is optically thick, a line must have higher excitation temperature to stand out on top of the dust emission. Observations of gas molecules directly enables the study of PPD chemistry hence the thermal environment in PPDs. Moreover, the molecular line profiles encodes important information about the gas dynamics such as potential sub-Keplerian motion and turbulence. The fundamental CO emission line has been frequently observed in CTTSs, with the likely origin of the protostellar disks within 1-2 AU (e.g., Najita et al. 2003). Recently, discoveries of organic and water molecules by *Spitzer* have been reported (Carr & Najita 2008; Salyk et al. 2008; Pontoppidan et al. 2010), many of which are important coolants and also of great astrobiological interest. Based on the derived temperature and column density, these emission lines may originate from a UV-heated layer above the disk surface

in the inner region (< 5 AU) of young PPDs. At (sub)millimeter wavelength regime, low-energy rotational transition lines provide sensitive probe of disk structure and temperature, as well as the gas dynamics. Most relevant to this thesis is the constraints on the level of turbulence in the outer disk of PPDs by Hughes et al. (2011), who obtained $\alpha \approx 10^{-2}$ (see Section 4 for definition).

1.5 Transition Disks

Transition disks are identified as YSOs with little or no excess emission at $\lambda < 10\mu$mm and a significant excess at $\lambda > 10\mu$m (e.g., Calvet et al. 2002, 2005). The lack of near-IR excess is indicative of missing dust emission from the inner disk, and millimeter interferometric observations have later confirmed the existence of the inner cavities in such disks (Hughes et al. 2007). Statistically, transition disks represent at most 20% of the total disk population (Najita et al. 2007), while they attract great research interest due to their natural connection with global disk evolution and potential association with planet formation. Recently, disks with evidence for an optically thin gap separating the optically thick inner and outer disk components have been discovered (Espaillat et al. 2007, 2010), and are termed "pre-transition" disks as they are believed to be precursors of transition disks. The nature and formation mechanisms for transition disks are still under active exploration. In particular, most recent observations of polarized near-IR light from transitional disks by the Subaru telescope have revealed no inner cavities, which may suggest the presence of small but not large dust in the inner disk (Dong et al. 2012).

1.6 Disk lifetime

PPDs disperse and dissipate as they evolve due to accretion, outflow and photoevaporation. Constraints on disk lifetimes are mostly obtained by observing the thermal emission of the dust grains in near-IR to mid-IR from the *Spitzer* telescope. By surveying the disks in nearby star-forming regions, it is found that the fraction of the YSOs containing near-IR and mid-IR excess emission (indicative of a dusty disk) decreases with the age of the star-forming region. Very young embedded clusters (age ≤ 1 Myr) show disk fractions of the order 70% to 80% (Gutermuth et al. 2008). For clusters with ages in the 2- to 3-Myr range, the disk fraction reduces to about 40% to 50% (Lada et al. 2006). The disk fraction drops to below 20% in clusters of about 5 Myr old, and by $\sim 8 - 10$ Myr, IR excess emission become exceedingly rare ($\lesssim 5\%$, Sicilia-Aguilar et al.

2006). Combining all the available observations, PPDs have a median lifetime of about 3 Myr but vary from less than 1 Myr to a maximum of about 10 Myr.

1.7 Accretion

Protostars accrete mass from PPDs. The accretion rate $\dot{M}$ can be inferred from the luminosity $L_{\rm acc}$ of the UV excess emission that veils the intrinsic photospheric spectrum of a YSO, which comes from the standing accretion shock formed at the stellar surface which converts gravitational energy into heat and radiation (Calvet & Gullbring 1998; Gullbring et al. 2000).

$$L_{\rm acc} = \frac{GM_*\dot{M}}{R_*}\left(1 - \frac{R_*}{R_{\rm in}}\right) \approx 0.8\frac{GM_*\dot{M}}{R_*} \ , \tag{1-1}$$

where M_* and R_* are the mass and radius of the protostar, $R_{\rm in} \approx 5R_*$ is the truncation radius of the inner disk, based on magnetospheric accretion models. In practice, the accretion rate $\dot{M}$ are more commonly inferred from emission line profiles, in particular the Hα line, whose strength correlate with $L_{\rm acc}$ (Muzerolle et al. 1998, 2001). Due to the large uncertainties in the magnetospheric models, the measured accretion rates are typically uncertain by to a factor of about 3.

Compiling large samples of CTTS, the accrretion rate $\dot{M}$ is found to be about $10^{-8\pm1} M_\odot$ yr^{-1} (Hartmann et al. 1998; Calvet et al. 2004). Over a mass range of protostars, accretion rate is found to scale with protostellar mass M roughly as $\dot{M} \propto M^2$, though with large scatter (Muzerolle et al. 2005; Natta et al. 2006; Herczeg & Hillenbrand 2008; Fang et al. 2009). Moreover, $\dot{M}$ decreases rapidly with stellar age (e.g., Sicilia-Aguilar et al. 2005). Transition disks are also observed to be actively accreting, with the median accretion rate of about a few times $10^{-9} M_\odot$ yr^{-1} (Najita et al. 2007; Sicilia-Aguilar et al. 2010). Note that accretion rates can only be measured or inferred at the protostellar photosphere. While it does not necessarily be equal to the $\dot{M}$ in the disk at all times and at all radii, the disk must supply such an inflow of mass in the time-averaged sense which provides a most useful constrains on the gas dynamics, as we shall discuss in Section 4.

1.8 Outflow

Jets and molecular outflows are ubiquitous among YSOs (see Ray et al. 2007 for a review). The velocity of the outflow ranges from a few hundred km s^{-1} for the axial high-velocity component (HVC) that propagate to large distances, to about $10 - 50$ km s^{-1} for the so-called low-velocity

component (LVC) that is more extended (Hirth et al. 1997; Pyo et al. 2003). The outflow is strongly collimated at large distance ($\sim$ 1000 AU scale), with typical opening angle of just a few degrees, while large opening angles ($20 - 30^\circ$) are inferred at scales of 10 AU or less (Woitas et al. 2002; Hartigan et al. 2004). It has been well established that outflow is associated with the accretion phenomenon, with the mass outflow rate being about 10% of the mass accretion rate (Cabrit et al. 1990; Hartigan et al. 1995). The accretion-ejection correlation leads to close studies of the launching region on the outflow. Using the Hubble Space Telescope, Bacciotti et al. (2002) obtained information about the wind velocity field within 100 AU scale of the source DG Tau and found evidence of jet rotation, and Anderson et al. (2003) further showed that the LVC in this source originates from an extended region of about $0.3 - 4.0$ AU from the disk. These observations reveal that the inner region of PPDs plays an important role in the connection between accretion and outflow.

2. The Minimum-mass Solar Nebular Disk Model

The starting point for the theoretical study of PPDs in this thesis work is a disk model[1]. Fiducially, we take the minimum-mass solar nebula (MMSN) model (Weidenschilling 1977; Hayashi 1981) , which is constructed by smearing the required total mass (including the gas) for forming the solar system planets *in situ* into a smooth surface density mass distribution. Obviously, the assumption of *in situ* planet formation scenario has become far outdated, and the exoplanetary systems do not obey the MMSN at all, it at least represents the minimum amount of disk mass need to form the solar system planets, and is widely adopted partly because of its simplicity, and also partly because of the lack of constraints from observations of nearby YSOs on the surface density profile of the inner disks.

We use cylindrical coordinate system (R, ϕ, z) to denote radial, azimuthal and vertical coordinates. In the MMSN model, the surface mass density $\Sigma(R)$ and disk temperature $T(R)$ are given by

$$\begin{aligned} \Sigma &= 1700 R_{\rm AU}^{-3/2} \text{ g cm}^{-2} \ , \\ T &= 280 R_{\rm AU}^{-1/2} \text{ K} \ , \end{aligned} \tag{1-2}$$

[1]Eventually, if one understood the process of angular momentum transport well enough, it would be possible to construct more realistic, steady state disk models. However, this is far from achieved, and this thesis aims at a better understanding of the angular momentum transport process in PPDs.

where $R_{\rm AU}$ is the cylindrical radius measured in AU, and the disk is assumed to be vertically isothermal, with pressure $P = \rho c_s^2$ where c_s is the isothermal sound speed. By default, we take the mass of the proto star to be $M_* = 1 M_\odot$, with Keplerian frequency $\Omega(R)$ given by

$$\Omega = \sqrt{GM_*/R^3} = 2.0 \times 10^{-7} R_{\rm AU}^{-3/2} \ {\rm s}^{-1} \ . \tag{1-3}$$

Taking the mean molecular weight of the gas to be $\mu = 2.34$, we obtain the sound speed

$$c_s = \left(\frac{kT}{\mu m_H} \right)^{1/2} = 0.99 \, R_{\rm AU}^{-1/4} {\rm km \, s^{-1}} \ , \tag{1-4}$$

disk scale height H:

$$H = c_s/\Omega = 0.03 R_{\rm AU}^{5/4} \ {\rm AU} \ , \tag{1-5}$$

and the volume density ρ:

$$\rho(R,z) = \rho_{\rm mid}(R) \exp(-z^2/2H^2) \, , \qquad \rho_{\rm mid}(R) = \frac{\Sigma}{\sqrt{2\pi} H} = 1.4 \times 10^{-9} R_{\rm AU}^{-11/4} \ {\rm g \, cm^{-3}} \, . \tag{1-6}$$

Note that the MMSN disk flares, that is, H/R increases with R, consistent with observations summarized in the previous section.

In Chapter 3, we also consider another solar nebula model proposed by Desch (2007), which takes into account the recent advances in the planet formation theory (in particular, the "Nice" model, Tsiganis et al. 2005), and is much more massive than the MMSN. The surface density and temperature profiles are given by

$$\begin{aligned} \Sigma &= 5 \times 10^4 R_{\rm AU}^{-2.17} \ {\rm g \ cm^{-2}} \ , \\ T &= 150 R_{\rm AU}^{-0.43} \ {\rm K} \ , \end{aligned} \tag{1-7}$$

where the temperature profile is estimated from Chiang & Goldreich (1997).

Submillimeter interferometric observations of the ~ 1 Myr old Ophiuchus star forming regions by Andrews et al. (2009, 2010) have revealed the density profiles in the outer regions ($\gtrsim 10$ AU, due to limited spatial resolution) for a sample of PPDs. The surface density for the majority of the disks appears to match the MMSN value reasonably well at $10 - 20$ AU. Although the fitted density profile in the outer disk is shallower than the MMSN and the Desch's model (with the median slope of -0.9 rather than -1.5 or -2.2), the surface density profile of the inner disk is not well constrained by observations, and both MMSN and the Desch's model may be viable choices.

3. Non-ideal MHD Effects

Most astrophysical gas is fully or sufficiently ionized so that it behaves as a perfect conductor, hence the electric field in a frame co-moving with the gas is zero. Such gas is said to be in the ideal magnetohydrodynamics (MHD) limit. Non-ideal MHD effects result from finite the conductivity of the gas, and is particularly important when the gas is very weakly ionized. To get a rough estimate on how weakly ionized the gas in PPDs is, we consider a simple ionization-recombination balance, with ionization rate of the order $\xi \sim 10^{-17}$ s^{-1}, appropriate for cosmic-ray ionization (Umebayashi & Nakano 1981), and an effective recombination rate coefficient $k_e = 3 \times 10^{-6}/\sqrt{T}$ cm^3 s^{-1} (Oppenheimer & Dalgarno 1974), where T is temperature measured in Kelvin. The ionization fraction $x_e = n_e/n_H$ is given by

$$x_e \approx \frac{1}{2}\sqrt{\frac{\xi}{k_e n_{\rm H_2}}} = 1.2 \times 10^{-12}\left(\frac{T}{300{\rm K}}\right)^{1/4}\left(\frac{\xi}{10^{-17}{\rm s}^{-1}}\right)\left(\frac{n_{\rm H_2}}{10^{13}{\rm cm}^{-3}}\right)^{-1/2} , \tag{1-8}$$

where $n_{\rm H_2}$ is the number density of the H_2 molecule (the predominant gas species). It becomes clear that PPDs are extremely weakly ionized.

Non-ideal MHD effects come in three flavors (see full derivations in Appendix A). They all derive from the generalized Ohm's law, which is essentially a force-balance between acceleration of charged particles by electromagnetic field and collisional drag with the neutrals. In the absence of magnetic field, current flows along the direction of the electric field $\boldsymbol{J} = \sigma \boldsymbol{E}$, which defines the conductivity σ, and resistivity $\eta_O = c^2/4\pi\sigma$. In the presence of magnetic field, however, the direction of $\boldsymbol{J}$ is no longer along $\boldsymbol{E}$ since the trajectory of charged particles are affected by the magnetic field $\boldsymbol{B}$. In this case, conductivity becomes a tensor, and gives rise to two additional non-ideal MHD effects, namely, the Hall effect and ambipolar diffusion (AD). The most commonly adopted (but not always applicable) formula for the non-ideal MHD electromotive force (EMF) $\mathcal{E}_n$ reads

$$\mathcal{E}_n = \frac{4\pi\eta_O}{c}\boldsymbol{J} + \frac{\boldsymbol{J}\times\boldsymbol{B}}{en_e} - \frac{(\boldsymbol{J}\times\boldsymbol{B})\times\boldsymbol{B}}{c\gamma_i\rho\rho_i} , \tag{1-9}$$

where n_e is the electron number density, ρ and ρ_i are the density of the gas and ions respectively, γ_i is the rate coefficient for ion-neutral momentum exchange, defined after Equation (A-1), and $\boldsymbol{J} \equiv (c/4\pi)\nabla \times \boldsymbol{B}$ is the current density. The three terms on the right hand side correspond to Ohmic resistivity, Hall effect and AD respectively. Ohmic resistivity mainly originates from collisions between electrons and neutrals, with diffusion coefficient approximately given by (Blaes

& Balbus 1994)

$$\eta_O = \frac{c^2 m_e \gamma_e \rho}{4\pi e^2 n_e} \approx 230 x_e^{-1} T^{1/2} \text{ cm}^2 \text{ s}^{-1} \ , \tag{1-10}$$

where γ_e is the rate coefficient for electron-neutral momentum transfer, again defined after Equation (A-1). It is common to quantify the strength of the Hall and AD terms with by their corresponding magnetic diffusion coefficients

$$\eta_H = \frac{cB}{4\pi e n_e} \ , \qquad \eta_A = \frac{B^2}{4\pi \gamma_i \rho \rho_i} \ . \tag{1-11}$$

For charged species (electrons and ions, and potentially grains), we further define the Hall parameter β_j (where $j = i, e$ for electrons/ions), ratio between the gyro-frequency and the momentum exchange rate with the neutrals

$$\beta_j \equiv \frac{|Z_j| eB}{m_j c} \frac{1}{\gamma_j \rho} \ , \tag{1-12}$$

where Z_j is the charge. Charged species j is strongly coupled with neutrals if $\beta_j \ll 1$, and is strongly tied to magnetic fields when $\beta_j \gg 1$. As electrons are much more mobile than the ions, $\beta_e \gg \beta_i$ (see Section 1.3 of Chapter 3 for an estimate the Hall parameters). Comparing the magnetic diffusion coefficients for Ohmic resistivity (1-10), Hall and AD (1-11), we find

$$\frac{\eta_H}{\eta_O} = \beta_e \ , \qquad \frac{\eta_A}{\eta_H} = \beta_i \ . \tag{1-13}$$

Therefore, Ohmic resistivity is the dominant non-ideal MHD effect when $\beta_i \ll \beta_e \ll 1$, where both electrons and ions are coupled to the neutrals, Hall effect dominates when $\beta_i \ll 1 \ll \beta_e$, where electrons are couple to the magnetic field and ions are coupled to the neutrals, while AD dominates when $1 \ll \beta_i \ll \beta_e$, where both electrons and ions are coupled to the magnetic field. Since $\beta_j \propto B/\rho$, we see that Ohmic resistivity dominates in high density regions with weak field, AD dominates in low density regions with strong field, while the Hall regime lies in between.

A simple way to understand the Hall effect and AD is by noticing that electrons are generally the most mobile species and dominate electric conduction, hence magnetic fields are effectively carried by the electrons. In the frame of the gas (or neutrals), the EMF is therefore $\boldsymbol{\mathcal{E}}_n = -\boldsymbol{v}_e' \times \boldsymbol{B}$ where $\boldsymbol{v}_e'$ is the relative velocity between the electrons and the neutrals. One can further decompose $-\boldsymbol{v}_e' = (\boldsymbol{v}_i' - \boldsymbol{v}_e') - \boldsymbol{v}_i'$ where $\boldsymbol{v}_i'$ is the relative velocity between the ions and the neutrals.. Note that $\boldsymbol{v}_i' - \boldsymbol{v}_e' = \boldsymbol{J}/en_e$, while $\boldsymbol{v}_i' = \boldsymbol{J} \times \boldsymbol{B}/c\gamma_i \rho \rho_i$ (see Equation A-1). Now it becomes clear that the Hall effect corresponds to the electron-ion drift, while AD corresponds to the ion-neutral drift.

We note that the non-ideal MHD effects for weakly ionized gas is incorporated into a single-fluid framework (or the "strong coupling" limit), where the fluid density and velocities represent the

density and velocities of the neutrals, while electron-ion drift and ion-neutral drift are reflected into the non-ideal MHD EMFs. The single-fluid framework applies when the inertia of all charged species are dynamically negligible[2], hence their motion is virtually force-free, set by the balance between Lorenz force and collisions with the neutrals (see Equation A-1). Multi-fluid prescriptions for AD are also common, where ions and neutrals are treated as separate fluids (e.g., Toth 1994; Stone 1997; Smith & Mac Low 1997; Falle 2003; Li et al. 2006; O'Sullivan & Downes 2006, 2007; Tilley & Balsara 2008). Although they are mathematically equivalent to the single-fluid framework as $\rho_i/\rho \to 0$ while keeping $\gamma_i \rho_i$ constant, multi-fluid numerical algorithms for AD are generally unable handle the stiffness of the strong-coupling limit, and are only applicable to the regime with much higher level of ionization and much lower gas density than that in PPDs when the ion inertia becomes non-negligible, such as in the study of star formation, turbulence and shocks in the interstellar medium.

Strictly speaking, the formula (1-9) applies only for the case where charged particles are exclusively made of electrons and a single species of ions. In practice, it also applies in the presence of multiple ion species, as long as no charged grains are involved (Bai 2011b). We use the simplified formula in this section since it best demonstrates the basic physics. In Appendix A, we provide the most generalized derivation of these non-ideal MHD terms that can incorporate arbitrary number of positively and negatively charged species. The generalized formula, given by equations (1-12), (A-4) and (A-6), are the ones used in all the chemistry calculations in this thesis work. In particular, we further derive analytically the limiting behaviors of η_H and η_A as a function of B in the presence of tiny grains $\lesssim 0.01\mu$m (Bai 2011b).

The non-ideal MHD effects affect the propagation of MHD waves, and lead to energy dissipation, with the energy dissipation rate given by

$$\dot{E} = \frac{1}{c}\mathcal{E}_n \cdot \boldsymbol{J} = \frac{4\pi}{c^2}(\eta_O J^2 + \eta_A J_\perp^2) \ , \tag{1-14}$$

where $\boldsymbol{J}_\perp$ is the current density perpendicular to the direction of magnetic field. We see that the Ohmic resistivity dissipates the total current (leading to magnetic reconnection), while AD damps the perpendicular component of the current (via ion-neutral drag). In the linear regime, Ohmic resistivity and AD simply damps all three families of MHD waves (but in different ways). On the other hand, the Hall effect is not dissipative. It describes magnetic diffusion due to the drift motion

[2]More formally, the time scale for a charged particle to exchange momentum with neutrals is much shorter than that for a neutral particle to exchange momentum with charged particles.

between electrons and ions without breaking magnetic field lines, and is also present in fully ionized plasma. As a non-dissipative effect, the Hall term does not give wave damping, but breaks the degeneracy between the left- and right-handed Alfvén waves, with the wave dispersion relation (see Appendix B, Section 4.4 for details)

$$\omega^2 = \left(1 \pm \frac{\omega}{\omega_h}\right) k^2 v_A^2 \cos^2\theta \ , \tag{1-15}$$

where the plus and minus sign corresponding to right- and left-handed Alfvén waves respectively. Here $v_A = B/\sqrt{4\pi\rho}$ is the Alfvén velocity, $\omega_h \equiv en_eB/\rho c = (\rho_i/\rho)\omega_i$ is the cutoff frequency of the left-handed Alfvén wave, $\omega_i = eB/m_ic$ is the ion cyclotron frequency, θ is the angle between the wave vector $\boldsymbol{k}$ and the direction of magnetic field. In particular, the right-handed Alfvén wave is well known as the whistler wave, whose dispersion relation at large k asymptotes to $\omega \propto k^2$, which is notoriously troublesome in numerical simulations.

The strength the non-ideal MHD terms is conveniently measured in dimensionless Elsasser numbers. In a rotation system with angular frequency Ω, Elsasser numbers for Ohmic resistivity, Hall effect and AD are defined respectively as

$$\Lambda \equiv \frac{v_A^2}{\eta_O\Omega} \ , \qquad Ha \equiv \frac{v_A^2}{\eta_H\Omega} \ , \qquad Am \equiv \frac{v_A^2}{\eta_A\Omega} \ . \tag{1-16}$$

The ideal MHD limit corresponds to $\Lambda \to \infty$, $Ha \to \infty$ and $Am \to \infty$, while when any of these numbers reaches order unity or smaller, non-ideal MHD EMFs become comparable or larger than the inductive EMFs, and the gas dynamics will significantly depart from the ideal MHD case. Using equations (1-11), we can re-arrange the Hall and AD Elsasser numbers into

$$Ha \equiv \frac{\omega_h}{\Omega} \ , \qquad Am \equiv \frac{\gamma_i\rho_i}{\Omega} \ . \tag{1-17}$$

Physically, the Hall Elsasser number is the ratio of the cutoff frequency of the left-handed Alfvén waves to the Orbital frequency, while the AD Elsasser number is the number of times a neutral molecule collides with the ions in a dynamical time.

To obtain a rough estimate on the strength of non-ideal terms in PPDs, we calculate the Elsasser numbers using Equations (1-10) and (1-11) for diffusion coefficients and the MMSN model for gas density and temperature, and obtain (Bai & Stone 2012b)

$$\Lambda = \frac{v_A^2}{\eta_O\Omega} \approx 0.12\left(\frac{x_e}{10^{-12}}\right)\left(\frac{100}{\beta}\right) R_{\rm AU}^{5/4} \ , \tag{1-18}$$

$$Ha = \frac{en_eB}{\rho c\Omega} \approx 0.037\left(\frac{x_e}{10^{-12}}\right)\sqrt{\frac{100}{\beta_{\rm mid}}} R_{\rm AU}^{-1/8} \ , \tag{1-19}$$

$$Am = \frac{\gamma_i \rho_i}{\Omega} \approx 3.3 \left(\frac{x_e}{10^{-12}} \right) \left(\frac{\rho}{\rho_{\rm mid}} \right) R_{\rm AU}^{-5/4} \ , \tag{1-20}$$

where plasma $\beta \equiv P_{\rm gas}/P_{\rm mag}$ is the ratio of gas to magnetic pressure, $\beta_{\rm mid}$ is otherwise the same as β but uses the midplane gas pressure (see Figure 3.2 in Chapter 3 for the relative importance of the three terms at different disk locations). We see that for the typical parameters in PPDs, all three non-ideal MHD effects are essential ingredients of the gas dynamics. In particular, Ohmic resistivity dominates in the very inner disk near the midplane, AD dominates in the outer disk as well as the surface of inner disk, while the Hall dominated regime lies in between. Most studies of non-ideal MHD effects in the literature considered only the Ohmic resistivity, while we see here that Hall effect and AD are equally (if not more) important in PPDs. This thesis represents the first through exploration on the effect of AD, while the exploration of the Hall effect is in progress while this thesis is being written.

4. Mechanisms of Angular Momentum Transport

The fact that PPDs are actively accreting requires outward transport of angular momentum. Angular momentum transport is the most fundamental problem in the accretion disk theory, which is determined by the internal gas dynamics in the disk, and largely determines the global disk evolution.

There are fundamentally two says angular momentum can be transported in accretion disks: radial transport (or redistribution) within the disk, and vertical transport (loss) from the disk. For a thin disk, the radial angular momentum flux $\dot{J}$ reads

$$\dot{J} = -\dot{M} j_0 + W \ , \tag{1-21}$$

where $\dot{M}$ is the mass accretion rate (positive), $j_0 = \Omega R^2$ is the specific angular momentum, and

$$W = 2\pi R^2 \int_{-\infty}^{\infty} dz T_{r\phi} = 2\pi R^2 \int_{-\infty}^{\infty} dz \left(\overline{\rho v_{R1} v_{\phi 1}} - \frac{\overline{B_R B_\phi}}{4\pi} + \frac{\overline{\partial_R \psi_i \partial_\phi \psi_i} - \overline{\psi_i \partial^2_{R\phi} \psi_i}}{8\pi G R} \right) . \tag{1-22}$$

In the above, the three terms represent torque generated by the turbulent Reynolds stress, Maxwell stress and gravitational stress respectively. Their sum gives the $R\phi$ component of the total stress tensor $T_{R\phi}$, with the overlines denoting azimuthal averages; v_{R1} and $v_{\phi 1}$ represent fluctuations over the mean flow (e.g., radial accretion flow and Keplerian motion), ϕ_i is the gravitational potential from the disk's self-gravity.

The radial transport of angular momentum generally requires MHD and/or gravitational turbulence. One can measure the time and spatial averaged stress from the saturated state of the turbulence to obtain $T_{R\phi}$, which is most conveniently normalized by the gas pressure (Shakura & Sunyaev 1973)

$$T_{r\phi} = \alpha P_{\rm gas} \ . \tag{1-23}$$

The value of α characterizes the efficiency of angular momentum transport and in general $\alpha \lesssim 1$. We emphasize that although most phenomenological disk models are assumes some constant value of α as a free parameter, the true value of α is determined by the microphysics in the accretion disk. One major strength of numerical simulations is to measure the value of α from first principles (as we study in Chapter 2) and to come up with a physical (rather than phenomenological) parameterization of α (as we use in Chapter 3).

The vertical angular momentum transport generally requires a disk wind, with integrated angular momentum loss rate given by

$$\dot{J}_w(R) = \int_{R_i}^{R} \frac{d\dot{M}_w}{dR'} j_0 dR' + \int_{R_i}^{R} dR' \int R' d\phi \left(\overline{\rho v_z v_{\phi 1}} - \frac{\overline{B_z B_\phi}}{4\pi} \right) R' \Big|_{z=-\infty}^{\infty} \ , \tag{1-24}$$

where R_i is the inner radius of the accretion disk, and

$$\dot{M}_w(R) = \int_{R_i}^{R} dR' \int R' d\phi (\rho v_z) \Big|_{z=-\infty}^{\infty} \ , \tag{1-25}$$

is the wind mass loss rate (positive for mass loss). The terms in the big parenthesis are again the the Reynolds sand Maxwell stresses, with their sum giving the $z\phi$ component of the total stress tensor $T_{z\phi}$.

With the above equations, the law of angular momentum conservation reads

$$\frac{\partial}{\partial t}(2\pi R \Sigma j_0) + \frac{\partial \dot{J}}{\partial R} + \frac{\partial \dot{J}_w}{\partial R} = 0 \ . \tag{1-26}$$

In the absence of wind, and further assuming isothermal equation of state (as in MMSN) and steady-state accretion, we find

$$\dot{M}\Omega = 2\pi \int dz T_{R\phi} = 2\pi \alpha c_s^2 \Sigma \ , \quad \Rightarrow \quad \alpha = \frac{\dot{M}\Omega}{2\pi \Sigma c_s^2} \ , \tag{1-27}$$

which reveals a direct relation between α and $\dot{M}$.

In the absence of radial transport, and further assuming steady-state accretion *in the disk zone*, we find

$$\dot{M} \frac{dj_0}{dR} = 2\pi R^2 T_{z\phi} \Big|_{-\infty}^{\infty} \ , \quad \Rightarrow \quad \dot{M}\Omega = 4\pi R T_{z\phi} \Big|_{-\infty}^{\infty} \ . \tag{1-28}$$

We see that given the same level of stress $T_{R\phi}$ and $T_{z\phi}$, wind transport is more efficient than the radial transport by a factor of about R/H.

In PPDs, several angular momentum transport mechanisms, by means of either turbulence or disk wind, are possible, as we summarize in this section. We show that the magnetorotational instability (MRI) and the magnetocentrifugal wind (MCW) are the most relevant for PPDs (i.e., for the Class II phase or CTTS where infall from gas envelope has ceased), and they will be the focus of this thesis.

4.1 Gravitational Instability

Gravitational instability (GI) in rotating disks occurs when the self-gravity of the gaseous disk overwhelms pressure support and rotation. In non-magnetized disks, the linear stability of a thin axisymmetric disk is determined by the Toomre's Q parameter (Toomre 1964)

$$Q \equiv \frac{c_s \kappa}{\pi G \Sigma} \ , \tag{1-29}$$

where κ is the epicyclic frequency (of radial oscillations), and in the case of Keplerian disks, we simply have $\kappa = \Omega$. The disk becomes gravitationally unstable when $Q < 1$. In the context of PPDs, achieving GI requires

$$\Sigma > 9.4 \times 10^4 \left(\frac{M_*}{M_\odot}\right)^{1/2} \left(\frac{T}{280\mathrm{K}}\right)^{1/2} R_{\mathrm{AU}}^{-3/2} \ \mathrm{g\ cm^{-2}} \ . \tag{1-30}$$

The above equation indicates that GI is more likely to occur in the outer disk. The MMSN model is essentially always stable to the GI because of its stiff density profile, while in early phases of PPDs (e.g., Class 0 and I sources) when PPDs are massive and their outer regions are building up mass from the envelope, the disk is likely to be unstable to GI beyond some critical radius.

The outcome of GI largely depends the thermodynamics, particularly on the cooling rate. Generally speaking, tt leads to gravitoturbulence if the cooling rate is less than the orbital frequency, and transports angular momentum outward via non-axisymmetric spiral waves very efficiently (Gammie 2001; Rice et al. 2005). For typical accretion rate in PPDs, and given the opacity dominated by dust grains, gravitoturbulence is likely to be present at intermediate disk radii between a few tens and ~ 100 AU (Vorobyov & Basu 2007; Rafikov 2009; Rice et al. 2010). However, time-dependent calculations of the PPD evolution indicate that after the envelope infall stops ($\lesssim 1$ Myr), the disk is generally not massive enough to sustain the GI (Zhu et al. 2010b).

Other driving mechanisms at the inner disk as well as beyond the infall (embedded) phase are clearly needed.

4.2 Magnetorotational Instability

A differentially rotating disk treaded by a weak magnetic field is subject to a local instability termed as the magnetorotational instability (MRI, Balbus & Hawley 1991). For a vertical field line that undergoes sinusoidal radial displacement, the fluid parcel that is displaced inward (outward) rotates faster (slower) due to the shear, which stretches the field line. Magnetic tension force then cause the inner (outer) fluid parcel to lose (gain) angular momentum, resulting further inward (outward) displacement, which runs away. The MRI simply requires

$$\frac{d}{dr}\Omega^2 < 0 \ , \tag{1-31}$$

a condition always satisfied by Keplerian disks such as PPDs, and that the net vertical magnetic field is well below equipartition strength with gas pressure. The linear growth rate of the MRI is of the order Ω for the fastest growing mode. The saturation of the MRI leads to strong magnetohydrodynamic (MHD) turbulence and efficiently gives outward transport of angular momentum (Hawley et al. 1995; Stone et al. 1996). The resulting α value depends on magnetic field geometry. In the ideal MHD case with zero net vertical magnetic flux, one finds $\alpha \sim 10^{-2}$ (Davis et al. 2010; Shi et al. 2010); the α value further increases with net vertical magnetic flus (Suzuki & Inutsuka 2009; Bai & Stone 2012a). Although there is no observational proof, the properties of the MRI strongly suggests that it is the source of angular momentum transport for the majority of accretion disks such as disks around white dwarfs, neutron stars and black holes.

MRI is also believed to be the primary mechanism of angular momentum transport in PPDs. However, due to the non-ideal MHD effects, whether the MRI is sufficient for driving rapid accretion in PPDs is unsettled (see Section 5). However, it is common in the literature to model the structure and evolution of PPDs using the so-called α-disk models, where the value of α in the disk is set by certain phenomenological prescriptions and is adjusted to match the observed accretion rate, implicitly assuming that the MRI is able to provide the desired α value. Such phenomenological approaches do not reflect the physical reality, and multiple parameterizations may all explain the data. Understanding the MRI in PPDs requires detailed study of the microphysics, i.e., the non-ideal MHD effects, which is one of the major goals of this thesis work, and the eventual

outcome would be realistic microphysical parameterizations that help model the global structure and evolution of PPDs, and constrain physical processes in PPDs from observational data.

4.3 Magnetocentrifugal Wind

The magnetocentrifugal wind (MCW) scenario relies on the presence of large-scale open magnetic field lines connected to the disk surface with an inclination angle larger than 30° relative to disk normal (Blandford & Payne 1982). Provided an outflow of gas from the disk be loaded to the open field lines, the gas can be centrifugally accelerated along the field lines, extracting angular momentum from the disk, and gradually becomes collimated by the magnetic hoop stress.

One of the main predictions of the MCW model is a strong correlation between the mass accretion rate $\dot{M}$ and the mass loss rate $\dot{M}_w$ through the wind

$$\frac{\dot{M}_w}{\dot{M}} = \frac{1}{2}\left(\frac{R_0}{R_A}\right)^2 , \tag{1-32}$$

where R_0 is the wind launching radius in the disk, and R_A is the cylindrical radius of the Alfvén point (for the field line originated from radius R_0), where the poloidal flow velocity along magnetic field lines equals to the poloidal component of the Alfvén velocity. In PPDs, is has been constrained that $R_A/R_0 \approx 2-3$ (Bacciotti et al. 2002; Anderson et al. 2003) which is consistent with observations that $\dot{M}_w/\dot{M} \approx 0.1$ (Hartigan et al. 1995; Gullbring et al. 1998).

A prerequisite for magnetocentrifugal acceleration is the mass loading to open magnetic field lines from the disk, a process that requires detailed understanding of the microphysics (turbulence and non-ideal MHD effects) within the disk, and is not properly captured in the currently available global simulations (e.g., Krasnopolsky et al. 1999; Casse & Keppens 2002). Local (semi-) analytical study of accretion disks wind showed that the launching of MCW generally requires a strong vertical background magnetic field of about equipartition strength (Wardle & Koenigl 1993; Ogilvie & Livio 2001; Ogilvie 2012), and it has been speculated that the MCW scenario (which operates with strong background field) and the MRI (which operates with weak background field) are unlikely to operate simultaneously (Salmeron et al. 2007; Bai & Stone 2012a). In Chapter 4, we demonstrate that in PPDs MCW is likely to operate even with relatively weak field at the inner disk, while the MRI operates in the outer disk.

4.4 Hydrodynamic Mechanisms

Hydrodynamic mechanisms for angular momentum transport have been studied over decades. It has been convincingly shown from both theoretical studies (Lesur & Longaretti 2005) and laboratory experiments (Ji et al. 2006) that pure hydrodynamic shear-driven instabilities are too inefficient to yield significant angular momentum transport. Turbulence driven by convections (which requires strong heating in the midplane), while speculated to be potential another mechanism for driving accretion (Lin & Papaloizou 1980; Ryu & Goodman 1992), was later shown to transport angular momentum to the wrong (inward) direction (Cabot 1996; Stone & Balbus 1996). Recently, Lesur & Ogilvie (2010) reported outward transport with larger (and more realistic) Rayleigh number. Nevertheless, it is unlikely for PPDs to have a strong heating source at disk midplane for driving convection in the first place.

Another hydrodynamic mechanism is the entropy-driven instabilities, which leads to vortex generation via the baroclinic term $\nabla P \times \nabla \rho$ and angular momentum transport (Klahr & Bodenheimer 2003). The instability was later termed as subcritical (non-linear) baroclinic instability (SBI, Petersen et al. 2007a,b; Lesur & Papaloizou 2010). The onset of the instability requires the interplay between a radially unstable entropy gradient and strong thermal diffusion. The saturation of the SBI produces large-scale vortices and density waves that transport angular momentum outwards with typical $\alpha \lesssim 3 \times 10^{-3}$ (Lesur & Papaloizou 2010), and the SBI is suppressed in the presence of magnetic field (Lyra & Klahr 2011), giving way to the MRI. The SBI has potential applications to the dead zone of PPDs where the MRI is suppressed due to large resistivity in the disk midplane (see next Section). It is unclear whether the radial entropy gradient and the thermal diffusion coefficient in (the inner region of) PPDs is appropriate for efficient driving of the SBI. Moreover, the level of $\alpha \lesssim 10^{-3}$ is also somewhat insufficient for the SBI to be the dominant mechanism of angular momentum transport in PPDs.

Keeping in mind these hydrodynamic possibilities (especially the SBI), we seek for MHD mechanisms of angular momentum transport in this thesis.

5. The Picture of Active Layer and Dead Zone

As introduced in Section 4, the MRI is widely believed to the the primary mechanism of angular momentum transport in astrophysical accretion disks. For MRI to to operate, the magnetic

field should be sufficiently coupled to the gas. In other words, the gas should be sufficiently ionized. However, the ionization level in PPDs, as we briefly discussed in Section 3, is extremely low. The main ionization sources such as cosmic rays and X-rays from the protostar have only limited penetration depth, giving more ionization to the disk surface. Moreover, recombination rate is slower in the disk surface due to it lower density. Both factors make the surface layer of PPDs better ionized than the disk midplane. Since Ohmic resistivity depends solely on the ionization fraction and temperature (see Equation 1-10), Gammie (1996) found that in the inner region of PPDs, resistivity in the disk midplane is too high for the MRI to operate, where the gas flow should be largely laminar, termed as the "dead zone"; in contrast, the surface layer is sufficiently ionized for the MRI to take place, and is termed as the "active layer" where the gas is turbulent. Accretion in the inner region of PPDs then proceeds through the active layer (see Figure 1.1 for a Cartoon picture).

Over the past fifteen years, the picture of layered accretion has received substantial research interest, aiming at understanding the properties and effectiveness of the MRI in PPDs with a wide range of astrophysical applications. This task largely relies on calculations of the ionization fraction at all locations of the PPDs, which requires solving a chemical reaction network, as well as knowledge about how the properties of the MRI depend on the Ohmic Elsasser number (1-18), which requires numerical simulations. There are generally four different approaches in the literature as we summarize below.

- Detailed chemistry calculations applied with criteria for the suppression of the MRI (Sano et al. 2000; Fromang et al. 2002; Semenov et al. 2004; Ilgner & Nelson 2006; Bai & Goodman 2009; Turner & Drake 2009). These calculations involve chemical networks of different complexities, and have the advantage of low computational cost to allow for more thorough exploration on the model dependence of chemical parameters. The highlight from these calculations is that the effectiveness of the MRI sensitively depends on the size and abundance small (submicron) grains, as small grains severely affect the ionization fraction.

- Local numerical simulations (Fleming & Stone 2003; Turner et al. 2007; Turner & Sano 2008; Ilgner & Nelson 2008; Oishi & Mac Low 2009; Suzuki et al. 2010; Hirose & Turner 2011; Okuzumi & Hirose 2011; Flaig et al. 2012). These simulations either adopt a fixed resistivity profile, or incorporate a simplest chemical network that co-evolves with the simulations. Despite compromises on the chemistry, these simulations have the proper resolution to study

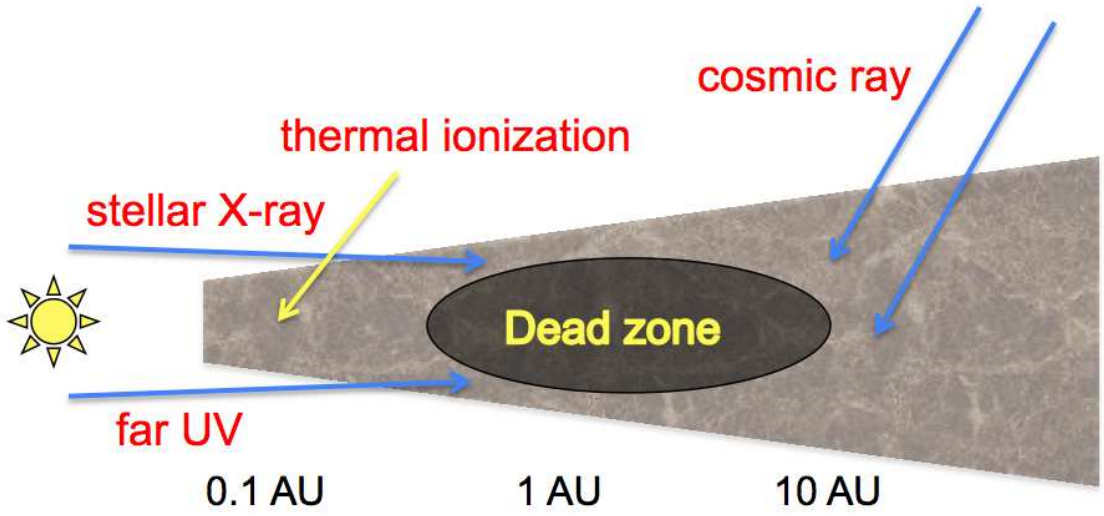


Fig. 1.1.— The conventional picture of the accretion process in PPDs. The midplane region at the inner disk is too resistive for the MRI to operate, which is called the dead zone, while the resistivity at the disk surface layer is sufficiently small for the MRI to operate, and is called the active layer where accretion proceeds. On the other hand, MRI is likely to operate through the disk midplane near inner edge of the disk, which is sufficiently hot for thermal ionization to take place, as well as in the very outer region of the disk, which is sufficiently thin for external ionizations to penetrate.

the gas dynamics in the disk in detail, confirming the picture of layered accretion, with accretion rate measure in the simulations of the order 10^{-8} yr^{-1}, roughly consistent with observations.

- Global numerical simulations. Global MRI simulations in the ideal MHD limit has already been routinely studied (e.g., Fromang & Nelson 2006; Flock et al. 2011), while the inclusion of Ohmic resistivity has only been pursued recently by Dzyurkevich et al. (2010). Although with relatively low resolution, they confirmed the picture of layered accretion and observed a local radial maximum in the midplane pressure that lies near the inner edge of the dead zone.

- Phenomenological global models (Zhu et al. 2009, 2010a,b; Martin & Lubow 2011; Martin et al. 2012). These models use phenomenological parameterizations of the accretion stress α to evolve one-dimensional (occasionally 2D) global disk models. Although the parameterizations reflect the disk microphysics very roughly, they are the only viable way to study the long-term evolution of PPDs. These models demonstrate cycles of steady accretion and outbursts at early stages of PPD evolution as a result of the MRI, dead zone mass accumulations and GI.

In light of all the past works, there is a consensus that a dead zone is expected at the inner part of the PPDs (about $0.5 - 10$ AU), though its radial and vertical extent depends on the ionization rate and the abundance of small (sub-micron) dust grains. However, all these results are obtained based on calculations that include only Ohmic resistivity. The other two non-ideal MHD effects, the Hall effect and ambipolar diffusion (AD), are rarely taken into account. As discussed in Section 3, Hall and AD effects dominate Ohmic resistivity in the surface and outer regions of PPDs. The linear dispersion relations for the MRI with Hall and AD are already been studied thoroughly (Wardle 1999; Balbus & Terquem 2001; Kunz & Balbus 2004; Desch 2004; Wardle & Salmeron 2012; Pandey & Wardle 2012), and they differ substantially with that in the Ohmic regime. However, there is a lack of study on the non-linear saturation of the MRI in Hall and AD regimes. In this thesis, we study the non-linear properties of the MRI in the presence of AD (Chapter 2, Bai & Stone 2011). Together with past simulation results on the MRI with Hall effect (Sano & Stone 2002a,b), we outline a general criterion for MRI turbulence to be self-sustained. We then adopt the first approach to estimate the effectiveness of the MRI in PPDs (Chapter 3, Bai 2011a,b), only to find disturbingly that the inclusion of AD substantially reduce the predicted accretion rate by at least an order of magnitude below typical observed values. Similar results have been obtained by Perez-Becker & Chiang (2011a,b). In Chapter 4 (Bai & Stone 2012b), we switch to the second approach to perform local numerical simulations that for the first time, self-consistently include the effects of both Ohmic resistivity and AD using a complex chemical reaction network. These simulations challenge the "layered accretion" paradigm in that we find that in the inner disk ($\sim 0.5 - 5$ AU), the MRI is likely to be completely suppressed, and the gas in the disk is almost completely laminar, launching a strong magnetocentrifugal wind (MCW). A new picture emerges that the MRI is active in the entire outer regions of PPDs, while the MCW operates in the entire inner region of PPDs (except for the hot inner disk rim where the disk is well ionized for the MRI to take place).

Chapter 2

Effect of Ambipolar Diffusion on the Magnetorotational Instability

As introduced in the end of Section 5, Chapter 1, non-ideal MHD effects plays a crucial role on the properties of the magnetorotational instability (MRI) in protoplanetary disks (PPDs), but so far most attention has been paid to only the effect of Ohmic resistivity. The other two effects, namely, the Hall effect and ambipolar diffusion (AD) have rarely been studied, particularly in the non-linear regime of the MRI. In this chapter, we explore the effect of AD on the non-linear evolution of the MRI in the strong coupling limit (see Section 3 of Chapter 1) using three-dimensional (3D) local shearing-box numerical simulations (see Section 2 of Appendix B). We motivate our study in more details in Section 1. Numerical setups of our simulations are then described in Section 2. Sections 3 to 5 present the main results of our simulations. These results are combined together for further analysis which lead to a quantitative criterion on the strength and sustainability of the MRI in the AD dominated regime, given in Section 6.

1. Introduction

One of the most fundamental questions in accretion disk dynamics is how the disk transports angular momentum and accretes to the central object. The magnetorotational instability (MRI, Balbus & Hawley 1991) is widely considered to be the most likely mechanism for the transport process. The non-linear evolution of the MRI under ideal MHD conditions has been studied extensively using both local (Hawley et al. 1995; Stone et al. 1996; Miller & Stone 2000) and global

(Armitage 1998; Hawley 2000, 2001; Fromang & Nelson 2006) numerical simulations. It has been found that MRI generates vigorous MHD turbulence and produce efficient outward transport of angular momentum whose rate is compatible with observations. However, accretion disks in some systems are only partially ionized, and non-ideal MHD effects need to be taken into account. In particular, most regions of the protoplanetary disks (PPDs) are too cold for sufficient thermal ionization, and effective ionization may be achieved only in the disk surface layer due to external ionization sources such as X-ray radiation from the central star and cosmic ray ionization (Gammie 1996; Stone et al. 2000). Non-ideal MHD effects reflect the incomplete coupling between the disk material and the magnetic field, and substantially affect the growth and saturation of the MRI.

There are three non-ideal MHD effects as manifested in the generalized Ohms's law, namely the Ohmic resistivity, Hall effect and ambipolar diffusion (AD), with three different regimes associated with the relative importance of these terms. In general, the Ohmic term dominates at high density and very low ionization, the AD term dominates in the opposite limit, and the Hall term is important in between. So far the majority of studies have been focused on the Ohmic regime. In this case, MRI is damped when the Elsasser number $\Lambda \equiv v_{\rm Az}^2/\eta\Omega$ falls below order unity (Jin 1996; Turner et al. 2007), where $v_{\rm Az}$ is the Alfvén velocity in the vertical direction, η is the Ohmic resistivity, Ω is the angular frequency of Keplerian rotation. Another often quoted criterion is the magnetic Reynolds number ${\rm Re}_M \equiv c_s^2/\eta\Omega \gtrsim 10^4$ for MRI to be self-sustained (where c_s is the sound speed), which has the advantage of being independent of the magnetic field (Fleming et al. 2000). Ohmic resistivity has been used extensively to model the layered accretion in PPDs, where the surface layer of the disk is sufficiently ionized to couple to the magnetic field and drive the MRI turbulence, while the midplane region is too poorly ionized and "dead" (Fleming & Stone 2003; Turner et al. 2007; Turner & Sano 2008; Ilgner & Nelson 2008; Oishi & Mac Low 2009).

The importance of Hall and AD terms in PPDs has been studied in a number of theoretical works, but relatively little attention has been paid to numerical simulations of the non-linear regime. Linear analysis of the MRI in the Hall regime have been performed by Wardle (1999) and Balbus & Terquem (2001). The growth rate is strongly affected by the Hall term and depends on the sign of $\boldsymbol{B} \cdot \boldsymbol{\Omega}$. Nevertheless, numerical simulations including both the Hall and Ohmic terms (where the Ohmic term dominates) showed that the Hall term does not strongly affect the saturation amplitude of MRI (Sano & Stone 2002a,b). It is yet to study the behavior of MRI in the regime where Hall effect dominates over other terms, and to include the Hall term in the more realistic vertically stratified simulations.

The relative motion between ions and neutrals leads to AD. AD is ideally studied using the two-fluid approach, where the ions and neutrals are treated as separate fluids, coupled by the ion-neutral drag via collisions. Moreover, ion and neutral densities are affected by the ionization and recombination processes. Most analytical studies in the linear regime adopt the Boussinesq approximation where ion and neutral densities are kept constant (Blaes & Balbus 1994; Kunz & Balbus 2004; Desch 2004). These studies show that the growth of MRI is suppressed when the collision frequency of a neutral with the ions falls below the orbital frequency. In the mean time, when both vertical and azimuthal field is present, unstable modes always exist due to the effect of AD, and these unstable modes require non-zero radial wavenumbers (Kunz & Balbus 2004; Desch 2004). Blaes & Balbus (1994) also studied the effect of ionization and recombination with compressibility (for vertical propagating waves), and found that the presence of azimuthal and radial field allows the coupling to acoustic and ionization modes, and the azimuthal field tends to stabilize the flow when the recombination time is not too long compared with dynamical time.

The effect AD on the MRI in the non-linear regime was first studied by Mac Low et al. (1995). They implemented and tested AD in the "strong coupling" limit in the ZEUS code and performed simulations with net vertical flux for various ion-neutral coupling strengths. Their results confirmed the stability analysis of Blaes & Balbus (1994), but their simulations were only two-dimensional and did not follow the evolution much beyond the linear stage. In another study, Brandenburg et al. (1995) included the effect of AD (also in the strong coupling limit) in their three-dimensional simulations of a local, vertically stratified disk. They found that turbulence remains self-sustained in a case where AD time is long compared with orbital time, although reduced in strength, and in another case where the AD time was set comparable to Ω^{-1}, turbulence decayed.

A systematic study on the non-linear evolution of MRI with AD was done by Hawley & Stone (1998) (hereafter HS) using three-dimensional (3D) numerical simulations. They used the two-fluid approach without considering the ionization-recombination processes, therefore ions and neutrals obey their own continuity equations. Both net-vertical and net-toroidal magnetic configurations were considered. They found that the system behaves like fully-ionized gas when the neutral-ion collision frequency is greater than 100Ω, while ions and neutrals behave independently when the collision frequency fall below 0.01Ω. The amplitude of magnetic field at saturation is proportional to the ion density when it is much smaller than the neutral density. The two-fluid approach adopted by HS is valid when the recombination time scale is long compared with the dynamical time. However, AD in PPDs is in general in the "strong coupling" limit (Shu 1991).

Two conditions must be satisfied in this limit: 1. The ion density ρ_i is negligible compared with the neutral density ρ_n. 2. The electron recombination time τ_r must be much smaller than the orbital frequency Ω. In this limit, the ion inertia is negligible and the ion density is purely determined by the ionization-recombination equilibrium with the neutrals, and the two-fluid formulation is simplified into a single-fluid formalism (for the neutrals). In PPDs, condition 1 is always met, and we will show in Section 3.2 of Chapter 3 that condition 2 is almost always satisfied.

The strong coupling limit is conceptually different from the simulations performed by HS in that the ion density does not obey continuity equation, and is set by the neutral density due to chemical equilibrium. Effectively, this allows the coupling of the MRI with acoustic and ionization modes, which leads to more complicated interactions (Blaes & Balbus 1994). Moreover, our simulations correspond to the limit where the ion density is negligibly small (i.e., $f \to 0$ in HS), which is difficult for two-fluid simulations due to the stiffness of the equations. In the strong coupling limit, there is only one controlling parameter, namely, the neutral-ion collision frequency $\gamma\rho_i$. We perform three sets of simulations with net vertical flux (Section 3), net toroidal flux (Section 4) and both (Section 3). In each group of runs, we systematically vary $\gamma\rho_i$ as well as the strength of the net field. Our main goal is to study the conditions under which MRI turbulence can be self-sustained or is suppressed due to AD. In addition, we study the properties of the MRI turbulence in the AD dominated regime.

2. Simulation Setup

We use the Athena, a grid-based MHD code based on higher-order Godunov method (see Section 1 of Appendix B) for all our simulations. We have implemented the non-ideal MHD terms to the Athena MHD code, and Appendix B provides the details about the implementation and a suite of test problems of the non-ideal MHD terms. In brief, we have demonstrated that the AD algorithm in Athena is robust in both linear and non-linear test problems; it is at least as accurate as previously published AD algorithms implemented on other MHD codes; calculations can be accelerated substantially (up to a factor of 10 when AD is strong) by using the super time-stepping technique.

All our simulations are local and adopt the shearing-box approach (Section 2 of Appendix B), which takes a local patch of a Keplerian disk and adopts a local reference frame at a fiducial radius corotating with the disk at orbital frequency Ω. In this frame, the MHD equations with AD in a

Cartesian coordinate system reads

$$\frac{\partial \rho}{\partial t} + \nabla \cdot (\rho \boldsymbol{v}) = 0 \ , \tag{2-1}$$

$$\frac{\partial \rho \boldsymbol{v}}{\partial t} + \nabla \cdot (\rho \boldsymbol{v}^T \boldsymbol{v} + \mathsf{T}) = \rho \left[2\boldsymbol{v} \times \boldsymbol{\Omega} + 3\Omega^2 x \hat{\boldsymbol{x}} \right] \ , \tag{2-2}$$

$$\frac{\partial \boldsymbol{B}}{\partial t} = \nabla \times \left[\boldsymbol{v} \times \boldsymbol{B} + \frac{(\boldsymbol{J} \times \boldsymbol{B}) \times \boldsymbol{B}}{c\gamma\rho_i\rho} \right] \ , \tag{2-3}$$

where T is the total stress tensor

$$\mathsf{T} = (P + B^2/8\pi)\, \mathsf{I} - \frac{\boldsymbol{B}^T \boldsymbol{B}}{4\pi} \ , \tag{2-4}$$

I is the identity tensor, P is the gas pressure. $\hat{\boldsymbol{x}}, \hat{\boldsymbol{y}}, \hat{\boldsymbol{z}}$ are unit vectors pointing to the radial, azimuthal and vertical directions respectively, where $\boldsymbol{\Omega}$ is along the $\hat{\boldsymbol{z}}$ direction. Disk vertical gravity is ignored and our simulations are vertically unstratified, as we focus on the basic non-ideal MHD physics without involving complications from buoyancy. We use an isothermal equation of state $P = \rho c_s^2$, where c_s is the isothermal sound speed. Periodic boundary conditions are used in the azimuthal and vertical directions, while the radial boundary conditions are shearing periodic as usual. For the ion density ρ_i, we adopt equation (B-13) in Appendix B

$$\frac{\rho_i}{\rho_{i0}} = \left(\frac{\rho}{\rho_0} \right)^{\nu} \ , \tag{2-5}$$

which assumes a simple ionization-recombination equilibrium, with $\nu = 1/2$ being the default value. Subscript '$_0$' for ρ_0 and ρ_{i0} denotes the background/equilibrium values of gas and ion densities, and the strength of AD is characterized by $Am \equiv \gamma\rho_{i0}/\Omega$ as introduced in Chapter 1. In code unit, we adopt $\rho_0 = c_s = \Omega = 1$, hence the disk scale height $H = c_s/\Omega = 1$.

As our simulations are vertically unstratified, we fixe the box height to be H. We initialize our simulations with Keplerian velocity and seed density perturbations of 2.5% of the background density $\rho_0 = 1$. We consider three different magnetic field geometries (net vertical flux, net toroidal flux, both vertical and toroidal flux) as described in the following three sections. Since all our simulations contain net magnetic flux, they are not subject to the issue of convergence found by (Fromang & Papaloizou 2007) in zero net-flux simulations, and numerical convergence is confirmed in our test simulations (and see Section 4.2 for the case of net toroidal flux). For relatively small AD coefficient (large Am), MRI grows quickly from seed perturbations and saturates into turbulence; when the effect of AD is strong, however, MRI does not grow from our seed perturbations. In such cases, we initialize the simulations from a turbulent state which is obtained from simulations with relatively large Am (see individual sections for details).

The most important diagnostics are the volume averaged (normalized) Reynolds stress, defined as

$$\alpha_{\rm Re} = \frac{\overline{\rho v_x v_y'}}{\rho_0 c_s^2} \ , \tag{2-6}$$

where the over bar indicates volume averaging, v_y' is the azimuthal velocity with the Keplerian velocity subtracted, and the volume averaged (normalized) Maxwell stress, defined as

$$\alpha_{\rm Max} = \frac{\overline{-B_x B_y}}{4\pi\rho_0 c_s^2} \ . \tag{2-7}$$

The total stress, namely, the α parameter (Shakura & Sunyaev 1973) is $\alpha = \alpha_{\rm Re} + \alpha_{\rm Max}$. We also monitor the kinetic and magnetic energy density, which characterize the strength of the MRI turbulence.

The main purpose of this study is to identify the criterion under which sustained turbulence generated by the MRI can be maintained. However, the term "sustained turbulence" is a somewhat ambiguous concept. In the context of 3D shearing box simulations, small-amplitude oscillations left from decayed hydrodynamical turbulence is present (Shen et al. 2006). Such oscillations produce Reynolds stress on the order of 10^{-4} with kinetic energy density on the order of 10^{-3}, both in normalized unit $\rho_0 c_s^2$. Such oscillations are likely to associate with linear modes in the shearing sheet with the origin of acoustic and/or nearly incompressible inertia waves (Balbus 2003). Being a conservative Godunov MHD code, the Athena code preserves the amplitude of these waves without much damping. Therefore, throughout this chapter, the level of turbulence we are interested in are those whose time and volume averaged kinetic energy density $E_k = \langle \rho v^2 \rangle$ is on the order of $10^{-3}\rho_0 c_s^2$ or higher, and/or whose total stress α is no less than 10^{-4}. Meanwhile, analysis of all our simulations show that the threshold where the MRI turbulence can be marginally self-sustained is roughly at the same level. (see Section 6 for further discussion).

Our simulations are run for at least 24 orbits ($150\Omega^{-1}$). A period of 24 orbits is sufficiently long for the MRI to saturate from initial growth, which typically occurs in $5-10$ orbits, or for the restart runs to reach a steady state, which typically occurs in $10-15$ orbits. Our time averaged quantities are mostly taken from after about 16 orbits (since $100\Omega^{-1}$) unless otherwise noted. Although a time average over 8 orbits ($50\Omega^{-1}$) is relatively short, it is sufficient for our purpose to judge whether MRI turbulence can be self-sustained[1]. Many of our simulations are run for 48 orbits or longer where better statistics on the turbulence properties can be obtained.

[1]Winters et al. (2003) found that more than a few hundred orbits as are required to accurately measure the properties of the MRI turbulence in ideal MHD. This conclusion is based simulations with radial box size being H,

3. Net Vertical Flux Simulations

In the first group of simulations, we choose the initial field configuration to be uniform along the vertical axis $\hat{z}$, characterized by the plasma $\beta_0 = 8\pi P_0/B_0^2$, where $P_0 = \rho_0 c_s^2$ is the background pressure and B_0 is the initial field strength. The vertical flux is conserved numerically by remapping the toroidal component of the magnetic field in the ghost zones of the radial boundaries (see Section 4 of Stone & Gardiner (2010) for details). For all simulations, we fix the box size to be $4H \times 4H \times H$ in the radial, azimuthal and vertical dimensions, with fixed grid resolution at 64 cells per H. We have chosen a relatively large radial box size ($4H$), as suggested by Pessah & Goodman (2009), which is needed to properly capture the parasitic modes to break the channel mode into turbulence. It also helps substantially reduce the intermittence of the MRI turbulence (Bodo et al. 2008). We note that for local unstratified net vertical flux MRI simulations without explicit dissipation, turbulence properties converge at about 32 cells per H (Hawley et al. 1995). The grid resolution in our simulations is two times higher, thus we expect numerical convergence.

All our net vertical flux simulations are listed in Table 2.1. We first perform a fiducial set of simulations with fixed $\beta_0 = 400$. We choose a series of Am values, ranging from 1000 down to 0.1, and study the critical value of Am below which MRI turbulence is no longer self-sustained (Section 3.1). In the next, we vary the net vertical flux by setting $\beta_0 = 100, 1600$ and 10^4 and run a number of simulations around $Am = 1$ to study how the critical value of Am is affected by the vertical flux (Section 3.2). Furthermore, in Section 3.3 we briefly investigate the effect of ν by varying ν from the fiducial value 0.5 to 0 (run Z5a) and 1 (run Z5b) (see equation (2-5)). Finally, we discuss the properties of the MRI turbulence in the presence of AD (Section 3.4).

Our choices of the net vertical flux derive from the linear dispersion relation of the MRI as well as physical considerations. In the case of ideal MHD, the wavelength for the fastest growing linear MRI mode is given by $\lambda/H = 9.18\beta_0^{-1/2}$ (Hawley et al. 1995). For $\beta_0 = 100, 400$ and 1600, our vertical box size of H fits $1, 2$ and 4 most unstable wavelengths respectively in ideal MHD. The ideal MHD dispersion relation is considerably modified when $Am \lesssim 10$. Unstable modes exist for wavelength longer than the critical wavelength (Wardle 1999)

$$\frac{\lambda_c}{H} = 5.13\left(1 + \frac{1}{Am^2}\right)^{1/2} \beta_0^{-1/2} \ . \tag{2-8}$$

---

while the radial box size in about half of our simulations is $4H$, which reduces the time fluctuations. Also, our Figures 2.1 and 2.6 show that the fluctuations in the Maxwell stress are less severe in the presence of AD than in the ideal MHD case.

The wavelength for the most unstable mode λ_m is about twice larger. Note that λ_c increases with decreasing Am, which is due to the damping of small-scale perturbations by AD. An approximate fitting formula that is accurate within 2% for all values of Am is

$$\frac{\lambda_m}{H} \approx 10.26\left(1+\frac{1}{Am^2}+\frac{1}{Am^{1.16\epsilon}}-0.2\epsilon\right)^{1/2}\beta_0^{-1/2}\,, \tag{2-9}$$

where $\epsilon \equiv Am/(1+Am)$. Note that for pure vertical magnetic field and vertical wavenumber, the linear dispersion relation for Ohmic resistivity is exactly the same as that for AD (Wardle 1999), with Am replaced by the Elsasser number $\Lambda = v_{Az}^2/\eta\Omega$. For $\beta_0 = 400$, the most unstable wavelengths at $Am = 1, 1/3$ and 0.1 are $\lambda = 0.87H$, $1.72H$ and $5.18H$ respectively. Clearly, the most unstable mode does not fit into our simulation box when $Am = 0.33$, and no unstable modes fit into the box for $Am = 0.1$. Since $\lambda \propto \beta_0^{-1/2}$, these modes do fit into our simulation box as we increase β_0 to 1600 and 10^4 respectively. In the mean time, since AD tends to be important in the more strongly magnetized upper layers of the protoplanetary disks (Wardle 2007; Bai 2011a), it is also interesting to study whether the MRI turbulence can be sustained when β_0 is relatively small, even if the most (or all) unstable modes do not fit into our simulation box. We have not run simulations with a taller box since we do not include vertical stratification.

3.1 A Fiducial Set of Runs

As the fiducial set of runs, we fix $\beta_0 = 400$, and run 7 simulations with different Am values (see Table 2.1), labeled from $Z1$ with $Am = 1000$, which essentially corresponds to the ideal MHD case, to $Z7$ with $Am = 0.1$, where the evolution of magnetic field is dominated by AD. Our scan of Am is more narrowly sampled near $Am = 1$ where the transition is expected to occur. In Figure 2.1, we show the time evolution of the Maxwell stress from the fiducial set of runs. We find that for $Am \geq 1$, the growth of the MRI from linear perturbations leads to vigorous MRI turbulence, while for the two runs with $Am < 1$, MRI either does not grow from the initial vertical field (Z7), or grows too slowly (Z6), since the most unstable modes do not fit into our simulation box. Therefore, for these two models, we start the simulations from the end of run Z5 ($Am = 1$), which is turbulent, and reset Am to be 0.33 and 0.1 respectively. Nevertheless, turbulence continues to decay throughout the span of our simulation in run Z7. Run Z6 is a marginal case where turbulence is neither fully sustained nor decayed continuously (see discussions below).

Table 2.1: Net vertical flux simulations.

Run	Am	β_0	ν	Orbits	Restart[1]	Turbulence[2]
Z1	1000	400	0.5	48	No	Yes
Z2	100	400	0.5	24	No	Yes
Z3	10	400	0.5	24	No	Yes
Z4	3.33	400	0.5	24	No	Yes
Z5	1	400	0.5	43	No	Yes
Z6	0.33	400	0.5	24	Z5	No
Z7	0.1	400	0.5	24	Z5	No
Z3s	10	100	0.5	24	No	Yes
Z5s	1	100	0.5	24	No	Yes
Z6s	0.33	100	0.5	24	Z5s	No
Z7s	0.1	100	0.5	24	Z5s	No
Z3w	10	1600	0.5	24	No	Yes
Z5w	1	1600	0.5	24	No	Yes
Z6w	0.33	1600	0.5	48	No	Yes
Z7w	0.1	1600	0.5	24	Z5w	No
Z6e	0.33	10^4	0.5	48	No	Yes
Z7e	0.1	10^4	0.5	48	Z6e	Yes
Z5a	1	400	0.0	24	No	Yes
Z5b	1	400	1.0	24	No	Yes

Box size is fixed at $4H \times 4H \times H$, grid resolution is 64 cells per H.
[1] whether simulation is initiated by restarting from a turbulent run.
[2] whether turbulence can be self-sustained.

We first look at run Z1 to Z5 with $Am \geq 1$. The initial growth of the MRI is due to the axisymmetric channel mode (Goodman & Xu 1994; Pessah & Chan 2008). The mode becomes non-linear (producing an overshoot in the Maxwell stress up to 1 in the ideal MHD case) until broken down by secondary parasitic modes to produce turbulence. In the turbulent state, it is evident that the Maxwell stress monotonically decreases as Am decreases, analogous to the Ohmic case (Sano et al. 1998; Fleming et al. 2000). In Table 2.2 we list the general properties of the turbulence from all our vertical net flux simulations. The quantities are averaged over space and time after saturation (after $100\Omega^{-1}$). The total stress $\alpha \approx 0.2$ in run Z1, which agrees with the ideal MHD case (Hawley et al. 1995). It drops slowly with decreasing Am when $Am \gg 1$, but very rapidly when Am is around 1. Moreover, as Am decreases, the ratio of kinetic to the fluctuating part (with background field B_{z0} subtracted) of the magnetic energy increases (see also Figure 2.3). Similarly, the ratio of Reynolds stress to Maxwell stress increases.

As we have discussed before, the most unstable mode does not fit into our simulation box for runs Z6 and Z7, and our simulations initiated from a turbulent state also show no sign of sustained

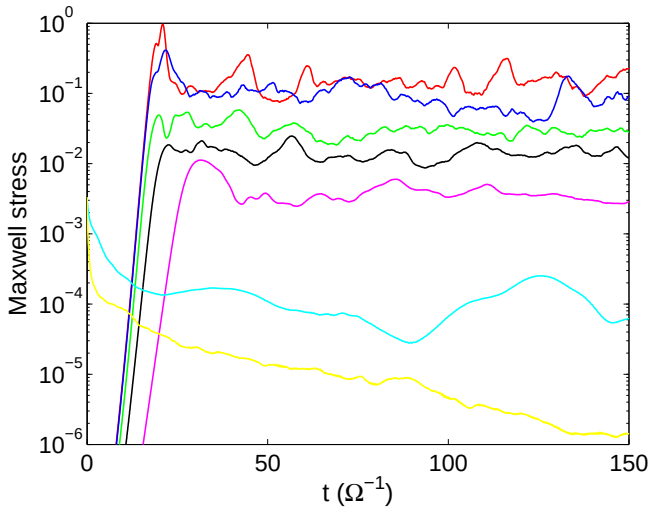


Fig. 2.1.— The evolution of Maxwell stress in our fiducial set of net vertical flux runs (from top to bottom: Z1, Z2, ..., Z7) normalized to $c_s H$. For models Z6 and Z7, the simulations are initiated from the end of run Z5.

MRI turbulence. This is not surprising for run Z7, where no unstable MRI mode even exists in the simulation box. Our run Z6 is a marginal case, where a wavelength of H is only slightly larger than the critical wavelength for instability ($\lambda_c = 0.89H$) but far from the most unstable wavelength ($\lambda_m = 1.72H$). This explains the long-term variations in the Figure 2.1 since the growth rate is only slightly larger than zero. Our analysis in Section 4.4 indicates that although some non-zero stress close to $\alpha = 10^{-4}$ is maintained in the simulation, it is unlikely to be due to the MRI turbulence. In real disks, one may expect sustained turbulence to be supported at $Am \approx 0.3$ if it were at the disk midplane, where the density variation over one H above and below the midplane is not significant. In the upper layers, β_0 may fall off substantially over one H, which strongly stabilizes the flow. In sum, we see from our fiducial set of net vertical flux simulations that presence of turbulence mainly depends on whether the most unstable mode of the MRI fits into the simulation box. This aspect will be further explored in the next subsection 3.2.

The results reported above are qualitatively different from those observed in HS using two-fluid simulations. One may compare our results with Table 3 of HS, where the Am value for their four runs Z24, Z17, Z25, Z28 are 0.11, 1.1, 11.1 and 111 respectively. The total stress α in these simulations does not scale monotonically with Am, and in particular α is on the order of 10^{-2} when Am is as small as 0.11, while in our simulations MRI is suppressed. This reflects the difference in the physical assumptions about the two approaches. In these two-fluid simulations,

the ion to neutral mass ratio ($f = \rho_i/\rho$) were kept to be relatively large (0.001 to 0.1) to avoid numerical stiffness, thus the ion inertia always plays a role and the ion drift velocity deviates from that in the strong-coupling limit. The departure is more and more significant as Am decreases, and in particular, for $Am \lesssim 0.1$, ions and neutrals behave as independent fluid in HS: vigorous MRI is generated in the ion fluid while the neutrals remain quiescent, and the overall α is simply proportional to f. In addition, the strong-coupling limit requires the recombination time to be smaller than the orbital time, which means that ions are continuously created and destroyed on a time scale that is shorter than the time scale for MRI to grow. This additional chemical coupling introduces ionization modes (Blaes & Balbus 1994) which were not captured in HS.

3.2 The Effect of Vertical Field Strength

We select a number of models from the fiducial series and rerun the simulations with three additional initial β_0 values: $\beta_0 = 100, 1600$ and 10^4 (e.g., with magnetic field strength two times and half of that in the fiducial models, as well as one case with an very weak field). These simulations are labeled with an additional letter "s" (for strong), "w" (for weak) and "e" (for extremely weak) in Table 2.1. For strong field simulations with $\beta_0 = 100$, the wavelength for the fastest growing mode exceeds the vertical box size when $Am < 10$. When $Am < 1$, there are essentially no unstable mode in the simulation box. Runs Z3s and Z5s are initiated from seed perturbations, while runs Z6s and Z7s are initiated from the turbulent state at the end of run Z5s. For weak field runs with $\beta_0 = 1600$, on the other hand, the most unstable mode can be fitted into the simulation box for all runs with $Am \gtrsim 0.3$. No unstable mode is fitted into the simulation box when $Am = 0.1$, and as before, Run Z7w is initiated from turbulent state from Z5w to test whether turbulence can be sustained. Our $\beta_0 = 10^4$ simulations allows the most unstable wavelength to be fitted in the simulation box at small Am. We conduct two runs in this case with $Am = 0.33$ (Z6e) and $Am = 0.1$ (Z7e). Run Z7e is initialized from the turbulent state in Z6e to avoid the extremely long time in the linear growth stage. Time averaging in runs Z6w, Z6e and Z7e are taken since $t = 200\Omega^{-1}$ (time averaging in other runs are taken since $t = 100\Omega^{-1}$ by default).

We find from our simulations that sustained MRI turbulence is present in all models except Z6s, Z7s and Z7w. In particular, the MRI turbulence can be self-sustained even if the Am value is as small as 0.1, provided that the net vertical field is sufficiently weak. These results confirm our

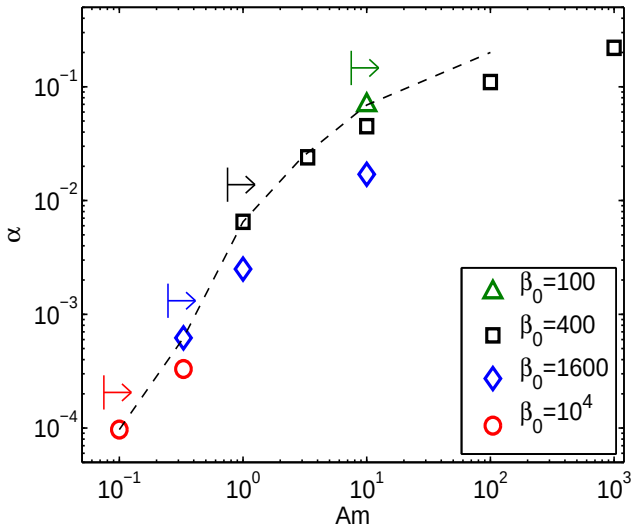


Fig. 2.2.— The time and volume averaged total stress α from all our net vertical flux simulations that sustain MRI turbulence. Simulations with different net vertical flux, characterized by the plasma β_0, are labeled by different symbols and colors. The arrows above the symbols indicate (for each β_0 as represented by the symbol) the range of Am where the most unstable wavelength is smaller than H. The dashed line connecting the symbols represents the maximum value of stress attainable from net vertical flux simulations.

speculation in the fiducial set of simulations that the MRI turbulence is self-sustained as long as unstable MRI modes fit into the simulation box.

The diagnostic quantities from time and volume averaged quantities in the turbulent state from the weak and strong field series of runs are also listed in Table 2.2. We see that for $Am = 10$, the averaged kinetic energy, Reynolds and Maxwell stress monotonically decreases with increasing β_0. Although not all our simulations are run long enough for these quantities to be measured accurately, the trend is significant enough and indicates that the MRI saturate at a higher level with higher net vertical flux (small β_0), in agreement with the ideal MHD case (Hawley et al. 1995). For $Am = 1$, the monotonicity trend is still present by comparing our fiducial run Z5 and the weak field run Z5w. The saturation level of the MRI turbulence in the strong field run Z5s is weaker than that for run Z5. This is most likely because the most unstable mode does not fit into our simulation box (but some less unstable modes fit) in run Z5s. The monotonicity trend further preserves at $Am = 0.33$, where the kinetic energy density and total stress from run Z6w is larger than those from run Z6e by about a factor of 2.

We summarize the main results from the net vertical flux simulations in Figure 2.2. Shown are the total stress α from all the simulations that the most unstable mode is properly resolved so that the MRI turbulence is self-sustained and a reliable value of α can be obtained. As discussed before, at a fixed β_0, there exists a critical value of Am below which the most unstable wavelength would exceed H and the mode tend to be suppressed due to the vertical stratification. This is effect is illustrated by the colored arrows in the Figure. Equivalently, for turbulence to be sustained at small Am, β_0 must be sufficiently large $\beta_0 \gtrsim 100/Am^2$, as can be obtained from equation (2-9). At a given Am, since the stress α monotonically increases with the net vertical flux, there exist a maximum stress, corresponding to the largest allowed net flux (smallest allowed value of β_0). This maximum value of α as a function of Am is illustrated in the dashed line by connecting results from runs Z7e, Z6w, Z5 and Z3s. We see that the maximum α drops by a factor of about 40 from the ideal MHD case to $Am = 1$, and another factor of about 60 as Am decreases to 0.1. By extrapolating this trend, we expect the MRI turbulence can be self-sustained for arbitrarily small value of Am, as long as the background magnetic field is sufficiently weak. Nevertheless, the turbulence would seem to be too weak ($\alpha < 10^{-4}$) to produce significant amount of angular momentum transport as required by most astrophysical disks.

3.3 The Effect of ν

The parameter ν reflects the sensitivity of how the AD coefficient depends on gas density (see Equation (2-5)). Most of our simulations are run with fixed value of $\nu = 0.5$, while ν can in principal span a range from 0 to 1. The significance about the effect of ν largely depends on the level of density fluctuation in the MRI turbulence. In Table 2.2, we list the rms density fluctuation relative to the background gas density from all vertical net flux runs (see column $\langle\delta\rho\rangle/\rho_0$). The rms density fluctuation in the ideal MHD case (run Z1) is relatively large, up to 0.3, and the largest and smallest densities reach about 0.2 and 4 times the background density. Since AD reduces the saturation level of the MRI turbulence, the density fluctuations become smaller as Am decreases. This fact undermines the importance of ν: when the effect of ν may be important (large density fluctuations), AD only plays an insignificant role in the MRI turbulence (large Am); when AD strongly affect the MRI turbulence (small Am), the density fluctuation becomes much smaller and ν is much less likely to be important. This above implies that variations in the value of ν should

not have a major impact, and in particular, the critical value of Am below which MRI is suppressed is unlikely to be altered by different choices of ν.

To confirm our expectations, we perform two additional runs with the same initial conditions as run Z5 ($Am = 1$, $\beta_0 = 400$), but set ν to be 0 and 1 respectively. These two runs are named Z5a and Z5b. We see from Table 2.2 that the turbulence properties from these two runs are essentially identical to those in run Z5. Even though our time averages are taken over relatively short periods, the deviations are generally within 10%. This is understandable since the density fluctuations in these runs are as small as 0.07. It appears certain that the value of ν only plays a very minor role in the MRI turbulence in the strong coupling limit. This result further implies that the requirement of electron recombination time being shorter than the dynamical time is secondary and may be moderately relaxed.

3.4 Properties of the MRI Turbulence with AD

Besides the general properties of the MRI turbulence listed in Table 2.2, we study two other aspects of the MRI turbulence with AD.

First, we study the power spectrum density (PSD) of magnetic and kinetic energies by Fourier analysis. The Fourier analysis in the shearing periodic system is performed by the remapping technique before and after Fourier transformation, as described in Section 2.4 of Hawley et al. (1995). Although the PSD is anisotropic in $k-$space, it would be beneficial to plot the PSD in one dimensional form by some averaging procedure. Following Davis et al. (2010), we compute shell-integrated power spectrum of the magnetic field $B_k^2 \equiv 4\pi k^2 |\widetilde{\boldsymbol{B}}(k)|^2$, where $|\widetilde{\boldsymbol{B}}(k)|^2$ denotes the average of $|\widetilde{\boldsymbol{B}}(\boldsymbol{k})|^2$ over shells of constant $k = |\boldsymbol{k}|$, and $\widetilde{\boldsymbol{B}}(\boldsymbol{k}) = \int \boldsymbol{B}(\boldsymbol{x}) e^{-i\boldsymbol{k}\cdot\boldsymbol{x}} d^3\boldsymbol{x}/V$ is the Fourier transform of $\boldsymbol{B}(\boldsymbol{x})$. Here V is the volume of the simulation box. The Fourier transformation is of course discrete, but for notational convenience we write the formulas in continuous form. According to Parseval's theorem, we have

$$\begin{aligned} \frac{1}{V}\int_V |\boldsymbol{B}(\boldsymbol{x})|^2 d^3\boldsymbol{x} &= \int |\widetilde{\boldsymbol{B}}(\boldsymbol{k})|^2 \frac{d^3\boldsymbol{k}}{(2\pi)^3} \\ &= \frac{1}{(2\pi)^3}\int 4\pi k^2 |\widetilde{\boldsymbol{B}}(k)|^2 dk \ . \end{aligned} \tag{2-10}$$

Dividing by a factor of 8π we obtain the PSD for the magnetic energy density $M_k = B_k^2/8\pi$. Similarly, one can obtain the PSD for the kinetic energy K_k.

Table 2.2: Time and volume averaged quantities in net vertical flux simulations.

Run	$\frac{E_{k,x}}{E_{M,x}}$	$\frac{E_{k,y}}{E_{M,y}}$	$\frac{E_{k,z}}{E_{M,z}}$	$\frac{\alpha_{\rm Re}}{\alpha_{\rm Max}}$	$\frac{\langle\delta\rho\rangle/\rho_0}{\alpha}$
Z1	7.0×10^{-2}	0.10	2.9×10^{-2}	5.4×10^{-2}	0.36
	8.4×10^{-2}	0.20	3.4×10^{-2}	0.17	0.22
Z2	4.4×10^{-2}	6.5×10^{-2}	1.9×10^{-2}	3.3×10^{-2}	0.31
	4.5×10^{-2}	8.7×10^{-2}	2.1×10^{-2}	7.4×10^{-2}	0.11
Z3	2.8×10^{-2}	2.7×10^{-2}	1.4×10^{-2}	1.6×10^{-2}	0.20
	1.4×10^{-2}	3.3×10^{-2}	9.9×10^{-3}	2.9×10^{-2}	4.5×10^{-2}
Z4	1.8×10^{-2}	1.3×10^{-2}	8.6×10^{-3}	9.0×10^{-3}	0.14
	6.5×10^{-3}	1.8×10^{-2}	6.3×10^{-3}	1.5×10^{-2}	2.4×10^{-2}
Z5	5.4×10^{-3}	1.9×10^{-3}	3.1×10^{-3}	2.4×10^{-3}	0.070
	1.2×10^{-3}	5.1×10^{-3}	3.3×10^{-3}	4.1×10^{-3}	6.5×10^{-3}
Z3s	3.5×10^{-2}	3.3×10^{-2}	9.6×10^{-3}	2.9×10^{-2}	0.18
	3.4×10^{-2}	5.0×10^{-2}	2.7×10^{-2}	4.0×10^{-2}	6.9×10^{-2}
Z5s	3.7×10^{-3}	1.8×10^{-3}	3.5×10^{-3}	2.4×10^{-3}	0.063
	1.2×10^{-3}	1.2×10^{-3}	1.0×10^{-2}	2.2×10^{-3}	4.6×10^{-3}
Z3w	1.0×10^{-2}	7.3×10^{-3}	4.6×10^{-3}	5.1×10^{-3}	0.091
	4.4×10^{-3}	2.0×10^{-2}	3.6×10^{-3}	1.2×10^{-2}	1.7×10^{-2}
Z5w	2.5×10^{-3}	1.1×10^{-3}	9.6×10^{-4}	9.5×10^{-4}	0.054
	3.6×10^{-4}	3.5×10^{-3}	1.1×10^{-3}	1.5×10^{-3}	2.5×10^{-3}
Z6w	9.3×10^{-4}	2.0×10^{-4}	5.8×10^{-4}	2.9×10^{-4}	0.037
	5.3×10^{-5}	7.7×10^{-4}	7.2×10^{-4}	3.3×10^{-4}	6.2×10^{-4}
Z6e	7.0×10^{-4}	1.5×10^{-4}	7.7×10^{-5}	2.1×10^{-4}	0.036
	2.1×10^{-5}	4.7×10^{-4}	1.5×10^{-4}	1.2×10^{-4}	3.3×10^{-4}
Z7e	2.8×10^{-4}	5.3×10^{-5}	3.4×10^{-5}	6.6×10^{-5}	0.023
	4.3×10^{-6}	1.3×10^{-4}	1.2×10^{-4}	3.1×10^{-5}	9.7×10^{-5}
Z5a	5.4×10^{-3}	2.0×10^{-3}	3.3×10^{-3}	2.4×10^{-3}	0.070
	1.2×10^{-3}	5.2×10^{-3}	3.3×10^{-3}	4.1×10^{-3}	6.4×10^{-3}
Z5b	5.0×10^{-3}	1.8×10^{-3}	3.3×10^{-3}	2.2×10^{-3}	0.068
	1.4×10^{-3}	4.9×10^{-3}	3.3×10^{-3}	3.8×10^{-3}	6.0×10^{-3}

In Figure 2.3, we show the PSDs computed from our runs Z1 and Z5. These two simulations are representative for the MRI turbulence in the ideal MHD and AD dominated regimes respectively, and are run for two times longer than many other simulations (thus giving better statistics). We see that the shape of the PSD obtained from our simulations are very similar. The PSD roughly follows a power-law form at small k, with the power law index approximately equals to $-11/3$, which is the index for incompressible Kolmogorov turbulence spectrum. There appears to be a spectral break at $kH \approx 70$ in both simulations, corresponding to a wavelength of about $0.1H$, and the PSD falls off rapidly toward smaller scales. The turbulent power in the $Am = 1$ case is about 20 times smaller than that in the ideal MHD case. Magnetic energy fluctuations dominate kinetic energy

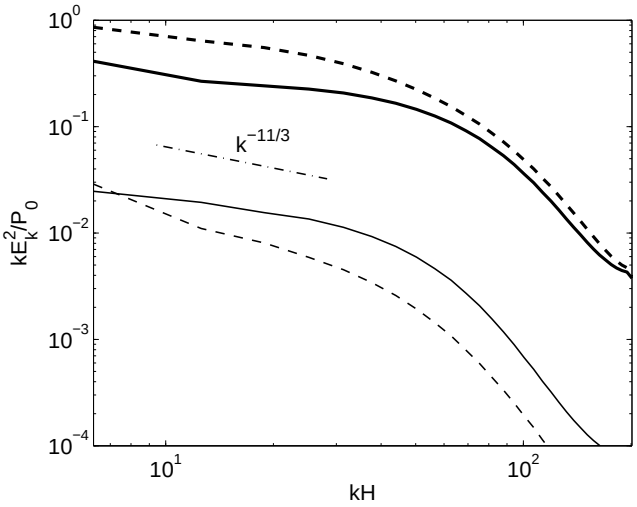


Fig. 2.3.— The power spectrum density of the kinetic (solid) and magnetic (dashed) energy densities, for two vertical net flux simulations with $Am = 1000$ (run Z1, bold) and $Am = 1$ (run Z5, thin). Plotted are the shell integrated spectrum, represented by $E_k^2 = 4\pi k^2 |\widetilde{\boldsymbol{E}}(k)|^2$ (where E denotes kinetic or magnetic energy density), normalized to background pressure $P_0 = \rho_0 c_s^2$. The area enclosed by each curve corresponds to the total energy density from turbulent fluctuations.

fluctuations in the ideal MHD case, while in the AD dominated regime, more turbulence power resides in the kinetic energy. We note that although AD provides explicit magnetic dissipation, the scale of the spectral break is similar to the ideal MHD case, which is mainly because no explicit viscosity is included and the viscous damping scale remains unchanged. Moreover, we have also checked the contour plot of vertically integrated PSD (not shown) and found that the turbulence becomes more anisotropic in the AD dominated regime: the turbulent power is more elongated in k_x than in k_y.

Second, we study the effect of AD on the distribution of current in the MRI turbulence. It has been shown that in one and two dimensions, sharp current structure can be developed around magnetic nulls in the presence of AD (Brandenburg & Zweibel 1994). To examine whether the same effect is present in the MRI turbulence, we show in Figure 2.4 the cumulative probability distribution of the current density $J = |\boldsymbol{J}|$ in our simulation runs Z1, Z3 and Z5. If sharp current structure were to form, one would expect to see extended tails in the probability distribution. However, we see that as Am decreases, the probability distribution shifts leftward since turbulence becomes weaker, but its shape remains largely unchanged. We note that the cutoff of current

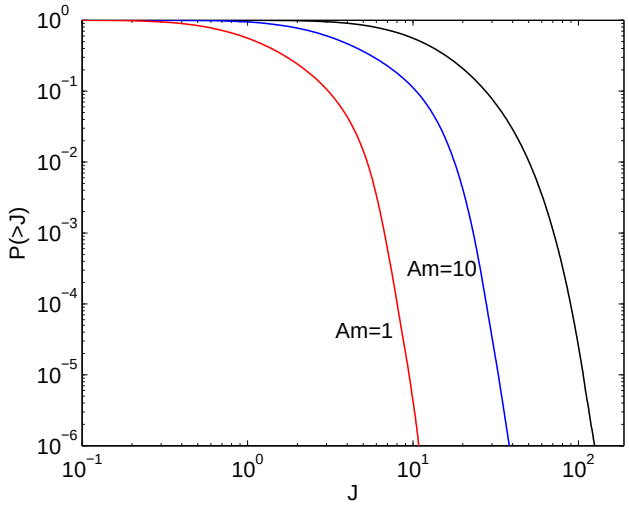


Fig. 2.4.— Cumulative probability distribution of current density J for our simulations Z1 ($Am = 1000$, black), Z3 ($Am = 10$, blue), Z5 ($Am = 1$, red). The current is normalized to $\sqrt{4\pi P_0}c/4\pi H$.

density in the ideal MHD case is likely to be due to numerical dissipation[2], while the cutoffs at $Am = 1$ and 10 are physical. We also note that the current sharpening phenomenon is not observed in simulations by (Brandenburg et al. 1995) either. It is likely the sharpening of current by AD is overwhelmed in 3D MHD turbulence.

AD has also been shown to tend to reduce the current component that is perpendicular to the magnetic field (Brandenburg et al. 1995) and make the magnetic configuration more force-free. To examine this effect, we show the cumulative probability distribution of $|\cos\alpha|$ from our simulation runs Z1, Z2 and Z3 in Figure 2.5, where α is the angle between the current and the magnetic field. The cumulative distribution functions from our runs Z4 and Z5 are almost identical to that from run Z3, where $Am = 10$. We confirm that AD makes the distribution more concentrated toward $|\cos\alpha| = 1$ (i.e., $\boldsymbol{J} \parallel \boldsymbol{B}$).[3] Nevertheless, since the distribution of $|\cos\alpha|$ is already peaked at 1 in

[2]For grid-scale dissipation, one expect $J \lesssim \sqrt{2/\beta}(H/\Delta)$, in normalization in Figure 2.4, where Δ is the size of a grid cell. For our run Z1, $\beta \sim 2$, $J \lesssim H/\Delta = 64$, and we see the probability is strongly reduced for $J \gtrsim 20$, consistent with numerical dissipation at the scale of ~ 3 cells.

[3]We also report a difference in our results from Brandenburg et al. (1995). In their simulations, the distribution function peaks at $|\cos\alpha| = 0$ in ideal the MHD case, and AD concentrate the current toward $|\cos\alpha| = 1$. In our simulations, we find that the distribution function is already concentrated at $|\cos\alpha| = 1$ under ideal MHD, and AD simply makes it more concentrated.

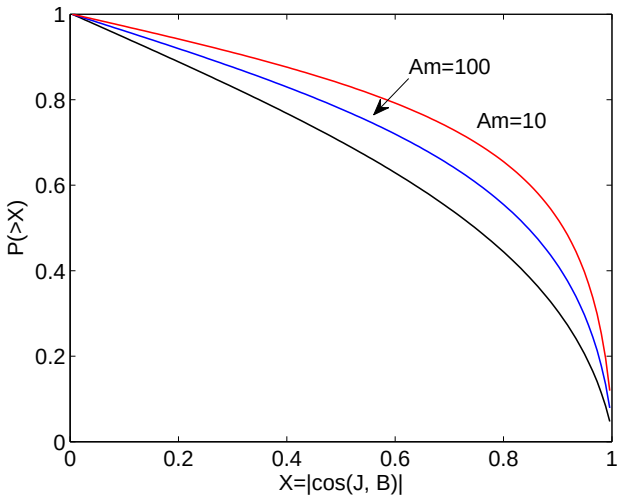


Fig. 2.5.— Cumulative probability distribution of $|\cos\alpha|$, where α is the angle between $\boldsymbol{J}$ and $\boldsymbol{B}$. Shown are the results from our runs Z1 ($Am = 1000$, black), Z2 ($Am = 100$, blue), Z3 ($Am = 10$, red).

the essentially ideal MHD run (Z1), the effect of AD does not modify the distribution of current orientation substantially.

4. Net Toroidal Flux Simulations

In the second group of simulations, the initial field configuration is chosen to be uniform along the azimuthal direction $\hat{y}$, with strength characterized by $\beta_0 = 2P_0/B_0^2$, where B_0 is the initial field strength. Following Simon & Hawley (2009), we fix the box size to be $H \times 4H \times H$ in the radial, azimuthal and vertical dimensions for all simulation runs in this group[4]. We choose the fiducial resolution to be 64 cells per H in the radial and vertical direction, and 32 cells per H in the azimuthal direction. All our net toroidal flux simulations are listed in Table 2.3, including one set of fiducial simulations with $\beta_0 = 100$, one set of higher resolution simulations, and one set of weak field simulations with $\beta_0 = 400$. Unlike net vertical flux, the net toroidal flux is not precisely conserved in our shearing box simulations. As discussed in (Simon & Hawley 2009), ensuring strict conservation of toroidal flux numerically is more complex, and is also less important than

[4]We have also performed our run series Y1 to Y6 using a larger box $4H \times 4H \times H$ and found that the turbulence properties are very similar.

Table 2.3: Net toroidal flux simulations.

Run	Am	β_0	Resolution	Restart	Turbulence
Y1	1000	100	$64 \times 128 \times 64$	No	Yes
Y2	100	100	$64 \times 128 \times 64$	No	Yes
Y3	10	100	$64 \times 128 \times 64$	Y1	Yes
Y4	3.33	100	$64 \times 128 \times 64$	Y1	Yes
Y5	1	100	$64 \times 128 \times 64$	Y1	No
Y6	0.33	100	$64 \times 128 \times 64$	Y1	No
Y7	0.1	400	$64 \times 128 \times 64$	Y1	No
Y1w	1000	100	$64 \times 128 \times 64$	No	Yes
Y2w	100	100	$64 \times 128 \times 64$	No	Yes
Y3w	10	400	$64 \times 128 \times 64$	Y1w	Yes
Y4w	3.33	400	$64 \times 128 \times 64$	Y1w	Yes
Y5w	1	400	$64 \times 128 \times 64$	Y1w	No
Y6w	0.33	400	$64 \times 128 \times 64$	Y1w	No
Y7w	0.1	400	$64 \times 128 \times 64$	Y1w	No
Y1h	1000	100	$128 \times 256 \times 128$	No	Yes
Y3h	10	100	$128 \times 256 \times 128$	Y1h	Yes
Y5h	1	100	$128 \times 256 \times 128$	Y1h	No
Y6h	0.33	100	$128 \times 256 \times 128$	Y1h	No

Box size is fixed at $H \times 4H \times H$, ν is fixed at 0.5. All simulations are run for 24 orbits ($150\Omega^{-1}$).

conserving net vertical flux because the saturation level of the MRI turbulence is not very sensitive to the toroidal flux. Throughout all our simulations in this group, we find that the deviation of net toroidal flux from the initial value is generally less than 2%.

The linear stability of Keplerian disks in the presence of pure toroidal field is more complex than that for the vertical field case. It requires consideration of non-axisymmetric perturbations (Balbus & Hawley 1992), and involves the time-dependent amplification of wave modes as the radial wave number swings from leading to trailing. In ideal MHD, pure toroidal MRI favors high k_z wave numbers, and requires relatively large numerical resolution. In the case of Ohmic resistivity, swing amplification of modes is suppressed when the diffusion time of the mode is comparable to the orbital frequency (Papaloizou & Terquem 1997). A linear stability with non-axisymmetric perturbations in AD dominated regime has yet to be performed. Nevertheless, one might expect that a similar argument holds for AD, with $Am \sim 1$ as the boundary for stability.

4.1 A Fiducial Set of Runs

We fix $\beta_0 = 100$ and run 7 fiducial simulations with different Am values, named from Y1 with $Am = 1000$ to Y7 with $Am = 0.1$ (see Table 2.3) similar to the case of net vertical flux runs. Initial growth of the MRI from pure toroidal field is more difficult and is only achieved when Am is greater than 10. We initialize the rest of the simulations from the turbulent state at the end of run Y1.

Figure 2.6 illustrates the time evolution of the Maxwell stress from this fiducial set of runs. The time and volume averaged quantities from these runs are listed in Table 2.4. We find that at a given value of Am, the saturation level of the MRI with net toroidal flux is much lower than the net vertical flux case. The turbulent energy density and total stress in run Y1 (essencially ideal MHD) is a few times 10^{-2}, about an order of magnitude less than run Z1. As Am drops below 10, the saturation level of the MRI turbulence falls off very rapidly. At $Am = 3$ (run Y4), the total stress falls below 10^{-3}. At $Am = 1$, although a total stress is maintained at a level of 10^{-5}, we do not observe any signature of the MRI turbulence by examining the structure of the velocity field, which is essentially laminar (see further discussion in Section 4.4). Since the simulation is initialized from a turbulent state, the low level of stress and kinetic energy are mostly due to the eigen-modes of the shearing box excited from the initial turbulence, and that are not damped due to the low dissipation in the Athena code. Unlike the case for net vertical flux, there appears to exist a critical value of Am below which MRI turbulence with net toroidal flux is not self-sustained. This critical value of Am is about 3. This fact will be further discussed shortly in Section 4.3.

HS also performed a number of net toroidal flux two-fluid simulations with $Am \approx 1$ and $Am \approx 100$, and in both cases turbulence is self-sustained with total stress α on the order of 10^{-4} to 10^{-3}. Again, these results are no longer valid in the strong-coupling regime and are not directly comparable to our results (see discussion in Section 3.1).

We see from Table 2.4 that the density fluctuations in the net toroidal flux simulations are generally smaller than those in the net vertical flux case. Therefore, following the discussion in Section 3.3, we expect the effect of ν has essentially no impact on the conclusions we have drawn above.

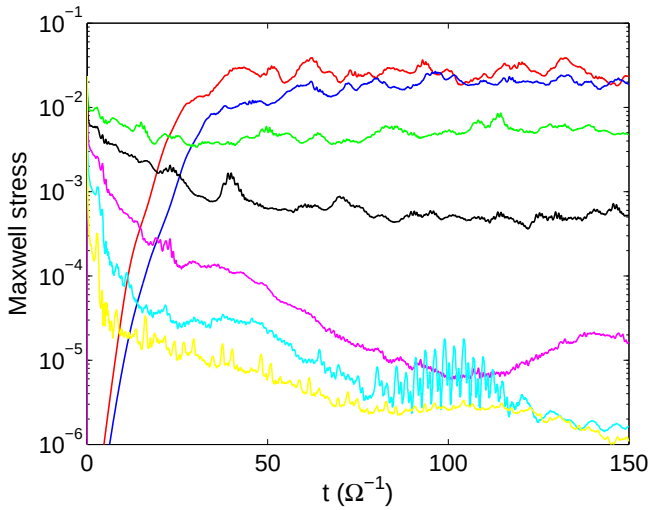


Fig. 2.6.— The evolution of Maxwell stress in our fiducial set of toroidal net-flux runs (from top to bottom: Y1, Y2, ..., Y7) normalized to $c_s H$. For all runs after $Y2$, the simulations start from the end of the Y1 run.

4.2 The Effect of Resolution

Relatively high resolution is needed for net toroidal flux MRI simulations in order to properly capture the amplification of wave modes as they swing from leading to trailing (Simon & Hawley 2009). In order to justify our results in the previous subsection, we perform a few of the simulations with doubled resolution. These runs are labeled with an additional letter "h" (i.e., high resolution) in Table 2.3.

The time and volume averaged quantities from these high resolution runs are shown in Table 2.4. We see that the kinetic and magnetic energy densities from in the high resolution simulations are generally larger than those in the low resolution runs, but only by a small factor. In particular, the difference between low and high resolutions with relatively large AD coefficient is only about 10% (e.g., comparing runs Y3 and Y3h), which strongly indicates numerical convergence. This is not surprising since small scale structures can be largely damped by AD thus higher resolution becomes unnecessary. Run Y5h is also very similar to run Y5, where the initial turbulence is damped with remnant small velocity and magnetic fluctuations unlikely to be associated with the MRI turbulence.

The inferences above are further justified by looking at the power spectrum of magnetic and kinetic energies. Following the same procedure described in Section 3.4, we show in Figure 2.7

Table 2.4: Time and volume averaged quantities in net toroidal flux simulations.

Run	$E_{k,x}$	$E_{k,y}$	$E_{k,z}$	$\alpha_{\rm Re}$	$\langle\delta\rho\rangle/\rho_0$
	$E_{M,x}$	$E_{M,y}$	$E_{M,z}$	$\alpha_{\rm Max}$	α
Y1	1.2×10^{-2}	1.1×10^{-2}	5.2×10^{-3}	7.4×10^{-3}	0.10
	9.7×10^{-3}	5.0×10^{-2}	4.4×10^{-3}	2.6×10^{-2}	3.4×10^{-2}
Y2	1.0×10^{-2}	8.2×10^{-3}	4.6×10^{-3}	6.2×10^{-3}	0.083
	8.2×10^{-3}	4.0×10^{-2}	4.0×10^{-3}	2.0×10^{-2}	2.6×10^{-2}
Y3	4.6×10^{-3}	2.4×10^{-3}	1.8×10^{-3}	2.5×10^{-3}	0.062
	2.4×10^{-3}	1.9×10^{-2}	1.4×10^{-3}	5.7×10^{-3}	8.2×10^{-3}
Y4	6.9×10^{-4}	2.8×10^{-4}	2.1×10^{-4}	3.0×10^{-4}	0.029
	3.4×10^{-4}	1.0×10^{-2}	2.4×10^{-4}	5.0×10^{-4}	8.1×10^{-4}
Y5*	3.5×10^{-5}	8.2×10^{-5}	1.8×10^{-5}	6.6×10^{-6}	0.008
	1.4×10^{-5}	9.7×10^{-3}	3.1×10^{-5}	1.2×10^{-5}	1.9×10^{-5}
Y1w	7.3×10^{-3}	5.6×10^{-3}	3.1×10^{-3}	4.5×10^{-3}	0.079
	4.8×10^{-3}	2.8×10^{-2}	2.1×10^{-3}	1.5×10^{-2}	1.9×10^{-2}
Y2w	4.9×10^{-3}	2.8×10^{-3}	1.8×10^{-3}	2.7×10^{-3}	0.063
	2.5×10^{-3}	1.6×10^{-2}	1.2×10^{-3}	7.7×10^{-3}	1.0×10^{-2}
Y3w	1.7×10^{-3}	5.8×10^{-4}	4.7×10^{-4}	7.2×10^{-4}	0.043
	4.9×10^{-4}	5.4×10^{-3}	2.6×10^{-4}	1.5×10^{-3}	2.2×10^{-3}
Y4w	3.3×10^{-4}	8.1×10^{-5}	8.1×10^{-5}	1.0×10^{-4}	0.022
	6.8×10^{-5}	3.4×10^{-3}	5.8×10^{-5}	2.2×10^{-4}	3.2×10^{-4}
Y5w*	1.2×10^{-4}	6.4×10^{-5}	1.4×10^{-5}	2.4×10^{-5}	0.014
	5.6×10^{-6}	2.4×10^{-3}	4.2×10^{-6}	1.1×10^{-5}	3.5×10^{-5}
Y1h	1.4×10^{-2}	1.7×10^{-2}	6.7×10^{-3}	8.4×10^{-3}	0.12
	1.6×10^{-2}	7.3×10^{-2}	8.1×10^{-3}	3.8×10^{-2}	4.7×10^{-2}
Y3h	4.5×10^{-3}	2.9×10^{-3}	1.9×10^{-3}	2.5×10^{-3}	0.056
	3.2×10^{-3}	2.3×10^{-2}	1.9×10^{-3}	6.8×10^{-3}	9.3×10^{-3}
Y5h*	7.4×10^{-5}	6.3×10^{-5}	8.7×10^{-6}	1.5×10^{-5}	0.011
	1.0×10^{-5}	1.0×10^{-2}	3.2×10^{-5}	7.5×10^{-6}	2.2×10^{-5}

*: These runs are not turbulent.

the shell integrated PSDs for runs Y1, Y1h and Y3, Y3h. The spectral shapes from the low resolution simulations appear to have a spectral peak at relatively large scales of about $0.5H$, while at higher resolution, a power law spectrum at intermediate scales from approximately $0.1H$ to $0.5H$ analogous to an inertia range appears to have developed. This observation may suggest high numerical resolution of at least 128 cells per H is needed for the toroidal field MRI simulations in order to resolve the inertia range in the turbulent spectrum, although smaller resolution of 64 cells per H appears to be sufficient for turbulence properties to converge. The shape of the PSDs at small k look very different from the PSDs in the net vertical flux simulations, indicating different

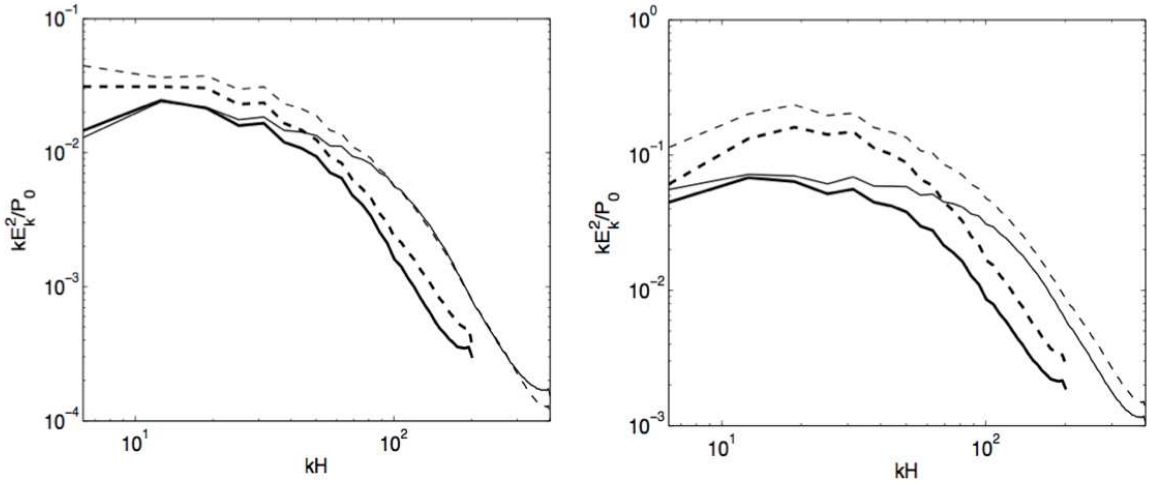


Fig. 2.7.— Similar to Figure 2.3, but for net toroidal flux simulations. Shown are the shell integrated power spectrum density of the kinetic (solid) and magnetic (dashed) energy densities. Left panel: results from simulations with $Am = 10$, with low-resolution (run Y3) and high-resolution (Y3h) results shown in bold and thin lines. Right panel: results from simulations with $Am = 1000$ (essentially ideal MHD). Our fiducial low-resolution results (run Y1) are shown in bold curves, while high-resolution results (run Y1h) are shown in thin lines. The uncertainty is about 10%.

energy injection mechanism, while at large k, the PSDs from both cases fall off in a similar manner, indicating similar dissipation mechanism.

4.3 The Effect of Toroidal Field Strength

We have also performed the same set of net toroidal flux simulations with the toroidal magnetic field strength lowered by one half, $\beta_0 = 400$, labeled with an additional letter "w" (i.e., weak field) in Table 2.3. General properties from the saturated state of these runs are also shown in Table 2.4. We see that at the same value of Am, the kinetic and magnetic energy density from the weak field simulations are smaller than those in our fiducial runs by a factor of 2-3. By inspection of the velocity field as well as the distribution of current density, we find that sustained turbulence is supported in run Y4w but not in run Y5w. Note that the time and volume averaged kinetic energy density from run Y4w is 4.9×10^{-4}, which is slightly below our limit of 10^{-3}, but the total stress $\alpha = 3.2 \times 10^{-4}$ is reasonably large and is unlikely to be caused by inertia waves in the simulation box. Further discussion will be given in the next subsection 4.4.

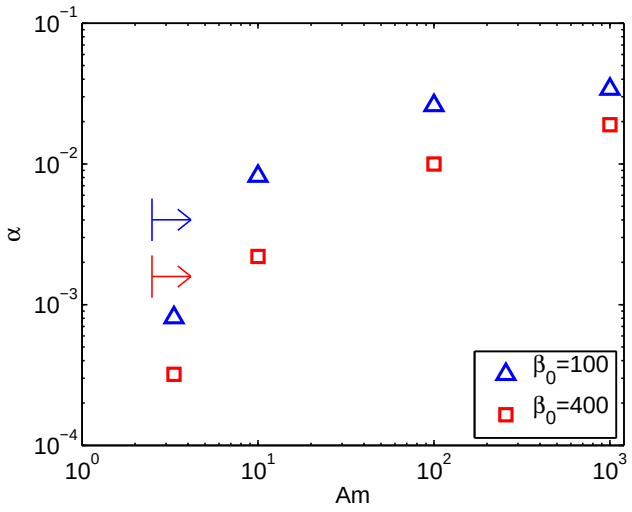


Fig. 2.8.— The time and volume averaged total stress α from our net toroidal flux simulations. Simulations with different net toroidal flux, characterized by the plasma β_0, are labeled by different symbols and colors. The arrows for each β_0 (as represented in red and blue) indicate the range of Am where MRI turbulence can be sustained.

Together with the results from Section 4.1, we summarize the results from net toroidal flux simulations in Figure 2.8. We see that for both values of β_0 (100 and 400), we do not observe any sustained MRI turbulence for $Am < 3$. Although we have not explored weaker net toroidal flux, based on the trend we see from the Figure, even if MRI can be self-sustained at $Am \lesssim 1$ with weaker net toroidal flux, the resulting total stress α is unlikely to be above 10^{-4}. This is in stark contrast with the net vertical flux simulations, and indicates that pure toroidal field geometry is more stable in the AD dominated regime.

4.4 Criterion for Sustained Turbulence

A key objective of this paper is to study when MRI turbulence can be self-sustained in the presence of AD in the strong coupling limit. For the net vertical flux simulations, the criterion is relatively clear: turbulence can be sustained as long as the most MRI unstable mode fits into the simulation box. The situation is less clear for net toroidal flux simulations, and it remains to be seen whether the latter can be characterized as self-sustained turbulence.

We take run Y5 as an illustrative example in this subsection, but the analysis also applies to other marginal runs including Z6, Y5w, Y5h. In run Y5, after the initial turbulence has

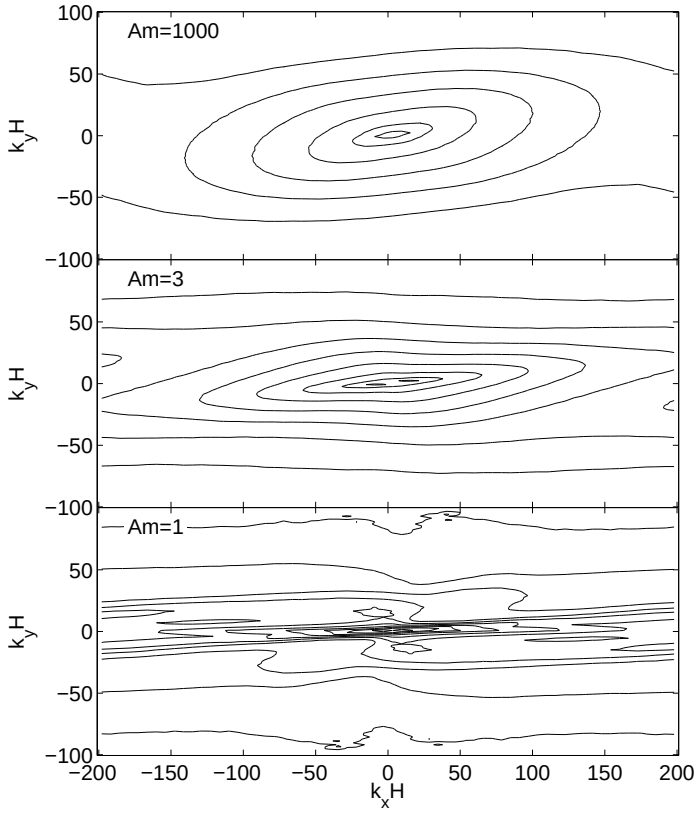


Fig. 2.9.— Contour plot of the vertically integrated power spectrum density of kinetic energy from our net toroidal flux simulation runs Y1 ($Am = 1000$), Y4 ($Am = 3$) and Y5 ($Am = 1$). Neighboring contours are separated by a factor of 10 in the power spectrum density.

damped, the flow is largely laminar, except in a few very localized regions where some narrow but azimuthally elongated current structure is present and evolves very slowly with time. These features can be better demonstrated by computing the vertically integrated Fourier power spectrum of magnetic and kinetic energies. Following the same procedure as described in Section 3.4 but integrating the full three-dimensional PSD over k_z, we show the contour plot of the kinetic energy PSD in the $k_x - k_y$ plane from our runs Y1, Y4 and Y5 in Figure 2.9. We see that in ideal MHD (Y1), the vertically integrated PSD has elliptic contours elongated and tilted toward the k_x axis. The contours are distorted and more elongated when AD is added (Y4). However, in run Y5, we see that the overall shape of the PSD contours are extremely elongated in the k_x direction. The original elliptic contours are almost destroyed, with irregular fragments distributed around the center. These irregular features in the vertically integrated PSD strongly indicate that the system

is not in a turbulent state. We have also found that such irregular features are also present in runs Z6, Y5w and Y5h, but not present in runs Z5, Y4w and Y3h.

In sum, we conclude that non-zero kinetic energy density and total stress do not prove the existence of the MRI turbulence in shearing box simulations. Transition from self-sustained turbulence to non-turbulent state can be judged by looking at the vertically integrated PSD of kinetic and magnetic energies.

5. Simulations with Both Vertical and Toroidal Fluxes

Motivated by the linear stability analysis of the MRI with AD by Kunz & Balbus (2004) and Desch (2004), we present simulations that include both vertical and toroidal fluxes. These authors found that in the presence of both vertical and toroidal field, unstable modes exists for any values of Am, and the fastest growth rate is non-vanishing even as $Am \to 0^+$. When $Am \lesssim 1$, the wave number of the most unstable mode has a substantial non-zero radial component. In this subsection, we explore whether this behavior in the linear regime affects the non-linear evolution of the MRI with AD.

We use the vertical plasma β: $\beta_{z0} = 8\pi P_0/B_z^2$ to specify the net vertical magnetic flux. The net toroidal flux is specified by its ratio to the net vertical field B_ϕ/B_z. We consider two sets of simulations, with $B_\phi/B_z = 4$ and $B_\phi/B_z = 1.25$ and labeled by letters "M" and "N" respectively. Parameters of these runs are given in Table 2.5. Similar to the previous subsections, we scan the parameter Am from 1000 down to 0.1. We use the dispersion relation (31) - (35) in Kunz & Balbus (2004) to find the wavenumber of the most unstable mode. We find that for $Am \gtrsim 3$, the most unstable wavenumber is essentially purely vertical, while for $Am \lesssim 1$, the most unstable wavenumber is oblique with $k_z \sim -k_r$. Correspondingly, we choose the box size to be $H \times 4H \times H$ for runs with $Am \geq 3$ and $4H \times 4H \times H$ for $Am \leq 1$. For simulations with $Am \leq 1$, we expect the fastest growth of the MRI to occur in the diagonal direction of the $x - z$ plane.

By default, we fix $\beta_{z0} = 1600$ in both sets of simulations. However, as Am falls below 1, we find that the fastest growing mode will no longer fit into our simulation box. Based on the results from Section 3, MRI turbulence would not be sustained in this case. Therefore, we increase β_{z0} to the value such that the most unstable mode just fit into the box. In the case of $B_\phi/B_z = 4$, β_{z0} is increased to 8000 and 3×10^4 for $Am = 0.33$ and $Am = 0.1$ respectively. For $B_\phi/B_z = 1.25$, we

Table 2.5: Simulations with both net vertical and toroidal fluxes.

Run	Am	Box size	β_{z0}[1]	B_ϕ/B_z	Orbits
M1	1000	$H \times 4H \times H$	1600	4	48
M2	100	$H \times 4H \times H$	1600	4	48
M3	10	$H \times 4H \times H$	1600	4	36
M4	3.33	$H \times 4H \times H$	1600	4	36
M5	1	$4H \times 4H \times H$	1600	4	42
M6	0.33	$4H \times 4H \times H$	8000	4	96
M7	0.1	$4H \times 4H \times H$	30000	4	96
N1	1000	$H \times 4H \times H$	1600	1.25	48
N2	100	$H \times 4H \times H$	1600	1.25	48
N3	10	$H \times 4H \times H$	1600	1.25	48
N4	3.33	$H \times 4H \times H$	1600	1.25	48
N5	1	$4H \times 4H \times H$	1600	1.25	46
N6	0.33	$4H \times 4H \times H$	1600	1.25	96
N7	0.1	$4H \times 4H \times H$	8000	1.25	96

The grid resolution is fixed at 64 cells per H. All simulations are initiated from seed perturbations, and generate sustained turbulence.
[1]: plasma β from the vertical magnetic field.

increase β_{z0} to 8000 at $Am = 0.1$. Consequently, for all simulations in this subsection, MRI grows from the initial seed perturbations, and generates sustained turbulence after saturation. Below we discuss the properties of the MRI turbulence in the two sets of simulations.

The first group of simulations (with $B_\phi/B_z = 4$) are run for at least 36 orbits. The initial growth of the MRI from runs M5 ($Am = 1$), M6 ($Am = 0.33$) and M7 ($Am = 0.1$) are slower than the ideal MHD limit due to strong effect of AD: the fastest growth rates σ_m predicted from the linear dispersion relation for these simulation runs are $0.189\Omega^{-1}$, $0.149\Omega^{-1}$ and $0.136\Omega^{-1}$ respectively. This is to be compared with the case with pure vertical field with the same Am, where the corresponding σ_m is $0.428\Omega^{-1}$, $0.218\Omega^{-1}$ and $0.074\Omega^{-1}$ respectively. The presence of both vertical and toroidal field gives a smaller growth rate at relatively large Am, but σ_m decreases much slower with decreasing Am than the pure vertical field case. At $Am \lesssim 0.1$, a field configuration with both net vertical and toroidal fluxes becomes more favorable than the pure net vertical field geometry by having substantially larger σ_m.

In the second group of runs, we choose $B_\phi/B_z = 1.25$, which generates the fastest grow rate at $Am \leq 1$ compared with any other values. The fastest growth rates σ_m for runs N5 ($Am = 1$),

Table 2.6: Time and volume averaged quantities in simulations with both net vertical and net toroidal fluxes.

Run	$E_{k,x}$	$E_{k,y}$	$E_{k,z}$	$\alpha_{\rm Re}$	$\langle\delta\rho\rangle/\rho_0$
	$E_{M,x}$	$E_{M,y}$	$E_{M,z}$	$\alpha_{\rm Max}$	α
M1	5.6×10^{-2}	5.8×10^{-2}	1.9×10^{-2}	3.4×10^{-2}	0.26
	6.7×10^{-2}	0.30	2.8×10^{-2}	0.17	0.21
M2	4.2×10^{-2}	3.4×10^{-2}	1.2×10^{-2}	2.4×10^{-2}	0.16
	4.3×10^{-2}	0.17	2.0×10^{-2}	0.10	0.13
M3	1.6×10^{-2}	9.2×10^{-3}	5.7×10^{-3}	9.1×10^{-3}	0.087
	1.1×10^{-2}	5.3×10^{-2}	6.3×10^{-3}	2.8×10^{-2}	3.7×10^{-2}
M4	9.5×10^{-3}	4.7×10^{-3}	3.7×10^{-3}	4.7×10^{-3}	0.075
	3.9×10^{-3}	2.2×10^{-2}	3.3×10^{-3}	8.7×10^{-3}	1.3×10^{-2}
M5	3.9×10^{-3}	2.8×10^{-3}	1.4×10^{-3}	1.7×10^{-3}	0.066
	1.3×10^{-3}	1.3×10^{-2}	1.7×10^{-3}	2.8×10^{-3}	4.5×10^{-3}
M6	1.7×10^{-3}	2.1×10^{-3}	2.2×10^{-4}	5.6×10^{-4}	0.058
	1.3×10^{-4}	2.6×10^{-3}	3.1×10^{-4}	4.0×10^{-4}	9.6×10^{-4}
M7	1.4×10^{-3}	4.0×10^{-4}	6.5×10^{-5}	4.8×10^{-4}	0.050
	3.0×10^{-5}	7.6×10^{-4}	7.3×10^{-5}	1.3×10^{-4}	6.1×10^{-4}
N1	3.8×10^{-2}	3.9×10^{-2}	1.4×10^{-2}	2.2×10^{-2}	0.20
	4.2×10^{-2}	0.20	1.8×10^{-2}	0.12	0.14
N2	2.8×10^{-2}	2.2×10^{-2}	9.4×10^{-3}	1.6×10^{-2}	0.13
	2.7×10^{-2}	0.11	1.3×10^{-2}	6.8×10^{-2}	8.3×10^{-2}
N3	1.4×10^{-2}	6.7×10^{-3}	4.5×10^{-3}	6.9×10^{-3}	0.080
	7.4×10^{-3}	3.6×10^{-2}	4.4×10^{-3}	2.0×10^{-2}	2.7×10^{-2}
N4	6.3×10^{-3}	3.4×10^{-3}	2.9×10^{-3}	2.6×10^{-3}	0.068
	1.7×10^{-3}	9.2×10^{-3}	2.1×10^{-3}	4.6×10^{-3}	7.3×10^{-3}
N5	3.2×10^{-3}	1.8×10^{-3}	1.3×10^{-3}	1.2×10^{-3}	0.065
	5.2×10^{-4}	4.7×10^{-3}	1.3×10^{-3}	1.8×10^{-3}	3.0×10^{-3}
N6	1.2×10^{-3}	1.1×10^{-3}	9.0×10^{-4}	3.8×10^{-4}	0.057
	1.2×10^{-4}	1.8×10^{-3}	8.7×10^{-4}	4.8×10^{-4}	8.6×10^{-4}
N7	9.9×10^{-4}	2.4×10^{-4}	1.1×10^{-4}	3.0×10^{-4}	0.042
	2.9×10^{-5}	5.7×10^{-4}	1.8×10^{-4}	1.6×10^{-4}	4.7×10^{-4}

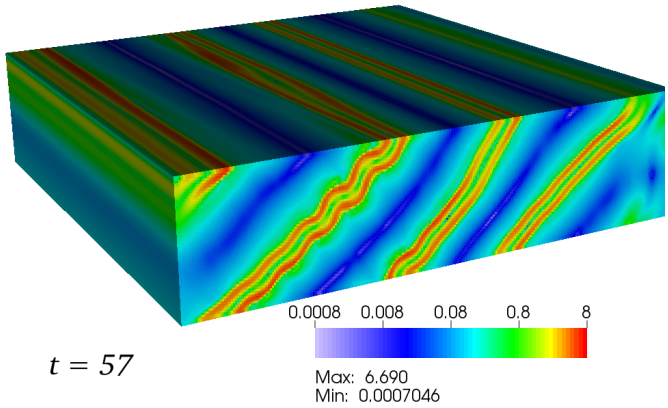


Fig. 2.10.— The distribution of current density in run M5 with $Am = 1$, $B_\phi/B_z = 4$ at the break down of the "channel flow" before saturating into turbulence (at time $t = 57\Omega^{-1}$).

N6 ($Am = 0.33$) and N7 ($Am = 0.1$) are $0.371\Omega^{-1}$, $0.253\Omega^{-1}$ and $0.206\Omega^{-1}$ respectively, which are nearly two times larger than those for $B_\phi/B_z = 4$.

Our simulations with $Am \leq 1$ (M5-M7, N5-N7) are particularly interesting because the fastest growing mode has a non-zero radial wave number $|k_r|$ comparable to $|k_z|$. During the linear growth stage, we observe axisymmetric structures in the $x - z$ plane similar to channel modes, but tilted toward the diagonal direction. These structures grow to a large amplitude, and finally break down into turbulence. As an example, we show in Figure 2.10 the distribution of current density right before the break down of the channel flow for run M5. In the turbulent state, one can still observe the emergence of structures elongated in the diagonal direction in the $x - z$ plane from time to time, which then fragment and inject kinetic energy into the system. For the simulations with $Am \leq 0.33$, these events lead to sporadic increase of kinetic energy and Reynolds stress on time scales of $10 - 20$ orbits. Due to such long time variability, we run these models for longer (to 96 orbits) and take the time average from about 56 orbits ($350\Omega^{-1}$) onward.

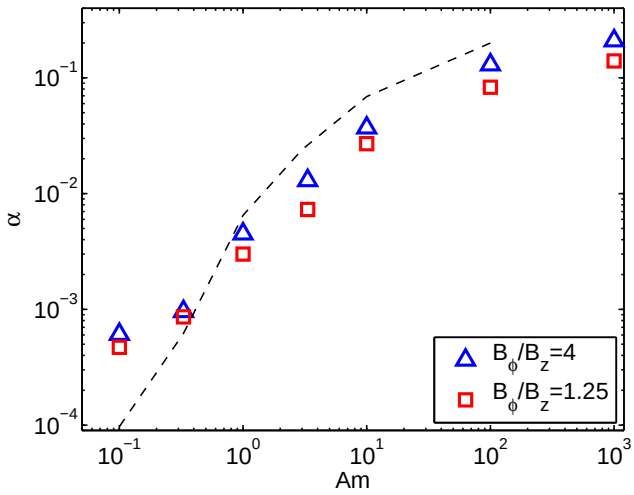


Fig. 2.11.— The time and volume averaged total stress α from our simulations with both net vertical and net toroidal flux. Shown are results from two groups of simulations with different ratio B_ϕ/B_z, are labeled by different symbols and colors. Dashed line represents the maximum value of α obtained from pure net vertical flux simulations (Figure 2.2).

The time and volume averaged properties of the MRI turbulence in all simulations with both net vertical and toroidal fluxes are listed in Table 2.6. In Figure 2.11 we plot the total turbulent stress α as a function of Am from the two groups of simulations. We see that at $Am \gtrsim 1$, where all simulations have the same net vertical flux $\beta_{z0} = 1600$, runs with $B_\phi/B_z = 4$ generate slightly stronger MRI turbulence than simulations with $B_\phi/B_z = 1.25$. This trend can be extrapolated down to zero net toroidal flux, as one can compare with results in runs Z3w and Z5w in Table 2.2. The dependence of turbulent strength on the toroidal flux is relatively weak, and when the net vertical flux in doubled, as in runs Z1 to Z5, the strength of the turbulence becomes stronger than our corresponding runs M1 to M5.

For simulations with $Am < 1$, we find that the turbulent stress α exceeds the maximum possible α attainable by the pure net vertical flux simulations. At $Am = 0.1$, the maximum value of α is 6.1×10^{-4}, as compared to about 9.7×10^{-5} from the pure net vertical flux case. This is consistent with the linear dispersion properties discussed before: the presence of both vertical and toroidal field raises the maximum growth rate in the $Am < 1$ regime. While the values of α given by the $B_\phi/B_z = 4$ group are still larger than those in the $B_\phi/B_z = 1.25$ group, the latter group produces larger Maxwell stress. We note that for $Am \leq 1$, we have chosen the largest possible net flux such that the vertical extent of the simulation box can fit only one most unstable

mode. According to the discussion in Section 3.2, the strength of the MRI turbulence from these simulations represents the highest possible level at the given value of Am and the given magnetic field geometry for our box size, and may also approach the highest level in real disks.

6. MRI with Ambipolar Diffusion: A Quantitative Criterion

In this section, we combine the results from all our simulations and further discuss the criteria for whether the MRI can be self-sustained with AD in a more general context.

The MRI acts as a dynamo which amplifies initially weak fields. Although the saturation mechanism of the MRI is not well understood (but see Pessah & Goodman (2009); Pessah (2010)), the magnetic field energy at the saturated state scales with the net magnetic flux and is generally below equipartition with thermal energy (Hawley et al. (1995); Sano et al. (1998) as well as this paper). Given the field geometry, there should exist a one-to-one correspondence between the initial field strength characterized by β_0 and the final field strength characterized by $\langle\beta\rangle$ (the space and time averaged gas to magnetic pressure at the saturated state), with $\langle\beta\rangle < \beta_0$ for weak field due to the MRI dynamo, and gradually transiting to $\langle\beta\rangle \approx \beta_0$ where the background field is too strong field to be destabilized.

The quantity $\langle\beta\rangle$ is also very useful for studying non-ideal MHD effects because the value it controls the relative importance of various non-ideal MHD effects (Ohmic, Hall and AD, e.g., see Wardle (2007); Bai (2011a)). Henceforth, we shall consider $\langle\beta\rangle$ as a main diagnostic quantity on the MRI turbulence.

In Figure 2.12 we show the scatter plot of α and $\langle\beta\rangle$ from all our simulations with sustained turbulence with different field geometries. We see that regardless of the initial field geometry and the value of Am, there is a remarkably tight correlation between the two quantities at the saturated state of the MRI turbulence. The correlation can be represented by

$$\langle\beta\rangle \approx \frac{1}{2\alpha} \ . \tag{2-11}$$

This result is consistent with findings by (Hawley et al. 1995) in ideal MHD simulations, and extends it to the non-ideal MHD regime. Analytical study of the saturation of the MRI with Ohmic resistivity by parasitic modes also predicts similar relations (Pessah 2010). More explicitly, this relation translates to

$$\overline{B^2} \approx 4\overline{B_r B_\phi}(1+R) \ , \tag{2-12}$$

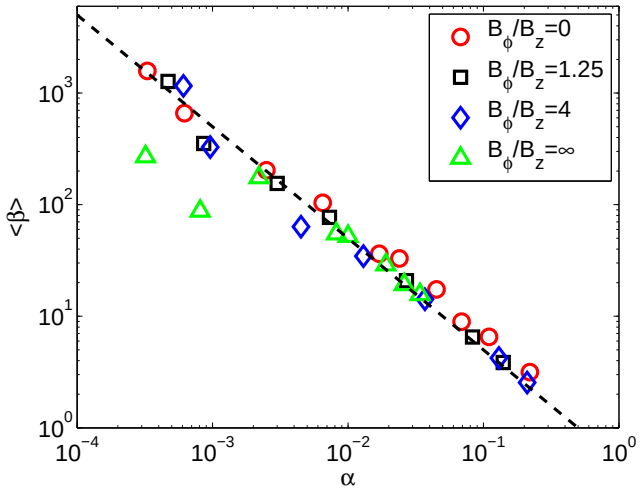


Fig. 2.12.— Scatter plot of the total turbulent stress α and the plasma β at the saturated state of the MRI turbulence from all our simulations. Simulations with different field geometries are marked by different symbols and colors as indicated in the legend, where $B_\phi/B_z = 0$ and $B_\phi/B_z = \infty$ correspond to pure net vertical and pure net toroidal flux simulations respectively. Dashed line shows the fitting curve $\langle\beta\rangle = 1/2\alpha$.

where R is the ratio of Reynolds to Maxwell stress (typically $\approx 1/3$ in the ideal MHD case). This relation implies that the Maxwell stress is approximately a fixed fraction of the total magnetic energy, a reasonable result if the magnetic field is dominated by turbulent fluctuations. Only two points appear to deviate from this correlation, which correspond to net toroidal flux simulations with $Am = 3$. We see from Table 2.4 that in these two simulations, the magnetic energy is dominated by the background toroidal field (i.e., in the transition where MRI is marginally sustained), therefore producing smaller $\langle\beta\rangle$ than predicted.

Next, we consider the relation between $\langle\beta\rangle$ and Am. In Figure 2.13 we show scatter plot of Am and $\langle\beta\rangle$. We see that $\langle\beta\rangle$ does not strongly correlate with Am, but also depends on the field geometry and the initial field strength. However, combining the simulation from all field geometries allow us to identify the lower bound of $\langle\beta\rangle$ at a given Am, denoted by $\beta_{\rm min}$, below which the field is too strong for to be destabilized based on our discussions before. For $Am \leq 1$, we have performed simulations with the smallest possible β_0 such that the most unstable mode marginally fit into the disk height H, and the value of $\beta_{\rm min}$ identified in this regime is robust. For $Am > 1$, the exploration on β_0 may not be as complete especially in the simulations with both net vertical and toroidal fluxes and the actual $\beta_{\rm min}$ may be somewhat smaller than obtained here. Nevertheless, this regime

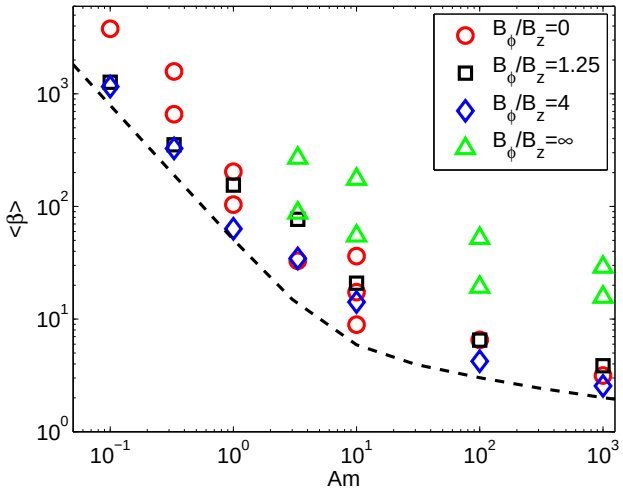


Fig. 2.13.— Scatter plot of AD coefficient Am and the plasma β at the saturated state of the MRI turbulence from all our simulations. Simulations with different field geometries are marked by different symbols and colors as indicated in the legend. The dashed curve shows the fitting formula (2-13) as a lower bound of $\langle\beta\rangle \geq \beta_{\rm min}(Am)$.

is closer to ideal MHD and is less concerning. By combining all the available simulations, we obtain a fitting formula for $\beta_{\rm min}$ given by

$$\beta_{\rm min}(Am) = \left[\left(\frac{50}{Am^{1.2}}\right)^2 + \left(\frac{8}{Am^{0.3}} + 1\right)^2\right]^{1/2}, \qquad (2\text{-}13)$$

and is indicated in Figure 2.13. It asymptotes to 1 at $Am \to \infty$ as one expects, while approaches $50/Am^{1.2}$ for $Am \lesssim 1$.

The constraint on $\beta_{\rm min}$ at a given Am allows us to identify the regions in the Am-$\langle\beta\rangle$ plane at which MRI can or can not operate. In the mean time the correlation between α and $\langle\beta\rangle$ provide the corresponding stress when MRI is permitted. Combining them together, the main results from the whole paper are best summarized in Figure 2.14. MRI permitted regions are in the upper right with the boundary given by equation (2-13). It provides useful diagnostics on the properties of the MRI in the AD regime in a concise fashion.

First, at a given Am, the ultimate strength of the MRI turbulence (e.g., α and $\langle\beta\rangle$) depends on the field geometry (including the net flux), but there exists a maximum α (or minimum $\langle\beta\rangle$) at the most favorable field geometry (usually contains both net vertical and toroidal fluxes). One way to think about it is to starts with a weak regular field as we perform our simulations. As the

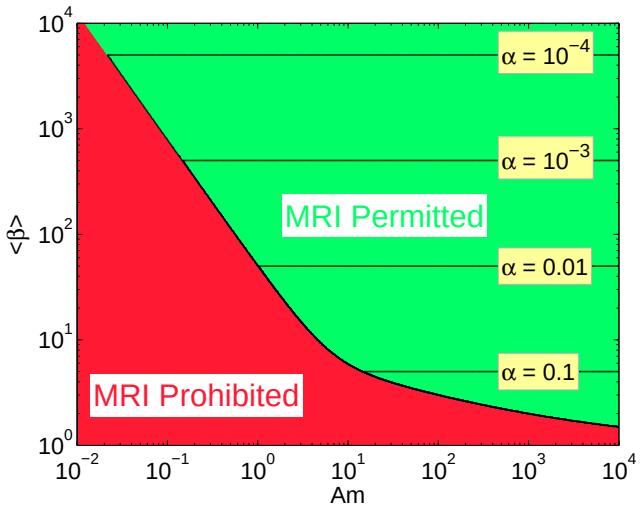


Fig. 2.14.— Diagnostics of the MRI in the AD regime. At a given Am, MRI is permitted when $\langle\beta\rangle \geq \beta_{\rm min}(Am)$ (see equation (2-13)), and in the MRI permitted region, the stress α can be inferred given the field strength at the saturated state characterized by $\langle\beta\rangle$.

system evolves and as the MRI amplifies the field, the corresponding position of the system in the diagram moves downward and until it stops at some $\langle\beta\rangle \gtrsim \beta_{\rm min}$.

Second, MRI can be self-sustained for any value of Am even for $Am \ll 1$. Although we have explored the Am parameter down to $Am = 0.1$, we believe that it can be extended to further smaller Am because of the following reasons. Linear analysis by Kunz & Balbus (2004) and Desch (2004) shows in the presence of both vertical and toroidal field, MRI can grow at appreciable rate (approximately $0.13\Omega^{-1}$ when $B_\phi/B_z = 4$) even in the limit of $Am \to 0^+$ provided that the field is sufficiently weak. This means that MRI turbulence can always be self-sustained. Meanwhile, we find that the linear dispersion relation has already approached the small Am asymptote for $Am \lesssim 0.3$. Therefore, we expect the trend in Figure 2.13 on $\beta_{\rm min}$ to hold to further smaller Am values.

Third, the boundary between the MRI permitted and prohibited regions is only suggestive but it does not necessarily imply sharp transitions. Our simulations are restricted by the limited box height (H) since they are unstratified. In reality, as one increases the field strength, the transition from sustained MRI turbulence to its suppression involves the effect of vertical stratification of gas density in the disks, and may be a smooth process. Before justified by stratified simulations, which is left for our future work, this result should be taken with some caution. In particular,

when vertical stratification is included, linear analysis by Gammie & Balbus (1994) and Salmeron & Wardle (2005) for ideal and non-ideal MHD have suggested the existence of global modes in the disk even in low β_0 and small Elsasser number. On the other hand, in the case of Ohmic resistivity, the criterion that Ohmic Elsasser number equals one being the boundary between MRI permitted and suppressed regions identified in unstratified simulations (Sano et al. 1998; Fleming et al. 2000; Sano & Stone 2002b) do agree with results from stratified simulations (Fleming & Stone 2003; Turner et al. 2007; Ilgner & Nelson 2008).

Our results are mostly relevant to the structure and evolution of the PPDs. Details about the application require considerations of the ionization and recombination processes in the disks with an appropriate chemistry model, which is the subject of the next Chapter.

Chapter 3

Magnetorotational-Instability-Driven Accretion in Protoplanetary Disks

In this chapter, we aim at studying the location and extent of the active regions in protoplanetary disks (PPDs), and predicting the magneto-rotational instability (MRI)-driven accretion rate in the most realistic manner by incorporating all the currently available numerical simulation results, particularly the results in Chapter 1 on the effect of ambipolar diffusion (AD). We do so by solving a complex set of chemical reaction network established in Bai & Goodman (2009), which is summarized in Appendix C. A single population of dust grains is also included in the network. Magnetic diffusion coefficients are calculated from the equilibrium abundance of charged species. A unique feature in our treatment is that we have included the full dependence of magnetic diffusion coefficients (hence the Elsasser number) on the magnetic field strength, with the field strength constrained by the results from non-ideal MHD simulations. This allows us to predict the magnetic field strength and the accretion rate in PPDs using the least amount of assumptions. One closely related work is by Wardle & Salmeron (2012), who performed similar chemistry calculations to obtain magnetic diffusivities of all non-ideal MHD effects with a simpler reaction network, but their estimate for the extent of the active layer was based on the results of linear analysis rather than non-linear numerical simulations. Another closely related work to ours is by Perez-Becker & Chiang (2011a), who were motivated by the accretion problem in transitional disks and the role of

tiny grains. They have considered both Ohmic resistivity and AD, although their adopted criteria were more simplified and did not account for the role of magnetic field strength.

A review of the non-ideal MHD effects in weakly ionized gas such as in PPDs is already given in Section 3 of Chapter 1, with more details given in Appendix A. We therefore begin this chapter by describing our chemistry calculation and the evaluation of magnetic diffusivities in Section 1. In Section 2, we discuss our adopted criteria for the MRI-active layer, and the relation between magnetic field strength and the accretion rate. In Section 3, we present the results of our fiducial model calculation, where a framework for estimating the accretion rate and the magnetic field strength is provided. Using this framework, we study the dependence of accretion rate on various ionization and disk model parameters in Section 4. In addition, an interesting effect arisen from the presence of tiny grains (i.e., PAHs) is explored in Section 5. We summarize and conclude in Section 6.

1. Calculations of Non-ideal MHD Effects in PPDs

Full assessment of the non-ideal MHD effects requires knowledge of the number densities of all charged species in PPDs (see Appendix A). In this section, we describe our chemistry calculations to infer magnetic diffusivities in PPDs. Most technical aspects of the chemistry calculation procedures can be found in Appendix C.

1.1 Ionization Sources

The PPDs are generally too cold for thermal ionization to take place except in the innermost regions (< 1 AU, Fromang et al. 2002). We are interested in regions with $r \gtrsim 1$ AU and consider the following three non-thermal ionization sources.

First, the X-ray ionization from the protostar. Most T-Tauri stars produce strong X-ray emission due to corona activities (see review by Feigelson et al. 2007). The X-ray fluxes are generally variable, with large X-ray flares recurring on time scale of a few weeks (Stelzer et al. 2007). The X-ray emission during the flares is harder than that in the quiescent state. The time averaged X-ray luminosity is roughly proportional to stellar mass, and is about 10^{29} to 10^{31} erg s^{-1} for solar mass stars (Preibisch et al. 2005; Güdel et al. 2007), with typical X-ray temperature

ranging from 1-8 keV (Wolk et al. 2005). We adopt the X-ray temperature $T_X = 5$ keV, and X-ray luminosity $L_X = 10^{30}$ erg s^{-1} as our standard model parameters. We take the ionization rate ($\xi_X^{\rm eff}$) calculated by Igea & Glassgold (1999), which takes into account both absorption and scattering of X-ray photons. In practice, we use the fitting formula given by Bai & Goodman (2009) (see their Equation (21))

$$\xi_X^{\rm eff} = \frac{L_{X,30}}{r_{\rm AU}^{2.2}}\Big[4.0\times10^{-11}e^{-(N_H/N_1)^{0.5}} + 2.0\times10^{-14}e^{-(N_H/N_2)^{0.7}} + \text{bot.}\Big]\text{s}^{-1}\ , \tag{3-1}$$

where $L_{X,30} = L_X/10^{30}$erg s^{-1}, $N_1 = 3.0\times10^{21}$ cm^{-2}, $N_2 = 1.0\times10^{24}$ cm^{-2}, N_H denotes the column number density of hydrogen nucleus from the point of interest to one side of the disk surface, while the "bot." symbol represents the dual terms with N_H being the hydrogen column number density to the other side of the disk surface. The column number densities N_1 and N_2 roughly correspond to column mass density of 1.2×10^{-2} g cm^{-2} and 3.9 g cm^{-2} respectively.

Secondly, the cosmic-ray (CR) ionization with ionization rate (Umebayashi & Nakano 1981) [1]

$$\xi_{\rm CR}^{\rm eff} = 1.0\times10^{-17}\exp\left(-\Sigma/96\text{g cm}^{-2}\right)\text{ s}^{-1} + \text{bot.} \tag{3-2}$$

The CR flux is highly uncertain because on the one hand, the flux may be much higher if a supernova explosion occurs in the vicinity of the protostar, and observations of the CR flux toward the diffuse cloud ζ Persei indicate enhanced ionization rate of 10^{-16} s^{-1} (McCall et al. 2003); but on the one hand, the CR flux may be substantially shielded by the stellar wind.

Third, the radioactive decay, primarily the decay of short lived ^{26}Al, produces ionization rate of 3.7×10^{-19} s^{-1} with half-life 0.717 Myr (Turner & Drake 2009). Here we adopt the ionization rate of 10^{-19} s^{-1} as appropriate for disk ages of around 3 Myr. The radioactive decay is generally too weak to provide sufficient ionization, but it prevents the midplane of the inner disk from being completely neutral.

Other possible ionization sources such as energetic protons from disk and stellar corona (Turner & Drake 2009) are ignored for simplicity. Although the resulting ionization rate may exceed X-ray and cosmic-ray ionization by a factor of as large as 40 (Perez-Becker & Chiang 2011a), their fluxes are highly variable and uncertain. In our calculations we also consider $L_X = 10^{32}$ erg s^{-1} whose ionization rate is likely to overwhelm this effect by at least an order of magnitude.

[1] See Umebayashi & Nakano (2009) for a more refined formula.

Very recently, Perez-Becker & Chiang (2011b) pointed out another potentially important ionization source: the far ultraviolet (FUV) radiation from the protostar. FUV photons are unattenuated by the hydrogen column, and efficiently ionize tracer species of heavy elements such as C and S with penetration depth of up to 0.1g cm^{-2}. FUV ionization is not included in our calculation, while its relative importance will be discussed in Sections 3 and 4.

1.2 Grain Size and Abundance

The abundance and size distribution of grains in PPDs are crucial for disk chemistry. Observationally, they are constrained by modeling the spectra energy distribution (SED) (Chiang & Goldreich 1997; D'Alessio et al. 1998; Dullemond & Dominik 2004). Although the parameters are very degenerate, there have been evidence of grain growth to above micron size (D'Alessio et al. 2001), as well as dust settling (to the midplane, which exhibits as grain depletion, Chiang et al. 2001; D'Alessio et al. 2006; Furlan et al. 2006; Watson et al. 2009). Results from mid-infrared spectroscopy from both T-Tauri stars and Herbig Ae/Be stars (van Boekel et al. 2003, 2005; Przygodda et al. 2003) also revealed the presence of micron-sized grains in a substantial fraction of PPDs.

Another important ingredient of dust grains is the polycyclic aromatic hydrocarbon (PAH), which represents the smallest end of grain size distribution. PAH emission has also been detected in majority of Herbig Ae/Be stars (Acke & van den Ancker 2004), as well as a small fraction of T-Tauri stars (Geers et al. 2006; Oliveira et al. 2010). As argued in Perez-Becker & Chiang (2011a), PAHs may be equally abundant in T-Tauri disks but they fluoresce less luminously due to fainter ultraviolet radiation field of their host stars. The existence of PAHs also suggests a continuous size distribution of grains to the smallest end of a few Å as a result of grain coagulation and fragmentation.

Throughout this thesis, we divide the grain population into two categories, normal grains (or just "grains"), which refer to grains with sizes larger than 0.01μm, and tiny grains for those with size $a \lesssim 0.01\mu$m. Also, we use the phrases "tiny grain" and "PAH" interchangeably. The specialty about $a = 0.01\mu$m will become clear later in Section 5.

For most of this Chapter, we consider only the normal grains. We fix the total grain abundance (or grain mass fraction) to be 0.01 (i.e., solar abundance) and adopt a simplified prescription

of single-sized, well-mixed grains, and consider grain sizes of 0.1μm and 1μm. At fixed grain abundance, the grain size determines the ability to recombine free electrons, and the effect from a continuous grain size distribution can be roughly approximated by a single grain size distribution given that they have the same S factor as defined in Equation (C-3) in Appendix C.

Tiny grains may dominate larger grains in abundance while contribute a negligible fraction of the total grain mass. For a grain density of 3 g cm^{-3} and the gas mean molecular weight μ_n to be 2.34 atomic mass (as appropriate for PPDs), the relation between grain mass fraction (f) and grain abundance per H_2 molecule (x) reads

$$\frac{f}{0.01} \approx 0.32\left(\frac{x}{10^{-9}}\right)\left(\frac{a}{0.01\mu\mathrm{m}}\right)^3 , \tag{3-3}$$

where a is grain size. The abundance of grains with $a \lesssim 0.01\mu$m may easily reach large abundance of 10^{-9} or higher, while the abundance of $a \gtrsim 0.1\mu$m grains would be at most about 10^{-12}.

1.3 Calculation of Magnetic Diffusivities

We evolve the chemical reaction network described in Appendix C for 10^6 years which is long enough to reach quasi-equilibrium[2], and we extract the number densities of all charged species. We then use Equations (A-4) and (A-6) in Appendix A to calculate the magnetic diffusivities. The evaluation process requires one to know the Hall parameter (1-12) or (A-2) for each charged species, which ultimately points to the momentum transfer rate coefficients $< \sigma v >$. For ion-neutral collisions, the neutral atom is induced with an electrostatic dipole moment as it approaches the ions, the resulting rate coefficient is approximately independent of temperature, and is inversely proportional to the reduced mass (Draine (2011), see Table 2.1 and Equation (2.34)):

$$< \sigma v >_i = 2.0 \times 10^{-9}\left(\frac{m_H}{\mu}\right)^{1/2} \mathrm{cm}^3\ \mathrm{s}^{-1} , \tag{3-4}$$

where $\mu = m_i\mu_n/(m_i + \mu_n)$ is the reduced mass in a typical ion-neutral collision.

For electron-neutral collisions, we adopt the approximate fitting formula from Draine et al. (1983), which applies at $T \gtrsim 100$K. The dependence of the rate coefficient on T becomes shallower at lower temperatures due to the polarization effects, and we adopt

$$< \sigma v >_e = 8.3 \times 10^{-9} \times \max\left[1\ ,\ \left(\frac{T}{100K}\right)^{1/2}\right] \mathrm{cm}^3\ \mathrm{s}^{-1} \tag{3-5}$$

[2]Although the abundances for a few species still vary slowly with time, they do not affect the magnetic diffusivities.

as an approximation.

For collisions between neutrals and charged grains, the rate coefficient follows equation (3-4) for sufficiently small grains, while the collision cross section becomes geometric for large grains. Therefore, we have

$$< \sigma v >_{gr} = \max\Bigg[1.3 \times 10^{-9}|Z| \ , \\ 1.6 \times 10^{-7}\left(\frac{a}{1\mu\mathrm{m}}\right)^2\left(\frac{T}{100K}\right)^{1/2}\Bigg] \ \mathrm{cm}^3 \ \mathrm{s}^{-1} \ . \tag{3-6}$$

With these collision rate coefficients, the Hall parameter for electrons and ions can be found approximately to be

$$\beta_i \approx 3.3 \times 10^{-3}\frac{B_G}{n_{15}} \ , \\ \beta_e \approx 2.1\frac{B_G}{n_{15}} \max\left[1, \left(\frac{T}{100\mathrm{K}}\right)^{1/2}\right] \gg \beta_i \ . \tag{3-7}$$

We see from the above that for $T \lesssim 1000$K, one has $|\beta_e| \approx 10^3\beta_i$ and the Hall parameters for essentially all ion species are similar (dependence on the ion mass is very weak). For singly charged grains, one has $\beta_{\mathrm{gr}} \propto a^2 \gg \beta_i$ when grain size $a > 0.1\mu$m, while $\beta_{\mathrm{gr}} \approx \beta_i$ when grain size $a \lesssim 0.1\mu$m.

1.4 Recombination Time

The recombination time t_{rcb} is an important quantity for studying the gas dynamics in PPDs. If t_{rcb} is much shorter than the dynamical time (Ω^{-1}), as is required in the "strong coupling" limit (Shu 1991), local ionization equilibrium would be a good approximation and the magnetic diffusion coefficients can be directly evaluated from the ionization rate and local thermodynamic quantities such as density and temperature. This will simplify numerical calculations considerably because a single-fluid approach is sufficient. In the opposite limit, if t_{rcb} is much longer than the dynamical time, a more appropriate approach would be the multi-fluid method.

The recombination time t_{rcb} is not a well-defined quantity when there are multiple species of ions and when grains are present. Here we propose an effective recombination time $t_{\mathrm{rcb}}^{\mathrm{eff}}$ by noticing the fact that resistivity scales linearly with the abundance of ionized species (especially free electrons, see Equation 1-10). After evolving the reaction network to chemical equilibrium, we turn off the ionization sources and let the system relax (recombine) for a short period of time ($\ll$1

year). We measure the rate of change of the Ohmic resistivity, and the effective recombination time is defined as

$$t_{\rm rcb}^{\rm eff} \equiv \frac{\eta_O}{|d\eta_O/dt|} \ . \tag{3-8}$$

This definition captures the contribution from all recombination channels and is sensitive to the most rapid recombination processes.[3]

2. Criteria for MRI Turbulence and Efficient MRI-driven Accretion

In this section, we provide a quantitative criterion for judging whether the MRI can operate or not under the given diffusivities based on results from numerical simulations. Further, we point out that for the MRI-driven accretion, there is a direct relation between the accretion rate and the strength of the magnetic field in the disk.

2.1 Criteria for Sustaining the MRI

In weakly ionized disks, non-ideal MHD terms dominate the inductive term if the Elsasser number is less than 1, where the Elsasser number based on the Ohmic, Hall and AD terms are defined as

$$\begin{aligned} \Lambda &\equiv \frac{v_A^2}{\eta_O \Omega} \ , \\ Ha &\equiv \frac{v_A^2}{\eta_H \Omega} \approx \frac{\omega_h}{\Omega} \ , \\ Am &\equiv \frac{v_A^2}{\eta_A \Omega} \approx \frac{\gamma_i \rho_i}{\Omega} \ . \end{aligned} \tag{3-9}$$

Here $v_A = \sqrt{B^2/4\pi\rho}$ is the Alfvén velocity, and the approximate equality in the definition of χ and Am holds in the grain-free case. The Hall frequency $\omega_h \equiv eBn_e/\rho c$ is the cutoff frequency of the left polarized Alfvén waves, which can be rewritten to $\omega_h = (n_e/n)(m_i/\mu_n)\omega_{ci}$ with ω_{ci} being the ion cyclotron frequency, n being the number density of the neutrals, m_i being the ion mass.

Non-ideal MHD effects change the linear properties of the MRI substantially when any of the above Elsasser numbers falls below 1 (Blaes & Balbus 1994; Jin 1996; Wardle 1999; Balbus &

[3]One can also define the effective recombination time based on Hall and ambipolar diffusivities, which gives similar numbers but may have weak dependence on the magnetic field strength.

Terquem 2001; Kunz & Balbus 2004). Below we summarize numerical studies on the non-linear evolution of the MRI in these non-ideal MHD regimes and provide our criteria on the strength and sustainability of the MRI turbulence, which are crucial to this work.

For the Ohmic resistivity, vertically stratified shearing box simulations have identified that the border between the MRI active and MRI inactive regions is well described by $\Lambda = 1$ (Ilgner & Nelson 2008), or $\Lambda_z = 1$ (Turner et al. 2007), where the vertical Elsasser number $\Lambda_z = v_{Az}^2/\eta_O\Omega$, with v_{Az} being the vertical component of the Alfvén velocity. The former criterion gives slightly thicker active layer since Λ is generally larger than Λ_z by a factor of $3-30$. The difference between these two criteria can be accommodated by noticing the the fact that transition from the MRI active to MRI inactive regions (i.e., the "undead zone") is relatively smooth, with the extent of the transition region to be about $0.5H$ (Turner & Sano 2008). Therefore, in our calculations, we will simply adopt $\Lambda \gtrsim 1$ as the criterion for the active layer in the Ohmic dominated regime. It provides an optimistic estimate of the lower boundary of the active layer.

For the Hall effect on the MRI, the only existing non-linear study is performed by Sano & Stone (2002a,b). They are motivated by whether the suppression of the MRI by Ohmic resistivity is affected by the Hall effect and performed simulations including both the Ohmic and Hall terms. They found that the saturation level of the MRI is not affected by the Hall effect by much. In particular, the condition for sustained MRI turbulence is still controlled by the Ohmic Elsasser number and appears to be independent of the Hall effect. However, the range of the Hall Elsasser number Ha (or $X = 2/Ha$ in their notation) studied by Sano & Stone is relatively narrow. Whether their conclusion can be generalized to the Hall dominated regime is still an open question. In this paper, we tentatively adopt Sano & Stone's conclusion and ignore the Hall effect on the sustainability of the MRI, but we also discuss the applicability and potential caveat about this simplification in Section 3.

The effect of AD on the non-linear evolution of the MRI has been studied by Hawley & Stone (1998) using a two-fluid approach, applicable when the ionization fraction is large and the recombination time is long, and by Bai & Stone (2011) (see Chapter 2) when the ion inertia is negligible and when $t_{\rm rcb}$ is much shorter than the orbital period (i.e., the strong coupling limit). The behaviors of the MRI in the two limits differ significantly. As we will show in Section 3.2, the strong coupling limit applies almost everywhere in typical PPDs. Therefore, we adopt the results in Chapter 2 that the MRI can be self-sustained for any value of Am as long as the magnetic field

is sufficiently weak. At a given Am, the maximum magnetic field strength is given by

$$\beta_{\rm min} = \left[\left(\frac{50}{Am^{1.2}}\right)^2 + \left(\frac{8}{Am^{0.3}} + 1\right)^2\right]^{1/2} , \tag{3-10}$$

where the plasma $\beta = P_{\rm gas}/P_{\rm mag}$ is the ratio of gas to magnetic pressure, with $P_{\rm mag} = B^2/8\pi$. Here β is not to be confused by the Hall parameter for charged particles β_j.

In sum, our adopted criteria for sustained MRI turbulence is

$$\Lambda \geq 1 , \quad \text{and} \quad \beta \geq \beta_{\rm min}(Am) . \tag{3-11}$$

Besides the potential uncertainty from ignoring the Hall effect, another uncertainty in our adopted criteria is that they are mostly based on unstratified simulations with vertical box size fixed at H (e.g., simulations by Sano & Stone and Bai & Stone). Although in the Ohmic regime unstratified and stratified simulations tend to yield similar criterion (Sano et al. 1998; Fleming et al. 2000; Turner et al. 2007), it is yet to be explored whether the same situation holds for the case of ambipolar diffusion. In addition, above the MRI active layer, magnetic dissipation may generate a hot disk corona, which on the one hand, possesses some stress (although much smaller than that in the active layer, Miller & Stone 2000), and on the other hand, increases β in the upper disk. Despite all these complications, our approach serves as the first step towards more realistic criteria, and moreover, it is sufficiently simple for illustrating our new method for estimating the location of the active layer and the accretion rate in Section 3.3.

2.2 Accretion Rate and Required Field Strength

In the active layer, the MRI generates turbulent stress $T_{r\phi}$ which transports angular momentum outward, and its strength is usually characterized by the α parameter (Shakura & Sunyaev 1973), defined as $T_{r\phi} = \alpha\rho c_s^2$. When MRI is self-sustained, there is a tight correlation between α and the time and volume averaged magnetic energy, which is again characterized by the plasma β (Hawley et al. 1995, BS11)

$$\alpha \approx \frac{1}{2\beta} . \tag{3-12}$$

Note that this relation holds only in the MRI-active layer.

If accretion in PPDs is solely driven by the MRI in the active layer, a simple relation can be derived connecting the accretion rate $\dot{M}$ to the magnetic field strength (Bai & Goodman 2009).

For steady state accretion, conservation of angular momentum demands

$$\dot{M}\Omega r^2 = 2\pi r^2 \int_{-\infty}^{\infty} dz T_{r\phi} \approx 2\pi r^2 \int_{\rm active} dz T_{r\phi} \ , \tag{3-13}$$

where the last integral is performed across the active layer. Although the dead zone has also been shown to transport angular momentum by non-axisymmetric density waves launched from the active layer (Fleming & Stone 2003; Oishi & Mac Low 2009), which is a generic process in shear turbulence (Heinemann & Papaloizou 2009a,b), its contribution is only a small fraction of that from the active layer, and can be safely ignored. From equation (3-12), we have $T_{r\phi} = \alpha P_{\rm gas} \approx P_{\rm mag}/2$ in the active layer, and the above equation turns to

$$\dot{M} \approx \int_{\rm active} dz \frac{B^2}{8\Omega} \ . \tag{3-14}$$

This is a very useful formula for accretion rate estimation and is quite general for MRI driven angular momentum transport in both ideal MHD or non-ideal MHD regimes. It will be used extensively in Sections 3 to 5.

In turn, for MRI driven accretion, one can estimate the strength of the magnetic field given the accretion rate. Let the thickness of the active layer be denoted by h_a for each side of the disk, the integral over the vertical height can be replaced by a factor of $2h_a$, which leads to

$$\langle B^2 \rangle \approx 4\dot{M}\Omega/h_a \ , \tag{3-15}$$

where the bracket $\langle\cdot\rangle$ means vertical averaging. To obtain a more quantitative estimate of the field strength applicable to PPDs, we consider the MMSN around a $1M_\odot$ protostar. The thickness of the active layer should generally be on the order of the disk scale height $h_a \approx H = c_s/\Omega$, and we obtain

$$\langle B \rangle \approx 2\sqrt{\dot{M}\Omega/H} \approx 1.0 \dot{M}_{-8}^{1/2} r_{\rm AU}^{-11/8} \ {\rm G} \ , \tag{3-16}$$

where $\dot{M}_{-8} = \dot{M}/10^{-8} M_\odot \ {\rm yr}^{-1}$. We note that in obtaining the above relation, only the temperature profile (to estimate the disk scale height) of the MMSN model is used (which is more reliable than the surface density profile). This relation states that for MRI driven angular momentum transport, strong magnetic field is needed for fast accretion.

For typical accretion rate of $10^{-8} M_\odot \ {\rm yr}^{-1}$, the implied magnetic field strength is strong, and is in fact close to the equipartition strength for the active layer. Assuming the column density of the active layer Σ_a to be 10 g cm^{-1} (as comparable to the penetration depth of the X-ray ionization), the equipartition field strength is

$$B_{\rm equi} \approx \sqrt{8\pi}\left(\frac{\Sigma_a}{h_a} c_s^2\right)^{1/2} \approx 2.3 \Sigma_1^{1/2} r_{\rm AU}^{-7/8} \ {\rm G} \ , \tag{3-17}$$

where $\Sigma_1 = \Sigma_a/10$ g cm^{-2}. The simple analysis here shows that to the limiting factor for MRI to drive accretion in PPDs is not only the level of ionization, but also the strength of the magnetic field. A quantitative manifestation of this effect will given in Section 3.3.

3. Active Layer in the Fiducial Model

We refer our fiducial model to the MMSN disk with X-ray luminosity of the protostar being 10^{30}erg s^{-1} and with cosmic-ray ionizations. Variations to the fiducial model are discussed in the next section. Other parameters are fixed at values specified in Section 1 in all calculations.

Using the fiducial model, we run four calculations at two disk radii 1AU and 10AU, with and without grains (0.1μm). In each calculation, we evolve the chemical network at fixed radius and scan from the disk midplane up to 5 disk scale heights. At each point, we extract the number density of all species from the end of the evolution (10^6 years) and calculate the magnetic diffusivities as a function of the magnetic field strength. Various aspects of the results are discussed in the following subsections.

3.1 Chemistry

In Figure 3.1, we show the vertical density profile of various chemical species normalized to the number density of the hydrogen nuclei for calculations at 1 AU. The most important quantity is the ionization fraction $x_e \equiv n_e/n_H$, as plotted in red, which largely determines the strength of the non-ideal MHD effects. In addition, we plot the profile of the ionization rate. This figure is to be compared with Figures 3 and 6 in Wardle (2007). It is clear that the ionization fraction is extremely small ($\ll 10^{-6}$ in general), hence the inertia of the charged particles is negligible compared with the inertia of the neutrals, justifying the first requirement of the strong coupling limit.

The main driving force of chemical evolution is the ionization reactions. In the Figure, there are several "steps" in the vertical profile of the ionization rate that are associated with transitions to different ionization regimes, as described in Section 1. These "steps" also make the vertical profile of the ionization fraction x_e exhibit similar features. At the uppermost layer, the ionization rate is the largest and is dominated by direct X-ray ionization from the protostar, with a very small column density of about 0.01 g cm^{-2}. Slightly deeper down, the ionization is still dominated

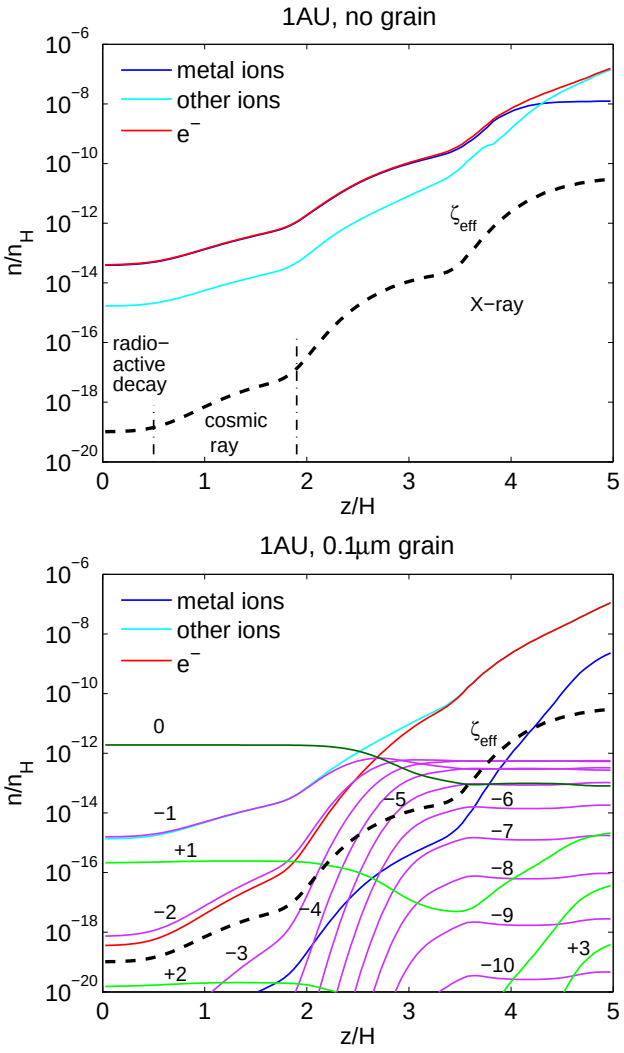


Fig. 3.1.— Fractional abundance of electrons (red), metal ions (blue) and other ions (cyan) relative to hydrogen nuclei as a function of height (z) above the midplane in our fiducial model at 1AU. Also shown is the ionization rate (bold dashed) as a function of z, divided into three segments where the dominant sources of ionization are labeled. Upper panel: calculation without grains. Lower panel: calculation with well mixed 0.1μm grains with 1% in mass. Abundance of positively charged (green), neutral (dark green) and negatively charged (magenta) grains are labeled by their elemental charge Z.

by the X-rays, but is mainly due to the Compton scattered X-ray photons from the upper layer, with penetration depth of about 4 g cm^{-1}. Further deeper, cosmic-ray ionization with penetration depth of about 100 g cm^{-1} takes over, while around the midplane, radioactive decay dominates. Comparing the result to Figure 3.2 shown in the next subsection reveals that the ionization rate provided by radioactive decay is generally too small to produce sufficient ionization in PPDs, and can be safely ignored for the purpose of estimating the extent of the active layer and dead zone.

In the grain-free calculation, we see that the ionization fraction primarily overlaps with the metal abundance at $z \lesssim 4H$, indicating that the metals are the dominant electron donor, which has been shown in many previous works (e.g., Fromang et al. 2002; Ilgner & Nelson 2006; Bai & Goodman 2009). Above $4H$, essentially all the metal atoms are ionized, and the main electron donor is taken over by other ions. The ionization fraction from our calculation differs from that in Wardle (2007) mainly because we use a more complex (and presumably more realistic) chemical network.

The inclusion of well-mixed dust grains with $a = 0.1\mu$m dramatically reduces the ionization fraction. At the midplane, x_e is reduced by 5 orders of magnitude as compared with the grain-free case. The reduction factor is still significant but smaller in the upper layers up to $z \gtrsim 5H$. With grains, the role for metals as the main electron donor is suppressed because the recombination of metal ions is facilitated by grains, consistent with Wardle (2007).

The reduction of electron density by grains has another consequence: when the electron abundance falls substantially below the grain abundance, the ions and grains take over from the electrons to play a decisive role on the conductivity. In the chemistry calculation shown in the bottom panel of Figure 3.1, this corresponds to regions close to the midplane with $|z| \lesssim 2.5H$. The grain-free formula (A-7) for magnetic diffusivities no longer holds in this regime: the resistivity η_O is smaller than η_e due to contribution from ions and grains. In addition, Am is no longer independent of magnetic field strength (as can be traced from Figure 3.3), and becomes larger in stronger field. This effect and its significance is discussed in full detail in Section 5.

One difference between our calculation and the calculations by Wardle (2007) is that we have considered the electron sticking probability s_e. This probability s_e was simply taken to be 1 in their calculation. In Perez-Becker & Chiang (2011a), s_e was fixed at 0.1 for PAHs, and 1 for normal grains, while in Okuzumi (2009), s_e was fixed at 0.3 for all grain sizes. However, because electron is much lighter than the grain surface atoms, energy transfer by inelastic collisions with grains is

inefficient and the electron may have a large chance to escape. The derivation of electron sticking coefficient with *neutrals* grains has been performed by Nishi et al. (1991), who showed that s_e decreases with increasing temperature, from about 1 at zero temperature to about 1-2 orders of magnitude less than unity at a few hundred K. Ilgner & Nelson (2006) and Bai & Goodman (2009) adopted this formula in their chemistry calculations, but they erroneously used the same formula for both neutral and charged grains. A generalized derivation of the electron sticking coefficient to include grain charges is given in Appendix of Bai (2011a), where we find that the sticking coefficient for more positively charged grains is progressively smaller than that for negatively charged grains. This is mainly because the electron is accelerated more as it approaches the more positively charged grains, making it more difficult to get rid of the excess energy for adsorption.

The inclusion of the sticking coefficient in grain-electron collisions reduces the electron recombination rate with grains, leading to less dramatic reduction of electron abundance and conductivity. Our test runs indicate that that the ionization fraction calculated with and without including the electron sticking probability can differ by up to a factor of 10 in certain regions. The electron sticking probability also affects the grain charge distribution. For example, in Figure 3.1, the mean grain charge in the disk upper layers from our calculation is about -2.5 elementary charge rather than around -8 in Wardle (2007)'s calculation. Our new result on the charge dependence of s_e implies that grains tend to be (slightly) more positively charged, although this is a relatively weak effect and is more relevant for sub-micron grains.

3.2 Magnetic Diffusivities and Recombination Time

The abundance of all charged species from the chemistry calculation is used to evaluate the magnetic diffusivities using equations (A-4) and (A-6), and the results are illustrated in Figure 3.2. Similar to the figures shown in Wardle (2007), we mark different magnetic diffusion regimes with different filling color. Six magnetic diffusion regimes are considered depending on the relative order among η_O, η_H and η_A. It is clear that Hall and AD becomes more and more important at smaller density (surface layer and large disk radii) and larger magnetic field strength, as expected (η_H scales as B/n_e while η_A scales as B^2/n_e). The addition of grains dramatically changes the pattern in the figure at $z \lesssim 3H$, this is because grains carry most of the negative charge instead of electrons (due to the extremely low ionization rate) and the magnetic diffusivity is largely determined by the less mobile ions and grains. In this region, different choices of chemical reaction networks can make

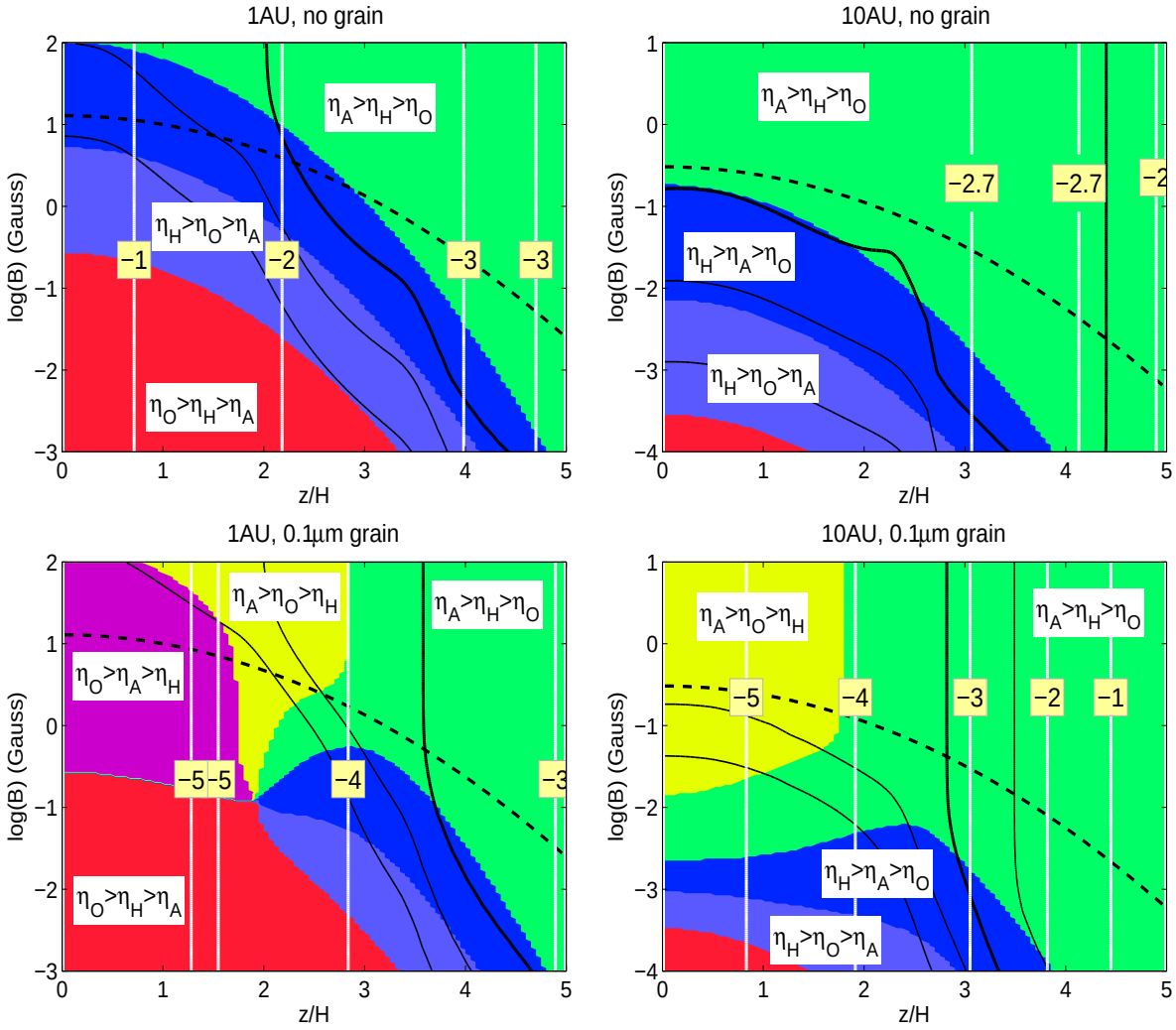


Fig. 3.2.— Regimes of non-ideal MHD effects in fiducial PPD models plotted as contours in the plane of disk height and magnetic field strength. The left (right) two panels correspond to 1 (10) AU of a MMSN model, and the upper (lower) two panels correspond to the case without grains (with 1% of well mixed 0.1μm grain). Different regimes of non-ideal MHD effects are painted with different background colors. *Red and magenta*: Ohmic resistivity dominated; *Dark and light blue*: Hall effect dominated; *Green and yellow*: AD dominated. Subdivisions of the color scheme are indicated in the plots. *Black contours* show constants of the Elsasser number $\Lambda_{\rm tot}$ which is increased by factors of 10 from bottom left to upper right, with the $\Lambda_{\rm tot} = 1$ contour marked in bold. *The bold dashed black line* indicates where the magnetic pressure equals to the gas pressure ($\beta = 1$). White *vertical lines* correspond to contours of constant effective recombination time $t_{\rm rcb}^{\rm eff}$, labeled by $\log_{10}(\Omega t_{\rm rcb}^{\rm eff})$.

a big difference in the resulting magnetic diffusivity pattern. At disk upper layers ($z \gtrsim 3H$), grains play a less important role on the pattern of magnetic diffusivities painted in the Figure since free electrons overwhelms the grains, although the ionization fraction is still affected by the grains.

White vertical lines in Figure 3.2 show the contours of constant effective recombination time (equation (3-8)). We see that in all of the four cases, the recombination time is at least one order of magnitude smaller than the dynamical time scale[4]. This result looks counterintuitive since the recombination time may be expected to be smaller in the disk upper layers due to the low gas density. However, this is compensated by the enhanced electron abundance near the disk surface (as $t_{rc} \sim 1/nx_e$). Together with the extremely low ionization level in PPDs, this result demonstrates that the strong coupling limit applies in essentially most regions of typical PPDs, and it justifies that single fluid treatment of the gas dynamics in PPDs is generally sufficient. In particular, the single fluid simulations described in Chapter 2 on the effect of AD on the MRI is directly relevant to PPDs, while two-fluid simulations by Hawley & Stone (1998) are not quite applicable.

Moreover, we emphasize that our conclusion that $\Omega t_{\rm rcb}^{\rm eff} \ll 1$ is obtained by using the complex chemical network. The usage of a simple network such as the Oppenheimer & Dalgarno (1974) model can lead to different conclusions: At 1 AU without grains, we find that $t_{\rm rcb}$ is about one order of magnitude longer when calculated with the simple network, and becomes longer than the dynamical time at $|z| \lesssim H$. This is because of the lack of recombination channels in the simple network, and is relevant to the "revival" of the dead zone by turbulent mixing of free electrons from the active layer to the midlane, as seen in multi-fluid simulations with a co-evolving simple chemical reaction network (Turner et al. 2007; Turner & Sano 2008; Ilgner & Nelson 2008). However, with a more realistic chemical network, the reactivation of the dead zone by turbulent mixing would appear less likely to occur, because the turbulent eddy time is comparable to the dynamical time (Fromang & Papaloizou 2006; Turner et al. 2006; Carballido et al. 2011) and most free electrons would be swallowed by the more rapid recombination process before being mixed down to the midplane. Therefore, the density profile of all charged species in PPDs should be close to local ionization equilibrium, which justifies our adopted criteria in Section 2.

[4]Note that our definition of $t_{\rm rcb}^{\rm eff}$ in equation (3-8) captures the most rapid recombination process. It is typically shorter than the chemical equilibrium time estimated in Perez-Becker & Chiang (2011a), which is sensitive to the slowest chemical processes

In Figure 3.2, we also plot contours of constant Elsasser number. Here we define the Elsasser number based on $\eta_{\rm tot}$ as

$$\Lambda_{\rm tot} \equiv \frac{v_A^2}{\Omega \eta_{\rm tot}} \ , \tag{3-18}$$

where $\eta_{\rm tot} = \sqrt{\eta_O^2 + \eta_H^2 + \eta_A^2}$, and it measures the importance of all non-ideal MHD effects as a whole. The Elsasser number is in general larger in upper right and smaller in lower left, with the $\Lambda_{\rm tot} = 1$ contours plotted in bold black lines. Non-ideal MHD terms dominate the induction term when $\Lambda_{\rm tot} < 1$, with the properties of the MRI significantly modified. In addition, we plot the contour of $\beta = 1$ in bold dashed line. Before applying our criteria (3-11), which will be the subject of the next subsection, we note that the bold solid and bold dashed lines may serve as *rough* boundaries enclosing the MRI active region. We see that in all cases the dominant non-ideal MHD processes in these regions are the Hall effect and AD.

As we discussed in Section 2, we have ignored the Hall effect on the sustainability of the MRI turbulence. Here we discuss the potential caveats from this simplification. We are most interested in the boundary between MRI active and inactive regions. The lower boundary set by $\Lambda = 1$ is relatively well constrained based on the study of Sano & Stone (2002b), although more numerical study in the Hall dominated regime is still necessary since it is generally the case that $\eta_H > \eta_O$ near the lower boundary. The main uncertainty comes from the upper boundary ($\beta \geq \beta_{\rm min}(Am)$), which is based on simulations in Chapter 2 that include only AD. From Figure 3.2, we see that AD is indeed the dominant non-ideal MHD effect close to the line of $\beta = 1$ at 10 AU. Therefore, our criterion $\beta \geq \beta_{\rm min}(Am)$ should provide a relatively reliable upper boundary on the strength of the magnetic field for MRI to operate. At 1 AU with grains, AD is also likely to be the main limiting factor on the magnetic field strength, while in the grain-free case, the location of the upper boundary is likely to be in the Hall dominated regime, and our criterion may require modification.

3.3 Active Layer and Accretion Rate

Using the profile of magnetic diffusivities in the previous subsection, we estimate the location of the active layer by applying our criteria (3-11). In Figure 3.3, we show the $\Lambda = 1$ contour (black bold solid) as well as contours of constant Am (black thin solid) in the z-B plane similar to Figure 3.2. The former (Ohmic resistivity) controls the lower boundary of the active layer, while its exact location is determined by the strength of the magnetic field: lower for strong field and higher for weak field. This is because the Ohmic Elsasser number $v_A^2/\eta_O\Omega$ is proportional to B^2,

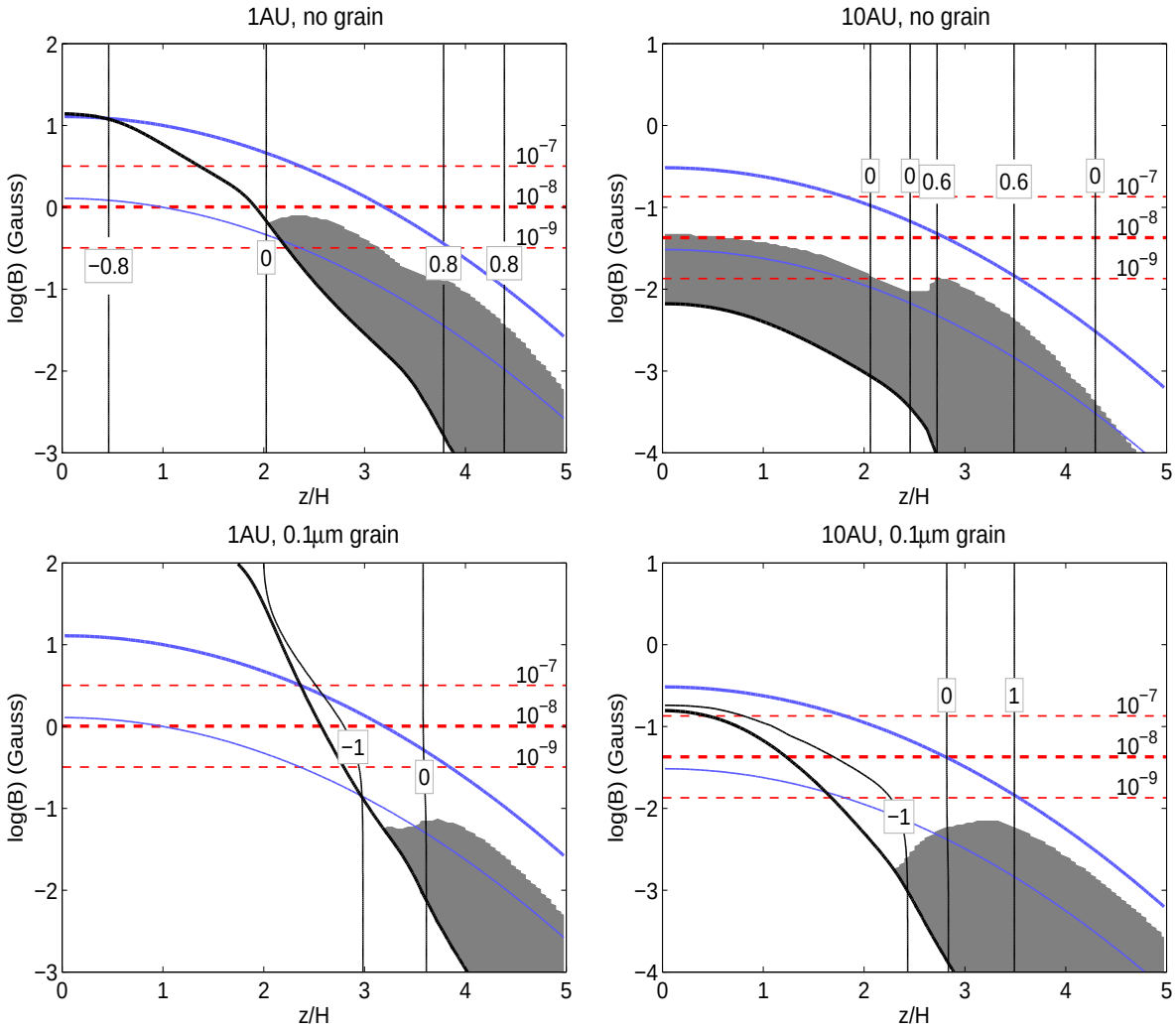


Fig. 3.3.— Similar to Figure 3.2, but for constraints on the MRI permitted region in PPDs. The bold solid contours correspond to the Ohmic Elsasser number $\Lambda = 1$, while the thin solid curves show the contours of constant Am labeled by $\log_{10}(Am)$, terminated at $Am = 0.1$. Blue bold and thin lines mark the plasma $\beta = 1$ and $\beta = 100$ respectively. Permitted regions for the MRI in PPDs based on criteria (3-11) are painted in gray. The red dashed lines indicate the required field strength in the MRI permitted region corresponding to accretion rate of 10^{-7}, 10^{-8} and $10^{-9} M_\odot$ yr^{-1}, respectively, based on equation (3-16).

and the disk is better ionized (smaller η_O) in the upper layer. The upper limit on the magnetic field strength characterized by β (blue solid) is controlled by AD, where smaller Am value requires weaker magnetic field. The value of Am above the lower boundary is generally greater than 0.1, and reaches up to 10 in the disk upper layers, which agrees with PAH-free model calculations in Perez-Becker & Chiang (2011a), and the minimum value of β ranges from about 10 to 800. The two constraints combined together give the MRI permitted region in the z-B plane at a given radius the PPD, as painted in gray.

We see that in all of the four cases, maintaining an MRI active layer is possible if the magnetic field is not too strong. That is, the required field strength to overcome the Ohmic resistivity in the disk upper layer is generally much weaker than the equipartition field. This is partly due to the fact that $\eta_O \propto 1/x_e$ decreases toward the disk surface more rapidly than density (at least for $z < 4H$), making the $\Lambda = 1$ contour steeper than the contours of $\beta =$ constant. Also, Am in the disk upper layer is generally greater than 1, where the required field reduction from equipartition strength is only moderate. The MRI permitted region in the z-B plane shifts to disk upper layers when sub-micron grains are included because of increased η_O. It extends toward the disk midplane as one moves to disk outer regions because the reduction of disk surface density slows the recombination process and allows ionization photons/particles to penetrate deeper. At 10 AU without grains, even the disk midplane becomes active for field strength of a few times 0.01G. These results are all consistent with previous chemistry calculations.

For MRI-driven accretion, the required magnetic field strength at various accretion rates from equation (3-16) is also shown in Figure 3.3 (red dashed). We see that in the grain-free calculations, the maximum field strength in the MRI permitted region corresponds to $\dot{M} \approx 10^{-8} M_\odot$ yr^{-1}, while in the presence of sub-micron grains, the maximum accretion rate is dramatically reduced to well below $10^{-9} M_\odot$ yr^{-1}. The reduction is mostly due to the retreat of the lower boundary: the $\Lambda = 1$ contour shifts upward, reducing the maximum allowed field strength because of reduced gas pressure; in addition, Am becomes smaller, reducing the allowed field strength further.

We note that most previous calculations either adopt the magnetic Reynolds number $\mathrm{Re}_M \equiv c_s^2/\eta_O\Omega = 100$ as the boundary between the active layer and the dead zone, which implicitly assumes $\beta = 100$ in the entire disk (Fromang et al. 2002; Ilgner & Nelson 2006; Bai & Goodman 2009; Perez-Becker & Chiang 2011a,b), or adopt the Elsasser number criterion, but assume some constant magnetic field strength (Turner & Drake 2009). From Figure 3.3, the $\mathrm{Re}_M = 100$ criterion

corresponds to using the intersection between the bold solid line ($\Lambda = 1$) and thin blue line ($\beta = 100$) as the boundary. We see that this criterion roughly applies in the grain-free case, but may substantially overestimate the active column when grains are present (i.e., the critical Re_M should be larger than 100). In other words, the reduction of the active layer column density by grains is more serious than previously estimated, complementing our discussion in the previous paragraph.

Our graphical illustration of the maximum accretion rate based on the approximate formula (3-16) can be improved with a more quantitative calculation to give an absolute upper limit of the accretion rate. This upper limit can be obtained from equation (3-14), where the integral is performed across the entire disk height that the MRI permitted region extends to, with B chosen to be the maximum value determined by $\beta_{\min}(Am)$. For the MMSN disk model, we have

$$\begin{aligned} \dot{M}_{\max} &\approx \frac{c_s}{8\Omega^2} \int_{\text{active}} B_{\max}^2 \frac{dz}{H} \\ &\approx 0.98 \times 10^{-8} r_{\text{AU}}^{11/4} \int_{\text{active}}^{z>0} \left(\frac{B_{\max}}{\text{G}} \right)^2 \frac{dz}{H} \ M_\odot \ \text{yr}^{-1} \ . \end{aligned} \tag{3-19}$$

For the four calculations in Figure 3.3, we find the maximum accretion rate (in unit of $M_\odot$ yr^{-1}) to be 4.5×10^{-9}, 1.5×10^{-8} for the grain free model at 1 AU and 10 AU respectively, 3.8×10^{-11} and 2.5×10^{-10} for well-mixed sub-micron grain model at 1 AU and 10 AU. As expected, they agree with the estimate from our graphical illustration.

Our equation (3-14) provides an convenient way for estimating the accretion rate from the magnetic field strength, but it does not predict as a priori the field strength in the disk. Here we consider the following thought experiment and hypothesis from which we propose a way to predict the strength of the magnetic field in the active layer hence the accretion rate.

Suppose the initial magnetic field strength in the disk is sufficiently weak (say, $\beta = 10^5$ at the disk midplane). According to Figure 3.3, the MRI first develops in the very upper layer of the disk. The MRI amplifies the magnetic field, and consequently, both the upper and lower boundaries of the active layer moves toward the midplane because of increased field strength[5]. The MRI ultimately saturates into turbulence, and turbulent stirring maintains roughly constant field strength across the active layer (e.g., Oishi & Mac Low 2009). We further hypothesize that

[5]This is somewhat related to the recurrent growth and decay of the MRI turbulence as a result of field amplification and resistive damping observed by Simon et al. (2011), who adopted a constant resistivity profile. In real situations with a rapidly increasing resistivity toward the disk midplane, the transition may be a more smoothed process.

the magnetic field in global disks is able to self-organize into a configuration to maximize the rate of angular momentum transport by the MRI turbulence. While unjustified due to the lack of systematic global studies (most global simulations of the MRI such as Fromang & Nelson (2006) and local stratified simulations have zero net vertical flux, which leads to relatively weak turbulence), this hypothesis predicts the magnetic field strength and accretion rate that lie on the larger side than in reality (i.e., an optimistic estimate).

Based on the discussion above, we predict the accretion rate as follows. We scan over the strength of the magnetic field B in the active layer (B is assumed to be constant across the active layer), where for each B, we calculate $\dot{M}$ using equation (3-14). The optimistically predicted accretion rate is the maximum $\dot{M}$ from the scan. For the four calculations in Figure 3.3, the predicted accretion rates (in unit of $M_\odot$ yr^{-1}) are 2.7×10^{-9}, 7.7×10^{-9} for grain free models at 1 AU and 10 AU respectively, and 2.3×10^{-11} and 1.3×10^{-10} for well-mixed sub-micron grain models at 1 AU and 10 AU. They are about half the value of the upper limits listed before.

While the framework we just described is fully general, the results reported in this paper are subject to a few caveats due to simplifications in the adopted disk and ionization models that may result in small uncertainties up to a factor of a few. These uncertainties are discussed below and can be overcome by adopting more realistic disk and ionization models that takes into account radiative transfer, thermodynamics and magnetic pressure support to yield more reliable estimate of the accretion rate.

We have assumed constant vertical temperature profile in our estimate of the accretion rate, while in reality, the upper layer of the disk is heated by both the X-ray photons which are responsible for the ionization (Glassgold et al. 2004; Gorti & Hollenbach 2004) and the MRI itself (Bai & Goodman 2009; Hirose & Turner 2011), raising the temperature above the midplane temperature by a factor of a few. This effect increases the gas pressure, hence plasma β, and allows stronger magnetic field in the active layer, which may lead to higher $\dot{M}$ than our predicted value by a factor of a few.

We have assumed that the gas density profile is Gaussian in our calculations. In reality, magnetic pressure plays more important role in the hydrostatic equilibrium at the disk surface, and local isothermal stratified shearing-box simulations by Miller & Stone (2000) show deviation from Gaussian density profile with gas density at the disk surface a factor of up to 10 higher than our adopted Gaussian model. This may promote accretion by allowing stronger magnetic field near

the surface. However, since the ionization rate depends on the column gas density from the disk surface, this effect is compensated by the reduced ionization rate and enhanced recombination rate (at given disk height), giving only order unity corrections to the predicted accretion rate. In fact, the predicted accretion rate does not sensitively depend on the density distribution across disk height, and the approximate calculations by Perez-Becker & Chiang (2011b) that are free from the vertical density distribution are generally consistent with ours within order unity.

Simulations by Miller & Stone (2000) also indicates non-zero stress in the magnetic corona, but the α value is generally one order of magnitude smaller than that in the disk. The coronal contribution to the accretion rate is about $\alpha P_c h_c$, with the coronal gas pressure P_c orders of magnitude smaller than that in the disk midplane / active layer, and the coronal thickness h_c on the order of a few disk scale height (not much thicker than that of the active layer). Therefore, for our purpose, accretion in the magnetic dominated disk corona can be safely neglected.

Recently, Perez-Becker & Chiang (2011b) called for attention to the role of the FUV ionization, which produces much higher ionization fraction than other ionization sources (making $Am \gtrsim 1000$) with penetration depth of about 0.01 g cm^{-2} $\lesssim \Sigma_{FUV} \lesssim$ 0.1 g cm^{-2}. We note that in the MMSN model, 0.1 g cm^{-2} corresponds to $z \approx 3.8H$ at 1 AU and $z \approx 2.9H$ at 10 AU, which are very upper layers in the disks. Comparing with Figure 3.3 we see that at such heights, the equipartition field strengths in the active layer correspond to $\dot{M}$ of a few times $10^{-10} M_\odot$ yr^{-1} and a few times $10^{-9} M_\odot$ yr^{-1} respectively, which set the upper limit for the MRI accretion rate driven by FUV ionization. The upper limit is a factor of a few below our predicted $\dot{M}$ in the grain-free case, but may well exceed the predicted rate when small grains are included.

In sum, we have provided a general framework for estimating the location of the active layer as well as the accretion rate at a given location of PPDs. The most important feature is that it explicitly incorporates the dependence on the magnetic field strength, with the field strength estimated by our physically motivated hypothesis. Furthermore, the simulation based relation $\alpha = 1/2\beta$ allows us to provide an optimistic estimate as well as a robust upper limit of the accretion rate, without involving additional assumptions about the value of α. This framework will be extensively used for parameter study of the accretion rate in the next section, and can be generalized with more realistic criteria and disk models in the future.

4. Parameter Study

In this section, we perform a series of chemistry calculations at different disk radii from 1AU to 100AU and explore a number of different model parameters including grain size, ionization rate and disk mass. In each series of the parameter study, we derive the MRI-driven accretion rate $\dot{M}$ as a function of disk radius using the method illustrated in the previous section, in parallel with the predicted magnetic field strength. The results are shown in Figures 3.4 and 3.5, with detailed description and discussion given in the subsections that follows. Obviously, using a fixed disk model, the predicted $\dot{M}$ is not necessarily constant as a function of disk radius, which would lead to non-steady accretion if MRI is the only driving mechanism. On the other hand, the predicted spatially varying $\dot{M}$ implies that modifications to the adopted disk model is necessary for steady state accretion. Detailed modeling of the disk structure to match the steady state accretion is beyond the scope of this paper, but the trend can be readily obtained from our studies.

4.1 The Effect of Grain Size

We begin by considering our fiducial model: MMSN disk with both cosmic ray ionization and X-ray ionization ($L_X = 10^{30}$erg s^{-1}). In the upper left panel of Figure 3.4 we show the predicted $\dot{M}$ as a function of disk radius. We have considered the grain-free case as well as models with 1μm and 0.1μm well-mixed grains with mass fraction of 1%. Again, we remind the reader that our predicted accretion rate is optimistic.

In general, the predicted $\dot{M}$ increases with disk radius r in the inner disk, and decreases with r in the outer disk. In the former case, the disk midplane is "dead" and accretion is layered. Since $\dot{M} \propto \alpha\Sigma_{\rm active}T/\Omega$ (where $\Sigma_{\rm active}$ is the column density of the active layer), assuming both $\Sigma_{\rm active}$ and α to be constant, one obtains $\dot{M} \propto r$ for the MMSN temperature profile. In reality, as we discussed in Section 2, α is controlled by Am (which is about 1-10 in the active layer), while the thickness of the active layer depends on the mutual effects of Ohmic resistivity and AD, neither assumptions strictly hold. In Figure 3.4, we see that the increase of $\dot{M}$ with disk radius in the inner disk is somewhat slower than r.

When the entire disk becomes active, Ohmic resistivity becomes essentially irrelevant in constraining the accretion rate (see the upper right panel of Figures 3.2 and 3.3 at $r = 10$ AU for reference). The accretion rate is mainly controlled by the disk surface density, temperature, and

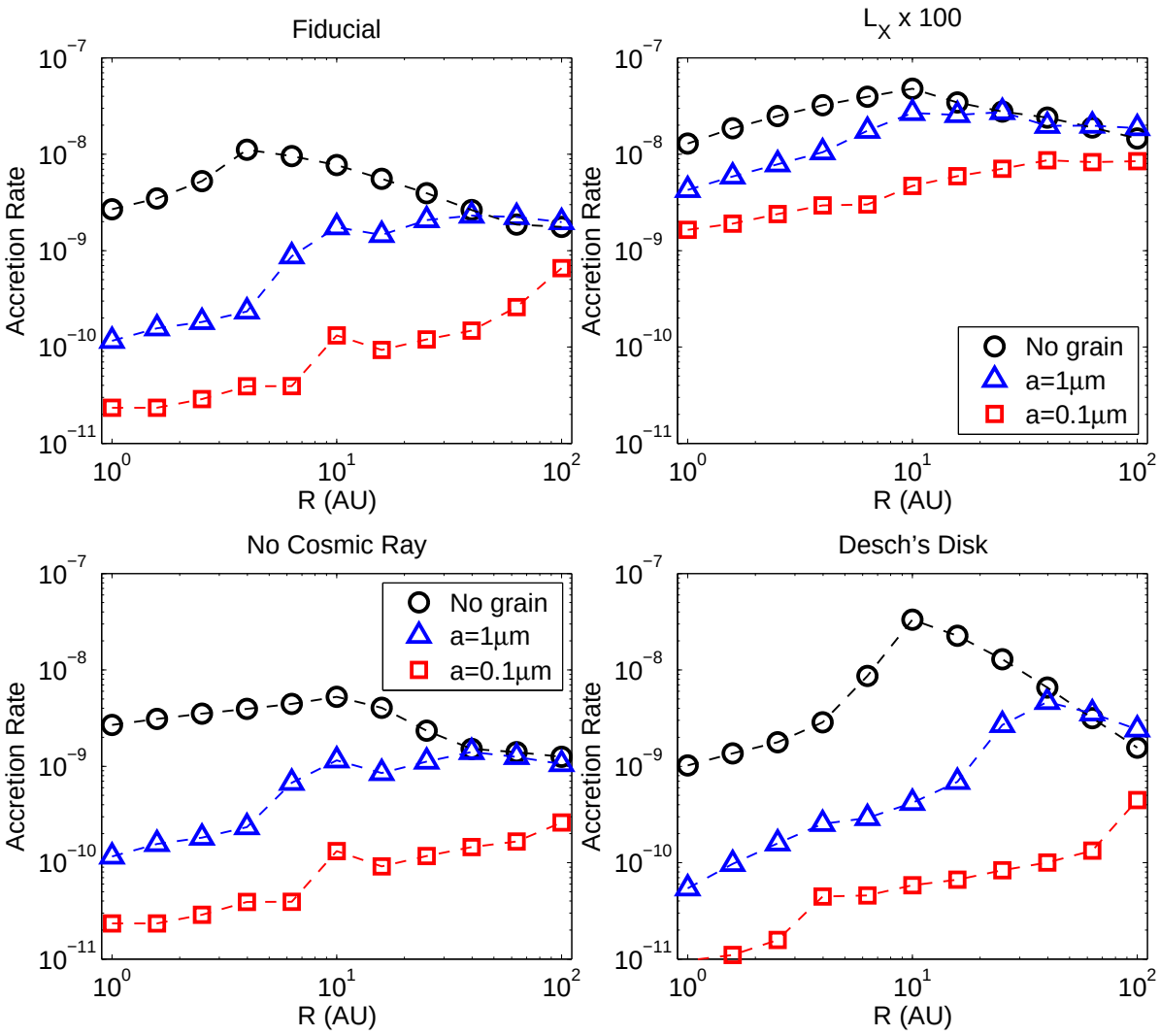


Fig. 3.4.— The optimistically predicted accretion rate (in unit of $M_\odot$ yr^{-1}) as a function of disk radius for our fiducial model (upper left): MMSN disk with cosmic ray and X-ray ionization, model with X-ray luminosity 100 times higher (upper right), model without cosmic-ray ionization (lower left) and model with the Desch's disk (lower right). In each panel, we show results for calculations in the grain-free case (black circles), with well-mixed 1μm grains (blue triangles) and with 0.1μm grain (red squares).

the magnetic field strength ($\dot{M} \propto \alpha \Sigma T/\Omega$) through AD. For MMSN, $\Sigma T/\Omega \propto r^{-1/2}$, which gives the main source of accretion rate reduction. The predicted profile of $\dot{M}$ is also affected by the radial profile of the α parameter determined by Am.

In the grain-free calculation, the entire disk becomes active at $r \gtrsim 4$ AU in our fiducial model, and the predicted $\dot{M}$ is between 10^{-9} and $10^{-8} M_\odot$ yr^{-1} at all disk radii considered. The reduction of the accretion rate caused by dust grains is substantial. At 1 AU, $\dot{M}$ is reduced by about two orders of magnitude in the presence of 0.1μm grains, while for 1μ grains the reduction is more than one order of magnitude. The entire disk becomes active for $r \gtrsim 70$ AU and $r \gtrsim 10$ AU respectively in the above two cases. By and large, the predicted $\dot{M}$ increases with disk radius and flattens out at large radii as discussed before. The rise in predicted $\dot{M}$ in the 0.1μm case toward 100 AU is mainly because the cosmic-ray ionization takes over the X-ray ionization (see next subsection).

We find an interesting fact that at very large disk radii ($\gtrsim 40$ AU), calculations with 1μm grains lead to comparable or slightly higher $\dot{M}$ than those without grains. By carefully checking the equilibrium abundance of all chemical species, we find that in the grain-free calculations, ionization level near the disk midplane is determined by metal abundance, while the number density of other ions is much smaller (see Figure 3.1 for example). In the presence of grains, metals are depleted at low temperature (see Equation (C-6)) due to adsorption onto grain surfaces, and the dominant ion component becomes species such as H_3^+ and HCO^+ (and others) depending on the gas density. The suppression of metals is one of the reasons for the reduction of ionization level, but it appears that at very low density and temperature, slightly higher ionization level can be achieved due to non-metal ions. Nevertheless, we also note that due to uncertainties in the reaction rate coefficients in the UMIST database, the equilibrium abundance of various chemical species such as HCO^+ can be uncertain up to a factor of ~ 4 (Vasyunin et al. 2008).

We see that even in the absence of dust grains, the optimistically predicted $\dot{M}$ is only comparable or below $10^{-8} M_\odot$ yr^{-1}, which is about the median value of the observed accretion rate in T-Tauri stars (Hartmann et al. 1998; Sicilia-Aguilar et al. 2005). In the presence of dust grains, the accretion rate that can be driven from the MRI is reduced dramatically. The situation is particularly serious for T-Tauri disks, since the gas has to enter through the inner disk to accrete. Given the fact that our choice of parameters are typical, these results pose strong challenge on the effectiveness of the MRI in driving rapid accretion in PPDs. Below we further explore other effects to see whether higher MRI-driven accretion rate can be achieved.

4.2 The Effect of Ionization Rate

Because of the uncertainty in the amount of cosmic-rays, which may be shielded by the stellar winds, we also perform a series of chemistry calculations without cosmic-ray ionization, and the results are shown in the lower left panel of Figure 3.4. We note that besides deeper penetration depth, the cosmic-ray ionization rate generally exceeds the scattering component of the X-ray ionization rate beyond about 25 AU, and one might expect that cosmic-ray ionization makes significant contributions to our predicted $\dot{M}$ in the outer disk. However, this does not seem to be the case.

In the grain-free case, we find that the the transition radius larger than which the entire disk becomes active shifts from about 4 AU in the fiducial model to about 10 AU in the absence of cosmic rays. Nevertheless, the predicted $\dot{M}$ does not change by much throughout the disk (only slightly reduced). In the presence of grains, the transition radius shifts outward to about 25 AU for the 1μm case, and is above 100 AU for the 0.1μm case. Again, our predicted $\dot{M}$ is also slightly reduced (generally within a factor of 2) but still similar to the fiducial results. To explain, we note that $\dot{M}$ largely depends on the magnetic field strength in the active layer. Although X-rays do not penetrate as deep as cosmic rays to activate the disk midplane in the outer disk, the permitted magnetic field strength in the active layer turns out to be similar to the case with cosmic rays. According to equation (3-14), given similar field strength, $\dot{M}$ is then determined by the *geometric* thickness of the active layer, which is on the order of H and is not sensitive to whether the active layer extends to the disk midplane or not.

To examine the role of X-ray ionization, we further consider a model with $L_X = 10^{32}$ erg s^{-1}, 100 times larger than our fiducial X-ray luminosity. Although such X-ray luminosity is unusually high for T-Tauri stars (Güdel et al. 2007), it provides an upper limit on the accretion rate that can be driven by X-ray ionization. Alternatively, one might also view this unrealistic choice of high X-ray luminosity as an incorporation of other possible but uncertain strong ionization sources such as energetic protons from protostellar activities (Turner & Drake 2009). We see from the upper right panel of Figure 3.4 that the predicted $\dot{M}$ is much higher than our fiducial model. The rise in $\dot{M}$ is mainly due to deeper penetration in the inner disk ($\lesssim 5$ AU) and due to reduced AD in the outer disk. Accretion rate in grain-free calculations reaches a few times $10^{-8} M_\odot$ yr^{-1}, which is close to the upper limit of the observed accretion rate. Also, comparing the three curves with their counterparts in the fiducial plot (upper left) indicates that increasing X-ray luminosity is more

efficient in raising accretion rate when small grains are present. In sum, it appears that for the MRI to explain the observed rate of accretion in PPDs, much stronger ionization rate than fiducial is needed.

We can also compare our results with the predicted $\dot{M}$ by FUV ionization shown by Perez-Becker & Chiang (2011b)[6]. With the FUV penetration depth of $\lesssim 0.1$ g cm^{-2}, they predict $\dot{M}$ of a few times $10^{-10} M_\odot$ yr^{-1} at 1 AU and it increases roughly linearly with radius since accretion only proceeds in the upper surface layer with roughly constant surface column density. Comparing with their Figure 5 we see that FUV ionization is likely to be a comparably important ionization source as X-rays (while they drive accretion in different layers), and in the presence of small grains, FUV ionization makes significant contributions to the total MRI-driven accretion rate in the inner disk, and could dominate other ionization sources in the outer disk.

4.3 The Effect of Disk Mass

We explore the role of disk mass by repeating our calculations using the Desch's disk model, while the adopted ionization rates remain fiducial, and the results are shown in the lower right panel of Figure 3.4. We see that at 1 AU, where the Desch's disk has about 30 times more surface density than the MMSN disk, the predicted $\dot{M}$ for all three cases (with and without grains) are smaller than the fiducial results. In the grain-free case, the predicted $\dot{M}$ rapidly increases with radius in the inner disk, and peaks at about $r = 10$ AU where the entire disk becomes active. The peak rate exceeds the MMSN model at the same location by a factor of several. The predicted rate falls off towards the outer disk more rapidly than that in the MMSN disk, which is essentially because the surface density of Desch's disk decreases with radius more rapidly. With the grains, the predicted $\dot{M}$ generally increases with disk radius until saturation (the entire disk becomes active), and the corresponding accretion rate in the outer disk is comparable or slightly exceeds that in the MMSN model. Finally, the rates approach the fiducial results at around 100 AU simply because the surface densities in the two disk models are comparable.

[6]Two order-unity effects may lead Perez-Becker & Chiang (2011b) to overestimating the accretion rate by a factor of a few compared with ours: (a) Their equation (6) underestimates the density in the disk upper layer by a factor of $\gtrsim 3$ in a Gaussian density profile, thus promoting higher ionization; (b) Their calculations correspond to the maximum possible accretion rate (3-19), while our predicted rate is about 2 times smaller (see Section 3).

Our results suggest that given the same ionization sources, a more massive disk leads to slower accretion if the accretion is layered, while it is able to sustain faster accretion if the entire disk is active. The reason is that at the same column density from the disk surface (hence the same ionization rate), the gas density is higher in a more massive disk (as one can check with the error function). Therefore, the recombination rate is enhanced, reducing the ionization fraction hence $\dot{M}$ roughly as $\rho^{-1/2}$. On the other hand, higher disk mass in the disk permits stronger magnetic pressure in the active layer, and dominates the former effect when the entire disk column is active.

We have seen that the predicted $\dot{M}$ by the MRI turbulence generally increases with radius in the inner disk, and decreases with radius in the outer disk, with the transition radius depending on the dust content. This result is obviously inconsistent with steady state accretion. Further evolution would lead to pile-up of mass towards the inner disk, with the density profile in the outer disk becoming more flattened. According to the results in this subsection, the pile-up of mass in the inner disk would lead to slower rather than faster accretion, which further enhances the mass pile-up. Therefore, the fact that $\dot{M}$ decreases with disk surface density in the inner disk leads to a runaway pile-up of mass, which may be unsustainable. This result further support the conclusion that mechanisms other than the MRI is needed to drive rapid accretion through the inner disk.

4.4 Predicted Magnetic Field Strength

In Figure 3.5, we show the (optimistically) predicted magnetic field strength in terms of the ratio of midplane gas pressure to the magnetic pressure in the active layer $\beta_s \equiv P_{\rm mid}/P_{\rm mag}$. This is a physically more convenient quantity than the absolute magnetic field strength and provides a guide to numerical modelers. The magnetic field strength can be obtained by

$$\begin{aligned} B &= 13\beta_s^{-1/2} r_{\rm AU}^{-13/8}\ {\rm G} \qquad \text{(MMSN)} \\ B &= 72\beta_s^{-1/2} r_{\rm AU}^{-1.94}\ {\rm G} \qquad \text{(Desch)} \end{aligned} \tag{3-20}$$

Note the steep dependence of the magnetic field strength on disk radius.

Because the active layer resides in the upper disk, with lower gas pressure hence smaller magnetic field, β_s is generally much larger than 1. We see that β_s spans a large range between about 100 and 10^5, depending on the surface density, ionization rate and disk radius. The predicted field strength is generally stronger (smaller β_s) in the grain-free case since the active layer resides higher in the disk surface in the presence of grains, with lower gas pressure hence smaller magnetic field.

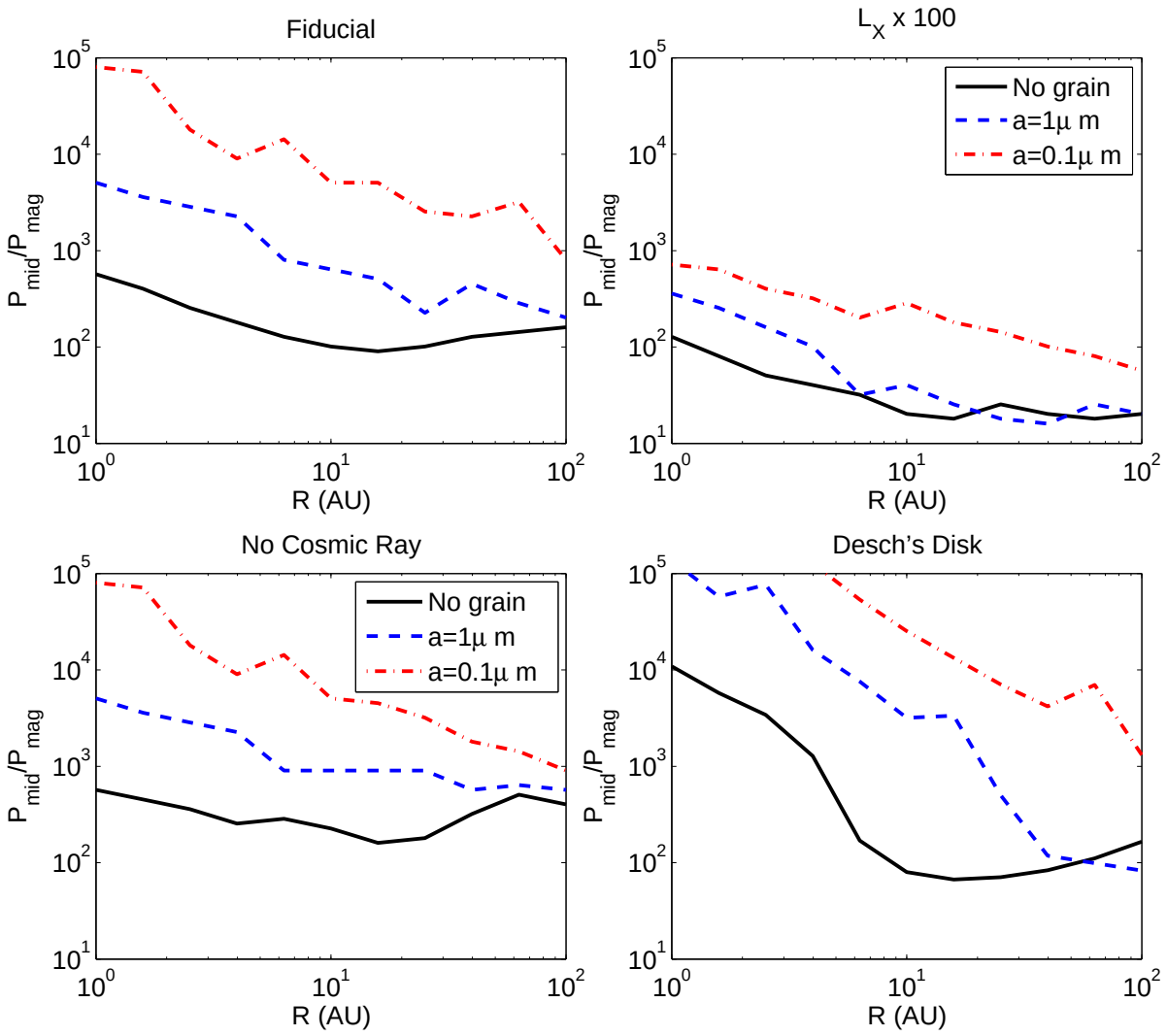


Fig. 3.5.— The ratio of midplane gas pressure to the optimal magnetic pressure at the active layer as a function of disk radius for our fiducial model (upper left): MMSN disk with cosmic ray and X-ray ionization, model with X-ray luminosity 100 times higher (upper right), model without cosmic-ray ionization (lower left) and model with the Desch's disk (lower right). In each panel, we show results for calculations in the grain-free case (black solid), with well-mixed 1μm grains (blue dashed) and with 0.1μm grain (red dash-dotted).

The field strength can be raised significantly by strong ionization (upper right panel), accompanied by increased accretion rate as discussed in Section 4. For the massive disk model (lower right), β_s in the inner disk is much higher than the fiducial case because the active layer resides at a higher position than in the fiducial model due to the finite ionization penetration depth.

It has been predicted that the presence of ordered magnetic field in PPDs can lead to grain alignment with the magnetic field and produce polarized emission in the millimeter continuum (Cho & Lazarian 2007). Grain alignment is expected in the outer disk, where radiative torque dominates thermal collisions. Recently, however, Hughes et al. (2009) reported non-detection of polarized emission using arcsecond-resolution Submillimeter Array (SMA) polarimetric observations. One suspected reason has to do with the magnetic field strength, which has to be above some critical field strength for the alignment to occur. For $10-100\mu$m grains, Hughes et al. (2009) calculated the critical field strength to be $10-100$mG at the location of $50-100$ AU (corresponding to the angular resolution of the SMA for the observed sources). However, at such distances, our predicted field strength is less than 2mG (taking $\beta_s = 100$). Therefore, the non-detection of polarized emission is, in fact, consistent with the presence of the MRI, while if polarized emission were detected, the implied magnetic field would be too strong for the MRI to operate in the outer disk.

5. Effect of Tiny Grains

The significance of tiny grains with sizes of 0.01μm or smaller is three-fold. First, they can reach large abundance (10^{-9} or higher), larger than the ionization fraction for most parts of PPDs, while still consist of a tiny fraction of total grain mass (see Section 1.2). Second, they are likely to be at most singly charged in weakly ionized environment due to the large potential barrier. Third, their conduction properties (i.e., the Hall parameter) are almost exactly the same as the ions (see Section 1.3). When the last two conditions are met, we can define $\bar{n} \equiv n_i + n_{\rm gr}^+ + n_{\rm gr}^-$ being the total number density of charged species that have the same conduction properties as the ions, and we have $\bar{n} \geq n_e$. Qualitatively new behaviors from the grain-free conductivity are derived in analytical form in Section 2 of Appendix A. We find when the charged tiny grains are the dominant charged species (when the first condition is met), the Hall effect is suppressed, and a net reduction of AD is possible if $\bar{n}$ exceeds the ion/electron number density n_{e0} in the grain-free case (Equation (A-17)).

In this section, we perform the same calculations as done in the previous sections but replacing normal grains by PAHs with fixed radius of 1nm. The PAH abundance in T-Tauri stars estimated

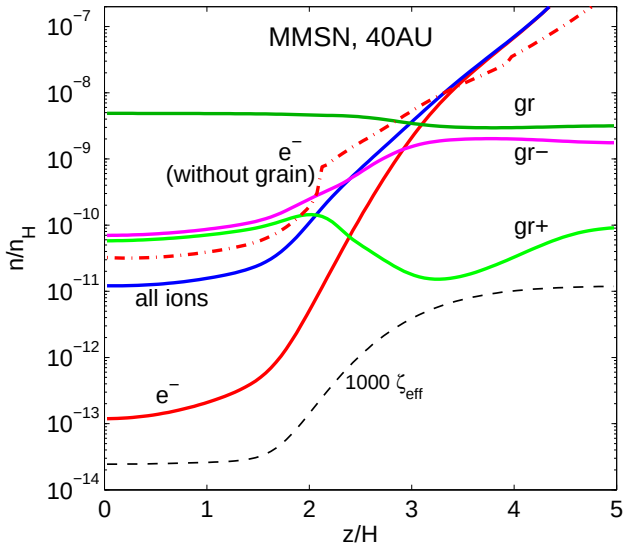


Fig. 3.6.— Abundance of charged species and grains (PAHs) as a function of disk height in our fiducial model calculation (MMSN disk with $x_{\rm PAH} = 10^{-8}$) at 40 AU, plotted as solid lines with labels. For comparison, red dash-dotted line shows the electron (and ion) abundance in the grain-free calculation. The ionization rate is plotted (black dashed) for reference.

by Geers et al. (2006) is about $x_{\rm PAH} \approx 10^{-8}$-$10^{-7}$ per H_2 molecule, while Perez-Becker & Chiang (2011a) argued for smaller abundance due to dust settling. Moreover, the distribution of PAHs in PPDs has been found to be spatially variable (Geers et al. 2007). For these reasons, we adopt $x_{\rm PAH} = 10^{-8}$ as fiducial, while we also consider $x_{\rm PAH}$ down to 10^{-11} and up to 10^{-7}. We will mainly focus on the outer disk ($\gtrsim 10$ AU) where AD rather than Ohmic resistivity plays the dominant role the gas dynamics and the effect discussed in Section 2 of Appendix A is most relevant.

5.1 Abundance of Charged Species

In Figure 3.6 we show the electron, ion and grain abundances at 40 AU in the MMSN model as a function of disk height (z/H). We see that electrons and ions are the dominant charged species (i.e., $\bar{n} \approx n_e$) above $\sim 3H$, while below it the abundances of ions and charged grains exceed electron abundance, and $\bar{n}/n_e$ reaches about 1000 at the disk midplane. The large value of $\bar{n}/n_e$ implies strong suppresion of AD and the Hall effect according to equation (A-16). To see its significance, we also show the electron (thus ion) abundance in the grain-free calculation as the red dash-dotted line

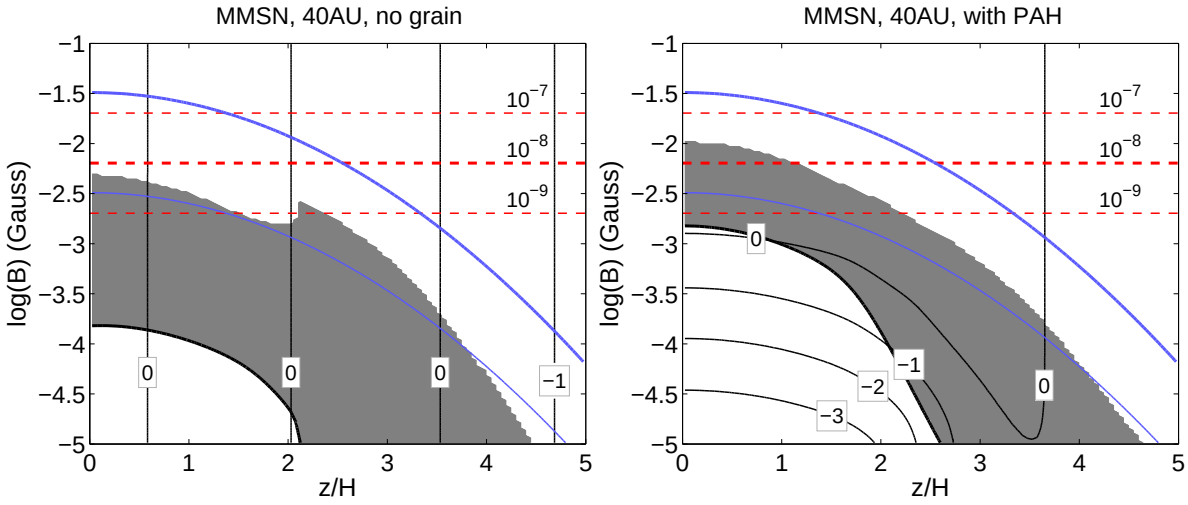


Fig. 3.7.— MRI permitted region (shaded) in the MMSN model at 40 AU from the grain-free calculation (left) and the calculation including PAHs with $x_{\rm PAH} = 10^{-8}$ (right). Bold black solid line marks the boundary given by the Ohmic Elsasser number criterion $\Lambda = 1$. Thin black solid lines show contours of constant AD Elsasser number Am, labeled by $\log_{10}(Am)$. Bold and thin blue lines mark plasma $\beta = 1$ and $\beta = 100$ respectively. The red dashed lines indicate the required field strength in the MRI permitted region in order for driving accretion rate of 10^{-7}, 10^{-8} and $10^{-9} M_\odot$ yr^{-1}.

in the Figure. Clearly, we see that $n_{e0} < \bar{n}$ for $z \lesssim 2H$. According to equation (A-17), this means that when tiny grains are present, there is a net reduction of AD compared with the grain-free case! Seemingly counterintuitive, one can qualitatively understand this result as follows.

Near the disk midplane, we see that $n_{\rm gr} \gg n_{\rm gr}^{\pm} \gtrsim n_i \gg n_e$. In this regime, the electrons produced from H_2 ionization is quickly swallowed by the grains. Similarly, the ions exchange charge with neutral grains to produce positively charged grains. Therefore, ionization effectively takes place on the grains: 2 gr $\rightarrow$ gr$^+$ + gr$^-$, with the same ionization rate $\zeta_{\rm eff}$. The dominant recombination channel is simply its inverse reaction, with recombination rate given by equation (3) of Umebayashi & Nakano (1990). For recombination between two equal sized tiny grains ($e^2/akT \gg 1$), it reduces to

$$\begin{aligned} \langle \sigma v \rangle_{gg} &\approx \left(\frac{48 e^4}{\rho_d a k T} \right)^{1/2} \\ &\approx 2.5 \times 10^{-8} a_1^{-1/2} T_{100}^{-1/2} {\rm s}^{-1} {\rm cm}^3 \ , \end{aligned} \tag{3-21}$$

where $\rho_d = 3$ g cm^{-1} is the grain mass density, k is the Boltzmann constant, T is the temperature. In the second equation a_1 denotes grain size normalized to 1 nm, and $T_{100} = T/100$ K. As long

as charged grain recombination is the dominant recombination process, the abundance of charged grains can be approximately given by

$$\begin{aligned}\frac{n_{\rm gr}^{\pm}}{n_H} &\approx \sqrt{\frac{\zeta_{\rm eff}}{2\langle\sigma v\rangle_{gg} n_H}} \\ &\approx 1.3\times10^{-10}\zeta_{\rm eff,-17}^{1/2}\, n_{H,10}^{-1/2}\, a_1^{1/4}\, T_{100}^{1/4}\ ,\end{aligned} \tag{3-22}$$

where $\zeta_{\rm eff,-17}$ is the ionization rate normalized to 10^{-17} s^{-1}, $n_{H,10}$ is the number density of the hydrogen atoms normalized to 10^{10} cm^{-3}. Plugging in the numbers relevant to Figure 3.6 at midplane, we find $n_{\rm gr}^{\pm}/n_H \approx 1.1\times10^{-10}$. Our chemistry calculation gives 6.5×10^{-11} for the averaged abundance of charged grains, which is slightly smaller due to small contributions from other recombination channels, but is within a factor of 2 from the analytical estimate. Our chemistry calculations further reveal that $n_{\rm gr}^{\pm}/n_H$ increases weakly with total grain abundance $n_{\rm gr}$ (or $x_{\rm PAH}$) and approaches the asymptotic value (3-22).

In the grain-free case, the electron abundance n_{e0} is determined by the balance between ionization and multiple recombination channels, dominated by dissociative recombinations. Typical electron-ion dissociative recombination rate coefficients are on the order of 10^{-7} s^{-1} cm^{-3} at 100K, which is a factor of several higher than the grain recombination coefficient (3-21). The higher recombination rate leads to smaller ionization level than our estimate (3-22), which explains why $n_{e0} < \bar{n}$ in the presence of abundant tiny grains. We note that the value of n_{e0} depends on the choice of chemical reaction network. Simple reaction network (such as Oppenheimer & Dalgarno 1974) generally produces larger n_{e0} mainly because of the lack of recombination channels. In our complex (and presumably more realistic) network, we find that the dominant recombination process is due to NH_4^+ and CH_3CNH^+ in this particular case, giving n_{e0}/n_H to be about 3.2×10^{-11}. As a result, we obtain $\bar{n}/n_{e0} \approx 4$ in the midplane, which leads to a substantial net reduction of the AD coefficient.

5.2 Active Layer and Accretion Rate

The fact that $\bar{n} > n_{e0}$ implies that tiny grains may facilitate the MRI by suppressing AD. For the number density profile given in Figure 3.6, we use the same methodology as in Section 3.3 to show the MRI permitted region and constraints on the magnetic field strength and accretion rate in Figure 3.7. We see that the inclusion of tiny grains strongly increases the Ohmic resistivity, as expected. At disk midplane, magnetic field has to be about 10 times stronger than the grain-free

case in order for Λ to be above 1 (i.e., η_O is about 100 times larger[7]). However, the ionization fraction at disk midplane is still large enough such that in both cases, the required field strength for $\Lambda > 1$ is still far from equipartition (i.e., $\beta \gg 1$). This fact makes Ohmic resistivity essentially irrelevant in determining the vertical extent of the active layer and the accretion rate (since the midplane is already active), while the decisive role is played by AD.

In Figure 3.7, contours of constant Am are straight lines in the grain free case, as Am is independent of the magnetic field. With the inclusion of tiny grains, we see that near the midplane region, Am increases by 3 orders of magnitude as magnetic field increases. This corresponds to the transition region in Figure A.1 with $\beta_i < 1 < \beta_e$. Eventually, at sufficiently strong magnetic field ($\beta_i > 1$), Am becomes independent of magnetic field again. Since $\bar{n} > n_{e0}$, Am is larger in the presence of PAHs than in the grain-free case. Therefore, according to (3-10), stronger magnetic field is permitted near the disk midplane thanks to the PAHs. Since stronger field leads to faster MRI-driven accretion, it becomes clear that PAHs are able to make PPDs accrete more rapidly than in the grain-free case.

We note that the above explanation for the enhancement of accretion by tiny grains no longer completely holds in the inner region of PPDs ($\lesssim 10$ AU), where the disk surface density is far above the X-ray penetration depth and accretion is layered. In such situations, the lower boundary of the active layer is determined by both Ohmic resistivity and AD for the two Elsasser number criteria to be satisfied. Since Ohmic resistivity is larger in the presence of grains, accretion is thus less efficient than the grain-free case. On the other hand, when PAHs are sufficiently abundant, the increase in Ohmic resistivity is bounded ($\lesssim 10^3$) since conductivity is dominated by the charged PAHs rather than electrons, and the reduction in accretion rate is in general no more than the case with 0.1μm grains (see the next subsection).

5.3 Parameter Study

To demonstrate the role of tiny grains more extensively, we perform our calculations for both the MMSN model and the more massive Desch's disk model at a wide range of disk radii from 1 AU to 100 AU, and consider PAH abundances of $x_{\rm PAH} = 10^{-9}$, 10^{-8} (fiducial) and 10^{-7}. In

[7]Note that since $\bar{n} \approx 10^3 n_e$ as read from Figure 3.6, electrons and other charged species contribute roughly equally to the Ohmic conductivity.

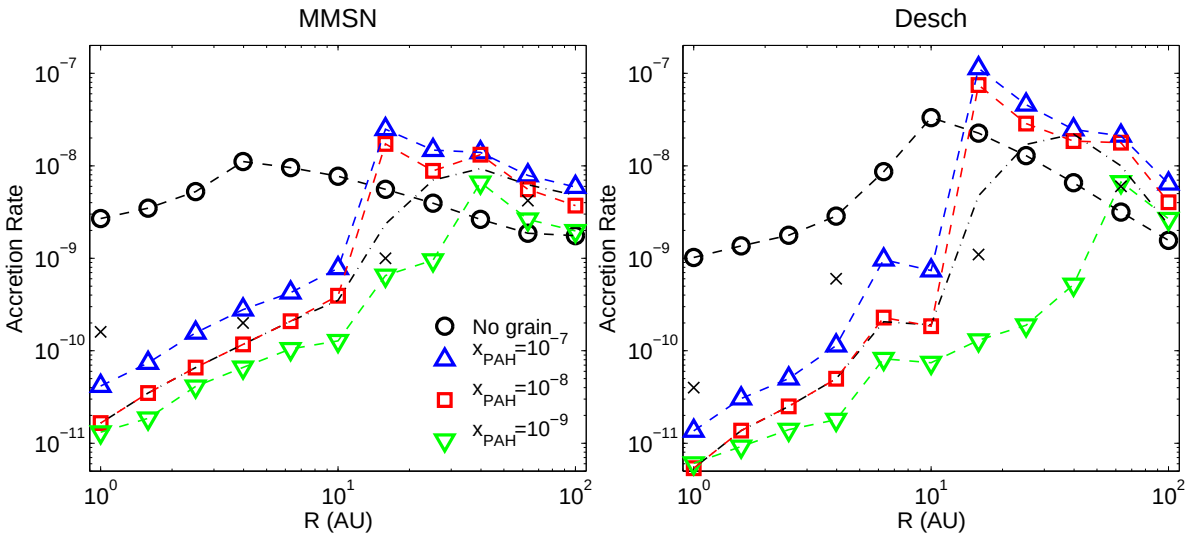


Fig. 3.8.— Optimistically predicted accretion rate as a function of disk radius for the MMAN disk (left) and the Desch's disk (right) models. In each panel, we show results from grain-free calculations (black circles) and calculations with various PAH abundances as indicated in the legend. For $x_{\rm PAH} = 10^{-8}$, we also show the results from calculations without cosmic-ray ionization in the black dash-dotted line. The cross symbols in each panel denote results from the same set of calculations at selected radii but with $x_{\rm PAH} = 10^{-11}$.

addition, we conduct one calculation with cosmic-ray ionization turned off at $x_{\rm PAH} = 10^{-8}$ for both disk models. Again using the methodology of Section 3.3, we estimate the optimistically predicted accretion rate $\dot{M}$ as a function of disk radius for these models, and the results are shown in Figure 3.8. This Figure is to be compared with Figure 3.4 for the cases with 0.1μm and 1μm grains. We see that the inclusion of tiny grains makes the predicted $\dot{M}$ comparable to that with solar abundance 0.1μm grains at 1 AU, which is one to two orders magnitude smaller than the grain-free case. However, at larger disk radii, tiny grains promote accretion compared with sub-micron grains, with predicted rate that even exceeds the grain-free case. Below we discuss the effect of PAHs in more detail.

We find that whenever the active layer extends to the disk midplane (the gray area touches the vertical axis in Figure 3.7, which makes the Ohmic resistivity irrelevant), the predicted $\dot{M}$ in the presence of PAHs exceeds the grain-free case, and the reason is simply due to the reduction of AD coefficients as discussed in the previous two subsections. This occurs at disk radii $r \gtrsim r_{\rm trans} \approx 15$ AU for $x_{\rm PAH} = 10^{-7}$ and 10^{-8}, and for $r \gtrsim r_{\rm trans} \approx 40$ AU for $x_{\rm PAH} = 10^{-9}$. Inside the transition radius $r_{\rm trans}$, accretion is layered and the predicted $\dot{M}$ is well below that in the grain-free case due

to Ohmic resistivity as discussed at the end of the previous subsection. The increase in predicted $\dot{M}$ near $r_{\rm trans}$ is very sharp, which is closely related to dependence of Am on magnetic field strength shown in Figure A.1, and is discussed in more detail in the Appendix of Bai (2011b).

An interesting and counterintuitive fact is that higher PAH abundance leads to faster accretion at all disk radii. This fact can be understood as follows. First of all, near the base of the active layer, we find that charged grain abundance is so much higher than the electron abundance that the Ohmic resistivity is determined by charged grains rather than electrons (i.e., $\theta \gtrsim 1$). Therefore, even though the abundance of free electrons rapidly decreases with increasing $x_{\rm PAH}$, the Ohmic resistivity approximately stays at the same level (while still much larger than the grain-free resistivity). Secondly, as we mentioned in the discussion after equation (3-22), the grain ionization level $n_{\rm gr}^{\pm}/n_H$ increases weakly with the total grain abundance $x_{\rm PAH}$. This fact reduces both the Ohmic resistivity and the AD coefficient, which leads to faster accretion. Only at $r \lesssim 1$ AU, and when $x_{\rm PAH}$ is small (10^{-9} or less), is the Ohmic resistivity at the base of the active layer determined by electrons, which produces higher accretion rate than larger $x_{\rm PAH}$ cases.

We see that in the presence of PAHs, the predicted $\dot{M}$ increases with disk radius for $r \lesssim r_{\rm trans}$ where accretion is layered, and falls off with radius for $r \gtrsim r_{\rm trans}$ as the disk midplane is activated. Also, larger disk surface density generally leads to smaller $\dot{M}$ in the inner disk when accretion is layered (although not by much), while when the disk midplane becomes active in the outer disk, the Desch's disk model gives higher $\dot{M}$. These features are all consistent with the results presented and discussed in Section 4.1.

In addition, we see in the dash-dotted line of Figure 3.8 that when cosmic-ray ionization is turned off (since it may be shielded by protostellar winds), the predicted $\dot{M}$ is almost indistinguishable with our fiducial case at the inner 10 AU. The predicted $\dot{M}$ still exceeds that in the grain-free case in the outer disk, with the transition radius $r_{\rm trans}$ slightly larger than that in the fiducial calculation, and the increase in $\dot{M}$ near $r_{\rm trans}$ is less sharp. Beyond $r_{\rm trans}$, the accretion rate reduction is generally within a factor of 2 of the fiducial result. These results are all consistent with our previous discussions in Section 5.2.

Finally, we emphasize that the existence of $r_{\rm trans}$ and the fact that $\dot{M}$ increases with $x_{\rm PAH}$ holds only when PAHs are sufficiently abundant ($x_{\rm PAH} \gtrsim 10^{-9}$). For comparison, we also show in Figure 3.8 with cross symbols the predicted accretion rate at selected disk radii with $x_{\rm PAH} = 10^{-11}$. At small radius of ~ 1 AU, the predicted $\dot{M}$ is well above the cases with higher PAH abundances.

This is because the free electrons is much more abundant so that electron conductivity dominates grain conductivity, and gives smaller resistivity. The disk midplane becomes active at $r \gtrsim 15$ AU, but we do not find the sharp jump in the predicted $\dot{M}$ as in the case with higher PAH abundances, and the predicted accretion rate is also smaller by a factor of up to 100. This is because $x_{\rm PAH}$ is so small that the grain number density is well below n_e (so $\bar{n}/n_e \approx 1$) and the effects we discussed before no longer apply.

6. Summary and Discussions

We have explored the non-ideal MHD effects in protoplanetary disks (PPDs) using chemistry calculations with a complex reaction network including both gas-phase and grain-phase reactions. Cosmic-ray and X-ray ionization processes are included with standard prescriptions. The equilibrium abundance of all charged species are used to calculate the full conductivity tensor, from which diffusion coefficients for Ohmic resistivity, Hall effect and ambipolar diffusion (AD) are evaluated. One major finding from our chemistry calculations is that the recombination time is much shorter than the orbital time in essentially all regions in PPDs, no matter grains are present or not. Together with the extremely low level of ionization in PPDs, this verifies the applicability of the "strong coupling" limit, and the gas dynamics in PPDs can be well described in a single-fluid framework with magnetic diffusion coefficients in non-ideal MHD terms given from chemical equilibrium. In particular, turbulent mixing of chemical species (especially electrons) can be compensated by the rapid recombination process.

Using the magnetic diffusion coefficients from the chemistry calculation, we estimate the location and extent of the regions in PPD models where the MRI can operate to drive disk accretion (i.e., the active layer). Our adopted criteria are based on the Ohmic Elsasser number Λ, where $\Lambda \gtrsim 1$ is required for the active layer as been shown by previous simulations (e,g., Turner et al. 2007; Ilgner & Nelson 2008), and the AD Elsasser number Am, where $\beta \gtrsim \beta_{\rm min}(Am)$ is required for sustained turbulence from the most recent study by BS11. We have ignored the Hall effect based on the study by Sano & Stone (2002b), although the Hall regime is still yet to be more carefully explored with numerical simulations. Unlike most previous studies, we have considered the dependence of the diffusion coefficients (translated to the Elsasser number) on the magnetic field strength and show that the magnetic field strength can be a main limiting factor on the extent of the active layer because of AD. Our study shows that the conventional magnetic Reynolds number

criterion with $\mathrm{Re}_M \geq 100$ for the MRI to operate may substantially overestimates the column density of the MRI active layer in the presence of small grains.

We provide a general framework for estimating the upper limit of the MRI-driven accretion rate. Furthermore, we hypothesize that the MRI amplifies the magnetic field to maximize the accretion rate, from which we are able to make optimistic predictions on the accretion rate as well as the magnetic field strength in PPDs. Using this framework, we run a series of chemistry calculations with different model parameters to study the location and extent of the MRI active layers in PPDs, and to study the dependence of MRI-driven accretion rate $\dot{M}$ on various parameters. We find that the MRI-active layer always exists at any disk radius as long as the magnetic field in PPDs is sufficiently weak. However, the optimistically predicted $\dot{M}$ in the inner disk ($r = 1 - 10$ AU) is of the order $10^{-9} M_\odot$ yr^{-1} or smaller, which is insufficient to account for the typical observed accretion rate in T-Tauri disks even in the grain-free case, and the presence of solar abundance sub-micron grains further reduces $\dot{M}$ by one to two orders of magnitude. This is mainly because the large AD in the disk surface layer strongly limits the maximum field strength to sustain the MRI turbulence. Moreover, we find that in the inner disk, the predicted $\dot{M}$ increases with radius in the inner disk, but decreases with disk surface density.

We further studied the role of tiny grains, or PAHs, on the MRI-driven accretion process in PPDs, and find that novel behaviors occur when the tiny grains are sufficiently abundant with $x_{\rm PAH} \gtrsim 10^{-9}$, regardless of whether larger grains are present or not. Although predicted accretion rate in the inner disk is still strongly reduced by the tiny grains due to higher resistivity, a sharp increase in the predicted $\dot{M}$ occurs at the transition radius $r_{\rm trans} \approx 15$ AU (in the fiducial model) beyond which the disk midplane becomes active, making Ohmic resistivity irrelevant to the accretion rate. Quite unexpectedly, we find that at $r \gtrsim r_{\rm trans}$, tiny grains make accretion even more rapid than the grain-free case. Moreover, our predicted accretion rate increases with PAH abundance. These results are due to that at large PAH abundance, ionization-recombination balance makes $\bar{n} \equiv n_{\rm gr}^+ + n_{\rm gr}^- + n_i$ orders of magnitude larger than n_e, and even exceeds the grain-free electron density n_{e0} at disk midplane. These facts prevent Ohmic resistivity from rapidly increasing as $x_{\rm PAH}$ increases, and lead to a net reduction of AD, thus facilitate the active layer to extend deeper into the disk midplane and permit stronger MRI turbulence. Our results highlight the importance of evaluating the full conductivity tensor in the calculation of the non-ideal MHD diffusion coefficients rather than using the simple grain-free formulae (1-9).

Our results place strong constraints on the effectiveness of the MRI-driven accretion in PPDs, especially for the inner disk with radius of about $1-10$ AU where accretion is likely to be layered. There are two main difficulties: (a) The optimistically predicted accretion rate under standard model prescriptions is about one order of magnitude or more smaller than the typical observed value; (b) MRI-driven accretion would lead to the runaway pile-up of mass in the inner disk. The first difficulty might be alleviated by incorporating additional (but uncertain) ionization processes such as energetic protons from the protostellar activities. The second difficulty does not appear to be easily reconciled, since external ionization sources always lead to layered accretion. The accumulation of mass may trigger the gravitational instability in the early phase of PPDs, which may further lead to outburst and episodic accretion as FU Ori-like events (Zhu et al. 2009). In later phases, mass accumulation may simply leads to very large surface density in the inner disk (Zhu et al. 2010b). Since the inner disk ($\lesssim 10$ AU) is smaller than the resolution of the currently available sub-millimeter observations (Andrews et al. 2009), whether mass accumulation occurs may be distinguishable in future observations such as ALMA.

The most probable resolution to the above difficulties may be achieved by a magnetized wind from the disk surface (Blandford & Payne 1982), which is introduced in Section 4.3 of Chapter 1. This scenario will be throughly explored in the next Chapter, where we show that a magneto-centrifugal wind can be launched naturally from the inner region of PPDs, and efficient angular momentum transport can be achieved with a modest net vertical magnetic field.

Our results are also applicable in the gas dynamics of transitional disks, where the MRI is likely to be responsible for driving accretion from the outer disk (Chiang & Murray-Clay 2007), with the inner gap / hole opened by multiple planets that guide the gas streams through (Perez-Becker & Chiang 2011a; Zhu et al. 2011). Our predicted accretion rate in the outer disk with $r \gtrsim 10$ AU is on the order of $10^{-9} M_\odot$ yr^{-1}, with relatively weak dependence on the dust content compared with the inner disk. In addition, we note that the observationally inferred outer boundary of the holes or gaps is typically at a few tens of AU (Hughes et al. 2009; Kim et al. 2009), which is generally greater than $r_{\rm trans}$ in our models with PAHs, therefore, enhancement of the accretion rate by the PAHs to the level of $10^{-8} M_\odot$ yr^{-1} is possible. This is sufficient to account for the observed accretion rate in transitional disks (Najita et al. 2007; Sicilia-Aguilar et al. 2010), thus MRI alone appears sufficient to account for the accretion rate in transitional disks. This conclusion can also be achieved with far UV ionization instead of X-rays (Perez-Becker & Chiang 2011b) .

Our study of the MRI active layer in PPDs represents a first attempt to estimate the MRI-driven accretion rate that is based on the most up-to-date non-ideal MHD simulations. In the mean time, it is limited by the predictive power of the simulations themselves. In particular, the non-linear properties of the MRI in the Hall dominated regime is still unexplored. Moreover, the AD simulations presented in Chapter 2 are unstratified, and whether their obtained criterion for sustained MRI turbulence holds remains to be verified in stratified simulations (work in progress in collaboration with J. Simon). In conclusion, our study calls for further progress in non-ideal MHD simulations, and in turn, more realistic criteria for sustained MRI turbulence can be easily incorporated into our general framework after future simulations.

Chapter 4

Launching Magneto-centrifugal Wind from Protoplanetary Disks

In the previous chapter, we predict the MRI-driven accretion rate for a given disk model based a number of criteria and semi-analytical estimates without dynamically evolving the gas dynamics, and found that the MRI-driven accretion is too inefficient to match the observed rates. In this chapter, we perform local shearing-box simulations of a PPD that for the first time, simultaneously include both Ohmic resistivity and ambipolar diffusion (AD) and follow the dynamical evolution of the disk structure in a self-consistent manner. We find that for the inner region of PPDs, the disk is likely to evolve into a laminar configuration with MRI being completely suppressed. Instead of MRI-driven, accretion is powered by a magneto-centrifugal wind (MCW), and the MCW-driven accretion rate easily matches the observed accretion rates.

In Section 1, we summarize the literature on the study of the MCW as well as its connections to PPDs to motivate our work. Detailed description of our simulation setup is provided in Section 2. We show two contrasting set of fiducial simulations in Section 3 which best demonstrate the important role played by AD on the gas dynamics in PPDs: launching of a laminar disk wind. The laminar wind solution from the fiducial simulation is examined in great detail in Section 4 which reveals its launching mechanism and physical importance. A parameter study is performed in Section 5, followed by conclusive remarks and discussion in Section 6.

1. Introduction

As introduced in Chapter 1, the MCW scenario was first proposed by Blandford & Payne (1982) (hereafter BP82). They considered cold MHD flow launched from a razor-thin disk threaded by vertical magnetic field lines. Under the assumption of self-similarity, which requires all quantities to scale with disk radius with certain power-law indicies, they were able to construct analytical global wind solutions that describe the magneto-centrifugal acceleration of disk outflows and their subsequent collimation by magnetic hoop stress. Although the BP82 model has been served as a prototype the MCW solution, it is idealized in several ways, especially because of the self-similarity assumption and the fact that it does not contain the fast magnetosonic point.

Global numerical simulations of the MCW have been successfully performed in the late 1990s. Early global simulations adopt similar assumptions as BP82 that treat the disk as a boundary condition (i.e., razor-thin) with axisymmetry, and prescribe the rate of outflow from the disk (Ouyed & Pudritz 1997; Krasnopolsky et al. 1999, 2003). These simulations demonstrated the robustness of the MCW acceleration and collimation, and further found that the flow structure is sensitive to the prescribe rate of mass loading from the disk, and may lead to episodic formation of jets (Ouyed et al. 1997; Krasnopolsky et al. 1999; Anderson et al. 2005). In reality, the mass loading rate is determined by the gas dynamics in the disk by requiring that the flow smoothly passes the slow magnetosonic point (Wardle & Koenigl 1993; Li 1995; Ogilvie & Livio 2001). More recent simulations (most of which are two-dimensional) that do resolve the disk generally rely on artificially prescribed resistivity in order for the magnetic field lines not to be dragged to the central object as mass accretes (Kato et al. 2002; Casse & Keppens 2002, 2004). The resulting wind properties, largely depend on the prescribed resistivity profile in the disk (Zanni et al. 2007).

To ultimately address the wind launching problem one needs to properly resolve the microphysics in the gaseous disk. Due to the complexity of the global problem, the wind launching process is best studied again with the local shearing-box approach. Under the assumption of "even-z" symmetry across disk midplane as expected for a global wind geometry (antisymmetric for horizontal magnetic field and vertical velocity while symmetric for the rest of variables), the launching of disk wind generally requires a relatively strong vertical background magnetic field that is of the order super-equipartition strength with midplane gas pressure (Wardle & Koenigl 1993; Ogilvie & Livio 2001). For PPDs, a conprehensive study of the wind-launching criteria and representative solutions are constructed and presented in Königl et al. (2010) and Salmeron

et al. (2011) where all the non-ideal MHD effects were taken into account. Two free parameters, including the mass loading rate, can be determined as the solution passes the slow magnetosonic point, as well as the Alfvén point. The latter is achieved by matching the one-dimensional local solution to the global BP82 wind solution.

The typical structure of a wind solution with "even-z" symmetry can be found in Figure 1 of Wardle & Koenigl (1993) (hereafter WK93). The solution can be divided into three separate regions: a quasi-hydrostatic midplane region where the bulk of the gas is sub-Keplerian and moves inward (i.e., accretion flow). The inward and sub-Keplerian motion bends the initially pure vertical field lines and shears the field lines in azimuth. The flow becomes magnetic dominated in the transition zone where the inflow diminishes with height, and the field lines straightens out. Finally, an outflow region at disk surface where the gas becomes super-Keplerian with magneto-centrifugal acceleration taking place.

The main reason that launching an MCW requires strong vertical background field is that a field configuration with weaker vertical field is prone to the MRI, hence the construction a stable laminar solution becomes impossible. It has been speculated the MRI and the wind scenario tend to mutually exclude each other (Salmeron et al. 2007): MRI operates for weak vertical field well below equipartition strength and the MCW operates for strong field around equipartition, with a very narrow intermediate window for a transition between the two scenarios. The strong magnetic field strength in these wind makes it more favored for efficiently driving disk accretion, while the magnetic field can not be too strong, which would make it difficult to be bent by the disk material, and would result in substantial sub-Keplerian rotation that hinders wind-launching (Shu et al. 2008; Ogilvie 2012).

For shearing-box simulations of the MRI that do take into account vertical stratification, it is conventional to adopt a zero vertical net magnetic flux field geometry (e.g., Stone et al. 1996; Davis et al. 2010; Shi et al. 2010; Simon et al. 2011), which essentially excludes the possibility of launching of an MCW. Including vertical net-flux in such simulations places strong demands on the robustness of numerical algorithms, especially in the magnetic dominated disk corona (Miller & Stone 2000). Recently, Suzuki & Inutsuka (2009) performed shearing-box simulations of the MRI that include relatively weak net vertical field and show evidence of wind launching from MRI turbulence, with the rate of outflow increasing with increasing net flux. Followup work that include Ohmic resistivity to mimic the conditions in PPDs also produced outflow from the vertical

boundaries (Suzuki et al. 2010; Okuzumi & Hirose 2011). Bai & Stone (2012a) performed similar simulations but with much stronger vertical net flux and confirmed the trend found by Suzuki & Inutsuka (2009), but argued that the outflow is unlikely to be connected to a global MCW because of magnetic dynamo action as well as symmetry problems. Although shearing-box approach is inappropriate to characterize the outflow since disk wind is intrinsically a global problem, these simulations open up a new window to explore the properties of the MRI turbulence in more realistic situations.

For PPDs, large number of shearing-box simulations have been conducted studying and characterizing the gas dynamics of the MRI active layer and the dead zone (e.g., Fleming & Stone 2003; Turner et al. 2007; Turner & Sano 2008; Ilgner & Nelson 2008; Oishi & Mac Low 2009; Hirose & Turner 2011). Including a vertical net magnetic flux or not does not change the basic picture of layered accretion, but stronger vertical net flux leads to stronger MRI turbulence in the active layer and reduces the vertical extent of the dead zone, as well as a stronger outflow (Okuzumi & Hirose 2011). However, we emphasize that all these simulations considered only the Ohmic resistivity, while in reality, the MRI active layer at disk surface would suffer from strong Hall effect and ambipolar diffusion (AD), as already stressed in the previous chapter.

In this work, we present vertically stratified shearing-box simulations of a local patch of a PPD that include a realistic profile of both Ohmic resistivity and AD coefficient. The profiles are interpolated from a pre-computed look-up table in real time based on the gas density, temperature (fixed) and ionization rate (calculated from the density profile). This is first time that AD is included in vertically stratified simulations. We have not yet included the Hall effect (which is numerically more challenging and demanding), and this is the first step towards understanding the non-ideal MHD of PPDs beyond Ohmic resistivity. In addition, our simulations by default include a weak vertical magnetic field, which is likely to be more realistic for a local patch of a PPD, and is essential for potentially launching a disk wind.

For all the simulations in this chapter, we focus on a series of numerical simulations that correspond to a minimum-mass solar nebular at 1 AU, with standard prescriptions for chemistry and ionization rates. We find the launching of the MCW from initially MRI-unstable disks that quickly relax into a pure laminar configuration. The MCW in our simulations differ critically from that in WK93 in that it follows an "odd-z" symmetry (symmetric for magnetic field and vertical velocity while antisymmetric for horizontal velocity). Conforming to a physical disk wind geometry

then requires the presence of a current sheet. The richness of the new wind launching results deserves a detailed study as we present in this chapter, while extension of the results at other radial locations is in progress but is not to be covered in this thesis work.

2. Simulation Setup

2.1 Formulation

We use the Athena MHD code (see Appendix B.1) to study the gas dynamics in PPDs and perform three-dimensional numerical simulations. Using the conventional shearing-box approach (see Appendix B.2), the MHD equations read:

$$\frac{\partial \rho}{\partial t} + \nabla \cdot (\rho \boldsymbol{v}) = 0 \ , \tag{4-1}$$

$$\frac{\partial \rho \boldsymbol{v}}{\partial t} + \nabla \cdot (\rho \boldsymbol{v}^T \boldsymbol{v} + \mathsf{T}) = \rho \left[2\boldsymbol{v} \times \boldsymbol{\Omega} + 3\Omega^2 x \hat{\boldsymbol{x}} - \Omega^2 z \hat{\boldsymbol{z}} \right] \ , \tag{4-2}$$

where T is the total stress tensor

$$\mathsf{T} = (P + B^2/2)\, \mathsf{I} - \boldsymbol{B}^T \boldsymbol{B} \ , \tag{4-3}$$

I is the identity tensor, ρ, $\boldsymbol{v}$, P are the gas density, velocity and pressure respectively, $\boldsymbol{B}$ is the magnetic field, which is rescaled so that magnetic pressure is $B^2/2$. Unit vectors $\hat{\boldsymbol{x}}, \hat{\boldsymbol{y}}, \hat{\boldsymbol{z}}$ are pointing to the radial, azimuthal and vertical directions respectively, where $\boldsymbol{\Omega}$ is along the $\hat{\boldsymbol{z}}$ direction. Vertical gravity is included to account for density stratification. We use an isothermal equation of state $P = \rho c_s^2$, where c_s is the isothermal sound speed. We use outflow boundary conditions in the vertical direction, described in Simon et al. (2011).

Recall from Section of 3 of Chapter 1 about the three non-ideal MHD effects, and the general derivation in Appendix A, the induction equation reads

$$\frac{\partial \boldsymbol{B}}{\partial t} = \nabla \times (\boldsymbol{v} \times \boldsymbol{B}) - \nabla \times [\eta_O \boldsymbol{J} + \eta_H (\boldsymbol{J} \times \hat{\boldsymbol{B}}) + \eta_A \boldsymbol{J}_\perp] \ , \tag{4-4}$$

where $\boldsymbol{J} \equiv \nabla \times \boldsymbol{B}$ is the current density our code unit, and $\boldsymbol{J}_\perp$ is the component of $\boldsymbol{J}$ that is perpendicular to the magnetic field, η_O, η_H and η_A are the magnetic diffusion coefficients for Ohmic, Hall and AD respectively. Ohmic resistivity and AD are included in our simulations, while we also evaluate η_H (but do not use it to evolve the induction equation) and assess its importance in our analysis.

The magnetic diffusivities depend on the number density of the charged species, and are characterized by the dimensionless Elsasser numbers, defined in Equation (1-16) in Chapter 1:

$$\Lambda \equiv \frac{v_A^2}{\eta_O \Omega} \ , \qquad Ha \equiv \frac{v_A^2}{\eta_H \Omega} \ , \qquad Am \equiv \frac{v_A^2}{\eta_A \Omega} \ , \tag{4-5}$$

for Ohmic, Hall and AD respectively, where $v_A = \sqrt{B^2/\rho}$ is the Alfvén velocity. In the absence of grains, we have $\Lambda \propto B^2$, $Ha \propto B$ and Am being independent of B (see Appendix B for details). Generally speaking (see Chapter 2 for more details), self-sustained MRI turbulence requires these Elsasser numbers to be greater than 1 and relatively weak magnetic field.

We use natural unit in our simulations, where $c_s = 1$, $\Omega = 1$. The initial density profile is taken to be Gaussian

$$\rho_0 = \rho_{0,\mathrm{mid}} \exp\left(-z^2/2H^2\right) \ , \tag{4-6}$$

with $\rho_{0,\mathrm{mid}} = 1$ in code unit, and $H \equiv c_s/\Omega = 1$ is the thermal scale height. All our simulations contain a net-vertical magnetic flux B_0, parameterized by the midplane plasma $\beta_0 = 2\rho_{0,\mathrm{mid}} c_s^2/B_0^2$. In addition, in order to avoid the initial (transient) channel mode from growing excessively in amplitude which would cause numerical difficulties, we further include a sinusoidally varying vertical field $B_1 \sin 2\pi x/L_x$, where L_x is the radial size of the simulation box, and $B_1 = B_0/4$.

Physically, we consider a patch of the PPD with the minimum-mass solar nebular (MMSN) disk model at 1AU assuming a $1M_\odot$ protostar. The surface density, temperature, sound speed and scale heights are provided in Section 2 of Chapter 1. These physical scales are needed to normalize the magnetic diffusivities (next subsection) to code unit. In particular, $B = 1$ in code unit corresponds to field strength of 18.6 Gauss.

We use outflow boundary condition in the vertical direction which copies the density, velocity and magnetic fields in the boundary cells to the ghost zones, with the density attenuated following the Gaussian profile to account for vertical gravity, which is described in the Appendix of Simon et al. (2011). A density floor of $\rho_{\mathrm{Floor}} = 10^{-6}$ (in code unit) is applied to avoid numerical difficulties at magnetic dominated (low plasma β) regions. We have checked that horizontally averaged densities in the saturated states of all our simulations are always well above the density floor. Moreover, the use of outflow boundary condition no longer conserves mass in the simulation box. To compensate for the mass loss/gain, the density of each cell is modified by the same proportion so that the total mass in the simulation box remains the same. We have also checked that in all our simulations, the mass change over the duration of our simulations (if mass conservation were not enforced) is only a tiny fraction of the total mass.

2.2 Calculation of Magnetic Diffusivities

The magnetic diffusivities are evaluated based on the chemistry calculation. Instead of evolving the chemical network in real time, as done by a number of previous works (Turner et al. 2007; Turner & Sano 2008; Ilgner & Nelson 2008), we assume equilibrium chemistry (similar to Hirose & Turner 2011), because the recombination time has been shown to be much shorter than the dynamical time scale (Bai 2011a). We adopt a complex chemical reaction network as described in detail in Appendix C. In our fiducial model, we fix the chemical composition to be with well-mixed 0.1μm grains whose abundance is 10^{-4} in mass (about 0.01 solar, corresponding to substantial grain growth and settling), while all the gas-phase elemental abundances are taken to be solar. We follow evolve the complex chemical reaction network for 10^7 years. Given the chemical composition, variable parameters of the network include gas density ρ, gas temperature T, and the ionization rate ξ, which are scanned to give a complete coverage of the parameter space relevant to PPDs. The outcome of the scan is a look-up table of magnetic diffusivities that is read into the code so that η_O, η_H and η_A can be evaluated by interpolation in the simulations in real time. Since we adopt an isothermal equation of state, T is fixed, hence our look-up table is essentially two-dimensional (ρ and ξ).

The ionization rate in the disk depends on the column density to the disk surface. We calculate the horizontally averaged vertical density profile in real time, from which a column density profile can be reconstructed, an approach similar to previous works (e.g. Turner et al. 2007). The sources of ionization include radioactive decay, cosmic ray and stellar X-ray ionizations, with prescriptions given in Section 1.1 of Chapter 3, with fixed X-ray luminosity of 10^{30}erg s^{-1}. In addition, we consider the effect of far-ultraviolet (FUV) ionization. According to the detailed study by Perez-Becker & Chiang (2011b), FUV photons almost completely ionize tracer species such as C and S and give ionization fraction of the order $f = 10^{-5} - 10^{-4}$ with penetration depth of $0.01 - 0.1$ g cm^{-2} depending on the effectiveness of dust attenuation and self-shielding. For simplicity, we assume an ionization fraction of $f = 2 \times 10^{-5}$ in the form of carbon in the FUV layer, whose column density is chosen by default as $\Sigma_{\rm FUV} = 0.03$ g cm^{-2}. We also vary $\Sigma_{\rm FUV}$ from 0.01 to 0.1 g cm^{-2} to assess its physical importance. Within the FUV layer, the magnetic diffusivities expressed

in the form of Elsasser numbers under the MMSN disk model are given by

$$\begin{aligned} Am &= \frac{\gamma\rho_i}{\Omega} \approx 3.3\times10^7\left(\frac{f}{10^{-5}}\right)\left(\frac{\rho}{\rho_{0,\rm mid}}\right)R_{\rm AU}^{-5/4}\ , \\ Ha &= \frac{en_eB}{c\rho\Omega} \approx 6.2\times10^6\left(\frac{f}{10^{-5}}\right)\frac{1}{\sqrt{\beta_{\rm mid}}}R_{\rm AU}^{-1/8}\ , \end{aligned} \tag{4-7}$$

where $\beta_{\rm mid}$ is ratio of magnetic pressure to midplane gas pressure. A smooth transition (across about 4 grid cells) on the magnetic diffusivities from the FUV ionization layer at $\Sigma < \Sigma_{\rm FUV}$ to the X-ray/cosmic-ray dominated ionization layer (based on our chemistry calculations) $\Sigma > \Sigma_{\rm FUV}$ is applied. As Ohmic resistivity plays essentially no role in the low density region of the FUV layer, we simply ignore the effect of FUV ionization on it.

We calculate the magnetic diffusivities from the number density of all charged species at the end of the chemical evolution following Section 1.3 of Chapter 3. Note that the Ohmic resistivity η_O is independent of magnetic field strength B, while Hall and ambipolar diffusivities do depend on B. In the grain-free case, we have $\eta_H \propto B$, and $\eta_A \propto B^2$. In this case, we can simply fit the proportional coefficients, Q_H and Q_A respectively, and put them into the look-up table. In the presence of small grains, a situation studied in detail in Bai (2011b), η_H (η_A) is proportional to B (B^2) when B is sufficiently weak or sufficiently strong respectively, while is roughly proportional to B^{-1} (B^0) at some intermediate field strength (see Appendix A for details). In this case, we include in the look-up table the two proportional coefficients Q_{H1}, Q_{H2} (Q_{A1}, Q_{A2}) at weak and strong field regimes from the fitting respectively, together with a transition field strength B_i so that

$$\eta_H = \begin{cases} Q_{H1}B\ , & B < \sqrt{Q_{H2}/Q_{H1}}B_i\ , \\ Q_{H2}B_i^2B^{-1}\ , & \sqrt{Q_{H2}/Q_{H1}}B_i < B < B_i\ , \\ Q_{H2}B\ , & B > B_i\ , \end{cases} \tag{4-8}$$

$$\eta_A = \begin{cases} Q_{A1}B^2\ , & B < \sqrt{Q_{A2}/Q_{A1}}B_i\ , \\ Q_{A2}B_i^2\ , & \sqrt{Q_{A2}/Q_{A1}}B_i < B < B_i\ , \\ Q_{A2}B^2\ , & B > B_i\ , \end{cases} \tag{4-9}$$

By comparing with Figure A.1, we see that the transition field strength B_i corresponds to the situation that the ion gyro-frequency equals its collision frequency with the neutrals (or the ion Hall parameter equals one), which can be directly calculated given the gas density.

Being diffusive processes, large Ohmic resistivity near the disk midplane and strong AD in the tenuous disk corona would significantly limit the code efficiency. In the Ohmic regime, the

time step scales as Δ^2/η_O where Δ is the minimum grid spacing. In practice, we add a floor to the Ohmic resistivity so that in code unit $\eta_O \leq 10$. Since the magnetic field strength near the disk midplane never reaches equipartition in all our simulations, the Elsasser number at the disk midplane is always smaller than 0.1, well below the threshold value 1. Also, this floor value of η_O makes the diffusion time scale much smaller than the dynamical time scale, hence captures the basic effect of strong diffusion at disk midplane even if resistivity is much higher in reality. Also note our resistivity cap is larger than most previous works, where the cap was of the order 0.01 in code unit (e.g., Fleming & Stone 2003; Okuzumi & Hirose 2011). In the AD regime, the time step scales as $\Delta^2 \cdot Am \cdot \beta$ (the plasma β is the ratio of gas to magnetic pressure). In the same spirit, we apply a floor to Am so that $Am \cdot \beta \geq 0.1$ in every grid cell. This floor value of Am is again sufficiently small so that it does not make the otherwise stable field configuration unstable to the MRI (see Figure 2.14 of Chapter 2), and it retains the effect of strong diffusion.

3. Fiducial Simulations and Results

We perform three-dimensional (3D) shearing-box simulations of a PPD with vertical stratification as described in the previous section. In our fiducial model, we adopt a MMSN disk at 1AU, using a chemistry model with well-mixed 0.1μm grains with abundance of 10^{-4} (1% solar), a net vertical magnetic flux of $\beta_0 = 10^5$ and a FUV column density $\Sigma_{\rm FUV} = 0.03$ g cm^{-2}. Figure 4.1 illustrates the *initial* profile of the Ohmic, Hall and ambipolar Elsasser numbers. Also shown is the initial profile of plasma β. From the disk midplane to surface, the dominant non-ideal MHD effects are Ohmic resistivity, Hall effect and AD respectively for the initial field configuration, and the MRI unstable region is located at around $z = \pm 3H$ where all Elsasser numbers are greater than 1 and plasma β is well above 1. The initial FUV ionization front is located at about $z = \pm 4H$. The density floor of $\rho_{\rm floor} = 10^{-6}$ is applied to regions beyond $z = \pm 5H$, hence the Am and β curves flattens out (this artifact will disappear as the system evolves).

We begin with two contrasting simulations: one with only Ohmic resistivity included (Run O-b5-F3), and the other with both Ohmic resistivity and AD (Run OA-b5-F3). For both cases, our simulation box size is $4H \times 8H \times 16H$ in the radial (x), azimuthal (y) and vertical (z) dimensions respectively, with a computational grid of $96 \times 96 \times 384$ cells. A relatively high resolution in x and z (24 cells per H, or 34 cells if one defines the scale height to be $\sqrt{2}H$, as in a number of works) is needed to properly resolve the MRI turbulence, if present (Davis et al. 2010; Bai & Stone

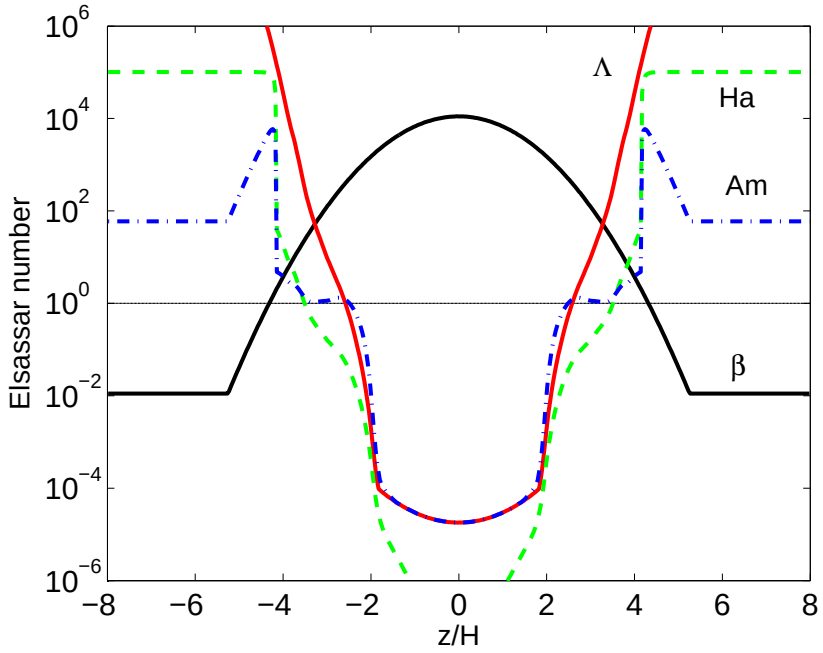


Fig. 4.1.— Initial Elsasser number profile for Ohmic resistivity (red solid), Hall diffusivity (green dashed) and ambipolar diffusivity (blue dash-dotted). Note the cap on Am and Λ around the disk midplane and on Am beyond about $\pm 5H$. Also shown is the initial profile for plasma β (black solid).

2011; Sorathia et al. 2011), and relatively large simulation box is needed to capture the mesoscale structures of the MRI turbulence (Simon et al. 2012). Both simulations are run for about 150 orbits ($900\Omega^{-1}$).

In this Section, we provide details of the two fiducial runs described above. For clarity, we further provide a list of all simulation runs for the fiducial as well as other (described in the remaining sections) models in Table 4.1. In particular, we introduce the letter "S" for runs with a very small horizontal domain, where the simulations are essential one-dimensional. We use the label "bn" to denote plasma $\beta = 10^n$ for the vertical background field. Label "Fn" represents $\Sigma_{\rm FUV} = 0.01n$ g cm^{-2}. All other simulations are run for about 200 orbits ($1200\Omega^{-1}$).

3.1 The Ohmic-Resistivity-Only Run

Run O-b5-F3 quickly develops into turbulence. The upper panel of Figure 4.2 shows the time history of its horizontally averaged Maxwell stress $-\bar{B}_x\bar{B}_y$. The separation between the highly

Table 4.1: Summary of All Simulations.

Run	Diffusion	β_0	Grain Abn.	$\Sigma_{\rm FUV}$ (g/cm^2)	Box Size	Section
O-b5-F3	Ohm	10^5	10^{-4}	0.03	$4H \times 8H \times 16H$	3.1
OA-b5-F3	Ohm,AD	10^5	10^{-4}	0.03	$4H \times 8H \times 16H$	3.2
S-OA-b5-F3	Ohm,AD	10^5	10^{-4}	0.03	$H/8 \times H/4 \times 16H$	4.1
S-OA-b3-F3	Ohm,AD	10^3	10^{-4}	0.03	$H/8 \times H/4 \times 16H$	5.1
S-OA-b4-F3	Ohm,AD	10^4	10^{-4}	0.03	$H/8 \times H/4 \times 16H$	5.1
S-OA-b6-F3	Ohm,AD	10^6	10^{-4}	0.03	$H/8 \times H/4 \times 16H$	5.1
S-OA-b5-F1	Ohm,AD	10^5	10^{-4}	0.01	$H/8 \times H/4 \times 16H$	5.2
S-OA-b5-F10	Ohm,AD	10^5	10^{-4}	0.1	$H/8 \times H/4 \times 16H$	5.2
S-OA-b5-nogr-F3	Ohm,AD	10^5	0	0.03	$H/8 \times H/4 \times 16H$	5.3
S-OA-b5-gr01-F3	Ohm,AD	10^5	10^{-3}	0.03	$H/8 \times H/4 \times 16H$	5.3

MMSN disk model at 1AU, uniformly mixed 0.1μm grains are assumed for all runs.

turbulent active layer and more or less quiescent midplane region is clearly seen. We further show the time and horizontally averaged vertical profiles of density, magnetic pressure, Maxwell and Reynolds stresses in Figure 4.3. The time averages are performed from $\Omega t = 450$ onward.

The MRI turbulence generates strong magnetic field that buoyantly rises, and the disk surface quickly forms a strongly magnetically dominated corona beyond $\pm 2H$, as shown in the bottom panel of Figure 4.3. The gas density in the corona follows a power-law distribution in the corona due to strong magnetic support, instead decreasing with height as an Gaussian as in the hydrostatic case. The velocity in the corona regions is highly supersonic, with turbulent kinetic energy exceeding the gas pressure beyond $\pm 5H$. A strong outflow is launched from the active layer of the disk as has been studied by Suzuki et al. (2010), who also found that the mass outflow rate scales roughly linearly with the vertical net magnetic flux. In our simulation, the time and horizontally averaged mass outflow rate $\rho \bar{v}_z$ is found to be about $3.7 \times 10^{-4} \rho_0 c_s$ from each side of the box, comparable with the measurements in Suzuki et al. (2010) with same β_0. Although the mass outflow rate is not a well-characterized quantity in shearing-box (S. Fromang, private communication, 2011), these measurements can still be taken as a reference.

The disk midplane is too resistive to become MRI active, with the boundary of the active layer well described by the Elsasser number criterion: $\Lambda_z \equiv v_{Az}^2/\eta_O \Omega = 1$, where v_{Az} is the vertical component of the Alfvén velocity. The Maxwell stress remains very small at the midplane for the first 40 orbits. However, the midplane magnetic field is then gradually amplified, while the flow in the midplane remains more or less laminar. This is related to the "undead" zone proposed by

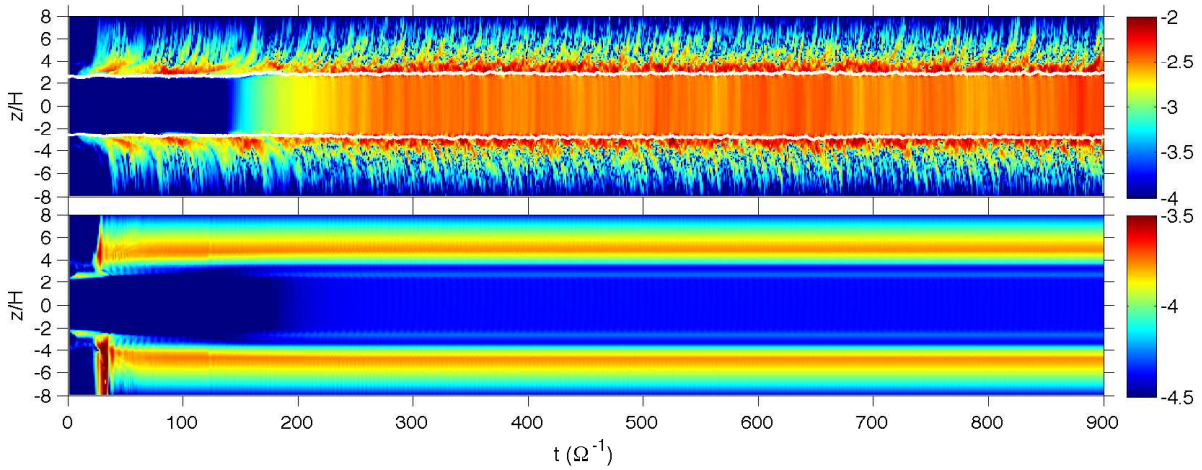


Fig. 4.2.— Time evolution of the horizontally averaged vertical profiles of the Maxwell stress in the fiducial run that includes only Ohmic resistivity (O-b5-F3, upper panel) and the fiducial run that includes both Ohmic resistivity and AD (OA-b5-F3, lower panel). The color corresponds to logarithmic scales. White contours in the upper panel corresponds to vertical Elsasser number $\Lambda_z \equiv v_{Az}^2/\eta_O\Omega = 1$.

Turner & Sano (2008), where the amplification of radial magnetic field to azimuthal field constantly takes place and is balanced by Ohmic dissipation, but no MRI is involved. We note that the Maxwell stress in the midplane is even larger than most regions in the active layer, which contrasts with some previous simulations with a similar setup, where the Maxwell stress becomes very small near in the midplane (Suzuki et al. 2010; Hirose & Turner 2011; Okuzumi & Hirose 2011). The main reason for the difference, while somewhat counterintuitive, lies in the usage of a much larger resistivity cap in our simulations. The large resistivity at the disk midplane in our simulations strongly suppresses the strength of current, leaving the horizontal magnetic field to be almost constant across the midplane (see the bottom panel of Figure 4.3). Matching to the field strength to that in the active layer gives the large field strength and Maxwell stress in the disk midplane.

By contrast, the Reynolds stress $\rho v_x v_y'$ as well as kinetic energy clearly have a large dip in the undead region between $\pm 2H$, where v_y' is the azimuthal velocity with the Keplerian velocity subtracted. There is still random motion near the midplane due to the sound waves shooting from the base of the active layer (Fleming & Stone 2003; Oishi & Mac Low 2009), though the velocity amplitude is at least an order of magnitude smaller than that in the active layer.

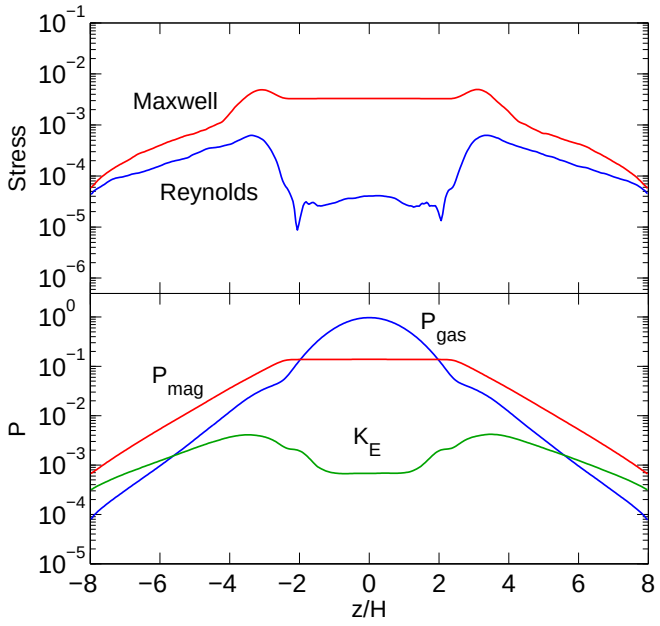


Fig. 4.3.— Vertical profiles of the Maxwell stress and Reynolds stress (upper panel), as well as gas/magnetic pressure and kinetic energy (lower panel) in the fiducial run with only Ohmic resistivity (O-b5-F3).

The radial transport of angular momentum is given by the Reynolds and Maxwell stresses

$$T_{r\phi} = T_{r\phi}^{\rm Rey} + T_{r\phi}^{\rm Max} = \overline{\rho v_x v_y'} - \overline{B_x B_y} \ , \tag{4-10}$$

where the over bar indicates time and spatial averaging. The overall efficiency of angular momentum transport is characterized by $\alpha = \int T_{r\phi} dz / \Sigma c_s^2$ (Shakura & Sunyaev 1973), with steady-state accretion rate given by

$$\dot{M} = \frac{2\pi\alpha\Sigma c_s^2}{\Omega} \approx 8.4\times10^{-6}\alpha R_{\rm AU}^{-1/2} M_\odot \ {\rm yr}^{-1} \ , \tag{4-11}$$

where we have assumed a MMSN disk model to obtain the numbers. In our simulation, we obtain $\alpha_{\rm Max} \approx 1.3\times10^{-2}$, $\alpha_{\rm Rey} \approx 1.2\times10^{-3}$. Therefore, in the absence of AD, we obtain an accretion rate of $1.2\times10^{-7} M_\odot$ yr^{-1} at 1 AU, large enough to account for the observed accretion rates in most T-Tauri stars.

Given the usage of more realistic resistivity profiles and chemistry models, as well as the much larger resistivity cap enabled by the super time-stepping technique, there are more to be discussed

about our Ohmic-resistivity only simulation and to compare with previous works. However, we only consider our run O-b5-F3 as a test and reference case since our main point of interest is the effect of AD on the gas dynamics of PPDs. We will see that the inclusion of AD makes a dramatic difference from the conventional picture of PPD accretion.

3.2 Run with Both Ohmic Resistivity and AD

The bottom panel of Figure 4.2 illustrates the time evolution of Maxwell stress in our fiducial run OA-b5-F3, where both Ohmic resistivity and AD are included. The initial field configuration is still unstable to the MRI, which gives rise to channel-flow like behaviors and initiates some turbulent activities in the surface layer. However, we find that quite surprisingly, the system then quickly relaxes into a non-turbulent state in about 10 orbits. The laminar configuration is then maintained for the remaining of the simulation time[1].

As the system settles to a completely laminar state, we are able to extract the exact vertical profiles of various physical quantities, as shown in Figure 4.4. The magnetic field is strongest within about $\pm 2.5H$ of the disk midplane, where the field is essentially constant due to the large resistivity and AD. There is no distinction between active layer and dead zone as the entire disk is laminar. The disk become magnetically dominated beyond $z = \pm 4H$. The FUV ionization front is located at about $z = \pm 4.5H$ as seen in the sharp increase of Am and Ha profiles, which also corresponds to the point where the gas density starts to deviate from Gaussian and follow a power-law distribution.

Being a time-dependent simulation, the fact that the system reaches a steady laminar state automatically proves the stability (particularly, against the MRI) of the configuration. This stability can be qualitatively understood using the criterion based on MRI simulations that include individual non-ideal MHD effects. In regions near the disk midplane where Ohmic resistivity dominates, the Ohmic Elsasser number is below one within about $z = \pm 2H$, too small for the MRI (Turner et al. 2007). Beyond this region where AD is the dominant non-ideal MHD effect, which requires weak magnetic field for the MRI to operate, the magnetic field is too strong, as judged from Figure 2.14 of Chapter 2. Even the FUV ionization increases Am substantially beyond $z = \pm 4.5H$, the disk has already become magnetically dominated ($\beta < 1$) at these regions. The

[1]To justify the validity of this result, particularly that it is not due to an unrealistic initial condition, we restart from the end of run O-b5-F3 with AD turned on and find that also in about 10 orbits of time, the system settles to the same laminar state.

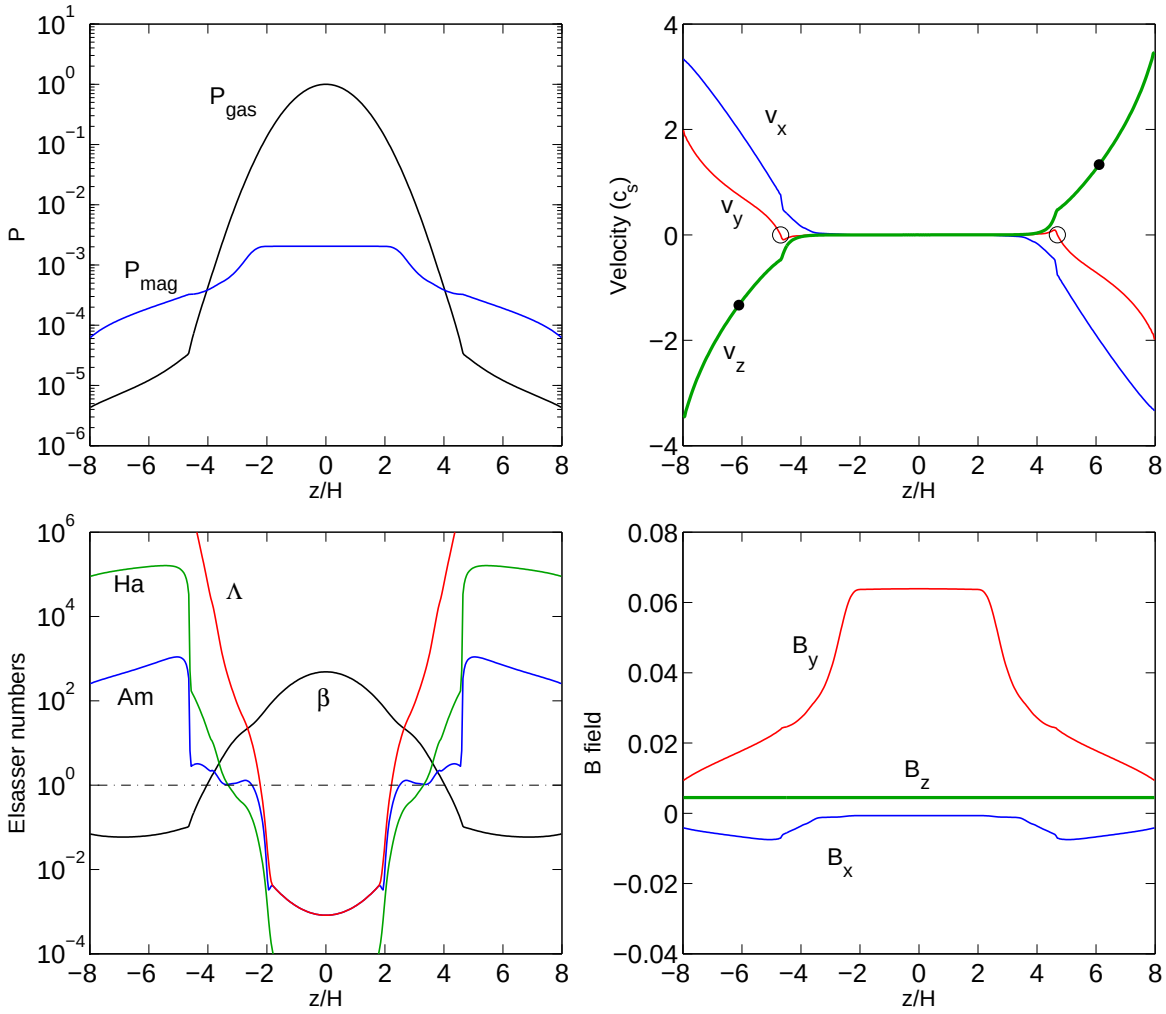


Fig. 4.4.— Vertical profiles of various quantities in the fiducial run with both Ohmic resistivity and AD (OA-b5-F3). Upper left: gas pressure and magnetic pressure. Lower left: Elsasser numbers for Ohmic resistivity (Λ), Hall term (Ha) and AD (Am), together with the plasma $\beta = P_{\rm gas}/P_{\rm mag}$. Upper right: three components of gas velocity. The locations of the Alfvén points are indicated as the two large filled black dots, and the base of the disk wind is indicated with two black circles. Lower right: three components of the magnetic field.

suppression of the MRI can be understood as a result of magnetic field amplification in the surface layer during the initial growth from the MRI-unstable configuration. The MRI is quenched once the field becomes too strong for MRI to operate thanks to AD. The fact that MRI is suppressed in the disk surface layer implies that the hypothesis proposed in Chapter 3 does not always hold. The main reason is likely to lie in buoyancy, which was not included in the unstratified simulations in Chapter 2. On the other hand, when AD become the dominant non-ideal MHD effect at the disk midplane, we do expect that our criterion, Equation (3-11), holds. In fact, ongoing effort by Simon et al. (in preparation) that perform stratified MRI simulations with AD is consistent with the findings in Chapter 2.

The most prominent feature of the laminar state is a strong outflow that leaves the vertical boundaries. All three components of the velocities exceed the sound speed relative to the background Keplerian flow, with the vertical component reaches about $3c_s$ at the vertical boundaries, and an outflow mass loss rate of $\rho v_z = 1.5 \times 10^{-5} \rho_0 c_s$ from each side of the simulation box. The Alfvén critical point, given by $v_z = v_{Az} = B_z/\sqrt{\rho}$, is contained within our simulation box and is indicated in the upper right panel of Figure 4.4, beyond which the gas is destined to leave the simulation box as an outflow. Moreover, according to the conventional definitions (Wardle & Koenigl 1993), we define the base of the wind at the location where the azimuthal velocity begins to super-Keplerian, and the it would become obvious later (see Figure 4.6) about this definition.

Our fiducial run OA-b5-F3 suggests the structure of the disk has a pure one-dimensional (1D) profile. To verify this result, we perform a new simulation (run S-OA-b5-F3) with everything kept the same except that the horizontal domain is reduced to $0.125H \times 0.25H$ resolved by 4×4 cells. We will refer to this type of runs as "quasi-1D" simulations. Both Ohmic resistivity and AD are turned on from the beginning. Such small box is obviously too small to study the MRI, and we find that except for different initial evolution of the orignal MRI-unstable configuration, the system relaxes to exactly the same laminar state with a strong outflow as in the fiducial run OA-b5-F3. Moreover, we have further checked that although the initial evolution involves radial and azimuthal variations, such variations vanish (to machine precision) as the system relaxes to the final steady state[2]. Therefore, we conclude that the inclusion of AD makes the disk structure purely 1D.

[2]However, if we start from a pure one-dimensional profile, the system will remain one-dimensional but does not relax to a steady state.

In brief, the inclusion of AD makes the structure of the disk completely different from the case with only Ohmic resistivity, at least in our fiducial setup (1AU with net vertical magnetic flux). The richness of the new findings deserves detailed study as we present in the next two sections. Moreover, the 1D nature of the new laminar solution allows us to perform the simulations using very small horizontal domains which saves a lot of computational cost.

4. Nature of the Laminar Wind Solution

In this section, we study in detail the wind solution from our fiducial run OA-b5-F3, focusing on the wind launching mechanism, angular momentum transport, magnetic field geometry and outflow.

4.1 Field Line Geometry and Wind Launching

We first consider the geometry of poloidal magnetic field lines, from which much insight can be gained on the wind launching mechanism. Using the magnetic field vectors from our run OA-b5-F3, we integrate a poloidal field line from the disk midplane all the way to the vertical boundary of our simulation box, and show the results in Figure 4.5. In the mean time, we overplot the direction of velocity vectors as red arrows.

The field line is straight within about $\pm 2.5H$ from the midplane due to the extremely large resistivity, where the gas and magnetic field are essentially decoupled as we discussed in the previous section. The field lines start to bend once the gas become partially coupled to the magnetic field, characterized by Ohmic as well as AD Elsasser numbers Λ and Am exceeding unity, which occurs at $z = \pm 2.3H$, as can be seen from the bottom left panel of Figure 4.4. We label this point as the launching point in Figure 4.5. Beyond this point, the azimuthal magnetic field decreases rapidly with height, creating large current density in the radial direction. Together with the vertical field, we obtain the following force balance equation in the azimuthal direction

$$B_z \frac{dB_y}{dz} - \frac{1}{2}\rho\Omega v_x = 0 \ , \tag{4-12}$$

which states that the Lorentz force is balanced by the Coriolis force. This explains the increase of radial velocity in the upper right panel of Figure 4.4 beyond about $\pm 2.5H$, as well as the direction of the arrows in Figure 4.5 at the same locations. In this region, AD is the dominant non-ideal

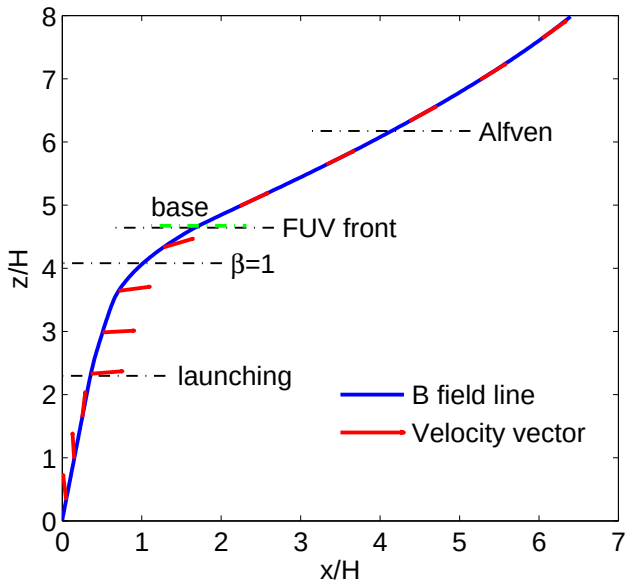


Fig. 4.5.— The poloidal field line geometry in our fiducial run OA-b5-F3 (blue solid line). Overplotted are the unit vectors of the poloidal gas velocity (red arrows). The location of the wind launching point and Alfvén point are indicated. Also marked are the point where plasma $\beta = 1$ (black dash-dotted), and the location of the base of the wind (green dashed).

MHD effect. The radial motion of the gas makes the velocity vector deviate from the direction of the magnetic field, which drags and bends the magnetic field lines towards the same direction via the ion-neutral drag. Correspondingly, $|B_x|$ increases in strength.

The field lines tend to become straight again as gas density decreases and the flow becomes magnetically dominated with total plasma $\beta < 1$. Beyond this point, the gas only has limited effect on the field line geometry. Eventually, at the base of the wind, defined as the location where the azimuthal velocity exceeds the Keplerian velocity, the magnetocentrifugal acceleration starts to operate.

We have also indicated the location of the FUV ionization front, beyond which the gas behaves more or less as ideal MHD due to the large ionization fraction. We see that the poloidal velocity of the gas is aligned with the poloidal velocity field beyond the FUV front, as expected for an ideal MHD wind. Below the FUV front, gas velocity deviates from the direction of the magnetic fields as a result of AD and Ohmic resistivity. In this fiducial run with $\beta_0 = 10^5$, the location of the FUV front overlaps with the base of the wind, which we note is just a coincidence.

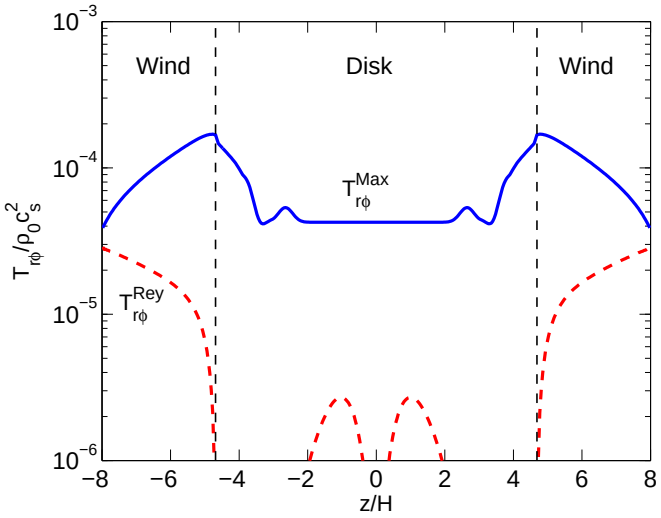


Fig. 4.6.— The vertical profiles of the $R\phi$ components of the Reynolds (red dashed) and Maxwell (blue solid) stresses in our fiducial run OA-b5-F3. The disk is divided into the wind zone and disk zone, given by $v'_\phi = v_\phi - v_K = 0$.

4.2 Angular Momentum Transport

As described in Section 4 of Chapter 1, angular momentum transport can be achieved by radial transport, due to the $R\phi$ component of the stress tensor, and by vertical transport, due to the $z\phi$ component of the stress tensor. We examine both transport mechanisms for our wind solution in this subsection.

Although the radial transport is usually a result of turbulence which gives correlated fluctuations of motion/field structure in the radial and azimuthal direction, ordered motion/field structure also produce radial transport. In Figure 4.6, we show the vertical profiles of the $R\phi$ components of the Reynolds and Maxwell stresses. Rather than a plot showing the rate of radial angular momentum transport, this Figure best demonstrates the rationality of the division of our solution into the disk zone and the wind zone: the Reynolds stress is by definition zero at the base of the wind, and dramatically increases in the wind zone as a result of radially-outward and super-Keplerian motion consequent of the magneto-centrifugal acceleration; the Maxwell stress has a prominent peak at the base of the wind, and decreases in the wind zone, as magnetic energy is converted to the kinetic energy of the outflowing gas.

We are interested in the radial angular momentum transport within the disk, hence we integrate $T_{r\phi}$ within the disk zone. Clearly, even when there is no turbulence, a non-zero Maxwell stress given by ordered magnetic fields dominates the radial transport in the disk zone. This corresponds to the undead zone scenario discussed in Turner & Sano (2008). We also see that contribution from the Reynolds stress is completely negligible. Integrating the Maxwell stress across the disk zone, we find $\alpha_{\rm Max} \approx 2.3 \times 10^{-4}$.

For the vertical transport, we need to measure the $z\phi$ component of the stress tensor $T_{z\phi}$ at the base of the wind. Here the definition of the wind base again exhibits its advantages: by definition, Reynolds stress is zero, and one only needs to consider the Maxwell stress, which we find is $T_{z\phi} \approx 1.1 \times 10^{-4}$. Hereafter, we refer to the $z\phi$ component of the Maxwell stress at the base of the wind to as "wind stress". We note that since $T_{z\phi}^{\rm Max} = -B_z B_\phi$ where B_z is constant, from Figure 4.4 we see that $T_{z\phi}^{\rm Max}$ varies smoothly within the disk should peak between $z = \pm 2.5H$. Although wind stress eventually drives accretion, the "decretion" to bend magnetic field lines for magneto-centrifugal acceleration (between the launching point and the wind base, discussed in the previous subsection) compromises the wind-driven accretion in the disk zone. This fact further justifies our choice to measure the Maxwell stress at the base of the wind rather than other locations.

The total rate of angular momentum transport, assuming steady-state accretion in the disk zone, can be obtained by combining equations (1-27) and (1-28), which gives

$$\dot{M} = \frac{2\pi}{\Omega} \int_{-z_b}^{z_b} dz T_{R\phi} + \frac{4\pi}{\Omega} R T_{z\phi} \Big|_{-z_b}^{z_b} = \frac{2\pi}{\Omega} \alpha_{\rm Max} c_s^2 \Sigma + \frac{8\pi}{\Omega} R |T_{z\phi}|_{z_b} \ , \tag{4-13}$$

where z_b denotes the vertical height at the base of the wind. Applying the MMSN disk model, we further obtain

$$\dot{M}_{-8} \approx 0.82 \frac{\alpha_{\rm Max}}{10^{-3}} R_{\rm AU}^{-1/2} + 4.1 \frac{|T_{z\phi}|_{z_b}}{10^{-4} \rho_0 c_s^2} R_{\rm AU}^{-3/4} \ , \tag{4-14}$$

where $\dot{M}_{-8}$ is the accretion rate measured in $10^{-8} M_\odot$ yr^{-1}. We see that the radial transport by the Maxwell stress at the bulk of the disk can drive the accretion for about $2 \times 10^{-9} M_\odot$ yr^{-1}, too small to account for the typical accretion rate for PPDs. The accretion driven by wind transport, on the other hand, reaches $5 \times 10^{-8} M_\odot$ yr^{-1}, which is sufficient to account for the observed accretion rate for most PPDs.

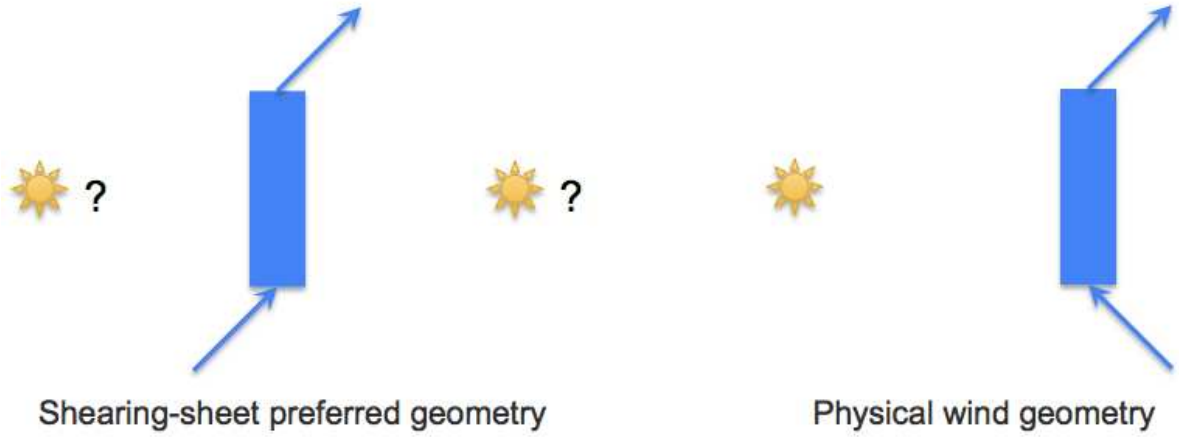


Fig. 4.7.— Cartoon illustration of the geometry of wind magnetic field lines in shearing-box simulations. The shearing-box approximation ignores all radial gradients (except the shear), hence does not contain information about the location of the central object. The natural wind geometry launched from shearing-box has the "odd-z" symmetry where the field lines on the top and bottom of the box bend toward opposite directions (left). In a physical situation, where the location of the star is fixed, the field lines on the top and bottom sides of the box should bend to the same direction away from the star.

4.3 Symmetry and Strong Current Layer

The previous subsection demonstrates the success of wind scenario as the the driving force of disk accretion. However, one problem was ignored in the previous discussion. The laminar wind solution obtained obeys the "odd-z" symmetry:

$$\begin{aligned} B_x(z) = B_x(-z)\ , \quad B_y(z) = B_y(-z)\ , \quad B_z(z) = B_z(-z)\ , \\ v_x(z) = -v_x(-z)\ , \quad v_y(z) = -v_y(-z)\ , \quad v_z(z) = -v_z(-z)\ . \end{aligned} \tag{4-15}$$

As a result, the wind field lines on the top and bottom sides of our simulation box bend to opposite radial and toroidal directions, as illustrated on the left of the Cartoon picture in Figure 4.7. However, physically, one expects the field lines on the top and bottom sides of the box to bend toward the same direction, pointing away from the central star, as illustrated on the right of Figure 4.7. A particularly disturbing fact is that in the case with odd-z symmetry, the "wind" does not transport angular momentum, since $T_{z\phi}$ at the top and bottom sides of the disk have the same value, and cancel out. The wind angular momentum transport mechanism works only for the physical wind geometry.

We note that all radial gradients except the azimuthal shear are neglected in the shearing-box approximation, hence one can not tell whether the location of the central star is in the "inner" or "outer" (radial) side of the box. In other words, the two radial sides of the box are symmetric. In our simulations, we find that the direction that the wind field lines bend as we start from the initial configuration is totally random, and the top and bottom sides of the disk evolve independently[3]. This suggests that the chances to find a solution with the unphysical odd-z symmetry and a physical geometry are equal. In fact, our 1D run S-OA-b5-F3 results in a solution with the physical geometry.

In Figure 4.8, we show the profiles of the magnetic field and velocity field from our run S-OA-b5-F3 that have the physical wind geometry. We see that this physical solution is NOT a solution under the "even-z" symmetry:

$$\begin{aligned} B_x(z) = -B_x(-z)\ , \quad B_y(z) = -B_y(-z)\ , \quad B_z(z) = B_z(-z)\ , \\ v_x(z) = v_x(-z)\ , \quad v_y(z) = v_y(-z)\ , \quad v_z(z) = -v_z(-z)\ , \end{aligned} \tag{4-16}$$

which is almost exclusively used for constructing semi-analytical local wind solutions (Wardle & Koenigl 1993; Ogilvie & Livio 2001; Königl et al. 2010; Salmeron et al. 2011). Very interestingly, the physical wind solution follows exactly the odd-z symmetry solution we obtained before, but the horizontal field lines (and horizontal velocities) are flipped at one side of the box to achieve the physical wind geometry. This flipping is mediated by a sharp transition of the horizontal fields, which exhibits as a strong current layer. The strong current layer is not located at the midplane, but is located at about $z = +3H$ (or at $z = -3H$, and the selection is random). Therefore, the physical solution does not have any symmetry about the disk midplane.

The location of the strong current layer roughly corresponds to where both the Ohmic and AD Elsasser numbers Λ and Am become greater than 1, as seen from the bottom left panel of Figure 4.4. The reason for such large offset from the disk midplane as one might naively imagine from an aesthetic point of view is that magnetic diffusion near the disk midplane is so strong that the gas and magnetic field are essentially decoupled. Correspondingly, the magnetic field lines must be straight and current is excluded, and the strong current layer can exist only when magnetic diffusion becomes weaker.

[3]We have performed more than one copies of each 3D and the quasi-1D fiducial simulations that verifies the randomness.

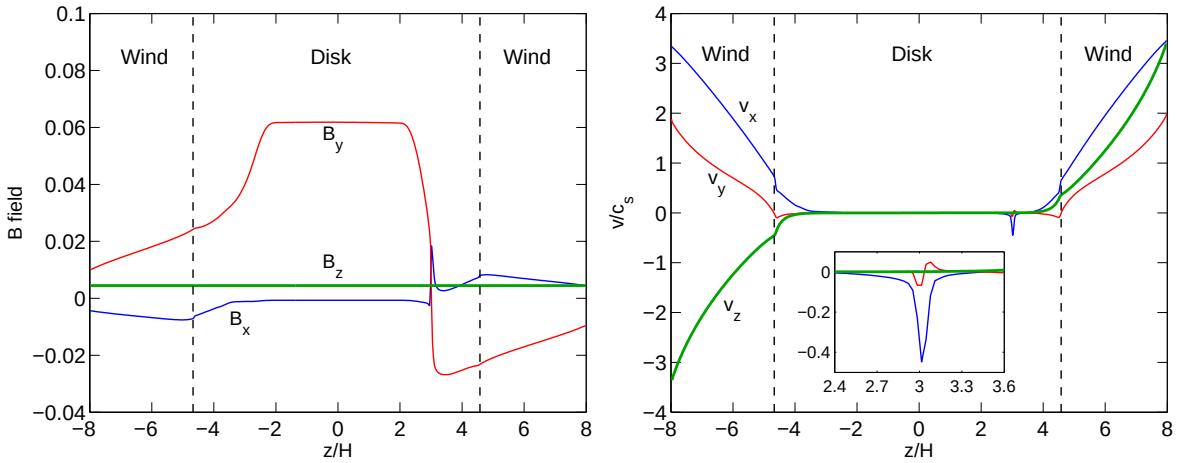


Fig. 4.8.— The vertical profiles of the magnetic fields (left) and velocities (right) in the laminar solution that has the physical wind symmetry. The inset on the right panel shows the zoomed-in view of the velocity profiles at the strong current layer.

The right panel of Figure 4.8 demonstrates the velocity profile of the physical wind solution. The strong current layer exhibits as a seemingly small feature at about $z = +3H$ in this plot, which is in linear scale. As we zoom into this region as shown in the inset, we find that the gas has a large inflow velocity of about $0.3c_s$ at the location of the strong current layer. The large inflow is directly the consequence of the wind stress: the Maxwell stress exerted at the base of the wind is released at the strong current layer, driving a large inflow which is essentially how accretion proceeds. More specifically, it is the balance between the Lorentz force and Coriolis force that leads to the large inflow and accretion in the strong current layer (see equation 4-12).

To further demonstrate the effectiveness of accretion in the current layer, we note that for a MMSN disk, in order to have accretion to approach $10^{-8}M_\odot$ yr^{-1}, a bulk radial drift velocity of about $10^{-5}c_s$ is required

$$\dot{M}_{-8} \approx 0.5\left(\frac{v_r}{10^{-5}c_s}\right)R_{\rm AU}^{-3/4}\ . \tag{4-17}$$

In the physical wind solution, we find that only a tiny fraction (about $\sim 4\times10^{-4}$) of disk mass is contained in the strong current layer, but it drifts at very large velocities ($\sim 0.3c_s$). The combined effect is an efficient accretion that easily accounts for the typical accretion rates observed for PPDs.

Finally, we note that the strong current layer is not a thin current sheet, since at its location there is still substantial magnetic diffusion (mainly AD). It has a thickness of about $0.2H$, which is well resolved in about 6 cells in our quasi-1D simulations. We have found that the strong current

layer is stable in our quasi-1D fiducial run S-OA-b5-F3. The stability of the strong current layer in 3D requires justification in the more geometrically appropriate global simulations[4].

4.4 Outflow

Strong outflows are launched in our fiducial simulations, and we have measured that the rate of mass outflow from each side of the box is about $1.4 \times 10^{-5}\rho_0 c_s$ from the quasi-1D run and $1.5 \times 10^{-5}\rho_0 c_s$ from the 3D run. Although mass loss is not significant for the duration of our simulations, the value is relatively high that without replenishing to the disk, the mass loss timescale is only $8 \times 10^4 \Omega^{-1}$, which amounts to only about 10^4 years. Moreover, the measured wind mass loss rate is in fact comparable to the mass accretion rate driven by the wind itself, which is inconsistent with the observationally inferred ratio that the mass loss rate is only about 10% of the accretion rate.

We note that, however, the magneto-centrifugal wind is intrinsically a global phenomenon. A global wind solution is not fully determined until all critical points (or surfaces), namely, the slow magnetosonic, Alfvén and fast magnetosonic points are passed, where the fast magnetosonic point is far beyond the extent of our simulation box. Meanwhile, the nature of the wind solution, and the location of the critical points, is set by the interplay between wind launching region in the disk, and the large-scale field structure (i.e., the magnetic flux distribution over the entire disk), where the latter is not reflected in a local simulation as in the shearing-box. Therefore, while useful for studying wind-launching, the shearing-box approximation has its limitations and the measured rate of outflow from our simulations should only be taken as reference values and may significantly overestimate the mass outflow rate in reality.

To further clarify the discussion above, we perform two additional quasi-1D simulations, changing the vertical size of our simulation box to be $12H$ and $20H$ respectively, and the two runs are labeled as S-OA-b5-F3-12H and S-OA-b5-F3-20H. We measure a series of quantities discussed before from these runs and list the results in Table 4.2. We find that as we increase the height

[4]We have repeated our fiducial run OA-b5-F3 with a different random seed which evolves to a physical wind solution with a strong current layer. We find that the strong current layer is maintained for about 100 orbits but eventually escapes the simulation box and the odd-z symmetry is recovered. This is likely to be due to the intrinsic limitations of the shearing-box, where curvature terms are neglected and hence favors the odd-z symmetry solution. Moreover, as the fast magnetosonic point is beyond our simulation box, the stability of the strong current layer can also be affected from outside of the simulation domain.

of our simulation box, the location of the Alfvén point moves to higher altitudes. In the mean time, the mass loss rate decreases. In fact, these two quantities are connected, and in a *global* magneto-centrifugal wind, one has for the ratio of mass loss and mass accretion rates (Pelletier & Pudritz 1992)

$$\frac{\dot{M}_w}{\dot{M}_a} \approx \left(\frac{R_A}{R_0}\right)^2 , \tag{4-18}$$

where R_A and R_0 are the Alfvén radius and the wind launching radius. Under the local shearing-sheet approximation, although there is no such simple analytical relation, the physics remains similar: higher location of the Alfvén point corresponds to larger R_A (although the exact value is still unknown since R_0 is not specified in shearing-box). Therefore, we expect smaller mass loss rate for higher Alfvén point.

The trend of deceasing mass outflow rate with vertical box size reflects one limitation to shearing-box: the gravitational potential increases quadratically with vertical height, hence no flow can really escape. Th outflow in our simulations is possible because gravitational potential is cut off at the vertical boundaries. In reality, the escape velocity is of the order the Keplerian velocity, and is achieved when $z \sim R$, hence the vertical gravitational potential ought to be truncated at $z \sim R$. Therefore, it would probably be more realistic to adopt a box size of $L_z = 2R$. In MMSN, we have $H/R \sim 0.03$ at 1 AU[5], which would need much taller simulation box, hence would result in much smaller mass loss rate, avoiding the problem with fast mass loss rate obtained in our fiducial simulation.

It is also interesting to note that although mass outflow is largely affected by the vertical box size, the angular momentum transport depends on the vertical box size very weakly. For box sizes of $12H$, $16H$ and $20H$, the value of $T_{z\phi}^{\rm Max}$ at the base of wind equals 0.97×10^{-4}, 1.06×10^{-4} and 1.13×10^{-4} respectively, hence increasing box size leads to slightly stronger wind-driven accretion. In sum, the trend that the mass outflow rate decreases with box size and mass accretion rate increases with box size implies that in a real system, the ratio of mass accretion rate to mass loss rate would be a factor of several larger than that obtained in our simulations, and would be more consistent with observations.

[5]We note that the ratio H/R is unspecified in shearing-box.

4.5 Energetics

Although our simulations assume an isothermal equation of state, hence energy is not conserved, it is important to verify that our simulation results are energetically feasible and also to examine the energy balance for real situations.

In shearing-box simulations, the energy is injected due to the work done by the shearing-box boundaries, given by

$$P_{\rm sh} = -\frac{1}{L_x L_y}\int \frac{3}{2}\langle B_x B_y\rangle \Omega L_x dy dz = \frac{3}{2}\Sigma c_s^2 \Omega \alpha_{\rm Max} \ . \tag{4-19}$$

Energy is lost through the open vertical boundaries, given by

$$\dot{E} = \dot{E}_K + \dot{E}_P = \left[\rho\left(\frac{v^2}{2}+c_s^2\right)\boldsymbol{v} - (\boldsymbol{v}\times\boldsymbol{B})\times\boldsymbol{B}\right]\cdot\boldsymbol{n}\Big|_{\rm top+bot} \ , \tag{4-20}$$

where $\boldsymbol{n}$ is the unit vector pointing away from the disk in the vertical direction, and we sum over contributions from the top and bottom vertical boundaries. The first terms in the bracket represent the kinetic energy loss and the PdV work done by the mass outflow, and the second term represents energy loss from the Poynting flux. We have ignored the energy loss term associated with internal energy loss due to the mass outflow, since we keep feeding mass to the system which balances this term exactly.

In Table 4.2 we also list the values of $P_{\rm sh}$, $\dot{E}_K$ and $\dot{E}_P$, normalized in natural units. We see that the sum of $\dot{E}_K$ and $\dot{E}_P$ comprises of about 60% of the total work done by the shear $P_{\rm sh}$, hence energy conservation is not violated. The extra energy is likely to be radiated away in real systems.

5. Parameter Study

To assess the importance of various physical effects on the properties of the laminar wind solution, we conduct a parameter study by surveying three parameters and compare the results from our fiducial model. All simulations in this parameter study are quasi-1D. First, we vary the vertical net magnetic flux, and consider $\beta_0 = 10^3$, 10^4 and 10^6. These runs are labeled as S-OA-bn-F3, where bn denotes $\beta = 10^n$. Second, we vary the penetration depth of the FUV ionization, and consider $\Sigma_{\rm FUV} = 0.01$ g cm^{-2} and 0.1 g cm^{-2}, and the runs labels are attached with "F1" and "F10" respectively. Finally, we consider the effect of grain abundance, and consider the case with grain-free chemistry (whose run label is attached with "nogr") and the case with

Table 4.2: Summary of all simulations with a laminar wind.

Run	$\alpha_{\rm Max}$	$T_{z\phi}^{\rm Max}$	$\dot{M}_w$	z_b	$z_{\rm A}$	$P_{\rm sh}$	$\dot{E}_P$	$\dot{E}_K$
OA-b5-F3	2.3×10^{-4}	1.1×10^{-4}	3.1×10^{-5}	4.7	6.1	1.9×10^{-3}	7.7×10^{-4}	4.4×10^{-4}
S-OA-b3-F3	1.2×10^{-2}	3.4×10^{-3}	4.8×10^{-4}	4.0	-	6.9×10^{-2}	4.3×10^{-3}	3.5×10^{-2}
S-OA-b4-F3	1.3×10^{-3}	5.9×10^{-4}	8.7×10^{-5}	3.9	7.5	9.3×10^{-3}	2.4×10^{-3}	3.3×10^{-3}
S-OA-b5-F1	1.9×10^{-4}	9.2×10^{-5}	1.6×10^{-5}	4.2	7.1	1.6×10^{-3}	6.1×10^{-4}	2.8×10^{-4}
S-OA-b5-F3	2.4×10^{-4}	1.1×10^{-4}	2.9×10^{-5}	4.6	6.2	2.0×10^{-3}	8.0×10^{-4}	4.0×10^{-4}
S-OA-b5-F10	1.6×10^{-4}	1.7×10^{-4}	5.3×10^{-5}	4.2	5.5	2.6×10^{-3}	1.1×10^{-3}	5.4×10^{-4}
S-OA-b6-F3	3.0×10^{-5}	2.9×10^{-5}	1.0×10^{-5}	4.5	5.5	4.6×10^{-4}	2.1×10^{-4}	4.2×10^{-5}
S-OA-b5-F3-12H	2.1×10^{-4}	9.7×10^{-5}	4.1×10^{-5}	4.4	5.3	1.3×10^{-3}	4.6×10^{-4}	2.3×10^{-4}
S-OA-b5-F3-20H	2.6×10^{-4}	1.1×10^{-4}	2.2×10^{-5}	4.7	7.1	2.8×10^{-3}	1.2×10^{-3}	5.3×10^{-4}
S-OA-b5-gr01-F3	1.3×10^{-4}	1.0×10^{-4}	2.7×10^{-5}	4.6	6.3	1.6×10^{-3}	7.8×10^{-4}	3.9×10^{-4}
S-OA-b5-nogr-F3	5.0×10^{-4}	1.2×10^{-4}	3.8×10^{-5}	4.9	5.9	2.9×10^{-3}	9.0×10^{-4}	4.6×10^{-4}

MMSN disk model at 1AU, uniformly mixed 0.1μm grains are assumed for all runs. The $r\phi$ component of the Maxwell stress, parameterized by $\alpha_{\rm Max}$ is measured in regions within the disk zone $-z_b < z < z_b$, the Maxwell component of the $z\phi$ stress $T_{z\phi}^{\rm Max}$ are measured at the base of the wind $z = \pm z_b$. Energy loss rates $\dot{E}_P$ and $\dot{E}_K$ are measured at the vertical boundaries (and take the sum).

grain abundance $\epsilon_{\rm gr} = 10^{-3}$ (run label attached with "gr01", indicating depletion factor of 0.1), 10 times the value in our fiducial run. A list of all these runs are given in Table 4.1.

All the additional quasi-1D simulations are run to $t = 1200\Omega^{-1}$. We extract the vertical profiles near the end of the runs and perform the same analysis as we did for the fiducial run. In particular, we identify the locations of the base of the wind, the Alfvén point, the $r\phi$ component of the Maxwell stress in the wind zone, the $z\phi$ component of the Maxwell stress at the base of the wind, and so on. The results of these measurements are listed in Table 4.2. Before discussing these physical effects in details, we further plot in Figure 4.9 the rate of mass outflow and the wind stress (the $z\phi$ component of the Maxwell stress measured at the base of the wind) as a function of net vertical field strength.

5.1 Effect of Net Vertical Magnetic Flux

The vertical net magnetic field is a crucial ingredient to launch a magnetic outflow. It allows the field lines to be connected to infinity, paving way for the outflow to escape from the disk. We see from Figure 4.9 that the rate of mass outflow $\dot{M}_w$ increases rapidly with increasing net vertical

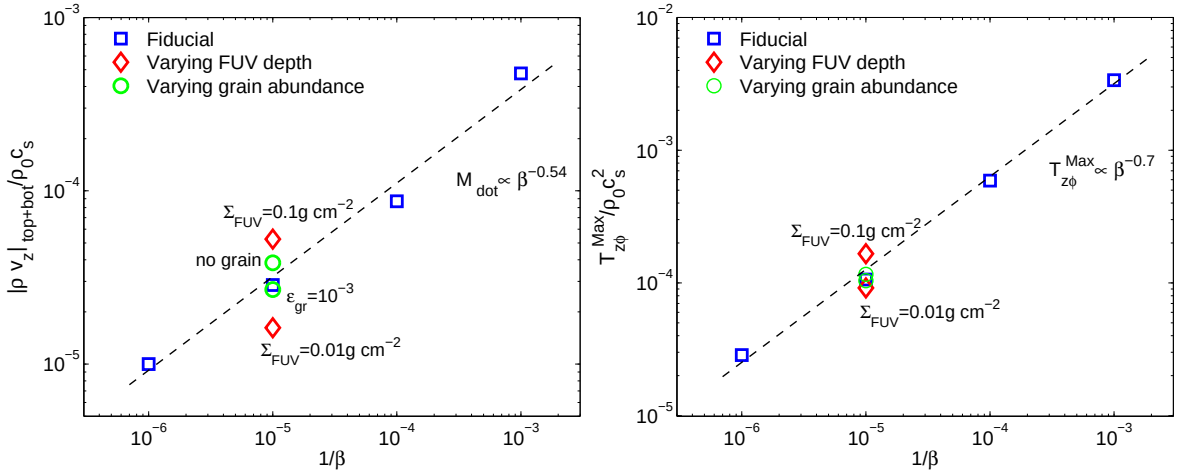


Fig. 4.9.— The rate of mass outflow (left) and the $z\phi$ component of the Maxwell stress at the base of the wind (right) as a function of vertical net field strength, indicated as $1/\beta_0$ for all our simulation runs. Particularly, blue squares represent simulations with varying vertical field strength, red diamonds represent simulations with varying FUV penetration depth, and green circles represent simulations with varying grain abundance.

field. A fit to the scattered plot gives $\dot{M}_w \propto \beta_0^{-0.54}$. In other words, we roughly have $\dot{M}_w \propto B_z$. This result is consistent with the ideal MHD shearing-box simulations by Suzuki & Inutsuka (2009), as well as more recently by Bai & Stone (2012a). Although the wind launching is associated with vigorous MRI turbulence in ideal MHD, the scaling of the mass loss rate with vertical background magnetic field is very similar.

On the right panel of Figure 4.9, we see that the rate of angular momentum transport, characterized by the wind stress, increases even more rapidly with background vertical field strength. A simple fit returns $T_{z\phi}^{\rm Max} \propto \beta_0^{-0.7}$. Therefore, increasing vertical net field reduces the ratio of $\dot{M}_w/\dot{M}_a$. This is accompanied by the outward shift of the location of the Alfvén point with increasing net vertical flux, and for $\beta_0 = 10^3$, the Alfvén point is beyond our simulation box. On the other hand, the location of the base of the wind remains more or less unchanged as vertical net flux varies. We also note for relatively large vertical net flux of $\beta_0 = 10^3$, the wind-driven accretion rate (Equation 4-14) would become too large compared with observations. Therefore, a reasonable wind-driven scenario in PPDs should involve only weak vertical background field with β_0 of the order 10^6 to a few times 10^4.

Increasing the net vertical field also leads to rapid increase in the midplane magnetic field (undead zone), which leads to larger $\alpha_{\rm Max}$. Applying Equation (4-14), we find the radial transport remains to play a minor role to the total accretion rate for all value of β_0 explored so far, but its contribution increases with increasing net flux.

Finally, we find that for relatively strong net vertical field with $\beta_0 \lesssim 10^4$, it is less likely to obtain a laminar solution with the physical wind geometry: the strong current layer would escape from our simulation box and one recovers the undesired solution with odd-z symmetry. This observation may suggest that maintaining the stability of the strong current layer becomes more difficult for larger field strength, although the issue can only be fully resolved by performing global simulations.

5.2 Effect of FUV Ionization

The FUV ionization is another crucial ingredient of wind launching: the large ionization fraction in the FUV layer makes the gas and magnetic field be strongly coupled to each other so that it is essentially in the ideal MHD regime. The strong coupling between the gas and magnetic field is essential for effectively loading mass onto open magnetic field lines for magneto-centrifugal acceleration. Therefore, we expect the rate of mass outflow to strongly depend on the penetration depth of the FUV ionization. Indeed, we see from Figure 4.9 that increasing $\Sigma_{\rm FUV}$ by a factor of 10 results in a factor of more than 3 increase of the mass outflow rate. Meanwhile, increasing $\Sigma_{\rm FUV}$ also leads to a moderate increase of the wind stress, as seen on the right panel of Figure 4.9. Correspondingly, the ratio of $\dot{M}_w/\dot{M}_a$ increases with $\Sigma_{\rm FUV}$, in parallel with the lowering of the the Alfvén point.

5.3 Effect of Grain Abundance

In the MRI-driven accretion scenario, we have seen that the predicted accretion rate sensitively depends on the size and abundance of grains. In the wind-driven accretion scenario, we find that the dependence on grains is much weaker. For the outflow rate, there is only a 50% difference between the grain-free chemistry and the case with 0.1μm grains with the abundance of 10^{-4}. The wind stress, on the other hand, is almost independent of grain abundance. The weak dependence on the grain abundance is mainly due to the fact that the wind launching process mainly depends

on the gas dynamics in the surface layer of the disk, where either the FUV ionization dominates (which is independent of grain abundance), or the long recombination time in the low gas density leads to large ionization fraction that well exceeds the grain abundance (hence grains have only very limited effect on the ionization level, see Figure 3.1 in Chapter 3). The grain abundance does have a strong effect on the radial transport, as we see from Table 4.2 that $\alpha_{\rm Max}$ increases relatively rapidly with decreasing grain abundance. Nevertheless, the overall picture is unchanged since radial transport only plays a minor role in driving disk accretion.

6. Summary and Discussions

In this Chapter, we have performed three-dimensional shearing-box simulations to study the gas dynamics in the inner region of a PPD (at 1 AU). Non-ideal MHD effects, namely the Ohmic resistivity, Hall effect and ambipolar diffusion (AD) are crucial in the weakly ionized gas as in PPDs. They affect the coupling between the gas and magnetic field in different ways and dramatically change the MHD stability of the system. Particularly, Ohmic resistivity dominates in the midplane region while AD dominates in the disk surface layer, and the Hall dominated regime lies in between. For the first time, we have included both Ohmic resistivity and AD in our vertically stratified simulations. The diffusion coefficients are obtained self-consistently by interpolating from a pre-computed look-up table (as a function of density and ionization rate at fixed temperature) based on equilibrium chemistry. We have included a weak vertical net magnetic field in all our simulations. Surprisingly, we find that the inclusion of AD makes a dramatic difference in the gas dynamics of PPDs: instead of having the classical layered accretion scenario with strong MRI turbulence in the surface layer and a quiescent midplane "dead" zone (which takes into account only the Ohmic resistivity), we find that the MRI is suppressed in the entire disk and the flow is completely laminar. In the mean time, the disk launches a strong outflow, which is accelerated to super-Alfvénic velocities within our simulation domain. The outflow is launched from the large vertical gradient of the azimuthal magnetic field which results in the bending of poloidal field lines to achieve the required angle for magneto-centrifugal acceleration. The smooth version of our solution has an odd-z symmetry about the midplane with field lines at two sides of the disk bending toward opposite directions and does not transport angular momentum. For our laminar wind solution to be physical, the horizontal field on one side of the disk must flip, which creates a strong current layer within the disk zone. The strong current layer is offset with disk midplane

(due to the large resistivity at midplane). It receives most of the wind stress and carries the entire accretion flow.

The magneto-centrifugal wind (MCW) scenario found in our simulations has a number of important advantages. In Section 6.1, we summarize the conditions to launch the laminar MCW and conclude that the launching mechanism is robust and is very likely to operate in the inner region of PPDs around 1 AU. This is consistent with the observational fact that the low velocity component of the outflow from young stellar objects is likely to originate from the inner region of PPDs (see Section 1.8 of Chapter 1). In Section 6.2, we compare our wind solution with the classical wind launching solution and show that different symmetries in the two solutions lead to crucial differences in their properties, and our solution makes wind launching much easier, while avoids the potential problem with having the rate of outflow being too large. In Section 6.3, we discuss the physical implication of our new MCW scenario, particularly on its importance on the angular momentum transport in PPDs and planetesimal formation. Finally, we discuss the open issues in Section 6.4 and conclude this chapter.

6.1 Conditions to Launch the Laminar Wind

Summarizing the results from the discussions throughout this paper, we identify the following criteria for launching a laminar magneto-centrifugal wind from PPDs.

- Presence of weak vertical net magnetic flux, which connects the disk field lines to infinity. The strength of the net vertical field determines the effectiveness of the wind transport, and weak field with $\beta_0 \sim 10^5$ is preferred to match the observed accretion rate in PPDs. Although there is no proof for the existence of such a vertical net field, a situation with absolutely zero vertical net field would be very unnatural.

- An Ohmic resistivity dominated midplane layer, which suppresses the MRI near the disk midplane. This condition is always met in the inner region of PPDs, as we have seen in Chapter 3. In the outer disk, AD dominates the entire disk, and MRI is likely to operate once an appropriate vertical net magnetic field is present. Although launching a wind is still likely as a result of the net vertical flux, the wind can not be laminar.

- An ambipolar diffusion dominated disk surface layer, which suppresses the MRI at the disk surface layer. This condition is always met at any location of PPDs as the low density region

is always AD dominated. Rather than self-sustained MRI turbulence, the MRI in vertically stratified disk with strong AD tends to over-amplify the field that eventually quenches itself.

- Strong FUV ionization, which is essential for mass loading from the disk to the magneto-centrifugal wind. As the FUV ionization results in an approximately fixed ionization fraction of the order 10^{-5}, it is effective only in the inner region of PPDs, as can be inferred from Equation (1-20) in Chapter 1. At 100 AU, the AD Elsasser number Am in the FUV layer would be of the order 10 or less, making it difficult to launch a magneto-centrifugal wind.

It is certain that the inner region of PPDs, around 1 AU, easily satisfies all of the above conditions, while the AD dominated outer disk does not due to the small Ohmic resistivity and weak FUV ionization. Work is in progress in locating the boundary between the laminar regions with wind-driven accretion, and the turbulent regions with the MRI-driven accretion.

6.2 Comparison with Wardle & Koenigl (1993)

The conventional scenario of launching a magneto-centrifugal wind was originally proposed by Wardle & Koenigl (1993) (hereafter WK93)[6]. As naturally expected from the physical wind geometry, an even-z symmetry (4-16) is assumed where the magnetic field in the midplane is purely vertical. WK93 considered the pure effect of AD and obtained families of solutions parameterized mainly by three parameters: Am (taken to be spatially constant), β_0 (at disk midplane), and $\epsilon \equiv v_{r0}/c_s$, where v_{r0} is the radial drift velocity at disk midplane, a free parameter in the for local shearing-sheet treatment. The typical solution obtained by WK93 involves three regions: a hydrostatic region near the disk midplane where the gas drifts inward due to the wind stress exerted above, a transition zone where the inflow gradually diminishes, and an outflow region where the flow is magneto-centrifugally accelerated. It was found that launching the MCW generally requires

$$\sqrt{1/(2Am)} \lesssim \beta_0^{-1} \lesssim 2 \lesssim \epsilon Am \ , \quad Am > 1 \ . \tag{4-21}$$

Judging from the above inequalities we find that for Am of the order $1-10$, typical for in PPDs at 1-10 AU, launching the wind requires $\epsilon \gtrsim 0.2$, and $\beta_0 \sim 2-4$. Such values of ϵ would result in extremely large accretion rate for a MMSN disk (see Equation 4-17). More recent works by Königl

[6]The idea of magneto-centrifugal wind driven accretion in PPDs was proposed much earlier (Pudritz & Norman 1983), but the wind launching problem was not properly addressed until WK93.

et al. (2010) and Salmeron et al. (2011) generalized the above criteria to include the Hall effect, while the generalized solutions share the basic properties. Combet & Ferreira (2008) applied the wind solution to construct global models of PPDs. The resulting disk structure involves a very thin inner disk with surface density of the order 10^3 smaller than the standard scenarios, but the strong depletion of the inner disk makes it difficult to match the SED observation data and the observed accretion rate simultaneously.

The wind launching criteria (4-21) derived in WK93 makes explicit use of the assumption of even-z symmetry, which does not apply for our new laminar wind solution with an odd-z symmetry. As we have seen in the previous subsection, the list of our wind launching criteria differs substantially from that in WK93. In particular, a weak vertical magnetic field well below equipartition strength is sufficient to launch the MCW in our scenario, while the WK93 solution would become unstable to the MRI for relatively weak vertical field. The launching mechanism in our MCW scenario also differs from that in WK93, as we have already explained in Section 4. Also, most of the gas in our MCW scenario stays static rather than having large radial drift velocities. Only a tiny fraction of the gas drift inward at large velocities that converts the wind stress into accretion power. This allows the inner disk to retain large surface densities and thickness to be consistent with the SED observations.

6.3 Implications

The fact that the inner PPDs is likely to be laminar with pure wind-driven accretion processing through a strong current layer offset from the disk midplane may have profound implications on many aspects of planet formation, particularly on the following two aspects.

The laminar inner disk is likely to become the mostly favored spot for grain growth, settling and planetesimal formation. In the conventional picture of layered accretion, the Ohmic dead zone region is found to be not completely static, but has random motion due to the sound waves shooting from the active layers (Fleming & Stone 2003; Oishi & Mac Low 2009; Turner et al. 2010; Okuzumi & Hirose 2011). The level of the random motion, albeit much smaller than that in the conventional active layers, can still be large enough to prevent the solids from settling completely. The random gas velocities also tend to dominate the collision velocity between dust grains that would impede grain growth. In particular, Okuzumi & Hirose (2012) found that increasing the vertical net magnetic flux strongly increases the level of random gas motion in the midplane hence

greatly reduces the maximum grain size achievable from grain growth, which would tremendously impede planetesimal formation (Bai & Stone 2010b). In our laminar wind solution, the disk midplane is essentially completely static. This provides the best environment for grain growth and settling, and is ideal for planetesimal formation either via the streaming instability mechanism (Johansen et al. 2009b; Bai & Stone 2010b), or the gravitational instability mechanism (Lee et al. 2010; Youdin 2011).

The efficient wind-driven accretion through the inner disk would change our understanding about the global evolution of PPDs. As introduced in Section 5 of Chapter 1, most current models on the long-term evolution of PPDs adopt a phenomenological approach that treats the disk physics very roughly. In particular, under the framework of layered accretion in the inner disk, the presence of the dead zone often leads to inefficient accretion and pile-up of mass. The pile-up gradually leads to gravitational instability which eventually drain most of the inner disk material onto the star, starting a new cycle. In the mean time, zero vertical net-flux global simulations by Dzyurkevich et al. (2010) found that the inner edge of the dead zone is likely to become a local pressure maxima which serves to trap solids. In reality, when more microphysics of the disk is taken into account, we see that as disk wind can be much more efficient in driving disk accretion at the location of the conventional dead zones, mass pile-up and building up a local pressure maxima can be completely avoided. What determines the surface density profile of the disk is the spatial distribution of the magnetic flux, rather than the grain abundance, etc. Although there is little knowledge on the magnetic flux distribution, attention should be drawn to re-consider the structure and evolution of the PPDs focusing more on the large-scale magnetic fields.

6.4 Open Issues

We have neglected the Hall effect in our calculation, which also plays an important role in the gas dynamics in PPDs. In the bottom left panel of Figure 4.4, we also show the profile of the Hall Elsasser number for our laminar wind solution. We see that the Hall effect at least dominates between $z = 2H$ and $3H$ (within $z = \pm 2H$, a floor is added to Ohmic resistivity and AD, but not to the Hall term since it is not included in the computation). At this location, we have $Ha \sim 0.1$, $\beta \sim 10$, and the azimuthal magnetic field dominates the vertical field. We note that for the Hall MRI, the stability depends on the sign of vertical magnetic field, while for Ohmic resistivity and AD, stability is independent of the sign of B_z. We expect the magnetic configuration in our

laminar wind solution to be stable to the Hall MRI when B_z is negative, in which case we expect the magnetic configuration to be adjusted to account for the Hall effect. For positive B_z, our laminar solution may become unstable to the Hall MRI according to the calculations by Pandey & Wardle (2012), but the unstable wavelength may well exceed H due to the small value of plasma β. Moreover, as vertical stratification is not included in their calculation, it is uncertain whether the disk would eventually relax to another laminar configuration or lead to sustained MRI turbulence, especially given the experience in this work that an initially MRI unstable disk evolves into a laminar configuration in non-linear simulations.

The magneto-centrifugal wind is intrinsically a global phenomenon. As we have discussed before, uncertainties remains in our local shearing-box simulations regarding problems with the stability of the strong current layer, the mass loss rate, and the rate of wind-driven angular momentum transport. Moreover, we have only studied the gas dynamics for a MMSN disk at 1 AU, it is yet to conduct the same study at other disk locations to study how the wind properties depend on the radius. Our analysis in Section 6.1, together with the optimistic estimate in Chapter 3 both imply that MRI is likely to be the dominant mechanism for angular momentum transport at the outer disk. Here, another interesting problem arises on how the transition occurs from a pure laminar wind-driven accretion region to a turbulent MRI-driven accretion region. Global simulations are essential to resolve the problems and uncertainties mentioned above, and are the ultimate way towards fully understanding the accretion processes in PPDs.

Chapter 5

Conclusions and Outlook

This thesis studies the gas dynamics in protoplanetary disks (PPDs) with focus on the role of magnetic fields, which is most likely responsible for driving disk accretion for the most regions of PPDs and most of the PPD lifetimes. We first complemented the literature of the MRI by studying the effect of ambipolar diffusion (AD) on the non-linear saturation of the MRI. The results, together with studies on other non-ideal MHD effects (Ohmic resistivity and the Hall effect) on the MRI in the literature, are applied to PPD models to examine the effectiveness of the MRI in driving accretion in PPDs. Finally, we perform the most realistic local shearing-box simulations that for the first time, take into account both Ohmic resistivity and AD. We summarize the major conclusions from these studies as follows in Section 1 and, combining the results, we propose a new scenario for the accretion process in PPDs in Section 2. Future directions are discussed in Section 3.

1. Major Achievements

1.1 Properties of the MRI in the AD Dominated Regime

We have performed shearing-box simulations of the MRI with AD in the strong-coupling (single-fluid) limit which is appropriate for PPDs, with a complete scan of parameters with different magnetic field geometries. The simulation results are summarized below.

1. Net vertical flux simulations. Unstable linear MRI modes always exist for any value of Am, with longer wavelength and smaller growth rate as Am becomes smaller (or AD

becomes stronger). MRI turbulence can be self-sustained as long as the wavelength of the most unstable mode λ_m is within the thickness of the disk (so the vertical field has to be progressively weaker as $Am \to 0^+$). At fixed Am, the total turbulent stress α increases monotonically with net vertical flux, until reaches maximum when $\lambda_m \approx H$. The maximum value of α rapidly decreases with Am when $Am < 10$, from about 0.4 at $Am \to \infty$ down to about 0.007 at $Am = 1$. It falls below 10^{-3} at $Am \approx 0.3$ and is around of 10^{-4} at $Am = 0.1$.

2. Net toroidal flux simulations. This field configuration is more stable. At fixed $Am \gtrsim 3$, the turbulent stress α from net toroidal flux simulations is smaller than that from net vertical flux simulations by about an order of magnitude. We do not find any evidence that MRI turbulence can be self-sustained at the level of $\alpha \gtrsim 10^{-4}$ when $Am \lesssim 1$ for any net toroidal flux.

3. Simulations with both net vertical and net toroidal fluxes. When $Am \gtrsim 1$ and fixed net vertical flux, the strength of the MRI turbulence is similar to the pure net vertical flux case, but slowly increases with the net toroidal flux. When $Am \lesssim 1$, the most unstable mode has non-zero radial wavenumber comparable to the vertical wavenumber, and the fastest growth rate asymptotes to some appreciable value even as $Am \to 0^+$. The maximum value of the turbulent stress α largely exceeds the pure net vertical flux case when $Am < 1$, with $\alpha \approx 6 \times 10^{-4}$ at $Am = 0.1$.

In addition, we find that similar to the effect of Ohmic dissipation, the ratio of the fluctuating part of the magnetic energy density to the kinetic energy density decreases as AD is stronger. Similarly, the ratio of Maxwell stress to Reynolds stress also drops at smaller Am. The power spectra density of the MRI turbulence in the AD dominated regime does not show any new features other than a rescaling from that in the ideal MHD case. We do not find any evidence that AD leads to the formation of sharp current structures in the MRI turbulence as proposed by Brandenburg & Zweibel (1994), but we confirm that AD tends to reduce the component of current perpendicular to the direction of magnetic field (Brandenburg et al. 1995), although to a lesser extent.

Combining the results from these three groups of simulations, we find a strong correlation between the turbulent stress α and the gas to magnetic pressure ratio β at the saturated state, given by $\langle\beta\rangle \approx 1/2\alpha$. The sustainability and saturation level of the MRI turbulence depends on the value of Am, the magnetic field geometry, and the magnetic field strength. It is best summarized in Figure 2.14. In short, at a given Am, there exists a maximum value of turbulent stress α

achievable from the most favorable geometries (generally with both net vertical and toroidal fluxes). Correspondingly, at a given Am, there exists a maximum field strength above which MRI is suppressed, and the maximum field strength rapidly decreases with decreasing Am.

For future reference, we quote the turbulent stress $\alpha = 7 \times 10^{-3}$ and 6×10^{-4} as the maximum value we have found in our simulations at $Am = 1$ and 0.1 respectively.

1.2 MRI-driven Accretion in PPDs

Adopting the criteria from numerical simulations of the MRI in the Ohmic and AD regimes (3-11), we have proposed a general framework for making optimistic predictions on the MRI-driven accretion rate and the magnetic field strength in PPDs. We evolve a complex chemical reaction network to estimate the magnetic diffusion coefficients. We have firstly considered both the grain-free case and the cases with well-mixed solar abundance normal grains (0.1μm and 1μm), and the main results are summarized below.

1. Active layer should exist as long as the magnetic field is sufficiently weak. Its upper boundary is set by AD, requiring the field strength not to be too strong. The lower boundary is generally determined by the Ohmic resistivity and the magnetic field strength, with the latter connected to the field strength in the upper boundary.

2. The predicted $\dot{M}$ increases with disk radius in the inner disk where accretion is layered, and flattens or decreases with radius in the outer disk when the disk midplane becomes active. The transition radius depends on grain abundance, and is $4 - 10$ AU in the grain-free case and above 50 AU in the presence of well-mixed sub-micron grains.

3. For our standard model, the predicted $\dot{M}$ is a few times $10^{-9} M_\odot$ yr $^{-1}$ in the grain-free case, and is reduced by one to two orders of magnitude in the presence of sub-micron grains in the inner disk. Reduction of $\dot{M}$ by grains is less significant in the outer disk.

4. The MRI-driven accretion rate is sensitive to the protostellar X-ray luminosity but insensitive to the deeper-penetrating cosmic-ray ionization rate. Extremely strong X-ray luminosity or additional strong ionization source with sufficient grain depletion is needed to achieve accretion rate of $\sim 10^{-7} M_\odot$ yr^{-1}.

5. In the inner disk where accretion is layered, the predicted $\dot{M}$ increases with disk radius, but decreases with increasing disk surface density. This situation would lead to runaway mass pile-up in the inner disk if the MRI were the only mechanism for driving accretion in the inner region of PPDs.

6. The midplane gas pressure is generally a factor of 100 to 10^5 times higher than the predicted magnetic pressure in the active layer. The ratio is smaller for stronger ionization and higher for larger disk mass or in the presence of small grains. The predicted magnetic field strength in the outer disk is consistent with the non-detection of polarized emission resulting from grain alignment.

Furthermore, we studied the role of tiny grains, or PAHs, on the MRI-driven accretion in PPDs. Tiny grains whose sizes are smaller than 0.01μm tend to be at most singly charged, whose conduction properties are almost identical to ions, which defines $\bar{n} \equiv n_{\rm gr}^{+} + n_{\rm gr}^{-} + n_i \geq n_e$. In addition, they can be very abundant ($x_{\rm PAH} \gtrsim 10^{-9}$) while still consist of a tiny fraction of total grain mass. These two facts lead to qualitatively new behaviors in the conductivity tensor. In particular, Hall effect is suppressed when $\bar{n} \gg n_e$, and AD can even be reduced relative to the grain-free case (with n_{e0} being the grain-free electron abundance) when $\bar{n} > n_{e0}$. Applying the same methodology, we find

1. At the inner disk where accretion is layered, the predicted accretion rate in the presence of tiny grains is one to two orders of magnitude less than the grain-free case due to increased Ohmic resistivity, but is similar to or higher than that with solar-abundance 0.1μm grains.

2. A sharp increase in the predicted $\dot{M}$ occurs at some transition radius $r_{\rm trans} \approx 15$ AU (in the fiducial model) where the disk midplane becomes active, making Ohmic resistivity irrelevant to the accretion rate. For $r \gtrsim r_{\rm trans}$, tiny grains make accretion even more rapid than the grain-free case, due to the net reduction of AD. The predicted accretion rate increases with PAH abundance.

3. The predicted accretion rate in the outer disk in the presence of abundant PAHs approaches the level of $10^{-8} M_\odot$ yr^{-1}, sufficient to account for the the observed accretion rate in PPDs and transitional disks.

In sum, our studies show that the MRI mechanism works more efficiently in the outer regions of PPDs ($\gtrsim 15$ AU), especially in the presence PAHs. However, in the inner disk, the MRI becomes

very ineffective and the optimistically predicted accretion rate is at most one order of magnitude smaller than the observed rate. We speculate magneto-centrifugal wind as a promising alternative to drive rapid accretion in the inner region of PPDs.

1.3 Magneto-centrifugal-Wind-driven Accretion in PPDs

We performed 3D vertically stratified shearing-box simulations to study the gas dynamics in the inner region of a PPD (at 1 AU). For the first time, both Ohmic resistivity and AD are included, with self-consistently evaluated the diffusion coefficients based on equilibrium chemistry. We find in our fiducial simulations that the MRI is completely suppressed from the the initially unstable configuration, relaxing to a laminar state with a supersonic outflow, which is launched from the magneto-centrifugal mechanism. Further studies show that the outflow can be launched once the following conditions are met. 1). The disk is threaded by a weak vertical magnetic field, with $\beta_0 \sim 10^5$ at the disk midplane. 2). Ohmic resistivity dominated midplane region, which suppresses the MRI near the disk midplane. 3). An ambipolar diffusion dominated disk surface layer, which suppresses the MRI at the disk surface layer. 4). Strong FUV ionization, which is effectively load mass from the disk to the wind. These conditions are matched very naturally in the inner region of the disks.

The wind structure and launching mechanism found in our study are qualitatively different from the conventional wind model originally proposed by Wardle & Koenigl (1993) (WK93), in the following aspects

1. Our basic wind solution obeys odd-z symmetry, where the field lines on the top and bottom sides of the disk bend toward opposite directions; the WK93 solution assumes an even-z symmetry, where the field lines on both sides bend to the same direction (i.e., opposite to the star), which is physical.

2. Our wind solution can achieve the physical wind geometry by flipping one side of the field lines. The flipping does not recover the even-z symmetry, but results in a strong current layer which is offset from the disk midplane.

3. With odd-z symmetry, launching a magneto-centrifugal wind only requires the presence of a weak vertical magnetic field, with plasma β for the vertical field at disk midplane to be

$\beta_0 \lesssim 10^6$, while in the WK93 model, launching a wind generally requires equipartition vertical field at disk midplane.

4. In our wind solution under the physical geometry, accretion proceeds through the thin strong current layer offset from the midplane, where a tiny fraction of mass drifts inward at a relatively large velocity (near sonic speed), and a weak vertical field with $\beta_0 = 10^5$ is sufficient to drive rapid accretion to match the observed rates. For the even-z symmetry solutions, accretion proceeds through the bulk of the gaseous disk.

Furthermore, we find that the rate of outflow and the rate of angular momentum transport through the wind increase rapidly with background vertical field strength. They are modestly sensitive to the column density of the FUV ionization, but are very insensitive to the grain abundance.

2. A New Scenario for the Accretion Process in PPDs

The study in Chapter 4 demonstrates a robust mechanism to launch the magneto-centrifugal wind (MCW) under the conditions where the MRI is widely believed to be able to operate (when AD is not considered). This result implies major modifications to the conventional picture of layered accretion introduced in Section 5 of Chapter 1. Compiling from all the results obtained in this thesis, a new scenario on the accretion process in PPDs emerges, which is illustrated in Figure 5.1.

As already been discussed thoroughly in Chapter 4, the four conditions for launching the MCW are met only in the inner region of PPDs. In this region, the disk is entirely laminar, and its vertical structure can be divided into three layers: 1). A disk zone near the midplane, which corresponds to the region within $\pm 4.5H$ in our fiducial model (see Figure 4.4). The disk midplane region is completely static. Slightly higher above, when the Elsasser numbers reach above one, the MCW starts to launch which is accompanied by the outward radial drift of gas that bends the field lines. 2). A wind zone which corresponds to the region above $\pm 4.5H$ in our fiducial model. In the wind zone the magneto-centrifugal mechanism starts to operate and efficiently accelerates the outflow launched from below. 3). A strong current layer within the disk zone but is offset from the midplane, where the radial and azimuthal field lines change sign in a very thin region of the order

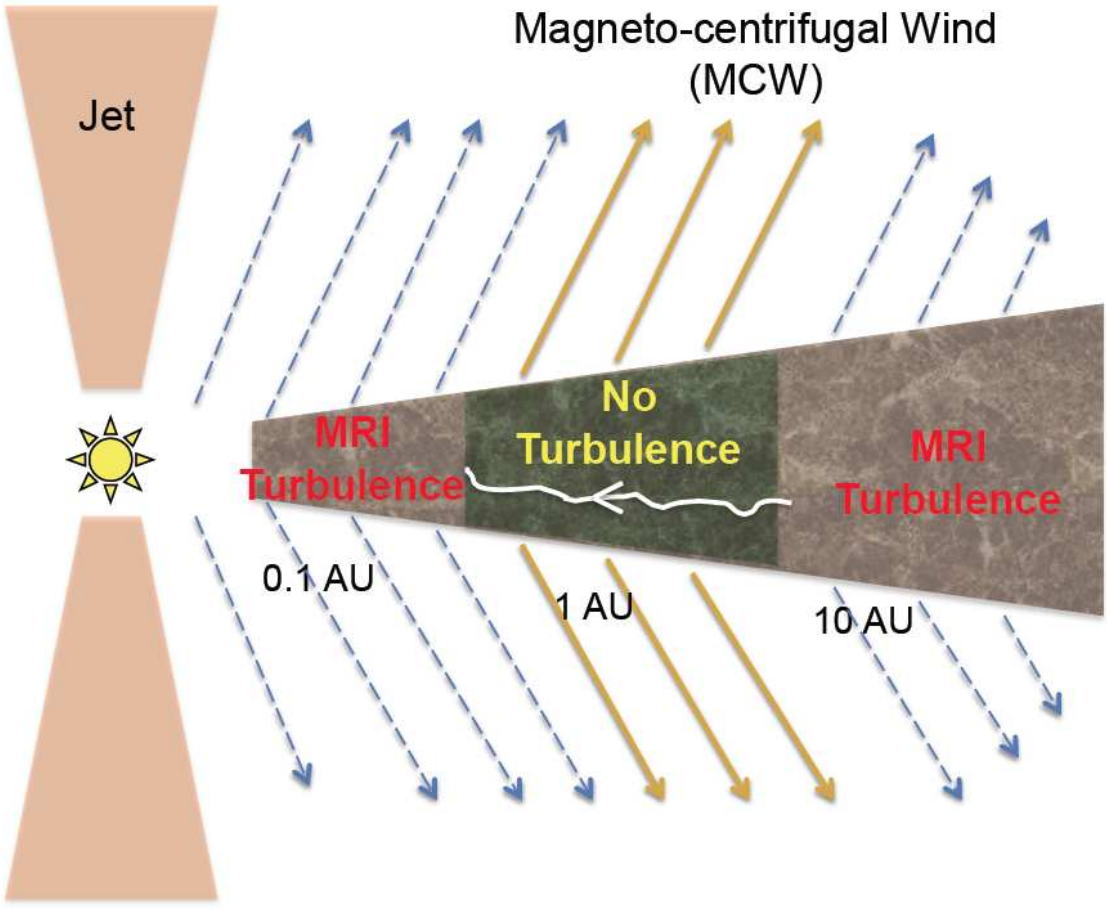


Fig. 5.1.— A new scenario for the accretion process in PPDs, which is to be compared with the conventional picture in Figure 1.1. Instead of having layered accretion, the inner disk near 1 AU is very likely to launch a laminar magneto-centrifugal wind which is the dominant mechanism for angular momentum transport. Very close to the star, as well as in the outer disk, where the MRI operates, an outflow might also be launched from the disk in the presence of a background magnetic field, though the outflow is unlikely to be laminar.

$0.2H$. Most of the wind stress is exerted in this layer which drives a high-velocity inflow. This inflow of gas carries the entire accretion flow in PPDs.

In the regions very close to the star, the disk is sufficiently hot ($\gtrsim 10^3$K) so that thermal ionization of Alkali species such as Na and K provides large ionization fraction so that the gas behaves essentially as ideal MHD. The gas dynamics in this region can be studied by ideal-MHD shearing-box simulations with vertical stratification. Most simulations of this type so far adopt a field geometry that has zero net vertical magnetic flux (Stone et al. 1996; Johansen et al. 2009a; Shi et al. 2010; Davis et al. 2010; Guan & Gammie 2011; Simon et al. 2012), where the total stress resulting from the MRI turbulence is $\alpha \sim 0.02$, which is more than sufficient to power PPD accretion. In more realistic situations, the inner rim of the disk is likely to possess some vertical background field either connected to the protostar or inherited from the disk. Stratified shearing-box simulations of the MRI including vertical net magnetic flux have only been performed recently, where it is found that a strong outflow is launched with the rate of the mass outflow increasing with increasing vertical net flux (Suzuki & Inutsuka 2009), which is similar to our findings in the laminar wind scenario. However, it is argued that such an outflow is unlikely to be connected to an MCW either because of dynamo activities when the vertical net flux is small ($\beta_0 \gtrsim 10^3$), which would make the direction of the outflow oscillate between radially inward and outward directions, or because of the symmetry problem when the vertical net flux is strong ($\beta_0 \lesssim 10^3$), where only the unphysical odd-z symmetry is preferred (Bai & Stone 2012a). Therefore, it is likely an outflow can be launched in the inner disk, but the fate of the outflow remains to be explored. We hence use dashed arrows to reflect this uncertainty in out cartoon Figure 5.1.

In the very outer region of the disk, MRI is likely to operate, although its property would be strongly affected by AD, which dominates the entire disk, with $Am \sim 1$ in most regions (see Figure 3.3). The disk midplane region is likely to be MRI-turbulent as long as a weak background vertical field is present, which appears very likely. The MRI-driven accretion rate, as studied in Chapter 3, can potentially achieve the level of observed range of PPD accretion rate. We emphasize that the presence of net vertical field is essential for the MRI to achieve the desired efficiency. Preliminary results by Simon et al. (in preparation) in their stratified shearing-box simulations with AD show that without a net vertical field, MRI can not be sustained for $Am < 10$. The presence of net vertical field, from our experience in both ideal MHD and non-ideal MHD simulations, is likely to drive an outflow. However, in the outer region of PPDs, even the FUV ionization can provide an ionization fraction of 10^{-5}, the extremely low density still makes the value of Am at disk surface

very small ($Am < 1$), as can be inferred from Equation (1-20) in Section 3 of Chapter 1. Under such situations, loading mass to the magnetized wind would become extremely inefficient. Therefore, it is unclear whether an outflow can be launched in the outer region of PPDs, and again we use dashed arrows in Figure 5.1 to reflect this uncertainty.

While the wind launching mechanism is robust, another question concerns the boundary between regions where the laminar MCW operates, and regions where the MRI operates. The inner boundary is largely determined by the thermodynamics, i.e., the location where thermal ionization becomes ineffective. It is likely to be a sharp boundary since the thermal ionization has extremely sensitive temperature dependence at low temperature. The location of the outer boundary may be more ambiguous, since the magnetic diffusivities vary more or less smoothly in radius, and the transition from the MCW dominated inner disk to the MRI dominated outer disk may take place across some finite radial intervals in PPDs. Global numerical simulations are required to fully resolving these issues.

3. Future Directions

Related to the topics of this thesis, several projects are ongoing as listed below.

1. The physical properties of the MRI with AD with vertical stratification, which is a continuation from Chapter 2. The first paper of this study is now under preparation (Simon et al. in preparation). Both zero and non-zero vertical net flux cases will be considered. The main goal is to verify the criterion illustrated in Figure 2.14, and to apply the results to the AD dominated outer regions of PPDs. In particular, the role of vertical net magnetic flux will be explored in detail, which will address whether the MRI-driven accretion is efficient, and whether the presence of net vertical field leads to wind launching.

2. The physical properties of the MRI in ideal MHD with a strong net vertical magnetic field (Bai & Stone 2012a). This project extends the earlier studies of the MRI with relatively weak vertical magnetic flux by Suzuki & Inutsuka (2009) and is applicable to regions near the hot inner rim of PPDs, as well as many other accretion disks. The results will be useful to address the flow structure and surface density and stratification in the inner PPDs, particularly on the properties and fate of the outflow.

3. The transition from the wind-driven accretion region in the inner disk to the MRI-driven accretion region in the outer disk. This project involves performing the same set of simulations in Chapter 4 at other radial locations of the disk. The goal is to provide a more detailed criterion for launching a laminar disk wind, as well as to identify how the transition occurs: whether it occurs smoothly over disk radii or more abruptly due to some sensitive dependence on certain parameters.

4. The Hall effect on the non-linear saturation of the MRI with unstratified shearing-box simulations. Although we have already implemented the Hall term into the Athena MHD code (see Appendix C), the operator-split method for the Hall term has not been cooperative with rotation in the shearing-box source terms. Progress is being made to resolve the inconsistencies. Once solved, a major gap in the non-ideal MHD MRI will be filled, and the outcome will be of great importance to examine whether the neglect of the Hall term in this thesis work can be properly justified.

Eventually, global simulations that include most of the non-ideal MHD physics must be conducted to address most of the above-mentioned issues. However, such simulations would be numerically challenging for several reasons. 1). Resolving the MRI in global disk simulations demands very high numerical resolution. 2). The gas density in the disk wind drops steadily along open magnetic field lines, which makes the wind zone numerically difficult to simulate in the highly magnetically-dominated regime. 3). Relatively large radial coverage is needed to properly reduce the artificial effects introduced from the radial boundaries, and to properly study the transition from wind-driven to the MRI driven regions. Overcoming the above difficulties would generally require the implementation of Alfvén limiters, non-uniform grid, as well as mesh refinement, which is planned for future development.

One important implication from the discussions in this thesis work is that the angular momentum transport process, no matter driven by the MRI or by the MCW, crucially depends on the distribution of poloidal magnetic flux, about which little is know from observations, and is not well appreciated in the literature. Therefore, it is crucial to theoretically/numerically study the distribution and evolution of magnetic flux in PPDs over long time scales, from the collapse of molecular cores all the way to the PPD formation and evolution. Studying the evolution of magnetic flux, in turn, requires detailed understanding of the microphysics: non-ideal MHD effects and turbulence, which is best studied from local shearing-box simulations. The mutual influence

between global evolution and local microphysics again makes it a very challenging problem, and a plausible approach would be not to simulate the whole processes, but to evolve a simple global one-dimensional model incorporating physically motivated parameterizations collected from local and global simulations on various stages of star and PPD formation.

Appendices

Appendix A

A General Derivation of Non-ideal MHD Terms in Weakly Ionized Gas

In this Appendix we first provide a detailed and general derivation of the non-ideal MHD terms in the "strong-coupling" limit for weakly ionized gas, as introduced in Section 3 of Chapter 1. Much of the derivation is a reproduction of Wardle (1999). Unfortunately, the general expression of magnetic diffusivities tends to elude physical interpretations, while the grain-free expression (1-11) is not applicable in the presence of small grains. We then proceed to discuss a interesting limiting case: when most grains are tiny (size $a < 1\mu$m). Much simpler and more meaningful expressions for magnetic diffusivities are derived that clearly reflect how conductivities of weakly ionized gas are affected by small grains. Much of Section 2 is based on the work by Bai (2011b).

1. General Derivation of Magnetic Diffusivities

In the single-fluid framework of weakly ionized gas (i.e., "strong coupling" limit where inertia of charge species are negligible), fluid density ρ and velocity $\boldsymbol{v}$ specify the density and velocity of the neutrals. Let charged species j has particle mass m_j, charge $Z_j e$, number density n_j, and drift velocity relative to the neutrals $\boldsymbol{v}_j$. Charge neutrality condition applies for non-relativistic MHD: $\sum_j n_j Z_j = 0$ (note that Z_j can be either positive or negative). Let $\boldsymbol{E}'$ be the electric field in the frame co-moving with the neutrals, while for non-relativistic MHD, the magnetic field $\boldsymbol{B}$ is the

same in all frames. In this co-moving frame, the equation of motion for charged species (whose inertia is negligible) is set by the balance between the Lorentz force and the neutral drag, given by

$$Z_j e(\boldsymbol{E}' + \frac{\boldsymbol{v}_j}{c} \times \boldsymbol{B}) = \gamma_j \rho m_j \boldsymbol{v}_j \ , \tag{A-1}$$

where $\gamma_j \equiv \langle \sigma v \rangle_j / (m + m_j)$ with $\langle \sigma v \rangle_j$ being the rate coefficient for momentum transfer between charged species j and the neutrals, and m is the averaged particle mass of the neutrals. The relative importance between the Lorentz force and the neutral drag is characterized by the ratio between the gyrofrequency and the momentum exchange rate, i.e. the Hall parameter

$$\beta_j = \frac{|Z_j| eB}{m_j c} \frac{1}{\gamma_j \rho} \ . \tag{A-2}$$

The physical significance of the Hall parameter is that, as we reiterate, charged species j is strongly coupled with neutrals if $\beta_j \ll 1$, and is strongly tied to magnetic fields when $\beta_j \gg 1$.

Since the current density is given by $\boldsymbol{J} = e \sum_j n_j Z_j \boldsymbol{v}_j$. The generalized Ohm's law can be obtained by inverting equation (A-1) to express $\boldsymbol{v}_j$ as a function of $\boldsymbol{E}'$. The result is

$$\boldsymbol{J} = \sigma_O \boldsymbol{E}'_{\parallel} + \sigma_H \hat{\boldsymbol{B}} \times \boldsymbol{E}'_{\perp} + \sigma_P \boldsymbol{E}'_{\perp} \ , \tag{A-3}$$

where subscripts $_{\parallel}$ and $_{\perp}$ denote vector components parallel and perpendicular to the magnetic field $\boldsymbol{B}$, and $\hat{}$ denotes unit vector. The Ohmic, Hall and Pedersen conductivities are (Wardle 2007)

$$\begin{aligned} \sigma_O &= \frac{ec}{B} \sum_j n_j |Z_j| \beta_j \ , \\ \sigma_H &= \frac{ec}{B} \sum_j \frac{n_j Z_j}{1 + \beta_j^2} \ , \\ \sigma_P &= \frac{ec}{B} \sum_j \frac{n_j |Z_j| \beta_j}{1 + \beta_j^2} \end{aligned} \tag{A-4}$$

respectively. Note that the Hall conductivity depends on the sign of Z_j, while σ_O and σ_P are always positive.

The Ohm's law (A-3) can be inverted to give the electric field using current densities, which then leads to the induction equation modified by non-ideal MHD terms in the most general form

$$\frac{\partial \boldsymbol{B}}{\partial t} = \nabla \times (\boldsymbol{v} \times \boldsymbol{B}) - \frac{4\pi}{c} \nabla \times [\eta_O \boldsymbol{J} + \eta_H (\boldsymbol{J} \times \hat{\boldsymbol{B}}) + \eta_A \boldsymbol{J}_{\perp}] \ , \tag{A-5}$$

where

$$\eta_O = \frac{c^2}{4\pi\sigma_O} ,$$
$$\eta_H = \frac{c^2}{4\pi\sigma_\perp}\frac{\sigma_H}{\sigma_\perp} , \tag{A-6}$$
$$\eta_A = \frac{c^2}{4\pi\sigma_\perp}\frac{\sigma_P}{\sigma_\perp} - \eta_O ,$$

are the desired Ohmic, Hall and ambipolar diffusivities as in equation (A-5), determined by the microphysics of ion-neutral and electron-neutral collisions, and $\sigma_\perp \equiv \sqrt{\sigma_H^2 + \sigma_P^2}$. Note that only η_O is independent of B. The absolute value of these diffusion coefficients determines the relative importance of the Ohmic, Hall and AD terms.

The most commonly used magnetic diffusivities are obtained by assuming that electrons and positively (and singly) charged ions are the only charge carriers, with all ions having the same Hall parameter. In this case, one can express the conductivities in terms of β_e and β_i for electrons and ions respectively, and since $|\beta_e| \gg \beta_i$, one finds (Salmeron & Wardle 2003)

$$\frac{\partial \boldsymbol{B}}{\partial t} = \nabla \times (\boldsymbol{v} \times \boldsymbol{B}) - \nabla \times \left[\frac{4\pi\eta_e}{c}\boldsymbol{J} + \frac{\boldsymbol{J}\times\boldsymbol{B}}{en_e} - \frac{(\boldsymbol{J}\times\boldsymbol{B})\times\boldsymbol{B}}{c\gamma_i\rho\rho_i}\right] , \tag{A-7}$$

from which Equation (1-9) in Chapter 1 was constructed. In the absence of grains, as the Hall parameters for different ion species are very similar (see Section 1.3 of Chapter 3), all the ions can be treated as a single species, hence the above formula is still valid. The Hall parameter for charged grains $\beta_{\rm gr}$ is generally different from that for ions β_i and for electrons β_e, hence the general formulae (A-4) and (A-6) should be used in the presence of grains.

2. The Effect of Charged Tiny Grains

In Section 1.3 of Chapter 3, we showed that for tiny grains whose size $a \lesssim 0.1\mu$m, they are dominantly singly charged and their Hall parameters become essentially the same as ions. Therefore, in terms of conductivity, tiny grains behave the same as ions. Below we derive the magnetic diffusivities in the limit that charged species are made of electrons, ions and singly charged tiny grains.

Let $\bar{n} = n_i + n_{\rm gr}^+ + n_{\rm gr}^-$ be the total number density of ions and charged tiny grains. Our derivation generalize the grain-free ($\bar{n} = n_e$) (formula (A-7)) to allow $\bar{n} \geq n_e$, as grains can carry negative charge. For brevity, we ignore the pre-factor en_ec/B in conductivities and $cB/4\pi en_e$ in diffusivities, which make them dimensionless.

The three components of the conductivity tensor read

$$\begin{aligned}
\sigma_O &= \beta_e + \frac{\bar{n}}{n_e}\beta_i = (\beta_e+\beta_i)(1+\theta) \ , \\
\sigma_H &= \frac{1}{1+\beta_e^2} - \frac{1}{1+\beta_i^2} = \frac{(\beta_e+\beta_i)(\beta_e-\beta_i)}{(1+\beta_e^2)(1+\beta_i^2)} \ , \\
\sigma_P &= \frac{\beta_e}{1+\beta_e^2} + \frac{(\bar{n}/n_e)\beta_i}{1+\beta_i^2} = \frac{(\beta_e+\beta_i)}{(1+\beta_i^2)}\left[\frac{(1+\beta_e\beta_i)}{(1+\beta_e^2)}+\theta\right] \ ,
\end{aligned} \tag{A-8}$$

where we have defined

$$\theta \equiv \frac{\bar{n}-n_e}{n_e}\frac{\beta_i}{\beta_e+\beta_i} \approx \frac{n_{\rm gr}^{\pm}\beta_i}{n_e\beta_e} \ . \tag{A-9}$$

The parameter θ is independent of magnetic field, and measure the ratio of grain conductivity to electron conductivity. Note that $\theta = 0$ in the grain-free case, and the Hall conductivity is independent of θ. The perpendicular conductivity is

$$\sigma_\perp^2 = \frac{(\beta_e+\beta_i)^2}{(1+\beta_e^2)(1+\beta_i^2)}\frac{1}{f(\theta)} \ , \tag{A-10}$$

where

$$f(\theta) \equiv \frac{(1+\beta_i^2)}{[(1+\theta)^2+(\beta_i+\theta\beta_e)^2]} \ . \tag{A-11}$$

Note that $f(\theta) = 1$ in the grain-free case ($\theta = 0$). It is straightforward to obtain the Ohmic, Hall and ambipolar diffusion coefficients, after some algebra

$$\eta_O = \frac{1}{(\beta_e+\beta_i)(1+\theta)} \approx \frac{1}{\beta_e(1+\theta)} \ , \tag{A-12}$$

$$\eta_H = \frac{\beta_e-\beta_i}{\beta_e+\beta_i}f(\theta) \approx f(\theta) \ , \tag{A-13}$$

$$\begin{aligned}
\eta_A &= \frac{[(1+\theta)+\beta_e(\beta_i+\theta\beta_e)]}{(\beta_e+\beta_i)}f(\theta) - \eta_O \\
&\approx \left[(1+\theta)(\beta_i+\theta\beta_e) - \frac{\beta_e\theta^2}{1+\beta_i^2}\right]\frac{f(\theta)}{1+\theta} \ ,
\end{aligned} \tag{A-14}$$

where the approximate formulae are obtained by noting that $\beta_e \gg \beta_i$, with error on the order of $\beta_i/\beta_e \sim 10^{-3}$.

We see that the grains affect the magnetic diffusion coefficients mainly via two factors: $(1+\theta)$ and $(\beta_i+\theta\beta_e)/\beta_i \approx \bar{n}/n_e$, both of which are independent of magnetic field strength. The former describes the ratio of total conductivity to electron conductivity, while the latter describes the number density ratio of ions / grains to electrons, and is much more substantial than the factor $(1+\theta)$ since $\beta_e \gg \beta_i$.

For $\theta \ll \beta_i/\beta_e \sim 10^{-3}$, we generally have $\bar{n} \approx n_i \approx n_e$, $f(\theta) \approx 1$, and the classical results (A-7) are recovered. Qualitatively new behaviors appear when $\theta \gtrsim \beta_i/\beta_e$, where grains play a dominant role in the abundance of charged particles ($n_{\rm gr}^{\pm} \gtrsim n_e$). In the next two paragraphs, we discuss the asymptotic behaviors of the diffusion coefficients, where comparison is made with the grain-free diffusion coefficients at fixed n_e. In reality, tiny grains strongly reduces n_e relative to the grain-free case, which will be discussed at the end of this Appendix.

The Ohmic resistivity is least affected by grains, which is simply reduced by a factor of $(1+\theta)$ relative to the electron resistivity regardless of magnetic field strength. Therefore, grain conductivity becomes important when $\theta \gtrsim 1$ or $\bar{n} \gtrsim 10^3 n_e$. For Hall and AD coefficients, we consider two separate limits. When $\beta_i \ll \beta_e \ll 1$ (Ohmic regime), we have

$$\eta_H \approx \frac{cB}{4\pi e n_e}\frac{1}{(1+\theta)^2}\ , \qquad \eta_A \approx \frac{cB\beta_i}{4\pi e n_e}\frac{\bar{n}}{n_e(1+\theta)^3}\ , \tag{A-15}$$

where we have factored out the results into the grain-free expression (left) multiplied by a correction factor (right). We see that the Hall diffusivity is only moderately affected by grains, being reduced by a factor of $(1+\theta)^2$ at fixed n_e. The AD, on the other hand, is enhanced by a factor of $\bar{n}/n_e$, in addition to a moderate reduction by $(1+\theta)^3$. Nevertheless, changes in Hall and AD coefficients do not play a significant role here since Ohmic resistivity is still the dominant effect.

In the opposite limit $1 \ll \beta_i \ll \beta_e$ (AD regime), we have

$$\eta_H \approx \frac{cB}{4\pi e n_e}\left(\frac{n_e}{\bar{n}}\right)^2\ , \qquad \eta_A \approx \frac{cB\beta_i}{4\pi e n_e}\frac{n_e}{\bar{n}}\ . \tag{A-16}$$

We see that in this limit and at fixed n_e, the Hall effect is reduced by a factor of $(\bar{n}/n_e)^2$, while AD is reduced by a factor of $(\bar{n}/n_e)$. The reduction of AD is easily understood. Without grains, the neutral gas is coupled to the magnetic field through ion-neutral collisions, hence $\eta_A \propto 1/n_i = 1/n_e$. Electrons play a negligible role because of its small inertia. Charged grains (no matter positive or negative) play exactly the same role as ions, hence we have $\eta_A \propto 1/\bar{n}$ in the presence of grains. We also note that the Hall effect vanishes if positive and negative charge carriers have the same mass, which is consistent with our result as $n_e/\bar{n} \to 0$.

In Figure A.1 we show two sample calculations of the magnetic diffusion coefficients for $\theta = 10^{-3}$ (dashed) and $\theta = 0.25$ (solid) respectively, which corresponds to situations where charged grain abundance is comparable to, and greatly exceed the electron abundance. The two asymptotic regimes derived above are clearly seen, with a transition region in between. The $\theta = 10^{-3}$ results are close to the grain-free case, where all three curves are close to straight lines except weak

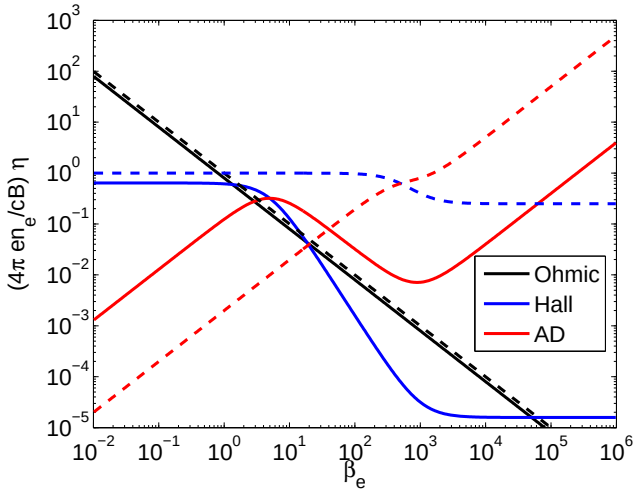


Fig. A.1.— Dimensionless Ohmic (black), Hall (blue) and ambipolar (red) diffusion coefficients as a function of the electron Hall parameter $\beta_e = 1000\beta_i$. We have considered two different values of the charged grain abundance parameter: $\theta = 10^{-3}$ ($\bar{n} = 2n_e$, dashed) and $\theta = 0.25$ ($\bar{n} = 251n_e$, solid).

transitions as β_i passes 1. For relatively large θ, the transition region extends from $\beta_e \approx 1$ to $\beta_i \approx 1$. Because of the suppression of the Hall diffusion beyond $\beta_e \approx 1$ and enhancement of AD before $\beta_e \approx 1$, AD becomes the dominant effect even when $\beta_i \ll 1$ ($\beta_e \ll 1000$), and the Hall regime gradually diminishes as θ increases.

Now let us take into account the chemistry in the gas. Assuming fixed gas density, temperature, and ionization rate, the equilibrium electron number density in the presence of small grains n_{e1} is much smaller than that in the grain-free case n_{e0} (Bai & Goodman 2009; Perez-Becker & Chiang 2011a). Therefore, Hall and AD coefficients are made larger by a factor of n_{e0}/n_{e1}. However, this factor is compensated by another reduction factor of $(n_{e1}/\bar{n})^2$ for the Hall effect and of $n_{e1}/\bar{n}$ for AD in the AD dominated regime. Here we focus on AD. In order to have a net reduction of AD coefficient when $\beta_i \gg 1$ (AD regime), it is required that

$$\bar{n} > n_{e0} \ . \tag{A-17}$$

That is, the charged grain abundance has to exceed the grain-free electron abundance. In Section 5 of Chapter 3 we show that this condition can be met. Similarly, for Ohmic resistivity to be reduced relative to the grain-free case, one requires $\bar{n} \gtrsim 10^3 n_{e0}$. This condition, however, is very unrealistic given the disk chemistry, thus Ohmic resistivity always increases in the presence of tiny grains.

Nevertheless, if condition (A-17) is met, Ohmic resistivity is enhanced by at most a factor of about 10^3 relative to the grain-free case.

Appendix B

The Athena MHD Code and Implementation of Non-ideal MHD Terms

This Appendix provides the background information about the Athena MHD code which used for all numerical simulations in this thesis (Section 1), as well as an introduction the local shearing-box approximation and its implementation to the Athena MHD code (Section 2). The last two sections provide the technical details about the implementation of the non-ideal terms in Athena (Section 3) and code tests (Section 4).

1. Basic Equations and Numerical Algorithms

Athena is a new grid-based code for compressible magnetohydrodynamics (MHD) based on higher-order Godunov methods. Briefly, it solves the ideal MHD equations in the conservative form

$$\frac{\partial \rho}{\partial t} + \nabla \cdot (\rho \boldsymbol{v}) = 0 \ , \tag{B-1}$$

$$\frac{\partial \rho \boldsymbol{v}}{\partial t} + \nabla \cdot (\rho \boldsymbol{v}\boldsymbol{v}^T - \boldsymbol{B}\boldsymbol{B}^T + \mathsf{P}^*) = 0 \ , \tag{B-2}$$

$$\frac{\partial E}{\partial t} + \nabla \cdot [(E + P^*)\boldsymbol{v} - \boldsymbol{B}(\boldsymbol{B} \cdot \boldsymbol{v})] = 0 \ , \tag{B-3}$$

$$\frac{\partial \boldsymbol{B}}{\partial t} - \nabla \times (\boldsymbol{v} \times \boldsymbol{B}) = 0 \ , \tag{B-4}$$

where P^* is a diagonal tensor with components $P^* = P + B^2/2$ (with P the gas pressure). E is the total energy density

$$E = \frac{P}{\gamma - 1} + \frac{1}{2}\rho v^2 + \frac{B^2}{2} \ . \tag{B-5}$$

All other symbols have their usual meaning. Note that these equations are written in units such that magnetic permeability is 1. For isothermal equation of states, which is considered throughout this thesis, the energy equation is omitted, replaced by $P = \rho c_s^2$ where c_s is the isothermal sound speed.

Being a finite volume (Godunov) code, Athena conserves mass, momentum and energy (for non-barotropic equation of state) exactly (to machine precision). Moreover, Athena uses constrained transport (CT) algorithm (Evans & Hawley 1988) to evolve the magnetic field using staggered mesh where magnetic field components are defined at cell faces and electromotive force (EMF) components are defined at cell edges, so that the divergence-free constraint is enforced (see Figure 1 of Stone et al. 2008 for more details). A consistent framework for computing the time- and edge-averaged EMFs from Godunov fluxes are developed and tested. Two distinct MHD algorithms are implemented in Athena, namely, the CTU (corner transport upwind) + CT and the VL (van Leer) + CT algorithms, both algorithms are dimensionally unsplit that preserve symmetries inherent in the flow. Both algorithms are second-order accurate in space and time in smooth solutions in all MHD wave families and in multiple dimensions. All our simulations in this thesis use the CTU integrator and third order spatial reconstruction, as it has very small numerical diffusion and is more accurate. A comprehensive description of the implementation and tests of the algorithms are provided in Stone et al. (2008), with more technical details described in Gardiner & Stone (2005) and Gardiner & Stone (2008).

2. Shearing-Box Approximation

All numerical simulations for the gas dynamics in PPDs presented in this thesis are set up in the shearing-box framework (Goldreich & Lynden-Bell 1965). It picks up a local patch of the disk at a fiducial radius R and adopts the local reference frame corotating with the disk at orbital frequency Ω. MHD equations are written in Cartesian coordinate as in equations (B-1) - (B-4), with source terms resulting from tidal gravity and Coriolis force added to the momentum equation

$$\frac{\partial \rho \boldsymbol{v}}{\partial t} + \nabla \cdot (\rho \boldsymbol{v}\boldsymbol{v}^T - \boldsymbol{B}\boldsymbol{B}^T + \mathsf{P}^*) = \rho \Big[2\boldsymbol{v} \times \boldsymbol{\Omega} + 3\Omega^2 x \hat{\boldsymbol{x}} - \Omega^2 z \hat{\boldsymbol{z}} \Big] \ , \tag{B-6}$$

where $\hat{\boldsymbol{x}}, \hat{\boldsymbol{y}}, \hat{\boldsymbol{z}}$ are unit vectors pointing to the radial, azimuthal and vertical directions respectively, and $\boldsymbol{\Omega}$ is along the $\hat{\boldsymbol{z}}$ direction. The source terms give the background shear flow, with

$$v_{y0} = -\frac{3}{2}\Omega x \ . \tag{B-7}$$

A characteristic length scale is the vertical scale height $H = c_s/\Omega$, and in hydrostatic equilibrium the density distribution in the disk is $\rho(z) = \rho_0 \exp -z^2/2H^2$, with ρ_0 being the midplane density. Note that the shearing-sheet approximation assumes $H \ll R$, while the ratio H/R is not reflected in the formulation. The vertical gravity term $-\Omega^2 z\hat{\boldsymbol{z}}$ is sometimes ignored (i.e., unstratified simulations) as appropriate for regions near the disk midplane, as opposed to stratified simulations that cover the entire disk vertical structure. Periodic boundary conditions are used in the azimuthal direction, while the radial boundary conditions are shear-periodic:

$$f(x, y, z) = f(x + L_x, y - \frac{3}{2}\Omega L_x t, z) \ , \tag{B-8}$$

where L_x is the size of the radial computational domain (see Figure 1 of Hawley et al. 1995 for more details).

Shearing-box source terms have been implemented in Athena using the Crank-Nicholson scheme which preserves the amplitude of epicyclic motion to round-off error (Stone & Gardiner 2010). In addition, an orbital advection scheme similar to Masset (2000) and Johnson et al. (2008) has been implemented in Athena. It splits the dynamical equations into two systems, one of which corresponds to linear advection operator with background shear velocity (B-7), and the azimuthal stretch of radial field

$$\frac{\partial B_y}{\partial t} = -\frac{3}{2}\Omega B_x \ , \tag{B-9}$$

and the other system evolves only velocity fluctuations, with $\boldsymbol{v'} = \boldsymbol{v} - v_{y0}\hat{\boldsymbol{y}}$, and

$$\frac{\partial \rho \boldsymbol{v'}}{\partial t} + \nabla \cdot (\rho \boldsymbol{v'}\boldsymbol{v'}^T - \boldsymbol{B}\boldsymbol{B}^T + \mathsf{P}^*) = \rho\left[2v'_y\Omega\hat{\boldsymbol{x}} - \frac{1}{2}v'_x\Omega\hat{\boldsymbol{x}} - \Omega^2 z\hat{\boldsymbol{z}}\right] \ . \tag{B-10}$$

As the background shear velocity, which becomes supersonic when the radial domain size exceeds $\sim H$, is subtracted, the orbital advection scheme significantly accelerates the calculation in simulations with large radial domain sizes. Moreover, it also makes the calculations more accurate, as it makes the the truncation error more uniform in radius (Johnson et al. 2008; Stone & Gardiner 2010).

3. Non-ideal MHD Terms: Implementation

Non-ideal MHD terms (e.g., the AD term) are implemented in Athena in an operator-split way. Over one time step, we first solve the induction equation separately using only the non-ideal MHD terms (with subscript "$_{NI}$")

$$\left.\frac{\partial \boldsymbol{B}}{\partial t}\right|_{NI} = -\nabla \times \mathcal{E}_{NI} = -\nabla \times [\eta_O \boldsymbol{J} + \eta_H (\boldsymbol{J} \times \hat{\boldsymbol{B}}) + \eta_A \boldsymbol{J}_\perp] \ . \tag{B-11}$$

Note that in code unit we redefine $\boldsymbol{J} = \nabla \times \boldsymbol{B}$. We then solves ideal MHD equations as described in Section 1. The overall accuracy for magnetic diffusion is therefore first order in time. The magnetic diffusion coefficient can be set by the user depending on specific problems.

Same as the ideal MHD algorithm, we use CT to update the magnetic field from the non-ideal MHD terms. Briefly, current density $\boldsymbol{J}$ is naturally stored at the center of cell edges. The main work is to calculate the non-ideal MHD EMFs, which are defined at the same locations of $\boldsymbol{J}$. The case with Ohmic resistivity is straightforward, for AD terms, we calculate the AD EMFs by interpolating all three components of face-centered $\boldsymbol{B}$ and edge-centered $\boldsymbol{J}$ to such locations. The induction equation is evolved using the fully explicit forward-Euler method, which is stable as both Ohmic and AD are dissipative terms.

The implementation of the Hall term, which is non-dissipative, is more subtle. A forward-Euler method with the Hall term is unconditionally unstable. Alternatively, a dimensional-split approach can be shown to be marginally stable which preserves the amplitude of the whistler waves exactly. In brief, we first do a partial update of $\boldsymbol{B}$ using the x-component of the Hall EMF. The partially updated $\boldsymbol{B}$ is then used to evaluate the y-component of the Hall EMF, which further gives another partial update of $\boldsymbol{B}$. Finally, the z-component of the Hall EMF is evaluated to give the final update of $\boldsymbol{B}$.

By default, the expressions for the Ohmic, Hall and AD terms are taken from the grain-free formulation (1-10) and (1-11), where

$$\eta_O = \eta_0 \left(\frac{n_{e0}}{n_e}\right) , \qquad \eta_H = Q_H B \left(\frac{n_{e0}}{n_e}\right) , \qquad \eta_A = Q_A B^2 \left(\frac{\rho_{i0}}{\rho_i}\right)\left(\frac{\rho_0}{\rho}\right) , \tag{B-12}$$

where subscript '$_0$' denote the reference value of various quantities. We use a simple treatment below to reflect the change of ionization fraction with gas density:

$$\frac{\rho_i}{\rho_{i0}} = \frac{n_e}{n_{e0}} = \left(\frac{\rho}{\rho_0}\right)^\nu , \tag{B-13}$$

here ν characterizes the sensitivity of the $\rho_i - \rho$ dependence. One expects $\nu \approx 1/2$ from simple ionization-recombination reactions. In the mean time, the code allows for fully flexible user-defined diffusivities that can depend on location and magnetic field strength, which is used in Chater 4.

For diffusion problems, in addition to the Courant-Friedrichs-Lewy (CFL) time constraint, the integration time step Δt is also limited by the diffusion time across the size of one grid cell

$$\Delta t < \frac{\Delta x_{\rm min}^2}{2D\eta_{\rm max}} \ , \tag{B-14}$$

where D is the dimension of the problem, $\Delta x_{\rm min}$ is the minimum grid spacing, and

$$\eta_{\rm max} = \max\{\eta_O + \eta_A, \eta_H\} \tag{B-15}$$

is the maximum of all diffusion coefficients over the computational domain.

3.1 Super Time-Stepping

When the diffusion coefficient is large, or when the grid resolution in the simulations is high, magnetic diffusion can place severe limit on the simulation time step. For Ohmic resistivity and AD, this numerical difficulty can be alleviated by using the so-called super time-stepping (STS) technique (Alexiades et al. 1996). Choi et al. (2009) has successfully implemented the STS for AD in their MHD code who demonstrated the feasibility of the STS approach.

The basic idea of the STS method is that instead of satisfying the stability criterion (B-14) over single timesteps, it demands stability over a compound timestep $\Delta t_{\rm STS}$ (called a super timestep) that consists of wisely designed N unequal substeps τ_j $(j = 1, ..., N)$ with

$$\Delta t_{\rm STS} = \sum_{j=1}^{N} \Delta\tau_j \ , \tag{B-16}$$

so that the averaged timestep $\Delta t_{\rm STS}/N$ can well exceed the normal diffusion timestep $\Delta t_{\rm diff}$ from stability requirement. The optimized lengths for the substeps were found to be (Alexiades et al. 1996)

$$\Delta\tau_j = \Delta t_{\rm diff}\left[(\nu-1)\cos\left(\frac{2j-1}{N}\frac{\pi}{2}\right) + \nu + 1\right]^{-1} \ , \tag{B-17}$$

where $0 < \nu < 1$ is a free parameter. The sum of the substeps gives

$$\Delta t_{\rm STS} = \Delta t_{\rm diff}\frac{N}{2\sqrt{\nu}}\left[\frac{(1+\sqrt{\nu})^{2N} - (1-\sqrt{\nu})^{2N}}{(1+\sqrt{\nu})^{2N} + (1-\sqrt{\nu})^{2N}}\right] \equiv G(N,\nu)\Delta t_{\rm diff} \ . \tag{B-18}$$

We note that as $\nu \to 0$, we have $\Delta t_{\rm STS} = N^2 \Delta t_{\rm diff}$ so that the STS approach is asymptotically N times faster than the standard explicit approach. However, the value of ν needs to be properly chosen to achieve optimal performance. In general, the STS method approaches better accuracy for as N decreases and ν increases, while large N and small ν leads to higher efficiency. In practice, we choose $\nu = 1/4N^2$ with a limit of $N \leq 12$ to keep the accuracy. At $N = 12$, one achieves an acceleration factor of about 9. It is also found that further increasing N would not significantly increase the efficiency without sacrificing for accuracy[1].

In our code, we first compute the ideal MHD timestep $\Delta t_{\rm MHD}$ and the diffusion timestep $\Delta t_{\rm diff}$. We set $\Delta t_{\rm STS} = \Delta t_{\rm MHD}$ if for some $N \leq 12$, one has $G[N-1, 1/4(N-1)^2] < \Delta t_{\rm MHD}/\Delta t_{\rm diff} \leq G(N, 1/4N^2)$, which determines N, and we further modify $\Delta t_{\rm diff}$ to be $\Delta t_{\rm MHD}/G(N, 1/4N^2)$. Otherwise, we fix $N = 12$, and set $\Delta t_{\rm STS} = \Delta t_{\rm diff} G[12, 1/(4 \times 12^2)]$. As we use operator-split algorithm for magnetic diffusion, we evolve N STS substeps of non-ideal MHD with τ_j before evolving one MHD timestep with $\Delta t_{\rm STS}$. Although the test problems in the next section are performed without STS, we have also performed the same tests with STS and found essentially the same results.

Finally, we note that STS method is designed for parabolic problems (i.e., diffusion). It does not work for the Hall term, which is not diffusive and is hyperbolic in nature.

4. Non-ideal MHD Terms: Tests

In this section we present three test problems for our non-ideal MHD algorithms: damping of MHD waves for Ohmic resistivity and AD, isothermal C-type shock test for AD, and the circular-polarized Alfvén wave test for the Hall term.

4.1 Damping of MHD Waves

Linear MHD waves are damped due to Ohmic resistivity and AD. Because the exact eigenvectors in the these regimes can be very complicated, we initialize the problem with ideal MHD wave eigenvectors and measure the damping rate. This means the initial conditions are a

[1] Based on the results from the Junior project by Sarah Wellons.

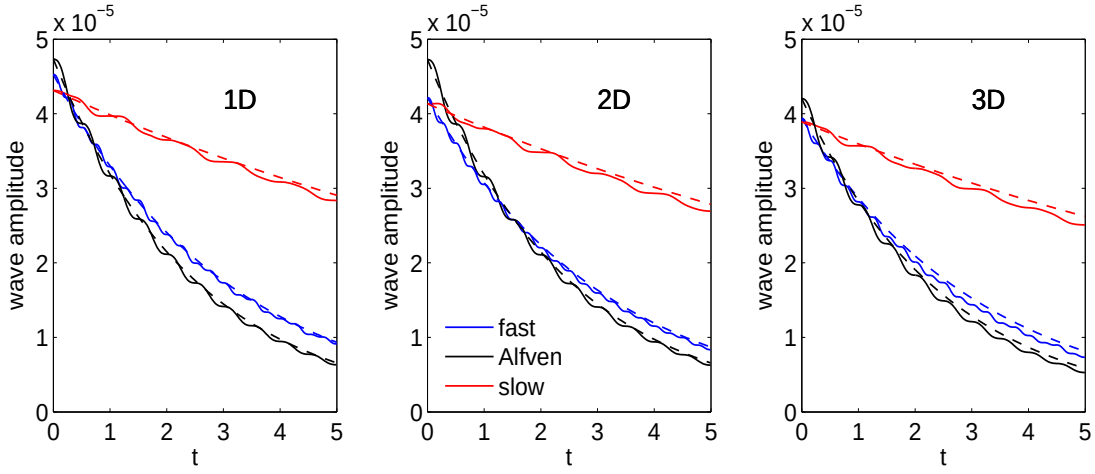


Fig. B.1.— The damping of linear MHD waves by ambipolar diffusion. Three panels from left to right show the test results for 1D, 2D and 3D, where in the latter two cases the waves are not grid-aligned. In each panel, black, blue and red curves show the damping of Alfvv́en, fast and slow waves respectively. Solid lines are the measured damping curve, while dashed lines are the expected damping curve.

linear superposition of more than one eigen-mode, but the averaged damping rate should approach the analytical value for a single mode as long as the Ohmic/AD coefficient is sufficiently small.

We consider the propagation of a linear MHD wave with wave vector $\boldsymbol{k}$ in a static medium with background magnetic field $\boldsymbol{B}_0$ and density ρ_0, and let θ be the angle between $\boldsymbol{k}$ and $\boldsymbol{B}_0$. For Ohmic resistivity, the damping rate Γ of MHD waves can be found in Section 3.2 of Ryu et al. (1995). For the Alfvén wave, we have

$$\Gamma_A = \frac{1}{2}\eta_O k^2 \ . \tag{B-19}$$

The damping rate for fast and slow magnetosonic waves are

$$\Gamma_f = \frac{1}{2}\left(\frac{v_f^2 - c_s^2}{v_f^2 - v_s^2}\right)\eta_O k^2 \ , \qquad \Gamma_s = \frac{1}{2}\left(\frac{c_s^2 - v_s^2}{v_f^2 - v_s^2}\right)\eta_O k^2 \tag{B-20}$$

respectively, where c_s is the sound speed, v_f and v_s are the wave speeds for fast and slow magnetosonic waves, given by

$$v_{f,s}^2 = \frac{1}{2}(v_A^2 + c_s^2) \pm \frac{1}{2}\sqrt{(c_s^2 + v_A^2)^2 - 4c_s^2 v_A^2 \cos^2\theta} \ , \tag{B-21}$$

with plus (minus) sign corresponding to v_f (v_s), and $v_A \equiv B_0/\sqrt{4\pi\rho_0}$ is the Alfvén velocity.

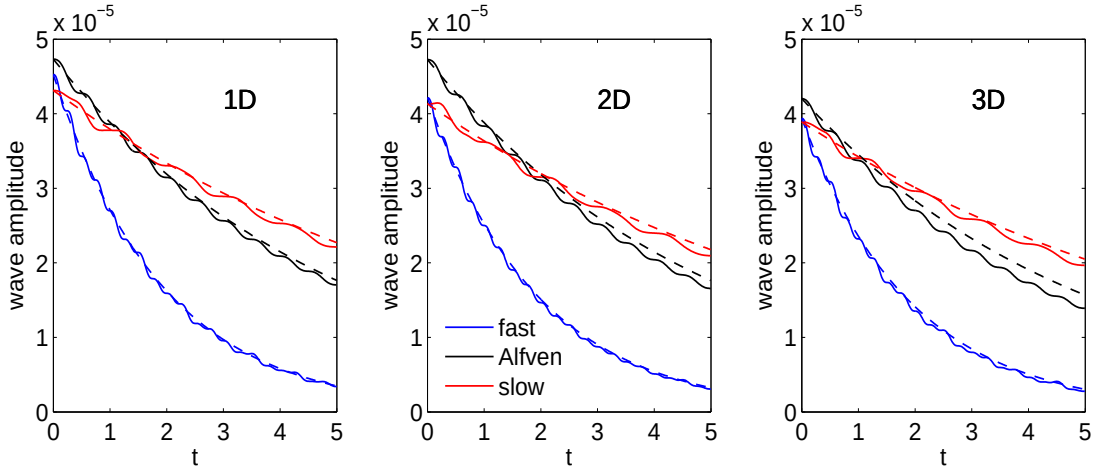


Fig. B.2.— The damping of linear MHD waves by ambipolar diffusion. Three panels from left to right show the test results for 1D, 2D and 3D, where in the latter two cases the waves are not grid-aligned. In each panel, black, blue and red curves show the damping of Alfvén, fast and slow waves respectively. Solid lines are the measured damping curve, while dashed lines are the expected damping curve.

The analytical damping rate for various MHD waves due to AD can be derived from Balsara (1996), as we summarize below. The damping rate of the Alfvén wave is given by the solution of

$$\omega^2 = k^2 v_A^2 \cos^2\theta \left(1 - \mathrm{i}\frac{\omega}{\omega_a}\right) . \tag{B-22}$$

where $\omega_a \equiv \gamma_i \rho_i$. The damping rate of fast and slow waves can be obtained by solving the quadratic equation

$$(\omega^2 - v_f^2)(\omega^2 - v_s^2) + \mathrm{i}(\omega^2 - k^2 c_s^2) k^2 v_A^2 \frac{\omega}{\omega_a} = 0 . \tag{B-23}$$

When $\omega \ll \omega_a$, the damping rate is small and can be found by expanding the ideal MHD dispersion relation to powers of ω/ω_a, and to the first order, we find for the damping rate of the Alfvén wave

$$\Gamma_A = \frac{1}{2}\frac{k^2 v_A^2 \cos^2\theta}{\omega_a} . \tag{B-24}$$

The damping rate for fast and slow magnetosonic waves are

$$\Gamma_f = \frac{1}{2}\left(\frac{v_f^2 - c_s^2}{v_f^2 - v_s^2}\right)\frac{k^2 v_A^2}{\omega_a} , \qquad \Gamma_s = \frac{1}{2}\left(\frac{c_s^2 - v_s^2}{v_f^2 - v_s^2}\right)\frac{k^2 v_A^2}{\omega_a} . \tag{B-25}$$

We perform the linear wave damping test in 1D, 2D and 3D. In 1D, the wave is grid-aligned, whose wave length equals 1 in code unit. In 2D and 3D test problems, the wave vectors are not grid-aligned, with box sizes chosen such that the wave length is also 1 [in 2D, the box size is

$(\sqrt{5}, \sqrt{5}/2)$ and in 3D, the box size is (3, 1.5, 1.5)]. We use isothermal equation of state with $c_s = 1$. The background gas density is $\rho_0 = 1$. We choose $\nu = 0$. In 1D, the wave vector is along the x direction, and the adopted magnetic field is $B_{0x} = 1.0$, $B_{0y} = \sqrt{2}$ and $B_{0z} = 0.5$. In 2D and 3D the background magnetic field vector is rotated with the wave vector accordingly while keeping θ the same as in 1D (and a vector potential is used to initialize the wave in order to preserve the divergence free condition). From the above we get $v_A = \sqrt{13/4}$, $v_f = 2$ and $v_s = 1/2$, therefore, for Ohmic resistivity, the damping rates are $\Gamma_A = 2\pi^2\eta_O$, $\Gamma_f = 1.6\pi^2\eta_O$, $\Gamma_s = 0.4\pi^2\eta_O$ respectively; and for AD, the damping rates are $\Gamma_A = 2\pi^2/\omega_a$, $\Gamma_f = 5.2\pi^2/\omega_a$ and $\Gamma_s = 1.3\pi^2/\omega_a$ respectively.

In practice, we adopt $\eta_O = 0.02$ for Ohmic resistivity and $\omega_a = 100$ ($Q_A = 1/\omega_a$) for AD. We run the wave damping test up to $t = 5$. By default, the grid size is 32 in 1D, 64×32 in 2D, and $64 \times 32 \times 32$ in 3D. Accounting for the box size in each dimension, the effective resolution, characterized by number of cells per wavelength, is 32, 28.6 and 21.3 in 1D, 2D and 3D respectively. The results are shown in Figure B.1 and Figure B.2 respectively. From left to right, we show the damping curves from 1D, 2D and 3D simulations in the solid lines, where black, blue and red lines label Alfvén, fast and slow MHD waves. Dashed lines show the theoretical exponential damping curve. We see that the numerical damping rates for both Ohmic and AD cases matche very well with the theoretical damping rates. In the 3D runs, the damping rates are slightly faster than expected, but this can be accounted for because the effective resolution is less.

We have also run the simulations with double and half resolutions. With double resolution, the numerical damping curves in 1D, 2D and 3D cases almost match exactly the analytical damping curves (besides some small oscillations due to the initial conditions). At half resolution, however, the numerical damping rate deviates substantially (about 15% to 30% at $t = 5$). These results indicate that at least 20 cells per wavelength is needed to accurately capture the effect of Ohmic dissipation and AD.

4.2 Isothermal C-type Shock Test

The effect of ambipolar diffusion is best manifested in C-type shocks (Draine 1980), which is a shock with continuous transitions consequent of the AD. For the purpose of the code test, here we consider the isothermal C-type test by Mac Low et al. (1995), which has become a standard test problem for AD.

We consider steady-state ($\partial/\partial t = 0$) shock and work in the shock frame, with upstream gas density ρ_0 moving at velocity v_s. The upstream gas is threaded by a uniform magnetic field $\boldsymbol{B}_0$ that lies at an angle θ to the velocity. Let $\boldsymbol{v}_s$ be in the $\hat{x}$ direction, and $\boldsymbol{B}_0$ be in the $\hat{x} - \hat{y}$ plane. For a continuous shock, the jump conditions reduce to $\partial/\partial x = 0$. Assuming the ion density ρ_i is constant ($\nu = 0$), the equations that describe the C-type shock read

$$\rho v_x = \rho_0 v_s \ , \tag{B-26}$$

$$\rho(v_x^2 + c_s^2) + \frac{B_y^2}{8\pi} = \rho_0(v_s^2 + c_s^2) + \frac{B_{0y}^2}{8\pi} \ , \tag{B-27}$$

$$\rho v_x v_y - \frac{B_x B_y}{4\pi} = -\frac{B_x B_{0y}}{4\pi} \ , \tag{B-28}$$

$$v_x B_y - v_y B_x - \frac{B^2}{4\pi\rho\gamma\rho_i}\frac{dB_y}{dx} = v_s B_{0y} \ . \tag{B-29}$$

Note that $B_x = B_{0x}$ is constant.

The shock is characterized by three dimensionless parameters: the sonic Mach number $M = v_s/c_s$, the Alfvén Mach number $A = v_s/v_A$ (where $v_A^2 = B_0^2/4\pi\rho_0$), and the angle θ of the magnetic field with the upstream flow. The characteristic length scale of the problem is given by $L = v_A/\gamma\rho_i$. We further define $D \equiv \rho/\rho_0$, and $b \equiv B_y/B_0$. After some algebra, we arrive at a dimensionless first order differential equation for D (Mac Low et al. 1995)

$$\begin{aligned}\left(\frac{1}{D^2} - \frac{1}{M^2}\right)\frac{dD}{d(x/L)} &= (b^2 + \cos^2\theta)^{-1} \times \\ &\times \frac{b}{A}\left[b - D\left(\frac{b - \sin\theta}{A^2}\cos^2\theta + \sin\theta\right)\right] \ .\end{aligned} \tag{B-30}$$

One can numerically integrate this ordinary differential equation to obtain the C-type shock profile. In Figure B.3 we show a semi-analytical solution for $M = 50$, $A = 10$ and $\theta = \pi/4$ obtained by using a 4th order Runge-Kutta method.

[t]

To use this solution as a code test, the shock is set to be aligned with the grid in the $\hat{\boldsymbol{x}}$ direction. We use outflow boundary conditions in this direction. In multi-dimensional tests, periodic boundary conditions are used in other directions. The shock solution should be stationary (i.e., a standing shock), thus we evolve the solution for sufficiently long time ($\sim 5L/c_s$) and compare to the initial conditions. In Figure B.3, we further show the absolute error of the shock profile compared with the semi-analytic solution. Since the shock is grid-aligned, 1D, 2D and 3D tests essentially produce the same result. In our tests, the grid resolution is chosen to be 2 and 4 cells

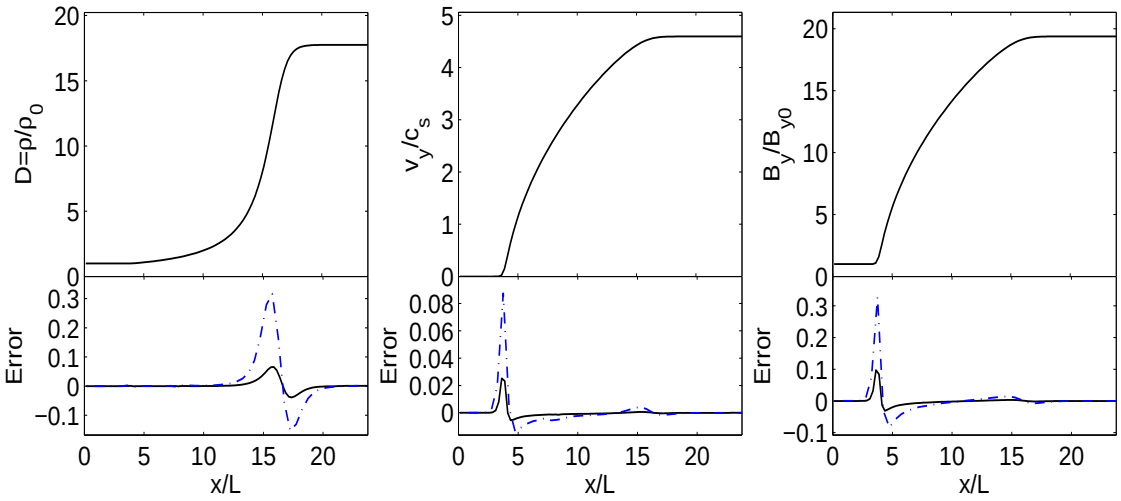


Fig. B.3.— The profile of a C-type shock with $M = 50$, $A = 10$ and $\theta = \pi/4$. The upper panels show the semi-analytical solution of gas density ρ, perpendicular velocity v_y and perpendicular magnetic field B_y. ρ and B_y are normalized to their upstream values, and v_y is normalized to the sound speed. The lower panels show the corresponding absolute errors (same units as the upper panels) from our numerical simulations, with resolutions of 4 cells per L (black solid) and 2 cells per L (blue dash-dotted).

per L.[2] We see that our code very accurately resolves the structure of the C-type shock using only a few cells per L. The main source of the error lie in the region where density and velocity profiles vary quickly. In our comparison, the position of the shock is fixed at the initial place, while in reality, the shock position can shift slightly during numerical relaxation.

4.3 Circular Polarized Alfvén Waves

The Alfvén waves break into left and right polarized Alfv́en with different wave speed in the presence of the Hall effect. To derive the dispersion relation and eigen vectors, we consider a uniform medium with density ρ_0 embedded in a uniform magnetic field $\boldsymbol{B}_0$, and assume the fluid is incompressible. Consider perturbations of the form $\exp[i(\omega t - \boldsymbol{k}\cdot\boldsymbol{x})]$ (if the fluid is moving at speed $\boldsymbol{v}_0$, one can simply shift $\omega \to \omega - \boldsymbol{v}_0\cdot\boldsymbol{k}$). Without loss of generality, we set $\boldsymbol{k}$ to be in the $\hat{z}$ direction. The perturbed quantities are denoted with a prefix δ. Considering only the Hall terms,

[2]In comparison, Mac Low et al. (1995) achieved comparable accuracy as ours using 5 and 10 cells per L, Choi et al. (2009) achieved similar or better accuracy at 6.4 cells per L.

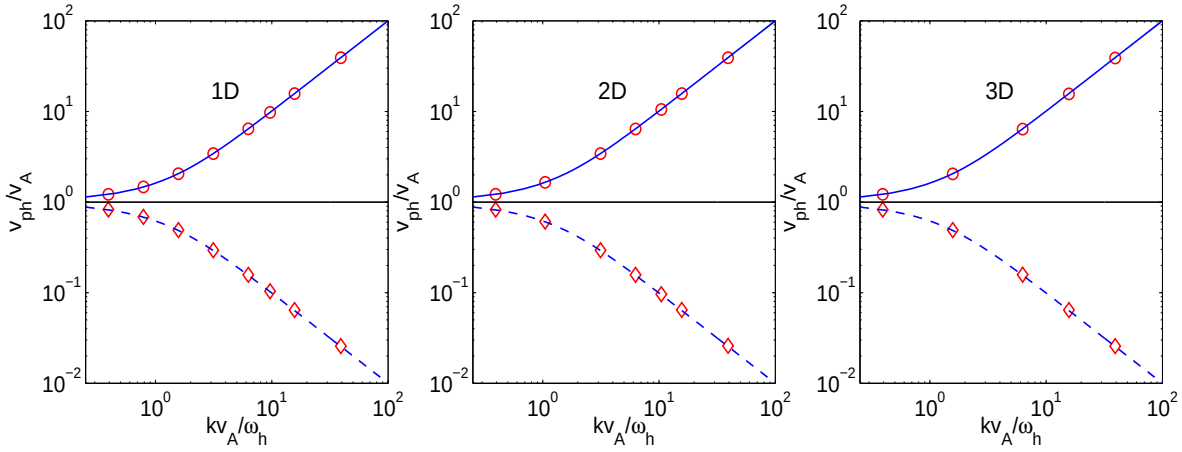


Fig. B.4.— The measured dispersion relation for circularly polarized Alfvv́en waves in 1D (left), 2D (middle) and 3D (right) grids. Upper panels show the results for right handed (whistler) waves, where red circles mark the measured phase velocity $v_{ph} = \omega/k$ normalized by v_A at various wave numbers k (normalized by ω_h/v_A), and solid blue line indicated the theoretical relation. Lower panels are for left handed waves, with red diamonds and blue dashed lines mark the measured and theoretical dispersion relations respectively.

the perturbation equations read

$$\begin{aligned} &\boldsymbol{k}\cdot\delta\boldsymbol{v} = 0\ , \qquad \boldsymbol{k}\cdot\delta\boldsymbol{B} = 0\ , \\ &i\omega\delta\boldsymbol{v} = -\frac{i}{4\pi}\frac{(\boldsymbol{k}\times\delta\boldsymbol{B})\times\boldsymbol{B}_0}{\rho_0} + i\frac{\delta P}{\rho_0}\boldsymbol{k}\ , \\ &i\omega\delta\boldsymbol{B} = -i(\boldsymbol{k}\cdot\boldsymbol{B}_0)\delta\boldsymbol{v} + \frac{c}{4\pi n_e e}(\boldsymbol{k}\cdot\boldsymbol{B}_0)(\boldsymbol{k}\times\delta\boldsymbol{B})\ . \end{aligned} \tag{B-31}$$

Dotting $\boldsymbol{k}$ to both sides of the momentum perturbation equation, we find $\delta P = -\delta\boldsymbol{B}\cdot\boldsymbol{B}_0/4\pi$, which means gas pressure has to respond to magnetic pressure perturbation such that the total pressure is unchanged. Note that $\delta P = 0$ only when perturbation in magnetic pressure is zero. This is the case for Alfvén wave in ideal MHD, but no longer true in general when non-ideal MHD effects come into play. Therefore, the eigenvectors obtained in this subsection deviate from real eigenvectors for a compressible fluid. Nonetheless, the basic physics is well captured in this simplified treatment.

Equation (B-31) can be simplified to

$$\begin{aligned} \omega\delta\boldsymbol{v} &= -\frac{kB_{0z}}{4\pi\rho_0}\delta\boldsymbol{B}\ , \\ (\omega^2 - k^2 v_{Az}^2)\delta\boldsymbol{B} &= -i\frac{c\omega}{4\pi n_e e}kB_{0z}(\boldsymbol{k}\times\delta\boldsymbol{B})\ , \end{aligned} \tag{B-32}$$

where $v_{Az}^2 = B_{0z}^2/4\pi\rho_0$ is the Alfvén velocity along the $\hat{z}$ direction. For non-trivial perturbations, one must have $\delta B_x = \pm i\delta B_y$, which corresponds to circularly polarized Alfvén waves. The dispersion relation reads

$$\omega^2 - k^2 v_{Az}^2 = \pm\omega k^2 \frac{cB_{0z}}{4\pi n_e e} \ , \tag{B-33}$$

where the plus (minus) sign correspond to right (left) hand Alfvén waves. The above dispersion relation can be rewritten into a more intuitive form as

$$\omega^2 = \left(1 \pm \frac{\omega}{\omega_h}\right) k^2 v_{Az}^2 \ , \tag{B-34}$$

where $\omega_h = en_e B/\rho c = (\rho_i/\rho)\omega_i$. The right-hand wave goes over to the whistler branch at large k (e.g., $\omega \propto k^2$), while the left-hand wave is cut off at frequency ω_h.

We normalize the frequency by $y \equiv \omega/\omega_h$, and normalize the wave number by $x \equiv kv_A/\omega_h$. The phase velocity is therefore normalized by v_A, given by

$$\frac{v_{\rm ph}}{v_A} = \frac{\sqrt{x^2+4} \pm x}{2} \ , \tag{B-35}$$

where the plus/minus sign corresponds to right (whistler)/left polarized Alfvén waves.

Below we describe the code test with Athena. We first note that for compressible gas, circularly polarized waves are incompressible (i.e., $\delta P = 0$) only when $\boldsymbol{k} \parallel \boldsymbol{B}$. Therefore, we always consider waves propagating along the magnetic field (since Athena deals with compressible gas). In this problem, the only time scale is ω_h, and the only velocity scale is v_A. Therefore, we can simply set $\omega_h = 1$ as the time unit, and $v_A/\omega_h = 1$ as the length unit. The background gas density in the code is $\rho_0 = 1$, thus the magnetic field $B_0 = 1$. We use isothermal equation of state with $c_s = 1$ (although it is irrelevant in this problem). Therefore, we set $Q_H = 1$.

We perform simulations in 1D, 2D and 3D with the same setup as in the linear wave damping test except with eigen-vectors set for the circularly polarized Alfvén wave problem. We run the test with different wave numbers k by changing the box size, where the wavelength varies from $\lambda = 0.16$ to $\lambda = 16$ (unit is $2\pi\omega_h/v_A$). The amplitude of the perturbed field is taken to be $|\delta\boldsymbol{B}| = 10^{-4}|\boldsymbol{B}|$. We run the waves from time $t = 0$ to $t = 5$, and measure the phase change at constant time intervals (by fitting a sinusoidal curve), and then fit the phase velocity by linear regression. In Figure B.4, we show the measured dispersion relation for right (whistler) and left handed circularly polarized Alfvén waves and compare them with analytical relations. We see that the agreement is excellent in all cases. In particular, we are able to resolve the whistler wave up to very large k.

Appendix C

Chemical Reaction Network: Description and Implementation

A chemical reaction network is essential for determining the level of ionization hence to evaluate the strength of all non-ideal MHD terms. The most convenient chemical reaction network is that proposed by Oppenheimer & Dalgarno (1974) for dense molecular clouds but also widely applied to protostellar disks (e.g., Gammie 1996; Glassgold et al. 1997; Fromang et al. 2002; Turner et al. 2007). This network is basically a two-element kinetic model involving five species: a molecular species m; a neutral atomic gas-phase metal M; their ionized counterparts m^+ and M^+, and free electrons e^-. There are four reactions representing ionization, recombination and charge exchange respectively with rate coefficients calibrated to match more realistic situations. In our work, we adopt a much more complex chemical reaction network by Ilgner & Nelson (2006) (hereafter IN06) that includes more than 2000 chemical reactions, which is presumably more realistic in nature. Comparison with the simple network does indicates non-negligible differences between the two networks (Bai & Goodman 2009). In this Appendix, we describe this complex network, providing the calculation of all reaction rate coefficients, as well as the numerical method for evolving the network for millions of years.

1. Gas-phase Reactions

Following IN06, our network includes nine elements (H, He, C, O, N, S, Si, Mg, and Fe) and 174 species as given by Table A.1 of IN06. We extract 2109 reactions involving these species from

1.	H_2	$\rightarrow$	$H_2^+ + e^-$	$0.97 \cdot \zeta^{\rm eff}$
2.	H_2	$\rightarrow$	$H^+ + H + e^-$	$0.03 \cdot \zeta^{\rm eff}$
3.	H	$\rightarrow$	$H^+ + e^-$	$0.50 \cdot \zeta^{\rm eff}$
4.	He	$\rightarrow$	$He^+ + e^-$	$0.84 \cdot \zeta^{\rm eff}$

Table C.1: Ionization reactions. Final column is the ionization rate for the reaction shown.

the latest version of UMIST database (Woodall et al. 2007) . Our selection for the gas-phase chemical reactions include ionization reactions, neutral-neutral reactions, ion-neutral reactions, charge exchanges, dissociative recombinations, radiative recombinations, radiative attachments, and collisional dissociations. Besides the ionization reactions, which is given in Table C.1, with $\zeta^{\rm eff}$ being the effective ionization rate, all the other reactions are extracted exclusively from the UMIST database. We have neglected photo reactions because of the poor penetration of UV into the disk. We also neglect "collider" reactions, which have very low rate coefficients. Reactions involving cosmic-ray (CR) protons and CR photons in the database are also excluded, since we have already included the dominant reactions in Table C.1. There are in total 2083 gas-phase chemical reactions, which is 117 more reactions than IN06, who used an older (1999) version of the database [1].

The rate coefficients in the UMIST database are given as functions of temperature, given in the form of

$$k = \alpha(T/300K)^{\beta} \exp(-\gamma/T) \mathrm{cm}^3 \ \mathrm{s}^{-1} \tag{C-1}$$

for two-body reactions and for a given temperature range. Where the local disk temperature lies outside the stated range of validity, we adopt the same procedure as IN06: we replace $T_{\rm disk}$ with the upper or lower bound of the valid range, as appropriate, before computing the rate.

2. Reactions with Dust Grains

Dust grains are efficient absorbers of free electrons. Grains also interact with other neutral and ionized species mainly by adsorption, desorption and charge exchange. Further, adsorbed species hop on grain surfaces, and reactions can take place on grain surfaces. There is currently no standard database for grain reactions. We follow the prescriptions of IN06 involving "mantle chemistry" and "grain chemistry". The maximum grain charge is taken to be ± 3, ± 10 and ± 30

[1] Also note that in the new version of UMIST database, several species names are changed.

for grains whose size is $\lesssim 0.01\mu$m, 0.1μm and 1μm respectively (note that IN06 adopted ± 2 for all grains). We adopt this choice since larger grains can possess more negative charges at the given electrostatic potential (Okuzumi 2009; Perez-Becker & Chiang 2011a).

Mantle species are adsorbed counterparts of gas-phase neutral species. Reactions that involve mantle species belong to mantle chemistry, as given by Table 3 of IN06. A mantle species X[gr] is formed by collisions between a neutral species X or its ionized counterpart X^+ with a grain particle, and is destroyed by desorption. The mantle species defined here are independent of grain charge.

Other grain-related reactions belong to grain chemistry, as given by Table 4 of IN06. These include charge-exchange reactions between ionized species and negatively charged grains, absorption of free electrons by grains, and grain charge-exchange reactions. Several ionized species do not have any neutral counterpart (e.g. H_3^+, H_3O^+), as needed in the charge-exchange reactions. Following IN06, we assume the products of these reactions to be the same as for dissociative reactions in the gas phase, e.g. $H_3^+ + gr^- \rightarrow 3H + gr$. If there are multiple final states, we adopt the gas-phase branching ratio.

Below we describe our adopted grain properties and outline the calculation of rate coefficients for grain reactions.

2.1 Assumptions about Grains

All grains are taken to be spherical with density $\rho_d = 3\,\mathrm{g\,cm^{-3}}$. Ideally, one should consider a size distribution of grains. The conventional choice for interstellar grains is the MRN size distribution (Mathis et al. 1977)

$$N(a)da \propto a^{-3.5}da, \qquad a_{\min} \le a \le a_{\max}\ , \tag{C-2}$$

where a is grain radius, and the usual cutoffs are $a_{\min} \approx 0.005\mu$m and $a_{\max} \approx 0.25\mu$m. Although our code is capable of handling multiple populations of grains, we adopt a simplified prescription of single-sized, well-mixed grains, with the default grain size to be 0.1μm, similar as most previous works (Ilgner & Nelson 2006; Salmeron & Wardle 2008). The calculations in Bai & Goodman (2009) found that when a range of grain sizes are considered, the controlling parameter lies somewhere between the total grain surface area, and the grain abundance weighted by linear size. For a population grains with *mass* distribution $f(a)$ (with $\int f(a)da = Z$, Z is the total abundance of

grains), one may conveniently consider

$$S \equiv \int_{a_{\rm min}}^{a_{\rm max}} da \left(\frac{a}{1\mu{\rm m}}\right)^{-3/2} \frac{f(a)}{0.01} \tag{C-3}$$

as a measure of the chemical significance of dust grains. Choices of $a = 0.1\mu$m and $a = 1\mu$m without depletion ($Z = 0.01$) correspond to $S = 32$ and $S = 1$ respectively. For a continuous size distribution of grains, the situation can be more complicated, but one may calculate the resulting S and use our results as a guide.

Each grain population has its own mantle and grain chemistry. Collisions between the two populations are allowed and cause charge exchange in the same way as collisions among members of the same size population. We assign equal branching ratios to the transfer of one or two electrons. In fact, we find that collisions between grains belonging to different size populations are unimportant. We will show that the electron abundance, and therefore the size of the active zone, is dominated by the smallest grains.

2.2 Grain reaction rates

1. Collisions between ions/electrons and grains. These reactions correspond to reactions 7, 8 in Table 3 and reactions 1-6 in Table 4 of IN06. They recombine free electrons and add to the Ohmic resistivity. The rate coefficients involve collision rates and the probability that an electron stays on a grain after colliding with it (sticking coefficient).

The collision rate is estimated following equations (3.1) and (3.3)-(3.5) of Draine & Sutin (1987), it is modulated by Coulomb interactions and induced polarization. The sticking coefficient S is estimated as follows. For ion-grain collisions S is insensitive to temperature, so we take $S_{X^+} = 1$. The sticking coefficient S_e for electron-ion collisions is more subtle. We follow the calculations in the Appendix of Bai (2011a) which generalizes the calculation by Nishi et al. (1991) from electron-neutral grain collisions to electron-charged grain collisions. In brief, electrons undergo elastic and inelastic scatterings (assumed to be isotropic) with grains until absorbed. The electron sticking coefficient depends sensitively on temperature. For the purpose of calculating S_e, we assume that the grains are made of graphite, with atomic weight 12, Debye temperature 420K, and electron binding energy $D_e = 1\,{\rm eV}$.

2. Collisions between neutral gas-phase particles and grains. These correspond to reactions 1-5 of Table 3 in IN06. These reactions can potentially deplete gas-phase species by adsorbing them onto grain surfaces, if the inverse of this process (desorption) is slow. Similar to the previous case, the rate coefficients are expressed by the product of collision rate and sticking coefficient. The collision rate is just geometric. For incident particle energy E_i, the probability of being adsorbed is approximately $P_\epsilon = \exp(-\epsilon^2/2)$, where $\epsilon = E_i/\sqrt{D\Delta E_s}$ (Hollenbach & Salpeter 1970); D and ΔE_s denote the dissociation energy and the amount of energy transferred to the grain particle as lattice vibrations, respectively. For each neutral gas-phase particle, D is approximated by its binding energy E_D as given in Table A 2 of IN06a, and ΔE_s is approximated by $2.0 \times 10^{-3}\,\mathrm{eV}$. The sticking coefficient is then obtained by integrating P_ϵ over a thermal energy distribution of E_i.

3. Collisions between grains. These are reactions 7-10 in Table 4 of IN06a. They redistribute charge among grain particles. We calculate the collision rates from equation (3) of Umebayashi & Nakano (1990). Note that we take $\rho_d = 3\,\mathrm{g\,cm^{-3}}$. Since the abundance and thermal velocities of grains are low, these reactions occur very slowly.

4. Desorption processes. These are described by reaction 6 in Table 3 of IN06a. Mantle species migrate among surface sites at a characteristic thermal hopping frequency (Hasegawa et al. 1992)

$$\nu_0 = \sqrt{\frac{2n_s E_D}{\pi^2 m}}\ , \tag{C-4}$$

where $n_s \approx 10^{15}\mathrm{cm^{-2}}$ is the surface number density of binding sites, and m is the mass of the adsorbed species. The desorption rate of mantle species via thermal hopping is then

$$k = \nu_0 \exp(-E_D/kT_d)\ , \tag{C-5}$$

where T_d is the temperature of the dust, taken to be the same as the gas temperature.

Note that both adsorption and desorption rates have an exponential factor. For adsorption rate, the exponential factor is $\sim \exp\left[-(T/T_0)^2\right]$, where T_0 depends on E_D and grain size. For desorption rate, the exponential factor is $\exp\left(-E_D/T\right)$. At relatively high temperature (e.g. $T \gtrsim 100\mathrm{K}$ for metals), the desorption rate is much higher than adsorption rate (since ν_0 is quite large), hence almost all species are in the gas phase. As the temperature decreases, the mantle abundance increases super-exponentially. This is particularly pronounced for metals because they

have large binding energy E_D. For example, the binding energy of magnesium is $E_D = 5300\,\mathrm{K}$. Balancing adsorption and desorption processes, we obtain

$$\frac{n_{\mathrm{Mg}}}{n_{\mathrm{Mg[m]}}} \simeq \frac{1.34\times10^{15}\exp\left(-5300\mathrm{K}/T\right)\exp\left[(T/496\mathrm{K})^2\right]}{(n_{\mathrm{gr}}/1\mathrm{cm}^{-3})\times(T/300\mathrm{K})^{1/2}(a/1\mu\mathrm{m})}\ . \tag{C-6}$$

For $n_{\mathrm{gr}} = 0.1\mathrm{cm}^{-3}$, $a = 0.1\mu$m, and $T = 300$K, the ratio (C-6) is about 4.1×10^9. However, at 100K, the ratio becomes as small as 2.3×10^{-6}. The critical temperature $T \approx 150$K, below which most metals are adsorbed onto grains.

2.3 H_2 Formation on Grain Surfaces

In the interstellar medium, grains catalyze many reactions. Adsorbed atoms and molecules hop among sites until they collide, and the heat of reaction is absorbed by grain lattices. Most importantly, H_2 is very efficiently formed on grains in dense molecular clouds, where $T \lesssim 20$K. Whether H_2 formation on grains is still important at the higher temperatures of protostellar disks is unknown. Cazaux & Tielens (2002, 2004) proposed a model incorporating both physisorption and chemisorption of H atoms on grains. Physisorption is the adsorption process mentioned above, whereas chemisorption involves much stronger ($\sim 1\,\mathrm{eV}$) chemical bonds. Radical species with unpaired electrons are likely to be chemisorbed. At low temperatures, H_2 forms mainly by interactions between a physisorbed and a chemisorbed H atom; at high temperature, two chemisorbed H atoms are involved. The works cited above found that H_2 formation can be efficient up to about 500K, with efficiency up to about 0.2. The formation efficiency was updated by Cazaux & Tielens (2010) after correcting for an error in their calculation found by Bai & Goodman (2009) that leads to a further increase in the formation efficiency.

In our calculations, we find that if H_2 formation were not considered, almost all hydrogen would ultimately be converted into atomic form, an unlikely state for a PPD. In Bai & Goodman (2009), we have included the H_2 formation on grain surface with a default efficiency of 10^{-3}. It was found as long as H_2 is the dominant form of hydrogen, the resulting ionization fraction is independent of the H_2 formation efficiency. Therefore, we simply add a gas-phase reaction of $\mathrm{H} + \mathrm{H} \rightarrow \mathrm{H_2}$ with appropriate rate coefficient (10^{-9} c.g.s) to guarantee the dominance of H_2.

3. Numerical Method

We normalize the abundance (proportional to number density) of hydrogen atoms to unity, and all other elements and grains proportionately, with the relative elemental abundances given in Table 6 of IN06. Elements in the gas phase other than hydrogen and helium are depleted compared with solar abundance. The abundances of the metals are taken to be 1.0×10^{-8} for Mg, and 2.5×10^{-9} for Fe. The grain abundance is variable. Note that we use x_i to denote elemental abundances, and $x[X]$ to denote the abundance of species X. All grains are initially neutral, and all elements in their atomic form except hydrogen.

The chemical evolution equations are a set of first order ordinary differential equations (ODEs). Due to a broad ranges of reaction rates, these equations are very stiff. We use the `stiff.c` subroutine described in Press et al. (1992) as the main integrator, which uses the Kaps-Rentrop algorithm, a 4th order implicit method. Also note that although the evolution equations conserve charge and elemental abundances, they are no longer conserved due to truncation errors. In our code, we enforce conservation after each step by adjusting the elemental abundances and x_e. The integrator efficiently evolves the system for 10^{6-7} years to reach chemical equilibrium.

Bibliography

Acke, B., & van den Ancker, M. E. 2004, A&A, 426, 151

Adams, F. C., Lada, C. J., & Shu, F. H. 1987, ApJ, 312, 788

Alexiades, V., Amiez, G., & Gremaud, P. 1996, Communications in Numerical Methods in Engineering, 12, 31

Anderson, J. M., Li, Z.-Y., Krasnopolsky, R., & Blandford, R. D. 2003, ApJ, 590, L107

—. 2005, ApJ, 630, 945

Andrews, S. M., & Williams, J. P. 2005, ApJ, 631, 1134

Andrews, S. M., Wilner, D. J., Hughes, A. M., Qi, C., & Dullemond, C. P. 2009, ApJ, 700, 1502

—. 2010, ApJ, 723, 1241

Armitage, P. J. 1998, ApJ, 501, L189+

—. 2011, ARA&A

Bacciotti, F., Ray, T. P., Mundt, R., Eislöffel, J., & Solf, J. 2002, ApJ, 576, 222

Bai, X.-N. 2011a, ApJ, 739, 50

—. 2011b, ApJ, 739, 51

Bai, X.-N., & Goodman, J. 2009, ApJ, 701, 737

Bai, X.-N., & Stone, J. M. 2010a, ApJS, 190, 297

—. 2010b, ApJ, 722, 1437

—. 2010c, ApJ, 722, L220

—. 2011, ApJ, 736, 144

—. 2012a, in preparation

—. 2012b, in preparation

Balbus, S. A. 2003, ARA&A, 41, 555

Balbus, S. A., & Hawley, J. F. 1991, ApJ, 376, 214

—. 1992, ApJ, 400, 610

Balbus, S. A., & Terquem, C. 2001, ApJ, 552, 235

Balsara, D. S. 1996, ApJ, 465, 775

Blaes, O. M., & Balbus, S. A. 1994, ApJ, 421, 163

Blandford, R. D., & Payne, D. G. 1982, MNRAS, 199, 883

Blum, J., & Wurm, G. 2008, ARA&A, 46, 21

Bodo, G., Mignone, A., Cattaneo, F., Rossi, P., & Ferrari, A. 2008, A&A, 487, 1

Brandenburg, A., Nordlund, A., Stein, R. F., & Torkelsson, U. 1995, ApJ, 446, 741

Brandenburg, A., & Zweibel, E. G. 1994, ApJ, 427, L91

Brauer, F., Dullemond, C. P., & Henning, T. 2008, A&A, 480, 859

Cabot, W. 1996, ApJ, 465, 874

Cabrit, S., Edwards, S., Strom, S. E., & Strom, K. M. 1990, ApJ, 354, 687

Calvet, N., D'Alessio, P., Hartmann, L., Wilner, D., Walsh, A., & Sitko, M. 2002, ApJ, 568, 1008

Calvet, N., et al. 2005, ApJ, 630, L185

Calvet, N., & Gullbring, E. 1998, ApJ, 509, 802

Calvet, N., Muzerolle, J., Briceño, C., Hernández, J., Hartmann, L., Saucedo, J. L., & Gordon, K. D. 2004, AJ, 128, 1294

Carballido, A., Bai, X., & Cuzzi, J. N. 2011, MNRAS, 415, 93

Carr, J. S., & Najita, J. R. 2008, Science, 319, 1504

Casse, F., & Keppens, R. 2002, ApJ, 581, 988

—. 2004, ApJ, 601, 90

Cazaux, S., & Tielens, A. G. G. M. 2002, ApJ, 575, L29

—. 2004, ApJ, 604, 222

—. 2010, ApJ, 715, 698

Chiang, E., & Murray-Clay, R. 2007, Nature Physics, 3, 604

Chiang, E., & Youdin, A. N. 2010, Annual Review of Earth and Planetary Sciences, 38, 493

Chiang, E. I., & Goldreich, P. 1997, ApJ, 490, 368

—. 1999, ApJ, 519, 279

Chiang, E. I., Joung, M. K., Creech-Eakman, M. J., Qi, C., Kessler, J. E., Blake, G. A., & van Dishoeck, E. F. 2001, ApJ, 547, 1077

Cho, J., & Lazarian, A. 2007, ApJ, 669, 1085

Choi, E., Kim, J., & Wiita, P. J. 2009, ApJS, 181, 413

Combet, C., & Ferreira, J. 2008, A&A, 479, 481

D'Alessio, P., Calvet, N., & Hartmann, L. 2001, ApJ, 553, 321

D'Alessio, P., Calvet, N., Hartmann, L., Franco-Hernández, R., & Servín, H. 2006, ApJ, 638, 314

D'Alessio, P., Canto, J., Calvet, N., & Lizano, S. 1998, ApJ, 500, 411

Davis, S. W., Stone, J. M., & Pessah, M. E. 2010, ApJ, 713, 52

Desch, S. J. 2004, ApJ, 608, 509

—. 2007, ApJ, 671, 878

Dong, R., et al. 2012, ApJ, 750, 161

Draine, B. T. 1980, ApJ, 241, 1021

—. 2011, Physics of the Interstellar and Intergalactic Medium (Princeton and Oxford: Princeton University Press)

Draine, B. T., Roberge, W. G., & Dalgarno, A. 1983, ApJ, 264, 485

Draine, B. T., & Sutin, B. 1987, ApJ, 320, 803

Dullemond, C. P., & Dominik, C. 2004, A&A, 417, 159

Dzyurkevich, N., Flock, M., Turner, N. J., Klahr, H., & Henning, T. 2010, A&A, 515, A70+

Espaillat, C., Calvet, N., D'Alessio, P., Hernández, J., Qi, C., Hartmann, L., Furlan, E., & Watson, D. M. 2007, ApJ, 670, L135

Espaillat, C., et al. 2010, ApJ, 717, 441

Evans, C. R., & Hawley, J. F. 1988, ApJ, 332, 659

Falle, S. A. E. G. 2003, MNRAS, 344, 1210

Fang, M., van Boekel, R., Wang, W., Carmona, A., Sicilia-Aguilar, A., & Henning, T. 2009, A&A, 504, 461

Feigelson, E., Townsley, L., Güdel, M., & Stassun, K. 2007, Protostars and Planets V, 313

Flaig, M., Ruoff, P., Kley, W., & Kissmann, R. 2012, MNRAS, 420, 2419

Fleming, T., & Stone, J. M. 2003, ApJ, 585, 908

Fleming, T. P., Stone, J. M., & Hawley, J. F. 2000, ApJ, 530, 464

Flock, M., Dzyurkevich, N., Klahr, H., Turner, N. J., & Henning, T. 2011, ApJ, 735, 122

Fromang, S., & Nelson, R. P. 2006, A&A, 457, 343

Fromang, S., & Papaloizou, J. 2006, A&A, 452, 751

—. 2007, A&A, 476, 1113

Fromang, S., Terquem, C., & Balbus, S. A. 2002, MNRAS, 329, 18

Furlan, E., et al. 2006, ApJS, 165, 568

Gammie, C. F. 1996, ApJ, 457, 355

—. 2001, ApJ, 553, 174

Gammie, C. F., & Balbus, S. A. 1994, MNRAS, 270, 138

Gardiner, T. A., & Stone, J. M. 2005, Journal of Computational Physics, 205, 509

—. 2008, Journal of Computational Physics, 227, 4123

Geers, V. C., et al. 2006, A&A, 459, 545

Geers, V. C., van Dishoeck, E. F., Visser, R., Pontoppidan, K. M., Augereau, J.-C., Habart, E., & Lagrange, A. M. 2007, A&A, 476, 279

Glassgold, A. E., Najita, J., & Igea, J. 1997, ApJ, 480, 344

—. 2004, ApJ, 615, 972

Goldreich, P., & Lynden-Bell, D. 1965, MNRAS, 130, 125

Goldreich, P., & Tremaine, S. 1980, ApJ, 241, 425

Goodman, J., & Xu, G. 1994, ApJ, 432, 213

Gorti, U., & Hollenbach, D. 2004, ApJ, 613, 424

Greene, T. P., Wilking, B. A., Andre, P., Young, E. T., & Lada, C. J. 1994, ApJ, 434, 614

Guan, X., & Gammie, C. F. 2011, ApJ, 728, 130

Güdel, M., et al. 2007, A&A, 468, 353

Gullbring, E., Calvet, N., Muzerolle, J., & Hartmann, L. 2000, ApJ, 544, 927

Gullbring, E., Hartmann, L., Briceno, C., & Calvet, N. 1998, ApJ, 492, 323

Gutermuth, R. A., et al. 2008, ApJ, 674, 336

Hartigan, P., Edwards, S., & Ghandour, L. 1995, ApJ, 452, 736

Hartigan, P., Edwards, S., & Pierson, R. 2004, ApJ, 609, 261

Hartmann, L., Calvet, N., Gullbring, E., & D'Alessio, P. 1998, ApJ, 495, 385

Hartmann, L., Megeath, S. T., Allen, L., Luhman, K., Calvet, N., D'Alessio, P., Franco-Hernandez, R., & Fazio, G. 2005, ApJ, 629, 881

Hasegawa, T. I., Herbst, E., & Leung, C. M. 1992, ApJS, 82, 167

Hawley, J. F. 2000, ApJ, 528, 462

—. 2001, ApJ, 554, 534

Hawley, J. F., Gammie, C. F., & Balbus, S. A. 1995, ApJ, 440, 742

Hawley, J. F., & Stone, J. M. 1998, ApJ, 501, 758

Hayashi, C. 1981, Progress of Theoretical Physics Supplement, 70, 35

Heinemann, T., & Papaloizou, J. C. B. 2009a, MNRAS, 397, 52

—. 2009b, MNRAS, 397, 64

Herczeg, G. J., & Hillenbrand, L. A. 2008, ApJ, 681, 594

Hillenbrand, L. A., Strom, S. E., Calvet, N., Merrill, K. M., Gatley, I., Makidon, R. B., Meyer, M. R., & Skrutskie, M. F. 1998, AJ, 116, 1816

Hirose, S., & Turner, N. J. 2011, ApJ, 732, L30

Hirth, G. A., Mundt, R., & Solf, J. 1997, A&AS, 126, 437

Hollenbach, D., & Salpeter, E. E. 1970, J. Chem. Phys., 53, 79

Hughes, A. M., Wilner, D. J., Andrews, S. M., Qi, C., & Hogerheijde, M. R. 2011, ApJ, 727, 85

Hughes, A. M., Wilner, D. J., Calvet, N., D'Alessio, P., Claussen, M. J., & Hogerheijde, M. R. 2007, ApJ, 664, 536

Hughes, A. M., Wilner, D. J., Cho, J., Marrone, D. P., Lazarian, A., Andrews, S. M., & Rao, R. 2009, ApJ, 704, 1204

Igea, J., & Glassgold, A. E. 1999, ApJ, 518, 848

Ilgner, M., & Nelson, R. P. 2006, A&A, 445, 205

—. 2008, A&A, 483, 815

Ji, H., Burin, M., Schartman, E., & Goodman, J. 2006, Nature, 444, 343

Jin, L. 1996, ApJ, 457, 798

Johansen, A., Oishi, J. S., Low, M.-M. M., Klahr, H., Henning, T., & Youdin, A. 2007, Nature, 448, 1022

Johansen, A., Youdin, A., & Klahr, H. 2009a, ApJ, 697, 1269

Johansen, A., Youdin, A., & Mac Low, M. 2009b, ApJ, 704, L75

Johnson, B. M., Guan, X., & Gammie, C. F. 2008, ApJS, 177, 373

Johnson, E. T., Goodman, J., & Menou, K. 2006, ApJ, 647, 1413

Kato, S. X., Kudoh, T., & Shibata, K. 2002, ApJ, 565, 1035

Kim, K. H., et al. 2009, ApJ, 700, 1017

Klahr, H. H., & Bodenheimer, P. 2003, ApJ, 582, 869

Kley, W., & Nelson, R. P. 2012, ARA&A, 50

Königl, A., Salmeron, R., & Wardle, M. 2010, MNRAS, 401, 479

Krasnopolsky, R., Li, Z.-Y., & Blandford, R. 1999, ApJ, 526, 631

Krasnopolsky, R., Li, Z.-Y., & Blandford, R. D. 2003, ApJ, 595, 631

Kunz, M. W., & Balbus, S. A. 2004, MNRAS, 348, 355

Lada, C. J. 1987, in IAU Symposium, Vol. 115, Star Forming Regions, ed. M. Peimbert & J. Jugaku, 1–17

Lada, C. J., et al. 2006, AJ, 131, 1574

Lee, A. T., Chiang, E., Asay-Davis, X., & Barranco, J. 2010, ApJ, 725, 1938

Lesur, G., & Longaretti, P.-Y. 2005, A&A, 444, 25

Lesur, G., & Ogilvie, G. I. 2010, MNRAS, 404, L64

Lesur, G., & Papaloizou, J. C. B. 2010, A&A, 513, A60

Li, P. S., McKee, C. F., & Klein, R. I. 2006, ApJ, 653, 1280

Li, Z.-Y. 1995, ApJ, 444, 848

Lin, D. N. C., & Papaloizou, J. 1980, MNRAS, 191, 37

—. 1986, ApJ, 309, 846

Lyra, W., & Klahr, H. 2011, A&A, 527, A138

Mac Low, M., Norman, M. L., Konigl, A., & Wardle, M. 1995, ApJ, 442, 726

Martin, R. G., & Lubow, S. H. 2011, ApJ, 740, L6

Martin, R. G., Lubow, S. H., Livio, M., & Pringle, J. E. 2012, MNRAS, 420, 3139

Masset, F. 2000, A&AS, 141, 165

Mathis, J. S., Rumpl, W., & Nordsieck, K. H. 1977, ApJ, 217, 425

McCall, B. J., et al. 2003, Nature, 422, 500

Miller, K. A., & Stone, J. M. 2000, ApJ, 534, 398

Muzerolle, J., Calvet, N., & Hartmann, L. 2001, ApJ, 550, 944

Muzerolle, J., Hartmann, L., & Calvet, N. 1998, AJ, 116, 455

Muzerolle, J., Luhman, K. L., Briceño, C., Hartmann, L., & Calvet, N. 2005, ApJ, 625, 906

Najita, J., Carr, J. S., & Mathieu, R. D. 2003, ApJ, 589, 931

Najita, J. R., Strom, S. E., & Muzerolle, J. 2007, MNRAS, 378, 369

Natta, A., Testi, L., Calvet, N., Henning, T., Waters, R., & Wilner, D. 2007, in Protostars and Planets V, ed. B. Reipurth, D. Jewitt, & K. Keil, 767–781

Natta, A., Testi, L., & Randich, S. 2006, A&A, 452, 245

Nelson, R. P., & Gressel, O. 2010, MNRAS, 409, 639

Nishi, R., Nakano, T., & Umebayashi, T. 1991, ApJ, 368, 181

Ogilvie, G. I. 2012, MNRAS, 423, 1318

Ogilvie, G. I., & Livio, M. 2001, ApJ, 553, 158

Oishi, J. S., & Mac Low, M. 2009, ApJ, 704, 1239

Okuzumi, S. 2009, ApJ, 698, 1122

Okuzumi, S., & Hirose, S. 2011, ApJ, 742, 65

—. 2012, ApJ, 753, L8

Oliveira, I., et al. 2010, ApJ, 714, 778

Oppenheimer, M., & Dalgarno, A. 1974, ApJ, 192, 29

Ormel, C. W., & Cuzzi, J. N. 2007, A&A, 466, 413

O'Sullivan, S., & Downes, T. P. 2006, MNRAS, 366, 1329

—. 2007, MNRAS, 376, 1648

Ouyed, R., & Pudritz, R. E. 1997, ApJ, 482, 712

Ouyed, R., Pudritz, R. E., & Stone, J. M. 1997, Nature, 385, 409

Paardekooper, S.-J., Baruteau, C., Crida, A., & Kley, W. 2010, MNRAS, 401, 1950

Pandey, B. P., & Wardle, M. 2012, MNRAS, 3001

Papaloizou, J. C. B., & Terquem, C. 1997, MNRAS, 287, 771

Pelletier, G., & Pudritz, R. E. 1992, ApJ, 394, 117

Perez-Becker, D., & Chiang, E. 2011a, ApJ, 727, 2

—. 2011b, ApJ, 735, 8

Pessah, M. E. 2010, ApJ, 716, 1012

Pessah, M. E., & Chan, C. 2008, ApJ, 684, 498

Pessah, M. E., & Goodman, J. 2009, ApJ, 698, L72

Petersen, M. R., Julien, K., & Stewart, G. R. 2007a, ApJ, 658, 1236

Petersen, M. R., Stewart, G. R., & Julien, K. 2007b, ApJ, 658, 1252

Pontoppidan, K. M., Salyk, C., Blake, G. A., & Käufl, H. U. 2010, ApJ, 722, L173

Preibisch, T., et al. 2005, ApJS, 160, 401

Press, W. H., Teukolsky, S. A., Vetterling, W. T., & Flannery, B. P. 1992, Numerical recipes in C. The art of scientific computing, ed. Press, W. H., Teukolsky, S. A., Vetterling, W. T., & Flannery, B. P.

Przygodda, F., van Boekel, R., Àbrahàm, P., Melnikov, S. Y., Waters, L. B. F. M., & Leinert, C. 2003, A&A, 412, L43

Pudritz, R. E., & Norman, C. A. 1983, ApJ, 274, 677

Pyo, T.-S., et al. 2003, ApJ, 590, 340

Rafikov, R. R. 2009, ApJ, 704, 281

Ray, T., Dougados, C., Bacciotti, F., Eislöffel, J., & Chrysostomou, A. 2007, Protostars and Planets V, 231

Rice, W. K. M., Lodato, G., & Armitage, P. J. 2005, MNRAS, 364, L56

Rice, W. K. M., Mayo, J. H., & Armitage, P. J. 2010, MNRAS, 402, 1740

Rodmann, J., Henning, T., Chandler, C. J., Mundy, L. G., & Wilner, D. J. 2006, A&A, 446, 211

Ryu, D., & Goodman, J. 1992, ApJ, 388, 438

Ryu, D., Jones, T. W., & Frank, A. 1995, ApJ, 452, 785

Salmeron, R., Königl, A., & Wardle, M. 2007, MNRAS, 375, 177

—. 2011, MNRAS, 412, 1162

Salmeron, R., & Wardle, M. 2003, MNRAS, 345, 992

—. 2005, MNRAS, 361, 45

—. 2008, MNRAS, 388, 1223

Salyk, C., Pontoppidan, K. M., Blake, G. A., Lahuis, F., van Dishoeck, E. F., & Evans, II, N. J. 2008, ApJ, 676, L49

Sano, T., Inutsuka, S., & Miyama, S. M. 1998, ApJ, 506, L57

Sano, T., Miyama, S. M., Umebayashi, T., & Nakano, T. 2000, ApJ, 543, 486

Sano, T., & Stone, J. M. 2002a, ApJ, 570, 314

—. 2002b, ApJ, 577, 534

Semenov, D., Wiebe, D., & Henning, T. 2004, A&A, 417, 93

Shakura, N. I., & Sunyaev, R. A. 1973, A&A, 24, 337

Shen, Y., Stone, J. M., & Gardiner, T. A. 2006, ApJ, 653, 513

Shi, J., Krolik, J. H., & Hirose, S. 2010, ApJ, 708, 1716

Shu, F. 1991, Physics of Astrophysics, Vol. II: Gas Dynamics, ed. Shu, F. (University Science Books)

Shu, F. H., Lizano, S., Galli, D., Cai, M. J., & Mohanty, S. 2008, ApJ, 682, L121

Sicilia-Aguilar, A., et al. 2006, ApJ, 638, 897

Sicilia-Aguilar, A., Hartmann, L. W., Hernández, J., Briceño, C., & Calvet, N. 2005, AJ, 130, 188

Sicilia-Aguilar, A., Henning, T., & Hartmann, L. W. 2010, ApJ, 710, 597

Simon, J. B., Bai, X., Stone, J. M., Armitage, P. J., & Beckwith, K. in preparation

Simon, J. B., Beckwith, K., & Armitage, P. J. 2012, MNRAS, 422, 2685

Simon, J. B., & Hawley, J. F. 2009, ApJ, 707, 833

Simon, J. B., Hawley, J. F., & Beckwith, K. 2011, ApJ, 730, 94

Smith, M. D., & Mac Low, M. 1997, A&A, 326, 801

Sorathia, K. A., Reynolds, C. S., Stone, J. M., & Beckwith, K. 2012, ApJ, 749, 189

Stelzer, B., Flaccomio, E., Briggs, K., Micela, G., Scelsi, L., Audard, M., Pillitteri, I., & Güdel, M. 2007, A&A, 468, 463

Stone, J. M. 1997, ApJ, 487, 271

Stone, J. M., & Balbus, S. A. 1996, ApJ, 464, 364

Stone, J. M., Gammie, C. F., Balbus, S. A., & Hawley, J. F. 2000, Protostars and Planets IV, 589

Stone, J. M., & Gardiner, T. A. 2010, ApJS, 189, 142

Stone, J. M., Gardiner, T. A., Teuben, P., Hawley, J. F., & Simon, J. B. 2008, ApJS, 178, 137

Stone, J. M., Hawley, J. F., Gammie, C. F., & Balbus, S. A. 1996, ApJ, 463, 656

Suzuki, T. K., & Inutsuka, S.-i. 2009, ApJ, 691, L49

Suzuki, T. K., Muto, T., & Inutsuka, S.-i. 2010, ApJ, 718, 1289

Tilley, D. A., & Balsara, D. S. 2008, MNRAS, 389, 1058

Toomre, A. 1964, ApJ, 139, 1217

Toth, G. 1994, ApJ, 425, 171

Tsiganis, K., Gomes, R., Morbidelli, A., & Levison, H. F. 2005, Nature, 435, 459

Turner, N. J., Carballido, A., & Sano, T. 2010, ApJ, 708, 188

Turner, N. J., & Drake, J. F. 2009, ApJ, 703, 2152

Turner, N. J., & Sano, T. 2008, ApJ, 679, L131

Turner, N. J., Sano, T., & Dziourkevitch, N. 2007, ApJ, 659, 729

Turner, N. J., Willacy, K., Bryden, G., & Yorke, H. W. 2006, ApJ, 639, 1218

Umebayashi, T., & Nakano, T. 1981, PASJ, 33, 617

—. 1990, MNRAS, 243, 103

—. 2009, ApJ, 690, 69

van Boekel, R., et al. 2004, Nature, 432, 479

van Boekel, R., Min, M., Waters, L. B. F. M., de Koter, A., Dominik, C., van den Ancker, M. E., & Bouwman, J. 2005, A&A, 437, 189

van Boekel, R., Waters, L. B. F. M., Dominik, C., Bouwman, J., de Koter, A., Dullemond, C. P., & Paresce, F. 2003, A&A, 400, L21

Vasyunin, A. I., Semenov, D., Henning, T., Wakelam, V., Herbst, E., & Sobolev, A. M. 2008, ApJ, 672, 629

Vorobyov, E. I., & Basu, S. 2007, MNRAS, 381, 1009

Wardle, M. 1999, MNRAS, 307, 849

—. 2007, Ap&SS, 311, 35

Wardle, M., & Koenigl, A. 1993, ApJ, 410, 218

Wardle, M., & Salmeron, R. 2012, MNRAS, 422, 2737

Watson, D. M., et al. 2009, ApJS, 180, 84

Weidenschilling, S. J. 1977, Ap&SS, 51, 153

Williams, J. P., & Cieza, L. A. 2011, ARA&A, 49, 67

Wilner, D. J., D'Alessio, P., Calvet, N., Claussen, M. J., & Hartmann, L. 2005, ApJ, 626, L109

Winters, W. F., Balbus, S. A., & Hawley, J. F. 2003, MNRAS, 340, 519

Woitas, J., Ray, T. P., Bacciotti, F., Davis, C. J., & Eislöffel, J. 2002, ApJ, 580, 336

Wolk, S. J., Harnden, Jr., F. R., Flaccomio, E., Micela, G., Favata, F., Shang, H., & Feigelson, E. D. 2005, ApJS, 160, 423

Woodall, J., Agúndez, M., Markwick-Kemper, A. J., & Millar, T. J. 2007, A&A, 466, 1197

Youdin, A. N. 2011, ApJ, 731, 99

Zanni, C., Ferrari, A., Rosner, R., Bodo, G., & Massaglia, S. 2007, A&A, 469, 811

Zhu, Z., Hartmann, L., Gammie, C., & McKinney, J. C. 2009, ApJ, 701, 620

Zhu, Z., Hartmann, L., Gammie, C. F., Book, L. G., Simon, J. B., & Engelhard, E. 2010a, ApJ, 713, 1134

Zhu, Z., Hartmann, L., & Gammie, C. 2010b, ApJ, 713, 1143

Zhu, Z., Nelson, R. P., Hartmann, L., Espaillat, C., & Calvet, N. 2011, ApJ, 729, 47

Zsom, A., Ormel, C. W., Güttler, C., Blum, J., & Dullemond, C. P. 2010, A&A, 513, A57+